FLOOD MAPPING IN THE ZAMBEZI REGION USING SYNTHETIC APERTURE RADAR

by

Maria Magaretha Magdalena Bessinger

Thesis submitted in fulfilment of the requirematerents for the degree Master of Science in Geoinformatics at Stellenbosch University.

Supervisor: Dr JN Kemp

Co-supervisor: Dr M Lück-Vogel

Department of Geography and Environmental Studies

March 2016

DECLARATION

By submitting this assignment electronically, I declare that the entirety of the work contained therein is my own, original work, that I am the sole author thereof (save to the extent explicitly otherwise stated), that reproduction and publication thereof by Stellenbosch University will not infringe any third party rights and that I have not previously in its entirety or in part submitted it for obtaining any qualification.

Date: March 2016

ABSTRACT

Floods occur annually in the Zambezi Region during the rainy seasons, causing economic losses and social disruption. Projected changes in climate and land use could worsen the effects of floods. SAR sensors are active sensors and operate in the microwave region and are therefore not restricted by time of day or inclement weather, making them well-suited for flood monitoring. The aim of this research is to examine the use of ASAR and PALSAR images (with acquisition dates ranging from 17 March 2009 to 30 May 2009) to determine flood extent by classifying open water bodies in the Zambezi Region using two different approaches: binary thresholding and active contour models (ACMs) using the Canny edge detector as initial contour. Classified images were then statistically and visually compared to Landsat images. For ASAR images, overall accuracies ranged between 70% and 99% for the threshold classification method and 58% and 98% for ACMs. For PALSAR images, overall accuracy ranged between 54% and 91% for the threshold classification method and between 60% and 96% for ACMs. Results obtained were adequate for both methods of classification, with thresholds only slightly outperforming ACMs for ASAR images, and ACMs only slightly outperforming thresholds for PALSAR images. These methods are binary classifications, which was acceptable for delineating open water bodies, but flooded vegetation areas were present and methods need to be extended to include these areas. Sensor properties such as wavelength, incidence angle and polarisation have an effect on the effectiveness of identifying flooded water bodies. Longer wavelengths are better suited for open water detection than shorter wavelengths, because of better penetration capabilities than shorter wavelengths. Shallower incidence angles are better suited for open water detection, but steeper incidence angles are better suited for flooded vegetation. HH-polarised imagery performed the best for open water body detection when open water surfaces were smooth, but cross-polarisations performed best when surface roughness was present. Therefore, HH- and HV- polarisations should provide sufficient discriminatory power required for open water and flooded vegetation regions.

KEY WORDS AND PHRASES:

Zambezi Region, floods, SAR, ASAR, PALSAR, thresholds, active contour models

OPSOMMING

Daar is jaarlikse vloede in die Zambezi Streek gedurende die reënseisoen wat ekonomiese verliese en ontwrigting in die gemeenskap tot gevolg het. Geprojekteerde veranderinge in klimaat en grondgebruik kan die gevolge van vloede vererger. SAR sensors is aktiewe sensors in die mikrogolf spektrum en word dus nie deur die tyd van die dag of gure weer beïnvloed nie, wat dit baie geskik maak om vloede te kontroleer. Die doelwit van hierdie navorsing is om die gebruik van ASAR en PALSAR beelde, wat tussen 17 Maart 2009 tot 30 Mei 2009 opgeneem is, te ondersoek ten einde die omvang van die vloed vas te stel deur die oopwaterliggame in die Zambezi Streek deur twee benaderings te volg: binêre drumpelwaardes en aktiewe kontoer modelle (AKMs) met die Canny rand detektor as aanvanklike kontoer. Geklassifiseerde beelde is dan statisties en visueel vergelyk met Landsat beelde. Die akkuraatheid vir ASAR beelde het tussen 70% en 99% gewissel vir die drumpel klassifikasie metode en tussen 58% en 98% vir die AKM klassifikasie metode. Die akkuraatheid vir PALSAR beelde het tussen 54% en 91% gewissel vir die drumpel klassifikasie metode en tussen 60% en 96% vir die AKM klassifikasie metode. Die resultate was voldoende vir beide klassifikasie metodes, maar drumpel waardes wat ietwat beter gevaar as AKMs met ASAR beelde en AKMs het ietwat beter gevaar as drumpelwaardes met PALSAR beelde. Hierdie metodes is binêre metodes wat aanvaarbaar was om oopwaterliggame af te baken, maar daar was oorstroomde begroeide gebiede teenwoordig en metodes moet aangepas en uitgebrei word om hierdie gebiede in te sluit. Sensor eienskappe soos golflengte, invalshoek en polarisasie het ’n invloed op die effektiwiteit van die identifisering van oorstroomde gebiede. Langer golflengtes is meer effektief om oopwaterliggame te identifiseer as kort golflengtes weens die beter deurdringing vermoëns as kort golflengtes. Groter invalshoeke is meer geskik vir oopwaterliggaam identifisering, maar kleiner invalshoeke is meer geskik vir oorstroomde plantegroei. HH-gepolariseerde beelde het die beste gevaar met die identifisering van oopwaterliggame met ’n gladde oppervlak, maar kruis-polarisering het beter gevaar as die oppervlakte onstuimig was, en daarom sal dit aanbeveel word om beide ’n HH-gepolariseerde en ’n HV-gepolariseerde beeld te gebruik om oopwaterliggame te klassifiseer.

TREFWOORDE EN -FRASES

Zambezi Streek, vloede, SAR, ASAR, PALSAR, drumpelwaardes, aktiewe kontoer modelle

ACKNOWLEDGEMENTS

My sincerest thanks to:

- My supervisor Dr JN Kemp for his enthusiasm and guidance through the entire research process;
- My co-supervisor Dr M Lück-Vogel for her invaluable advice, much needed technical assistance and encouragement;
- Mrs Z Munch for her insight, reassurances, constructive comments and significant contribution to the finished product;
- My family for their support and advice;
- Friends, especially my fellow Master's students, Tiani Moolman, Hendrik van der Merwe, Christian Smit, Gerrit Louw, Jason Gilbertson, Mokhine Motswaledi, Thendo Mugwena, Khaleed Ballim and Sebastian Wenger for support, helpful suggestions and assistance during the research process;
- Ms S Ortell for assistance during the submission process;
- Dr HM De Klerk and Mr NK Poona for advice and assistance;
- The Department of Geography and Environmental Studies;
- The European Space Agency for access to SAR data;
- The USGS Earth Explorer for access to Landsat data;
- The Okavango Basin Information System for access to data needed for mapping purposes;
- Dr J Mendelsohn for access to research data, thereby providing insight into the study area.

CONTENTS

DECLARATION ii
ABSTRACT iii
OPSOMMING iv
ACKNOWLEDGEMENTS v
CONTENTS vi
TABLES ix
FIGURES x
ACRONYMS AND ABBREVIATIONS xvi
CHAPTER 1 INTRODUCTION 1
1.1 BACKGROUND 1
1.2 RESEARCH PROBLEM 2
1.3 RESEARCH AIM AND OBJECTIVES 3
1.4 METHODOLOGY AND RESEARCH DESIGN 3
1.5 STUDY AREA 6
1.6 OUTLINE 11
CHAPTER 2 LITERATURE REVIEW 13
2.1 FLOODS AND FLOOD RISK 13
2.2 FACTORS INFLUENCING FLOOD FREQUENCY AND FLOOD RISK 14
2.2.1 Physical factors affecting floods and flood risk 14
2.2.1.1 Riverine floods 14
2.2.1.2 Coastal floods 15
2.2.2 Human activities affecting floods and flood risk 16
2.2.3 Climate change and its effect on flood risk 17
2.3 IMPACTS OF FLOODS 18
2.3.1 Human impacts 18
2.3.2 Economic impacts 19
2.3.3 Environmental impacts 19
2.4 REGIONAL FLOOD TRENDS IN THE LESS ECONOMICALLY DEVELOPED COUNTRIES 20
2.4.1 Asia 20

2.4.2 Central and South America **21**
2.4.3 Africa **22**
2.5 BASIC PRINCIPLES OF SAR IMAGERY **23**
2.5.1 General overview of SAR imagery **23**
2.5.2 Factors affecting received backscatter for SAR images **23**
2.5.2.1 Wavelength 23
2.5.2.2 Incidence angle 24
2.5.2.3 Polarisation 25
2.5.2.4 Surface roughness 26
2.5.2.5 Double bounce 27
2.5.2.6 Dielectric properties 28
2.5.3 Pre-processing of SAR imagery **28**
2.5.3.1 Terrain correction and geocoding 28
2.5.3.2 Radiometric calibration 29
2.5.3.3 Speckle 29
2.6 SAR INTERACTION WITH FLOODED LANDSCAPES **30**
2.6.1 Open water **30**
2.6.2 Flooded vegetation **31**
2.6.3 Flooded urban areas **37**
2.7 APPROACHES TO FLOOD EXTENT DELINEATION USING SAR IMAGERY 38
2.7.1 General overview **38**
2.7.2 Thresholds **41**
2.7.3 Active contour model **43**
CHAPTER 3 RESEARCH METHODS **49**
3.1 DATA COLLECTION **49**
3.2 PRE-PROCESSING **51**
3.2.1 Landsat imagery **52**
3.2.2 SAR imagery **52**
3.2.2.1 Terrain correction and geocoding 52
3.2.2.2 Calibration 52
3.2.2.3 Speckle filtering 52
3.3 CLASSIFICATION OF THE OPEN WATER BODIES **53**
3.3.1 Areas of interest for classification **53**
3.3.2 Thresholds **56**

3.3.3 Active contour models **58**
3.4 EVALUATION OF FLOOD MAPS **60**
CHAPTER 4 RESULTS AND DISCUSSION **63**
4.1 RESULTS **63**
4.1.1 ASAR **63**
4.1.1.1 Thresholds 63
4.1.1.2 Active contours 67
4.1.2 PALSAR **68**
4.1.2.1 Thresholds 68
4.1.2.2 Active contours 71
4.2 DISCUSSION **73**
4.2.1 Active contours versus thresholds **73**
4.2.2 Wavelength **82**
4.2.3 Incidence angle **88**
4.2.4 Polarisation **99**
CHAPTER 5 CONCLUSION **105**
5.1 REVISITING THE OBJECTIVES **105**
5.2 LIMITATIONS AND RECOMMENDATIONS **109**
5.3 CONCLUDING REMARKS **110**
REFERENCES **112**
APPENDICES **129**
APPENDIX A **130**
APPENDIX B **132**
APPENDIX C **140**
APPENDIX D **149**
APPENDIX E **164**

TABLES

Table 2.1: Radar classifications and wavelength for imaging SAR systems 24
Table 2.2: Average backscatter (dB) threshold values in different water features 43
Table 3.1: SAR image and sensor specifications of relevance in this study 50
Table 3.2: Acquisition dates of SAR imagery and corresponding Landsat reference imagery 50
Table 3.3: All thresholds summarised for each ASAR image (dB) 57
Table 3.4: All thresholds summarised for each PALSAR image (dB) 58
Table 3.5: Scalar value to determine the upper and lower thresholds for the Canny edge for the ACM segmentation process for each ASAR image. Number of iterations the ACM ran for was 1000 for all ASAR images. 59
Table 3.6: The number of iterations for the ACM segmentation process for each PALSAR image. Canny scalar value was 0.3 for all PALSAR images 60
Table 3.7: Number of collected points from the Landsat images and the ASAR images for which the points will be used. 61
Table 3.8: Number of collected points from the Landsat images and the PALSAR images for which the points will be used. 61
Table 3.9: Interpretation of Kappa values 62
Table 4.1: Confusion matrix results for best threshold slices for the ASAR WSM images 66
Table 4.2: Confusion matrix results for active contours for the ASAR WSM images 68
Table 4.3: Confusion matrix results for best threshold slices for the PALSAR PLR images 71
Table 4.4: Confusion matrix results for active contours for the PALSAR PLR images 72

FIGURES

Figure 1.1: Research design 5
Figure 1.2: Study area 6
Figure 1.3: Monthly average temperature and rainfall chart at Katima Mulilo 7
Figure 1.4: Major rivers and their tributaries 8
Figure 1.5: Elevation of the Zambezi Region 8
Figure 1.6: Sharp eastern edges due to the Mambova and Chobe faults 9
Figure 1.7: Vegetation structures of the eastern Zambezi Region 11
Figure 2.1: Basic geometry of a radar image: nomenclature 25
Figure 2.2: Electric field (E) and magnetic field (M) of electromagnetic radiation 25
Figure 2.3: The effect of incidence angle and surface roughness on the received backscatter for the L-band (a), C-band (b) and the X-band (c). 27
Figure 2.4: The major sources of backscatter from flooded woody vegetation: surface backscatter (σ_s), canopy backscatter (σ_c), tree trunk backscatter (σ_t), ground-trunk backscatter (σ_d) and multiple path backscatter (σ_m) 32
Figure 2.5: SAR signal interaction with trunks in non-flooded conditions (left) and flooded conditions (right). Signal return is higher in flooded conditions because of less surface scattering 33
Figure 2.6: The major sources of backscatter from flooded herbaceous vegetation: surface backscatter (σs), canopy backscatter (σc) and multiple path backscatter (σm). 34
Figure 2.7: Theoretical scattering mechanisms of C-band energy from flooded versus non-flooded conditions in forested areas 35
Figure 2.8: Theoretical scattering mechanisms of C-band energy flooded versus non-flooded conditions for herbaceous vegetation areas 36
Figure 2.9: Urban areas during non-flooded conditions (a) and flooded conditions (b). Changes are not apparent in urban areas 37
Figure 2.10: Histogram showing the intensity distribution of a SAR image during flooded conditions. The low intensity range is the water, while the higher intensity range is the surrounding non-flooded land. The threshold is set at the local minimum between the two peaks. 42
Figure 2.11: In (a), the initial contour can be seen, while in (b), the contour settled along the edges of the desired object. 44
Figure 2.12: An illustration of level sets. Original curve seen in (a), while in (b) the curve is represented as contours. The blue plane in (a) is the red level set in (b). 45

Figure 2.13: The initial contour is seen in (a) and in figure (b) it is displayed in three dimensions. Figure (c) is shows the final contour and (d) shows the final level set function. 45
Figure 2.14: Original image shown in (a), while the edge map as identified by the Canny algorithm is seen in (b). 47
Figure 3.1: Extents of the SAR and Landsat images 51
Figure 3.2: ASAR image of Open waterbodies of interest for classification (shown by the red arrows). Backscatter is very low. 53
Figure 3.3: Lake Liambezi. ASAR image of 25 April 2009 is shown in (a), while (b) shows the Landsat image of 20 April 2009. Points show different land cover classes. 54
Figure 3.4: Spectral signatures extracted from points shown in Figure 3.3. 54
Figure 3.5: Region at the Zambezi River. ASAR image of 25 April 2009 is shown in (a), while (b) shows the Landsat image of 20 April 2009. Points show different land cover classes 55
Figure 3.6: Spectral signatures extracted from points shown in Figure 3.5 55
Figure 3.7: Threshold slices for the ASAR image captured on 20 March 2009. 57
Figure 4.1: The original ASAR WSM image, captured on 20 March 2009 (a), the classified image with a threshold of -12 dB (b), which had the highest overall accuracy, and the stacked threshold levels with threshold values ranging from -9 to -13.5 dB (c). The area classified as flooded increases with an increase in threshold as seen in the inset on (c). 64
Figure 4.2: Overall Accuracy for each threshold value for all ASAR WSM images 65
Figure 4.3: Kappa statistic for each threshold value for all ASAR WSM image 66
Figure 4.4: ASAR image of 23 March 2009. The Canny edge in light blue can be seen in (a). The inserted image in (a) outlined in red gives a close-up view of the edge. The segmented flooded region as identified by the ACM is shown in (b) 67
Figure 4.5: PALSAR HV-polarised image of 19 March 2009. The original PALSAR image captured on 19 March 2009 (a), the classified image with a threshold value of -27 (b) which had the highest overall accuracy, and the stacked threshold values ranging from -26 to -28.5 dB (c). The area classified as flooded increases with an increase in threshold as seen in the inset on (c). © ESA. 69
Figure 4.6: Overall Accuracy for each threshold value for all PALSAR PLR images 70
Figure 4.7: Kappa statistic for each threshold value for all PALSAR PLR images 70
Figure 4.8: PALSAR HV-polarised image of 19 March 2009. Canny edge in light blue as can be seen on the left in (a). The inserted image outlined in red gives a close-up view of the edge. (b) shows the segmented flooded region as identified by ACMs. © ESA. 72

Figure 4.9: Comparison of the overall accuracy percentages for ACMs versus thresholds for ASAR images 74
Figure 4.10: Comparison of the kappa statistic for ACMs versus thresholds for ASAR images . 74
Figure 4.11: Relationship between the producer's and the user's accuracy for the flooded and non-flooded classes for thresholds and ACMs for the ASAR images. 75
Figure 4.12: Comparison of the overall accuracy percentages for ACMs versus thresholds for PALSAR images 77
Figure 4.13: Comparison of the kappa statistic for ACMs versus thresholds for PALSAR images 77
Figure 4.14: Relationship between the producer's and the user's accuracy for the flooded and non-flooded classes for thresholds and ACMs for the PALSAR images..... 78
Figure 4.15: PALSAR image of 19 March 2009 (second set). Kasane airport and a road to its left misclassified as flooded region due to low backscatter. © ESA. 79
Figure 4.16: ASAR image, captured on 23 March 2009, showing a segment of the Zambezi River. Some flooded areas, such as the dark areas around the river (shown by the red arrows), were not segmented into flooded regions by the ACM classifier. 80
Figure 4.17: HV-polarised PALSAR image (second set). Some non-flooded areas close to water (Figure 4.17a) were also incorrectly classified as flooded region (Figure 4.17b) © ESA. 81
Figure 4.18: Differences in backscatter return based on wavelengths. The HH-polarised PALSAR image of 19 March 2009 is shown in (a) and the classified regions for this image is shown in (b). The ASAR image of 20 March 2009 is shown in (c) and the classified regions for this image is shown in (d). Red and yellow arrows in (a) and (c) are examples where differences arise due to different wavelength. The Landsat image of 19 March 2009 is shown in (e). The vegetation structure of the region is mostly tall open grassland (f). 82
Figure 4.19: The dominant vegetation structure near the Bukalo channel is woody vegetation (a), but along the banks of the channel within the region outlined in red (b), the dominant vegetation structure is herbaceous and cultivated areas (c). Outside the region, the dominant vegetation structure is woody vegetation as can be seen in (d). 84
Figure 4.20: The Bukalo channel. The HH-polarised PALSAR image of 5 April 2009 is shown in (a) and the classified regions for this image is shown in (b). The ASAR image captured on 25 April 2009 is shown in (c) and the classified regions for this image is shown in (d). The channel is flooded as can be seen from the Landsat image of 20

April 2009 (e). Dominant vegetation structure is tall closed woodland (f) but herbaceous vegetation is present along the banks of the channel (see Figure 4.19). Yellow arrows in (a) and (c) show the northern regions of the channel where the flooded woodland causes high backscatter return for both the ASAR and the PALSAR images. © ESA. 85

Figure 4.21: Classified flooded regions of HH-polarised (a), VV-polarised (b), HV-polarised (c) and VH-polarised (d) images of 5 April 2009. On both like-polarised images, a large area (indicated by the red arrows) which is actually flooded when compared to the Landsat image of 12 April 2009 (e) remained unclassified. Dominant vegetation structure in this area is grassland (f). © ESA. 87

Figure 4.22: The Landsat image subset of 19 March 2009 is shown in (a). Dominant vegetation structure in this region is high closed woodland (b). The ASAR image subset of 20 March 2009 is shown in (c) and the classified regions for this image is shown in (d). The ASAR image subset of 23 March 2009 is shown in (e) and the classified regions for this image is shown in (f). Incidence angles for the subsets are shown in (c) and (e). Red and yellow arrows in (c) and (e) highlight examples of differences in backscatter return at different incidence angles for flooded woody vegetation. 88

Figure 4.23: The Landsat image subset of 6 May 2009 is shown in (a). Dominant vegetation structure in this region is high closed woodland (b). The ASAR image subset of 10 May 2009 is shown in (c) and the classified regions for this image is shown in (d). The ASAR image subset of 11 May 2009 is shown (e), and the classified regions for this image is shown in (f). Incidence angles for the subsets are shown in (c) and (e). Red and dark blue arrows in (c) and (e) highlight examples of differences in backscatter return at different incidence angles for flooded woodland. 90

Figure 4.24: The Bukalo channel. The ASAR image subset of 10 May 2009 shown in (a) and the classified regions for this image is shown in (b). The ASAR image subset of 11 May 2009 is seen in (c), and the classified regions for this image is shown in (d). The Landsat 5 image of 6 May 2009 where low spectral signatures indicate flooded areas can be seen in (e). Dominant vegetation in the area is tall closed woodland (f), however herbaceous vegetation is found along the channel banks (see Figure 4.19). Incidence angles for the subsets are shown in (a) and (c). Red and yellow arrows in (a) and (c) highlight examples of differences in backscatter return at different incidence angles. 91

Figure 4.25: Landsat image of 19 March 2009 is shown in (a), while (b) shows the dominant vegetation structure in the region to be tall open grassland. The ASAR subset of 20

March 2009 is shown in (c), and the classified flooded regions for this image is shown in (d). The ASAR subset of 23 March 2009 is shown in (e), and the classified flooded regions for this image is shown in (f). Incidence angles for the subsets are shown in (c) and (e). Red and yellow arrows in (c) and (e) are examples where differences arise due to different incidence angles. 93

Figure 4.26: Landsat image of 6 May 2009 is shown in (a), while (b) shows the dominant vegetation structure in the region to be tall open grassland. The ASAR subset of 10 May 2009 is shown in (c), and the classified flooded regions for this image is shown in (d). The ASAR subset of 11 May 2009 is shown in (e), and the classified flooded regions for this image is shown in (f). Incidence angles for the subsets are shown in (c) and (e). Red and green arrows in (d) and (f) are examples where classification are different due to different incidence angles. 94

Figure 4.27: 24 March 2009, with steep incidence angles and severe surface attenuation had poor contrast between flooded and non-flooded areas. 96

Figure 4.28: ASAR image of 17 March 2009 (a). When the flooded regions such as the area shown by the red arrow is compared to the Landsat image (such as the region shown by the yellow arrow) of 19 March 2009 (b). These areas had steep incidence angles and were sensitive to surface roughness. 97

Figure 4.29: ASAR image of 10 May 2009 (a). When the flooded regions such as the area shown by the red arrow is compared to compared to the Landsat image of 6 May 2009 (b). These areas had steep incidence angles and were sensitive to surface roughness. ... 98

Figure 4.30: Overall accuracy for the different polarisations of each set of PALSAR images for the threshold classification method 99

Figure 4.31: Kappa statistic for the different polarisations of each set of PALSAR images for the threshold classification method 99

Figure 4.32: Overall accuracy for the different polarisations of each set of PALSAR images for the ACM classification method 100

Figure 4.33: Kappa statistic for the different polarisations of each set of PALSAR images for the ACM classification method 100

Figure 4.34: PALSAR image of 19 March 2009 (first set). The HH-polarised image (a) and VV-polarised image (b) shows a section of the Zambezi River. On the VV-polarised image, a slightly larger extent of the river has higher backscatter returns than the other polarisations, such as the HH-polarisation shown. VV-polarised images was the most sensitive to surface roughness. © ESA. 101

Figure 4.35: Area to the north of the Bukalo channel. HH-polarised image (Figure 4.35a), VV-polarised image (b), HV-polarised image (c) and VH-polarised image (d) captured on 5 April 2009. On the Landsat image of 20 April 2009 (e) dark areas are flooded. Dominant vegetation structure is tall closed woodland (f). © ESA. 103

ACRONYMS AND ABBREVIATIONS

ACM	Active contour model
ASAR	Advanced synthetic aperture radar
DGPS	Differential Global Positioning System
DNs	Digital Numbers
ENSO	El Niño–Southern Oscillation
ESA	European Space Agency
GDP	Gross domestic product
GLOF	Glacial Lake Outburst Floods
PALSAR	Phased Array type L-band Synthetic Aperture Radar

CHAPTER 1 INTRODUCTION

1.1 BACKGROUND

Floods are the most frequent natural hazards and the most significant cause of fatalities related to disasters worldwide (Holloway et al. 2013). Annually, floods cause tremendous economic losses and social disruption globally. Impacts of floods include mortality, adverse health repercussions and damage to and loss of infrastructure, agricultural areas and properties. Between 1980 and 2009, floods have impacted the lives of 2.8 billion people, while 4.5 million people were left without a home and 540 000 fatalities and 360 000 injuries were recorded. These figures could be underestimations because of the vast number of unreported events (Doocy et al. 2013).

Factors that lead to flood events vary, and are complex and interrelated. Causes related to weather include heavy or prolonged precipitation events, cyclones causing storm surges or snowmelts. Human-induced causes are structural failure of dams and levees and the changing of land cover with absorptive properties by replacing it with impermeable surfaces with poor drainage systems. The extent and the impact are affected by precipitation duration, as well as land features such as vegetation type, slope of the terrain, geological composition and soil properties – such as porosity, permeability, moisture content and crusting (Reed 2002, Doocy et al. 2013).

Reported floods related to extreme weather events and caused considerable losses have increased significantly in the past three decades (Kundzewicz et al. 2014). The risk of economic losses because of flooding is significant due to deforestation and an increase in the trend of large populations living in close proximity to coastal areas, river basins, lakeshores and floodplains, areas which are all high flood risk areas (Doocy et al. 2013).

Rapid urbanisation in Africa has been a major factor in the observed increase in flood damage and fatalities, and cities develop in flood-prone areas because there is no safe space left for development. Furthermore, cities develop because of favourable conditions for settlement and economic growth (Douglas et al. 2008; Di Baldassare et al. 2010; Jha, Bloch & Lamond 2012). In southern Africa, rapid urbanisation will likely lead to a greater variety of flood conditions in urban areas which have inadequate storm water drainage systems and sanitation. The intensification of the water cycle will be important to monitor in southern Africa, since flooding is a strong driver of change for this region (Holloway et al. 2013). The Zambezi Region in Namibia, which is the region of interest in this study, is located in southern Africa. In this area floods occur annually

during the rainy season. Floods can severely affect the poor communities at risk from the flooded areas (Mendelsohn 2007).

Because of the risk floods pose to human activities and infrastructure, it is imperative to examine different techniques for flood monitoring (Vanneuville et al. 2011). For better response to (and prevention of) flood disasters, the use of remote sensing technology has been explored. Remote sensing can potentially provide near real-time information about flood events. It can be a cost-effective monitoring technique and is becoming more important as a technique for the identification, analysis and understanding of flooded areas, since satellite sensors are often the only source of information.

However, passive optical sensors (such as Landsat) are dependent on good weather conditions. Bad weather conditions such as cloud cover impedes the capturing of useful imagery for purposes of analysis. Data capturing is also restricted to daytime (Campbell & Wynne 2011). SAR imagery is derived from active SAR sensors which emit radiation in the microwave region and the backscatter received is recorded and analysed. Therefore these sensors are not restricted to daylight and images can be captured during the night as well. Images are also not obstructed by weather conditions since the long wavelengths in the microwave regions have minimal interaction with the atmosphere and can penetrate clouds (Campbell & Wynne 2011).

1.2 RESEARCH PROBLEM

In the Zambezi Region, floods occur annually, causing economic losses and social disruption. Climate changes, such as an increase in the intensity of precipitation could potentially influence the rain-generated floods (Kundzewicz et al. 2007, 2008). Furthermore, changes in land cover and land use, such as deforestation and the urbanisation of Africa, have an impact on flood risk in the area (Bradshaw et al. 2007; Di Baldassare et al. 2010). These variables bring a further dimension of uncertainty to flood risk in the area and could potentially exacerbate the adverse effects of floods experienced in the region. It is therefore important to examine different approaches for flood monitoring to aid disaster mitigation and rapid response.

There are several approaches to flood extent delineation which include multi-temporal approaches (e.g. Heremans et al. 2003; Long, Fatoyinbo & Policelli 2014), coherence based approaches (e.g. Horritt, Mason & Luckman 2001; Refice et al. 2014) or single date approaches such as active contour models (ACMs) and thresholds (Voigt et al. 2008). However, when using thresholds or ACMs (both single date approaches) it is not clear which method yields superior results when

different sensor parameters are taken into account. Each method has its advantages and disadvantages. It is therefore important to investigate which method is most suitable for flood extent delineation. Furthermore, sensor properties such as wavelength, incidence angle and polarisation have an impact on effectiveness of identifying flooded open water bodies (e.g. Richards, Woodgate & Skidmore 1987; Hess, Melack & Simonett 1990; Dallemand et al. 1993; Henderson 1995; Wang et al. 1995; Kasischke, Melack & Dobson 1997; Horritt et al. 2003; Solbø & Solheim 2004; Bourgeau-Chavez et al. 2005; Töyrä & Pietroniro 2005; Henry et al. 2006; Matgen et al. 2007; Martinis, Twele & Voigt 2009). It is therefore imperative to determine the optimal sensor properties for flood extent delineation.

The key problems in this study are whether thresholds or ACMs are better suited for flood extent delineation and which wavelength, incidence angle and polarisation is optimal for determining flood extent in the Zambezi Region.

1.3 RESEARCH AIM AND OBJECTIVES

The aim of this study is to evaluate the use of ENVISAT ASAR and ALOS PALSAR imagery to estimate open water flood boundaries in the Zambezi Region using two different classification algorithms on the SAR imagery, thereby dividing the image into flooded and non-flooded regions: ACMs and thresholds. Flooded regions of interest for classification are open water areas. The flooded vegetation were not considered for classification in this study. The results will then be statistically and visually assessed with the aid of Landsat 5 and Landsat 7 imagery captured close to the same date as the captured SAR imagery.

The following objectives were set to achieve the aim:

1. Derive the flood extent from the SAR images using thresholds and ACMs.
2. Qualitatively assess classified images obtained from thresholds and ACMs.
3. Determine the accuracies of the two classification methods when compared to Landsat imagery.
4. Determine the impact of sensor parameters on classification results.
5. Synthesize the results and assess the suitability of SAR-based flood mapping using the techniques and sensors employed.

1.4 METHODOLOGY AND RESEARCH DESIGN

In this study, different methodologies for the classification flooded areas using SAR images were evaluated. This study followed an empirical research approach based on the five objectives stated in section 1.3. Some aspects of the research are quantitative, since statistical properties of the SAR image will be used for image classification and statistical measures will be taken to compare SAR images with Landsat images, while other aspects of the research are qualitative, with SAR images be visually compared with Landsat images.

The research design is illustrated in Figure 1.1 as 7 phases. Phase 1 laid the foundation of the study by identifying the research problem, thereby developing the aim and the five objectives. Phase 2, the literature review, provided a conceptual framework for the study by providing an overview of floods, flood risk, causes of floods, impacts and regional perspectives in less economically developed countries. The literature review also provided a short overview of SAR imagery, its interaction with different flooded landscapes and common approaches to flood extent delineation using SAR imagery. Phase 3 described the data necessary to meet the objectives, while phase 4 described the pre-processing steps required for preparation of SAR and Landsat data and before analysis can commence. Phase 5 is the classification phase, where SAR images were classified into flooded and non-flooded regions, first using thresholds, then using active contours. During phase 6, the classified images were statistically compared to Landsat in the form of accuracy assessment reports as well as qualitatively assessed through visual inspection of results obtained and a comparison between SAR images based on sensor properties. Phase 7, the concluding phase, revisited the aim and objectives and determined whether they were achieved, highlighted limitations, summarised the main findings of and assessed the suitability of SAR images for flood mapping in this study. Through the completion of these phases, the set objectives were met, thereby achieving the aim set in section 1.3.

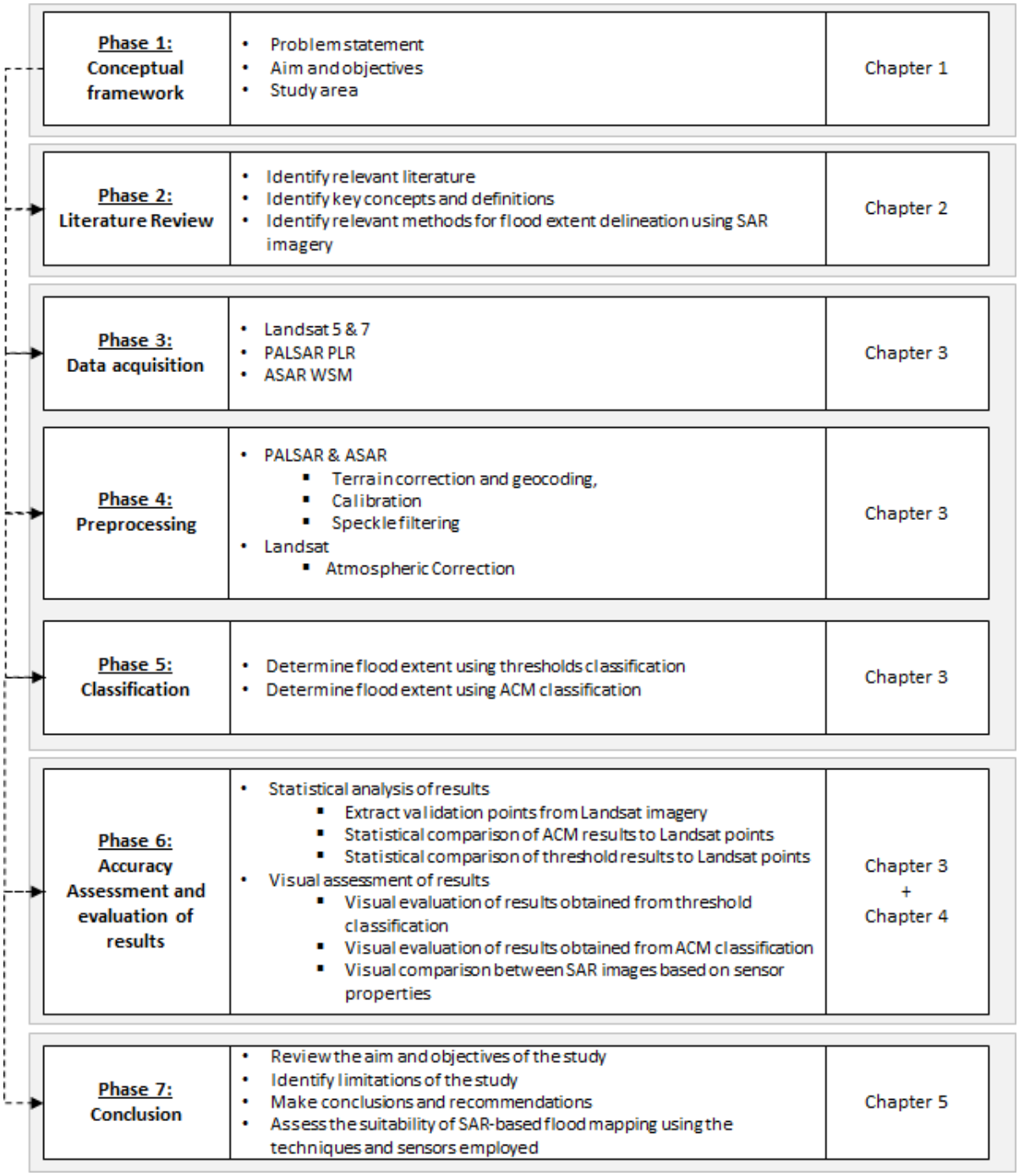

Figure 1.1: Research design

1.5 STUDY AREA

The study area is located in the eastern Zambezi Region (formerly known as Caprivi Region), in the north-eastern part of Namibia (Figure 1.2). The Zambezi Region shares its borders with Angola, Botswana, Zambia and Zimbabwe. Its anomalous shape is due to its colonial history and the long, narrow strip of land was used to connect the north-eastern colonial territories to the southwestern colonies (Mendelsohn & Roberts 1997; Mendelsohn et al. 2002).

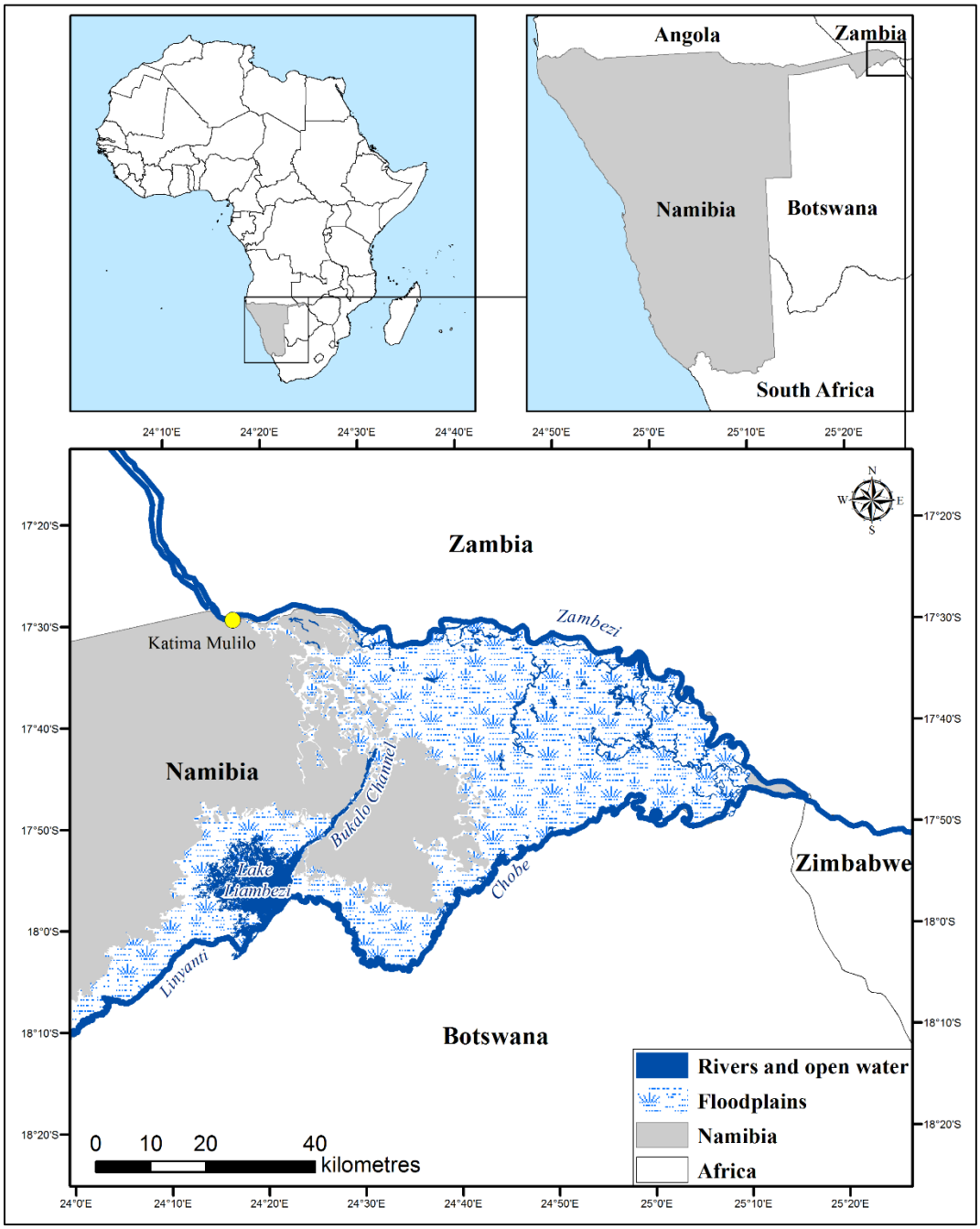

Figure 1.2: Study area

The eastern Zambezi Region is a relatively flat area and the mean elevation of the area is approximately 900 m. The annual rainfall in this region is about 500-700 mm and the rainfall

distribution can be seen in Figure 1.3 (Mendelsohn & Roberts 1997; Namibia Meteorological Service 2015). Three prominent seasons can be defined: a cool dry season from May to July, a hot dry season from August to October and a warm rainy season during the summer months from November to April (Chase & Griffin 2009). Figure 1.3 also charts the monthly temperatures recorded at Katima Mulilo. Maximum temperatures range from 26°C during winter to 34°C during summer, while minimum temperatures range between 4°C and 19°C (Jensen, Eriksen & Eliassen 2015). Mean annual temperatures range between 15 °C and 26 °C. (Jensen, Eriksen & Eliassen 2015).

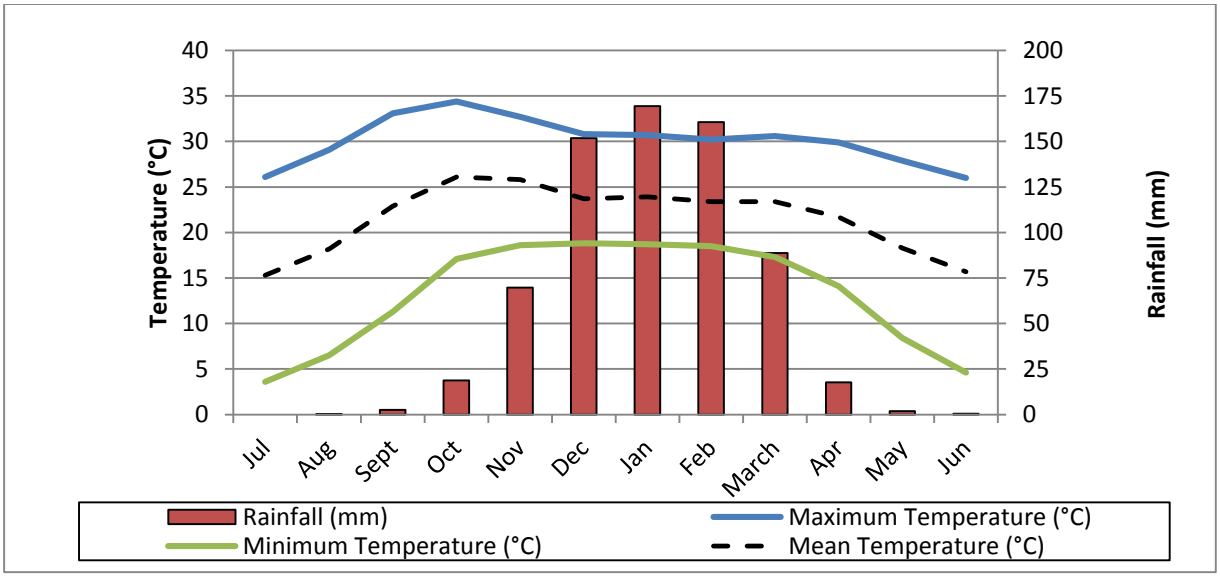

Adapted from Jensen, Eriksen & Eliassen (2015) & Namibia Meteorological Service (2015)

Figure 1.3: Monthly average temperature and rainfall chart at Katima Mulilo

The Zambezi Region is part of the Kalahari Basin, a large inland depression mostly filled with sandy soils. However, heavier soils are present in regularly flooded regions and water does not easily infiltrate these soils due to its high clay content (Mendelsohn & Roberts 1997; Mendelsohn 2007). Three permanently flowing rivers are found in the Zambezi Region – the Okavango, Kwando and Zambezi rivers (PDNA 2009). These rivers originate in Angola and Zambia (Figure 1.4). The Chobe and the Linyanti rivers are extensions of the Zambezi and the Kwando rivers but are regarded as rivers in their own right (Mendelsohn et al. 2002). This area, being relatively flat and at an elevation lower than that of the surrounding countries (Figure 1.5), is susceptible to floods and flooding may occur over an extensive area during in the eastern Zambezi Region during years of high rainfall, when the flows of the Zambezi River begin to rise in December and January and volume discharge peaks in February in April (Mendelsohn & Roberts 1997; Mendelsohn et al. 2002).

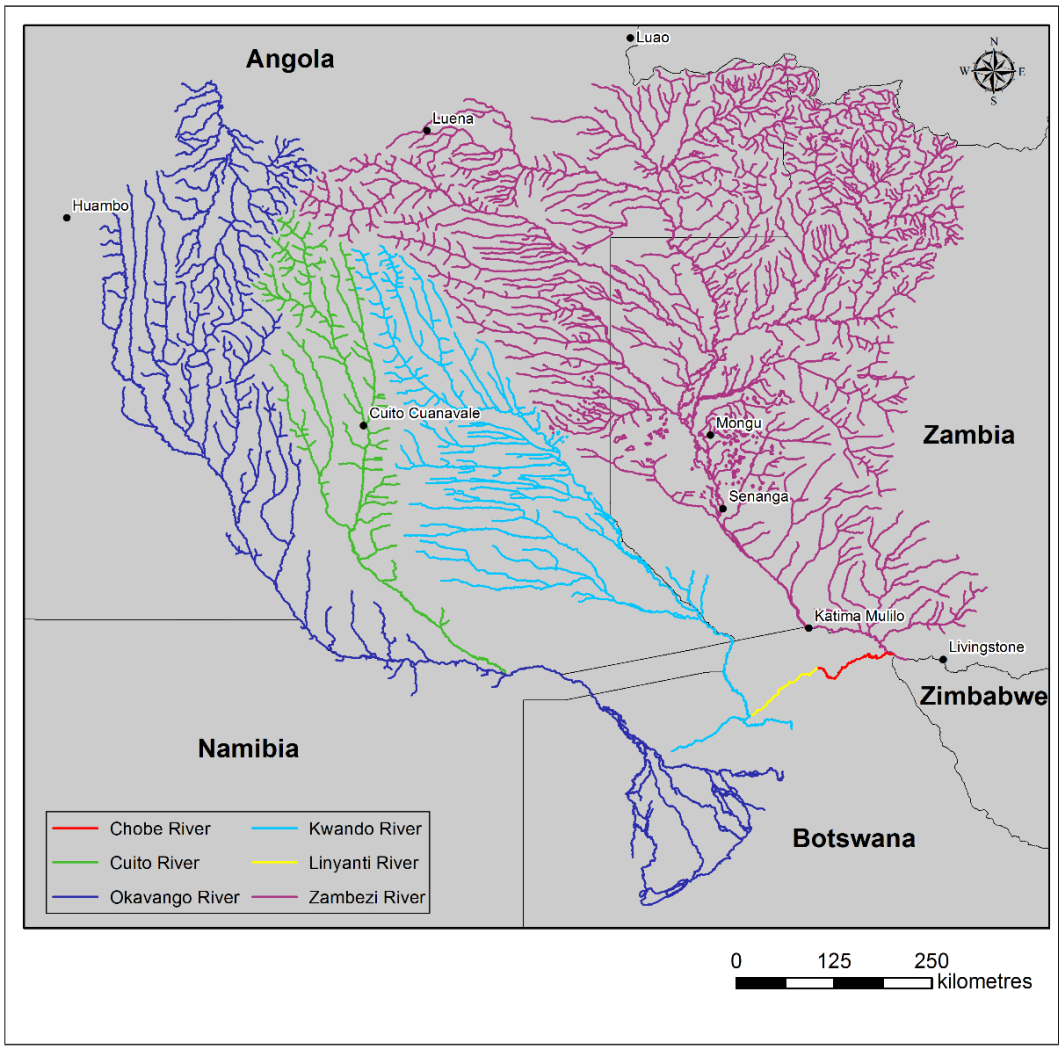

Adapted from Mendelsohn & Roberts. (1997)

Figure 1.4: Major rivers and their tributaries

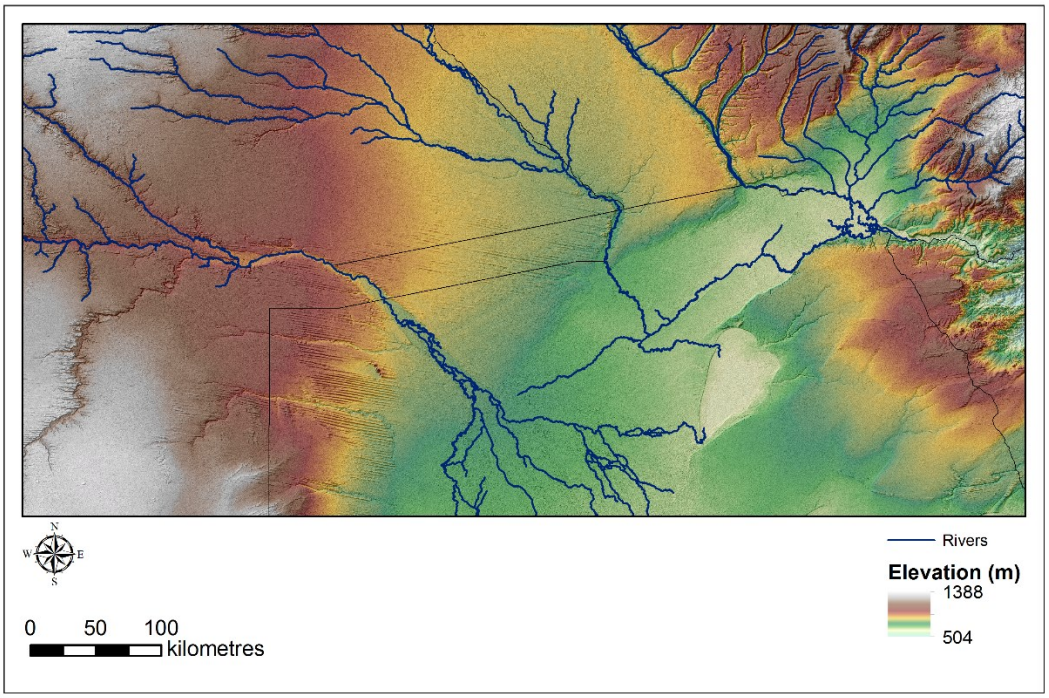

Figure 1.5: Elevation of the Zambezi Region

The upper end of the Chobe River flows eastward to the Zambezi River during the initial stages of the flood season and can contribute considerable runoff to the Zambezi River system (Beilfuss 2012). As the Zambezi levels rise however, the Chobe River changes direction and flows back to the northwest where it discharges into Lake Liambezi (Beilfuss 2012). When Chobe and Zambezi River flooding is in phase an area as large as 1700 km^2 can become flooded, forming extensive marshlands, channel networks and lakes (Mendelsohn & Roberts 1997; Mendelsohn et al. 2002).

The flooded regions are usually confined between the Zambezi and Chobe Rivers. The floodplains carry on for several kilometres to the west of the confluence, but the sharp eastern edge of the floodplain is due to the Mambova and Chobe faults (see Figure 1.6Figure 1.5) which raised the elevation on the eastern side (Riebeek & van Langenhove 2010; Moore, Cotterill & Eckardt 2012).

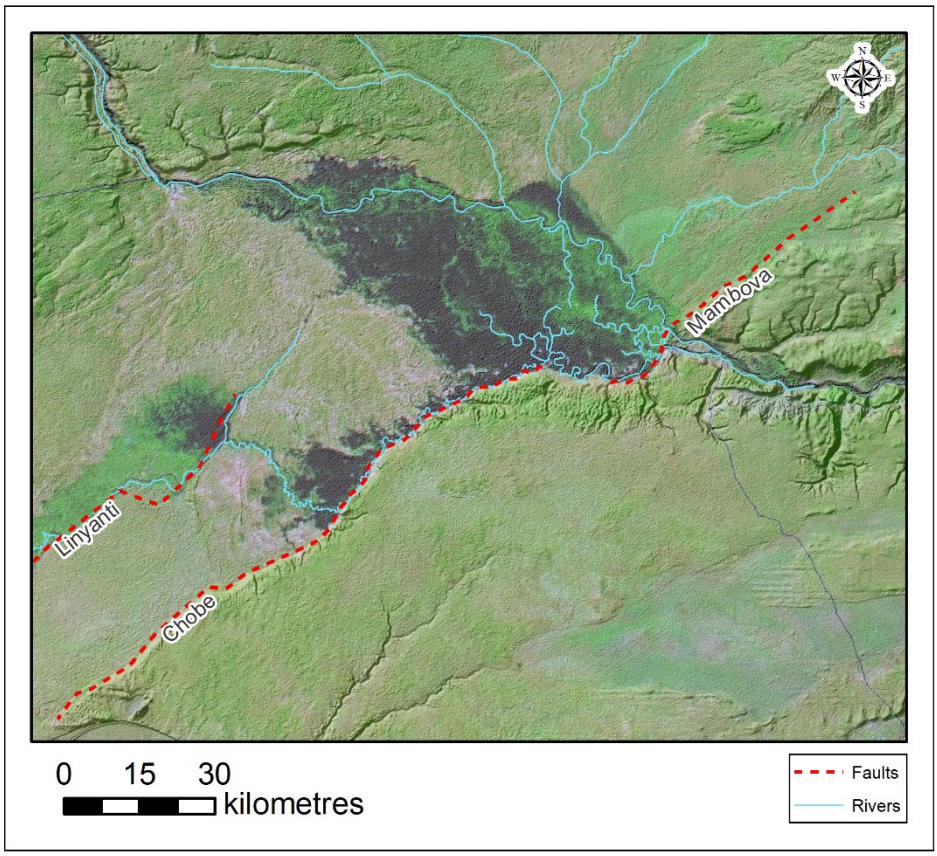

Figure 1.6: Sharp eastern edges due to the Mambova and Chobe faults

There is substantial variation in runoff in the Upper Zambezi River from year to year. Analysis of long term runoff reveals long term cyclic patterns of high, medium and low runoff and influences runoff efficiency (Beilfuss 2012; Moore et al. 2007). During low rainfall years the runoff is low, while water tables are high during the wet year sequences which contributes to higher runoff efficiency (Beilfuss 2012; Moore et al. 2007).

The floods occurring during the 2009 rainy season were particularly problematic as reported by the PDNA (2009). During March 2009, rains in Namibia, Zambia and Angola led to an increase in water levels in the Zambezi, Chobe, Kavango and Kunene Rivers, to such a vast extent that six regions in Namibia, including Zambezi Region, were affected by the floods. The Zambezi Region was the region most severely affected by floods and water levels had reached the highest levels recorded since 1963, reaching a height of 7.85 m. The floodwaters increased sharply around 20 March 2009, peaking around 26 March 2009, after which waters slowly receded (De Groeve & Riva 2009). Aerial surveys showed stranded livestock and flooded villages (PDNA 2009). About 9000 people were relocated to four relocation camps which had insufficient water and sanitation facilities (PDNA 2009). Major road access was cut in the Northern Zambezi Region at four locations and access to health clinics was limited (PDNA 2009). Only four out of eleven health facilities were operational directly after the disaster (PDNA 2009). Damages, defined as the replacement value of totally or partially destroyed physical assets by the PDNA (2009), were estimated to be US$19 million, while losses, defined as that arising from the temporary absence of the damaged assets, were estimated to be US$12.4 million

The dominant vegetation structures for the region are shown in Figure 1.7. The important variable for vegetation structure is whether grassland/wetland or woodland structures dominate in a region (see section 2.6.2). The floodplain areas are dominated by grasslands and wetlands, and vegetation structures would therefore mostly consist of a canopy layer and a surface layer. In woodland areas trees would be more dominant and the vegetation structure would have a canopy layer, a trunk layer and a surface layer.

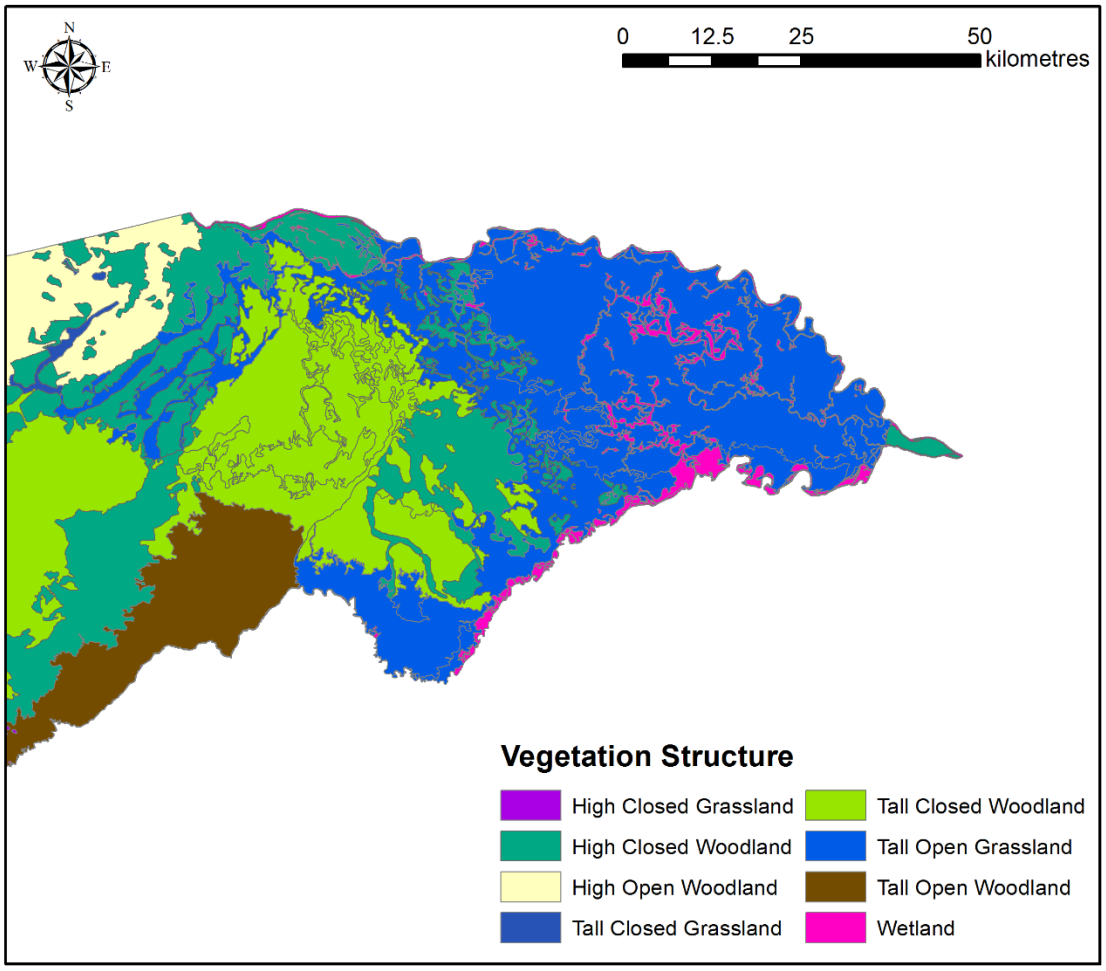

Adapted from Mendelsohn & Roberts (1997)

Figure 1.7: Vegetation structures of the eastern Zambezi Region

The population of the Zambezi Region is estimated to be about 90 596. The population density of the region is estimated to be 6.1 people per km^2 (Namibia Statistics Agency 2011). People are mostly situated in Katima Mulilo, along the main roads and in villages across the eastern floodplains where many are at risk from the frequent seasonal floods (Mendelsohn 2007). Economic activity in this region mostly consists of fishing and subsistence farming and floods can lead to losses of the farming stocks (PDNA 2009; Mendelshohn 2002).

1.6 OUTLINE

This thesis consists of 5 chapters. Chapter 1 serves as a short overview to the study and gives a brief description of the study area. Chapter 2 presents the literature review, providing a short overview and conceptualisation of floods in a real-world context, as well as examining the basics of SAR and its interaction with different flooded landscapes. Chapter 2 also reviews and examines previous research which employed SAR imagery for flood extent delineation, while also giving a theoretical background of the two methods employed in this study for flood delineation: thresholds and ACMs. Chapter 3 provides a description of the data collection, pre-processing steps,

classification methods and accuracy assessment performed in this study. Chapter 4 provides the results and a discussion which includes a quantitative and a qualitative assessment of the attained results. Chapter 5 summarises the main findings, offers limitations and recommendations of the study and provides conclusions.

CHAPTER 2 LITERATURE REVIEW

The following chapter provides a brief overview of literature relating to floods and SAR imagery. First, floods and flood risk are briefly described. This is followed by a brief overview of factors influencing flood frequency and flood risk, the impacts of floods and regional flood trends in the developing world, thereby providing a real world context for the significance of flood monitoring. The basic principles of SAR relevant to this research are then discussed, followed by the interaction of SAR signals with different landscapes. Finally, methods using SAR for flood mapping in previous studies are examined, followed by a more in-depth description of methods of importance in this study, which are thresholds, active contours and the Canny edge detector.

2.1 FLOODS AND FLOOD RISK

A flood can be defined as a flow of water that rises over the natural or artificial bank of a river or waterbody and submerges the floodplain. A channel is at bankfull discharge when the water is at the same level as the floodplain and geomorphically, a flood occurs when the river flows at a greater rate than bankfull discharge. Sources of water include: rainfall; snowmelt; sea surges and dam breaks (Holden 2012). Types of floods include: fluvial floods, when riverbanks overflow; coastal floods caused by tidal and storm surges and tsunamis; groundwater floods (when soils become saturated and additional water becomes runoff); and pluvial floods, where extremely heavy rainfall causes concentrated overland flow (Holden 2012).

According to Petersen (2001), the characteristic of the flood event can also be used as a basis for classification and floods can be classified into four categories: flash floods; single-event floods; multiple-event floods; seasonal floods. Flash floods are extreme, sudden, short-lived floods usually lasting less than 24 hours. The long-rain floods (single- and multiple-event floods) have a longer span than flash floods, and can last days or weeks (Bell 2004). Single-event floods have one discharge peak, while multiple-event floods have a consecutive series of discharge peaks (Bell 2004). More intricate weather systems are associated with multiple-event floods than those associated with single event floods, and repercussions are more severe due to the long extent of their duration (Bell 2004).

Because floods progress at different time-scales, their effects are varied. Flash floods, for example, have higher associated death rates due to their rapid arrival, and are the leading cause of flood-related deaths in developed countries. Fluvial floods on the other hand are less likely to lead to

death due to the gradual accumulation of precipitation, but affect a larger population and cover larger areas of land (Jonkman 2005; Doocy et al. 2013).

The European Commission (2007) defines flood risk as "the combination of the probabilities of a flood event and of the potential adverse consequences for human health, the environment, cultural heritage and economic activity associated with a flood event". Schumann (2011), however argues that this definition means these adverse impacts will definitely result from flood events. Generally, risk however does not only depend the hazard (in this case the floodwaters), but also on the vulnerability of people to hazards (e.g. settling in floodplain areas) and their capacity to adapt to these hazards (Isunju, Orach & Kemp in press). Risk can therefore be related to hazard, vulnerability and capacity to adapt using the following formula (Isunju, Orach & Kemp in press):

$$Risk = \frac{Hazard * Vulnerability}{Capacity} \qquad \text{Equation 2.1}$$

This relationship suggests that risk increases when flood hazard and/or vulnerability is high, but decreases when the capacity to adapt to adverse effects is high.

Globally, no widespread climate-driven changes in the magnitude and frequency of floods during the past decades have been found based on gauge data, despite projected changes in extreme weather events which could potentially alter flood patterns (Kundzewicz et al. 2014). Flood risk is however higher. The number of reported flood disasters and losses have increased due to factors such as an increase in population, urbanisation in flood-prone areas, higher property value and less awareness about natural risks (Kundzewicz et al. 2014). Improvements in disaster coverage, however, can also contribute to a perceived increase in flood since news coverage tends to focus on negative aspects (Kundzewicz 2011).

2.2 FACTORS INFLUENCING FLOOD FREQUENCY AND FLOOD RISK

2.2.1 Physical factors affecting floods and flood risk

2.2.1.1 Riverine floods

Although precipitation is considered to be the physical control having the most significant influence on flood severity, other controls determine what happens to precipitation on the ground. They are of considerable importance when considering the location, timing and the severity of

flooding events. These factors include the size, shape, relief and land cover of the catchment area, soil and rock type, vegetation cover and the number of tributaries (Waugh 1995).

The size and relief of the river catchment area determines the amount of precipitation a river can receive and the time it takes for precipitation to reach the main river channel. Larger catchment areas will have less runoff than smaller catchment areas, since large catchment areas will have slower water flow and water will also take longer to pass a location and reach the runoff outlet (Yevjevich 1994). The relief of the catchment area determines how fast water will reach the river channel and water will drain more rapidly for steeper catchment and river channel slopes, thereby increasing the discharge of the river (Yevjevich 1994). The land cover of the catchment area is also important since rural and urban catchment areas similar in size and topography will have different reactions to the same amount of precipitation. For rural areas, the peak discharge will usually be lower and the lag time longer than for urban areas (Kundzewicz et al. 2012)

Soil and rock type impacts flooding within the catchment areas. Low permeability of the soil and underlying rock and soil decreases the infiltration rate of the precipitation, thereby increasing the runoff and increasing discharge (Waugh 1995; Darby 1999). Additionally, if soil is saturated, precipitation cannot infiltrate and rainfall becomes runoff and discharges into the rivers, thereby increasing its discharge (Allaby 2003).

Vegetation within a landscape buffers flood events (Bradshaw et al. 2007). Energy of the precipitation infiltrating the soils is reduced, thereby reducing soil erosion (Watson & Adams 2010). The vegetation cover reduces the moisture content of the soil by intercepting the precipitation and enhancing evapotranspiration, thereby reducing infiltration into soil (Watson & Adams 2010). Vegetation not only carries water along stems and trunks into the soil, but also carries water into the deeper soils when surfaces are waterlogged (Watson & Adams 2010). Additionally, vegetation also adds organic material to soils, thereby creating more absorbent soils (Watson & Adams 2010).

The drainage density, or the total amount of tributaries of a river, also impacts flood likelihood. Discharge will be higher when a greater number of tributaries are present, since discharge will increase particularly at the confluences, where discharge is greatest (Pallard, Castellarin & Montanari 2009; Holden 2012).

2.2.1.2 Coastal floods

Factors affecting coastal floods include storm surges, seal-level rise, land reclamation and tsunamis. Storm surges are sudden or unexpected rises of the water levels near the shorelines due to strong winds usually associated with cyclones and hurricanes (Holden 2012). Water levels can be significantly higher than the predicted tide levels (Holden 2012). Water levels can be higher than 5 m during extreme conditions, thereby leading to widespread coastal floods (Holden 2012). Storm surges caused by Hurricane Katrina, for example, caused water levels along the Mississippi coastline to reach 8.8 m (Dietrich et al. 2010).

It is generally expected that the sea-level will rise on global level in the future and Nicholls et al. (2010) projected that the global average sea-level could increase between 0.5 m and 2 m. A rise in the sea-level could have several effects on coastal regions, including submergence and an increase in floods (Nicholls et al. 2010). As sea-levels rise, flood-risk increases since the higher water levels will move flood risk zones upward along the coastal floodplain, thereby exposing more people along coastal regions (Nicholls, Hoozemans & Marchand 1999). Additionally, wind-driven surges will increase with an increase in sea-level, since they mainly develop in relatively shallow depths and where shallow waters stretch far offshore (Woodruff et al. 2013).

Land reclamation, or areas reclaimed from the sea by constructing embankments, can also increase flood risk, since the tidal range increases (Embleton & Embleton-Hamann 1997). The area available for water storage is also reduced (Adelekan 2010). Additionally, a reclaimed land area is usually flat, making it more susceptible to storm surges (Embleton & Embleton-Hamann 1997).

Tsunamis, or large waves caused by earthquakes, volcanic activity, landslides and meteor impacts, can cause devastating floods (Holden 2012; Allaby 2003). Due to the energy of these waves they can flood a substantial amount of coastal regions and cause considerable damage to property (Nadal et al. 2009; Mimura et al. 2011).

2.2.2 Human activities affecting floods and flood risk

High levels of urbanisation led to an increase in the population residing in floodplain areas and drainage planning in these areas is often inadequate. Generally, urbanisation leads to construction of more impermeable surfaces. Runoff therefore higher and the water storage capacity is low. The peak discharge in urban areas is generally higher than rural areas of similar size and the time it takes for floods to reach their peak is also shorter (Kundzewicz et al. 2012).

Often one of the effects of urbanisation is a decrease in forested and wetland areas. A decrease forest and wetland areas reduces the buffering of flood events which these land cover types provide. A loss of vegetation leads to an increase in runoff because of decreases in the water evaporation from tree crowns and intersection of rainfall, as well as the infiltration rate of soils (Reed 2002; Watson & Adams 2010). The loss of natural habitat causes an increase in the risk and severity of extreme floods as well as the associated damages to properties and impact on human life. When natural vegetation cover is lower, the flood severity – expressed as the total flood duration, number of people killed and damage to infrastructure – is greater (Bradshaw et al. 2007).

The recent surge in population as well as land use changes have increased human exposure to floods (Doocy et al. 2013). Currently, about 800 million people around the world reside in areas prone to floods, with about 70 million people exposed to floods each year (UNISDR 2011). Over 60% of the world's population reside within 1 km of water surfaces, mostly along coastlines and rivers. It is projected that 60% of the world's population will reside in large cities by 2025 (Tockner & Stanford 2002). An increase in urbanisation in developing countries will lead to pressure on riparian systems and by 2025 Africa and Asia will be the most water-stressed countries (Tockner & Stanford 2002).

An increase in population and its resulting urbanisation increases and economic expansion will put pressure on freshwater resources primarily due to developments in infrastructure and an increase in water extraction for agricultural use, industrial use and human consumption (Tockner & Stanford 2002). Land use changes, changes in the flow and flood system of water resources and an increase in human water consumption will contribute to the intensification of the water cycle. Water will move more rapidly into and out of reservoirs in some regions and other regions will experience a considerable decrease in water and water flow (Tockner & Stanford 2002; Collins et al. 2013).

2.2.3 Climate change and its effect on flood risk

Evidence suggests that precipitation events have intensified because of a changing climate (Zwiers et al. 2013). Statistically, increases in the number of heavy precipitation events outnumber the number of decreases on a global level. These trends, however, show strong regional and sub-regional variations (Kundzewicz et al. 2014). From 1900 to 1998 precipitation over land showed a global increase of 2%. On a regional scale precipitation has increased 7%-12% in latitudes between 30°N and 85°N and 2% between 0°S -55°S latitudes, while it considerably decreased in other regions (Huntington 2006).

It is projected from global and regional studies that the 21st century could bring more intense precipitation events over many areas, but an overall decrease in total precipitation, especially in the high latitude areas and the tropical regions, as well as in the northern mid-latitudes during winter (Kundzewicz et al. 2014; Tockner & Stanford 2002; Pachauri & Meyer 2014). An increase in summer drought over the mid-latitude continental interiors is projected which adds to the related risk of higher minimum temperatures.

The extent to which changes in climate can change patterns in the magnitude and the frequency of flood events is uncertain, dependent also on the regional characteristics of the climate variables and the respective river catchments (Kundzewicz et al. 2012; Zwiers et al. 2013). Some studies suggests that the increase in precipitation intensity could possibly contribute to rain generated local floods such as flash floods and urban floods (e.g. Kundzewicz et al. 2007, 2008; Bates et al. 2008). Milly et al. (2002) project an increase in great floods i.e. "floods with discharges exceeding 100 year levels in basins larger than 200 000 km^2" (Milly et al. 2002: 514). Furthermore, a rise in the sea level and an increase in frequency of storms could potentially lead to increased flood risk in coastal areas (Nicholls, Hoozemans & Marchand 1999; Doocy et al. 2013).

However, several studies either suggest no climate changes, or findings are regionally inconsistent, or find changes in the characteristics of floods because of global warming. The empirical evidence does not suggest global widespread change in flooding, but does suggest earlier spring peak floods as well as an increase in winter base flows in basins which are characterised by snow storage (Zwiers et al. 2013).

2.3 IMPACTS OF FLOODS

2.3.1 Human impacts

The most evident impact of floods on humans is the loss of human life (Ahern et al. 2005). This could either be directly due to drowning, or being struck by debris or objects picked up by fast-flowing water (Ahern et al. 2005). Flood-related injuries include cuts, contusions and sprains (Ahern et al. 2005). The type of flood, however, has an impact on the flood-related death rates. More fatalities are associated with flash floods, for example, and these type of floods are the leading cause of flood-related deaths in developed countries (Jonkman 2005). Riverine floods in contrast, affect a larger population and covers larger areas of land, but death is less likely due to its gradual accumulation (Jonkman 2005; Doocy et al. 2013).

Floods also impact human health. Infectious diseases such as diarrhoea, typhoid and cholera can potentially increase during flood events, especially where people do not have access to proper sanitation and clean water (Ahern et al. 2005; Ivers & Ryan 2006). Mental health impacts of floods can potentially include depression, anxiety, irritability, sleeplessness and in severe cases post-traumatic stress disorder (Ahern et al. 2005).

2.3.2 Economic impacts

Extreme floods can cause billions of dollars of economic damages to infrastructure and property, especially in developing countries which have large populations in rural and agricultural areas (Jonkman 2005; Bradshaw et al. 2007). When corrected for inflation, reported flood losses have increased from an average of US$ 7 billion from 1980 to 1989 to an average of US$ 24 billion in 2011 (Kundzewicz et al. 2014).

There has been a significant increase in economic losses because of the rise in exposure of assets at risk. Assets unprotected from floods have grown faster than overpopulation or economic growth (Bouwer et al. 2007; Di Baldassare et al. 2010; Jongman, Ward & Aerts 2012). This reflects that exposure of population and assets to floods are the main cause of an increase in flood-related losses and not primarily anthropogenic climate change. Environmental regions and resources, private and public residences and facilities, infrastructure and the commercial, industrial and agricultural sectors are all assets which can be adversely affected by flooding (ECLAC 2003; Kundzewicz et al. 2014). Secondary impacts include alternative means to produce and distribute products and services because of the disruption of the status quo (e.g. the disruption of ports and transport routes) by floods, thereby hindering economic activity (Cavallo & Noy 2009).

Losses related to flood disasters are greater in developed countries. In developing countries, however, economic losses and death rates related to flood disasters expressed as a proportion of the gross domestic product (GDP) are greater (Kundzewicz et al. 2014). These findings are consistent with the established findings that poverty leads to a higher disaster risk. Early warning systems can successfully reduce mortality risk through evacuation procedures, but crops and infrastructure are left behind, which leads to a severe increase in economic risk (Bouwer 2011; UNISDR 2011).

2.3.3 Environmental impacts

Floodwater runoff can become contaminated with pollutants found in urban areas such as sewage, household waste, industrial waste and other toxic substances (Rossi, Harmanciogammalu & Yevjevich 1994; Adelekan 2010). These substances can infiltrate and contaminate resources such

as rivers, groundwater and soils (Gautam & van der Hoek 2003; Euripidou, & Murray 2004). Similarly, if floodwaters reach agricultural areas, pesticides, fertilisers and other chemicals used in farming practices can contaminate water resources and lead to loss or disturbance of wildlife when water re-enters the rivers (Rossi, Harmanciogammalu & Yevjevich 1994; Gautam & van der Hoek 2003).

Depth of floodwaters has an effect on severity of flood impacts and floods of greater depth can cause more damage to the environment partly because more area is being flooded (Gautam & van der Hoek 2003). Longer floods will exacerbate environmental problems due to clean-up being delayed and contaminants remaining in the environment for longer (Gautam & van der Hoek 2003).

2.4 REGIONAL FLOOD TRENDS IN THE LESS ECONOMICALLY DEVELOPED COUNTRIES

This section focuses on flood trends in less economically developed regions, since some regions in these countries (including Namibia) are severely impacted by floods due to insufficient disaster management strategies, human capital and infrastructure when compared to developed countries. The importance of flood monitoring is therefore highlighted by providing a real-world context for the need for effective flood-monitoring techniques.

2.4.1 Asia

In Asia, flood risk is high and floods are concentrated in Bangladesh, China and India (Kundzewicz et al. 2014) Bangladesh is flood-prone due to its proximity to the confluences of major rivers and its hydro-meteorological and topographical traits (Mirza 2002). Monsoon floods, flash floods, riverine floods and floods caused by poor drainage are considered to be frequently occurring events in this region (Mirza 2002). Floods in Bangladesh can also cause health problems among communities who do not have access to fresh drinking water. In China, floods in Pyongyang Lake have increased due to the construction of levees since the area previously available for storing floodwaters decreased, thereby causing higher water levels of the lake during the summer flood seasons. Additionally, in Northern China, areas such as Beijing, Tianjin and part of Hebei Province were subject to severe flooding in July 2012 due to a heavy rainfall event centred in Beijing spanning over 2 days (Zhou et al. 2013). In India severe floods were caused by heavy rainfall in a short period and affected many households due to poor urban drainage.

Rajeevan, Bhate & Jaswal (2008) found that there is an increase in extreme rainfall events which could be associated with an increase in sea surface temperatures and surface latent heat flux over

the tropical Indian Ocean. The relationship between extreme rainfall events and the sea surface temperature of the Indian Ocean could mean an increase in flood risk for central India. May (2004) predicted that heavy rainfall events in areas including northwest India and Bangladesh will increase in the future, while Shahid (2011) observed an increase in the number of heavy precipitation days while the number of consecutive dry days is decreasing. These trends could adversely impact flood risk in Bangladesh. In China, there is an overall decrease in the total summer rainfall. However, the intensity of the rainfall is increasing, thereby increasing flood risk in this area, leading to floods such as these in Northern China described above (Zhou et al. 2013).

2.4.2 Central and South America

Areas in Central and South America are also vulnerable to floods. In areas such as Peru and Chile, glacial lake outburst floods (GLOFs) can lead to the discharge of considerable amounts of water in the respective lakes and rivers (e.g. Carey 2005; Dussaillant et al. 2010). The 2009 GLOFs in Chile led to considerable damage to farm settlements and stocks (Dussaillant et al. 2010). There is however uncertainty as to the relationship between GLOFs and higher global temperatures (Dussaillant et al. 2010).

Rising water levels in the Amazon River catchment in 2009 and 2012 led to floods in rural and urban areas in South American regions such as Peru, Colombia and Bolivia and the riverine communities of Brazil, leading to economic losses (Marengo et al. 2013a; 2013b). The 2009 flood event was linked to surface waters in the tropical South Atlantic being warmer than usual, leading to a longer than expected rainy season, while the 2012 event was linked to La Niña events of El Niño–Southern Oscillation (ENSO) years, characterised by a decrease in surface temperatures of the central equatorial Pacific during summer (Espinoza et al. 2012; Marengo et al. 2013b) ENSO events are naturally occurring fluctuations in the tropical Pacific. The event generally varies between two states: El Niño, where sea surface temperatures in central-eastern equatorial Pacific are warmer than usual and La Niña, where sea surface temperatures in central-eastern equatorial Pacific are colder than usual (Sarachik & Cane 2010).

In Central and South America, there are regional variations in extreme rainfall, which could impact flood risk. However, projections have a low to medium confidence level (Field 2012). Haylock et al. (2006) found that areas such as Ecuador, northern Peru, southern Brazil, Paraguay, Uruguay, and northern and central Argentina seems to move to wetter conditions, while a decrease in rainfall was perceived in southern Peru and southern Chile. Aguilar et al. 2005 found that although there are no significant increases in the total number of rainfall events in Central and South America, these events are intensifying and the impact of rainy days are greater. Giorgi (2006) found that

there is a decrease in precipitation, but an increase variability of precipitation events in Central America.

2.4.3 Africa

In Africa, floods can have a significant impact on the African environment and economies (Field 2012). The onset of heavy rains in the Sahel region in 2007 led to extensive floods, affecting 792 676 people in West Africa and leading to 210 deaths (Samimi et al. 2007). The most affected regions were Ghana, followed by Togo and Burkina Faso. Other affected countries included Benin, Côte d'Ivoire, Gambia, Liberia, Mali, Mauritania, Niger, Nigeria, Senegal and Sierra Leone (Samimi et al. 2007). In 2009, the seasonal floods in this region affected more than 940 000 people, and led to about 193 deaths (UNOCHA 2009). Southern Africa is also subject to severe floods. In Mozambique the 2000 floods led to 699 reported fatalities and hundreds of thousands of people were displaced (Moore, Eng & Daniel 2003). During the 2008 floods in Mozambique, there were 20 reported dead, while 113 000 were displaced (WWAP 2009). Areas like Angola, Namibia and Zambia are prone to seasonal floods during the rainy seasons of December to April (PDNA 2009). In 2011, for example, floods occurring in Angola and Namibia adversely affected about 260 000 Namibian residents (NASA 2011; UNOCHA 2011).

Several studies have noted a correlation between ENSO events and extreme rainfall and periodic floods. Reason & Keibel (2004), for example, found that floods in Mozambique, South Africa and Zimbabwe in 2000, were linked to a La Niña event. Washington & Preston (2006) found that two of the wettest years in Southern Africa (1974 and 1976) were linked to La Niña events. Additionally, in Equatorial east Africa heavy rain-induced floods related to ENSO in dry arid and semi-arid regions increased of vector and epidemic diseases (Anyamba et al. 2006).

Di Baldassarre et al. (2010) examined 79 major rivers in Africa and found that floods in Africa have not significantly increased in the 20th century and climate changes have not been a major factor in the observed increase in flood damage and fatalities. Yet it was found that rapid, unplanned urbanisation in flood-prone areas led to an increase in the vulnerability of populations to floods. Areas such as Lusaka in Zambia, Dakar in Senegal, Alexandria in Egypt, Ouagadougou in Burkina Faso, and Kampala in Uganda, where an increasing number of people inhabit flood-prone areas, are examples of this phenomenon (Brauch 2003; Nchito 2007; Di Baldassarre et al. 2010; Diallo et al. 2012; Isunju, Orach & Kemp in press). Usually, the poorest and most marginalised tend to locate in areas with high flood risk, not being aware of the risk and unequipped to respond properly to floods and mitigate its adverse effects (Di Baldassarre et al. 2010).

2.5 BASIC PRINCIPLES OF SAR IMAGERY

This section serves as an introduction to the basic principle of SAR images. The section begins general overview SAR, followed factors affecting received backscatter for SAR images. Pre-processing of SAR imagery is also described.

2.5.1 General overview of SAR imagery

SAR sensors have certain advantages over optical sensors. They are active sensors that transmit their own energy and record the echoes reflected off the Earth's surface (Campbell & Wynne 2011). Their use is therefore not constrained by the time of day and missions using active microwave sensors can be scheduled during unsatisfactory times for optical sensors (Horritt 1999). Because they use longer wavelengths in the microwave region of the electromagnetic spectrum, images are not severely affected by atmospheric attenuation such as clouds and light rain (Horritt 1999). SAR images are also sensitive to small scale surface roughness, soil moisture and slope (Kussul, Shelestov & Skakun 2008). The properties of the transmitted energy are also known, since it is generated by the sensor itself. The transmitted energy can therefore be compared to the received energy to determine characteristics of the illuminated surface (Campbell & Wynne 2011).

A SAR image represents the backscattered power received by the antenna from the targeted area on the Earth's surface. This backscatter is the portion of the transmitted signal returned towards the antenna (Campbell & Wynne 2011). The backscatter values of each pixel in the SAR image are often converted to a physical quantity known as the backscattering coefficient or the normalised radar cross section and expressed in decibel (dB) (Lillesand, Kiefer & Chipman 2008). The strength of the returned backscatter depends on the characteristics of the target on the Earth's surface as well as the properties of the SAR systems (Campbell & Wynne 2011).

2.5.2 Factors affecting received backscatter for SAR images

As stated in the previous section, the received SAR backscatter depends on the SAR system properties and surface properties. System properties include wavelength, incidence angle and polarisation, and surface parameters include surface roughness, topography and the dielectric properties of the target object (Campbell & Wynne 2011).

2.5.2.1 Wavelength

SAR sensors operate within a small range of wavelengths within the microwave region of the electromagnetic spectrum. Satellite-borne sensors mostly operate at L-, X- and C-band wavelengths, as summarised in Table 2.1 below (Tiner, Lang & Klemas 2015).

Table 2.1: Radar classifications and wavelength for imaging SAR systems

Band	**Wavelength [cm]**	**Frequency [GHz]**
L	15-30	1-2
C	3.7-7.5	4-8
X	2.5-3.7	8-12

Adapted from Tiner, Lang & Klemas (2015)

For SAR systems, surface roughness depends on the wavelength as will be discussed in section 2.5.2.4. The wavelength also influences the penetration depth of the SAR signal. Longer wavelengths, such as the L-band, can penetrate denser vegetation canopies and the signal is mostly scattered by larger elements of vegetation elements such as tree trunks and the larger branches of a tree, as well as the surface (Kasischke, Melack & Dobson 1997). Shorter wavelengths, such as the C-band and the X-band, are mainly scattered by smaller elements such as the smaller leaves and branched of the crown (Kasischke, Melack & Dobson 1997).

2.5.2.2 Incidence angle

The incidence angle is the angle between the incident radar beam at the ground and the line perpendicular to the surface of the earth at the point of incidence as seen in Figure 2.1 (Campbell & Wynne 2011). Backscatter generally increases as the incidence angle decreases (Mather 2004). Generally, incidence angles between 0° and 30° causes radar backscatter to be dominated by topographic slope. For angles between 30° and 70°, surface roughness dominates the image. For incidence angles greater than 70°, radar shadows dominate the image (Lillesand, Kiefer & Chipman 2008).

Incidence angle has an influence on the penetration depth through canopy of surface vegetation. Shallower incidence angles increases the path length of the incoming SAR signal, thereby increasing attenuation of the signal by vegetation canopy and increasing volume scattering (Töyrä & Pietroniro 2005). Steeper incidence allow for better penetration through the vegetation canopy (Töyrä & Pietroniro 2005).

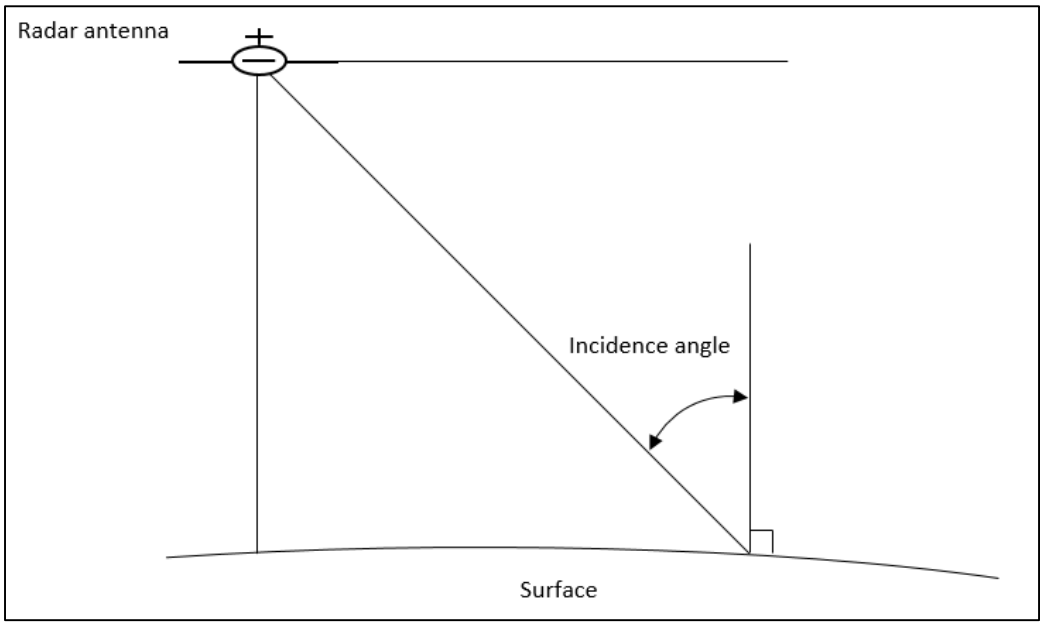

Adapted from Campbell & Wynne (2011)

Figure 2.1: Basic geometry of a radar image: nomenclature

2.5.2.3 Polarisation

The transmitted and recorded signals of SAR systems consist of an electrical field and a magnetic field, perpendicular to and in phase with each other, both oscillating in direction perpendicular to the direction of propagation (Figure 2.2) (Raney 1998).

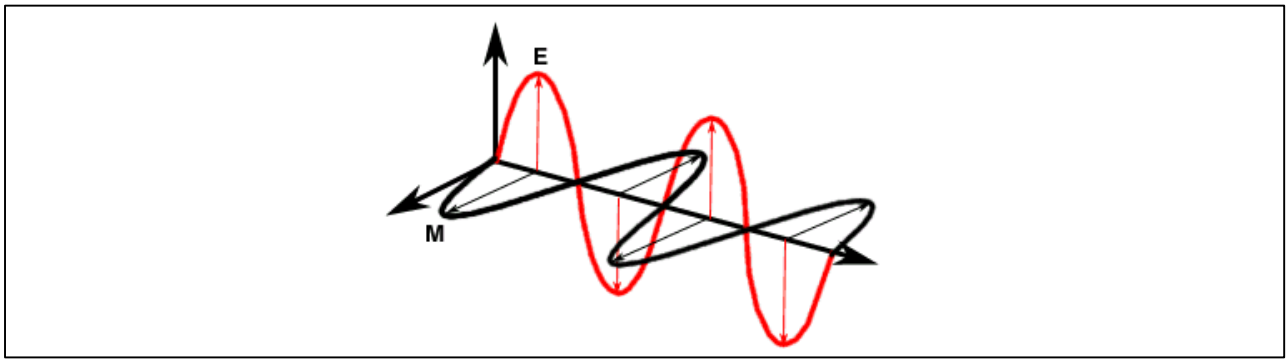

Source: ESA (2014)

Figure 2.2: Electric field (E) and magnetic field (M) of electromagnetic radiation

The polarisation describes the orientation of the electric field of the transmitted and recorded signal. Radar systems normally transmit and receive either horizontally polarised (H) or vertically polarised (V). VH-polarisation will therefore represent vertically transmitted signal and horizontally received backscatter. The four possible combinations of transmission and reception are therefore the two like-polarisations (HH- and VV-polarisation) and two-cross polarisations (HV-and VH-polarisation) (Campbell & Wynne 2011). Physical and electrical properties of the objects on the ground can have an effect on the polarisation of the reflected signal. Supplementary

information regarding an object can therefore be derived as some surfaces tend to depolarise the signal, causing a lower signal return in the like-polarised images (Campbell & Wynne 2011).

2.5.2.4 Surface roughness

Surface roughness is a very important factor when considering backscatter return received from the surface. The roughness of a surface depends on the wavelength to a large extent since the SAR signal interacts with features similar or greater in size than its wavelength. However, both incidence angle and wavelength determine whether a surface is considered to be smooth or rough. A method to quantify surface roughness is using the relationship between the standard deviation of the surface height (S_h), the wavelength (λ) and incidence angle (θ) as given in Equation 2.2, Equation 2.3 and Equation 2.4 by Peake & Oliver (1971). A smooth surface is defined as one where S_h is less than the expression given below:

$$S_h < \frac{\lambda}{25\cos(\theta)} \qquad \text{Equation 2.2}$$

A rough surface is defined as one where S_h is greater than the expression given below:

$$S_h > \frac{\lambda}{4.4\cos(\theta)} \qquad \text{Equation 2.3}$$

Surfaces of intermediate roughness is one where S_h lies between these two values:

$$\frac{\lambda}{25\cos(\theta)} > S_h > \frac{\lambda}{4.4\cos(\theta)} \qquad \text{Equation 2.4}$$

As stated previously, backscatter received from the surface partly depends on the wavelength, incidence angle and surface roughness and the relationship between these variables has been examined by Ulaby, Moore & Fung (1986) and can be seen in Figure 2.3:

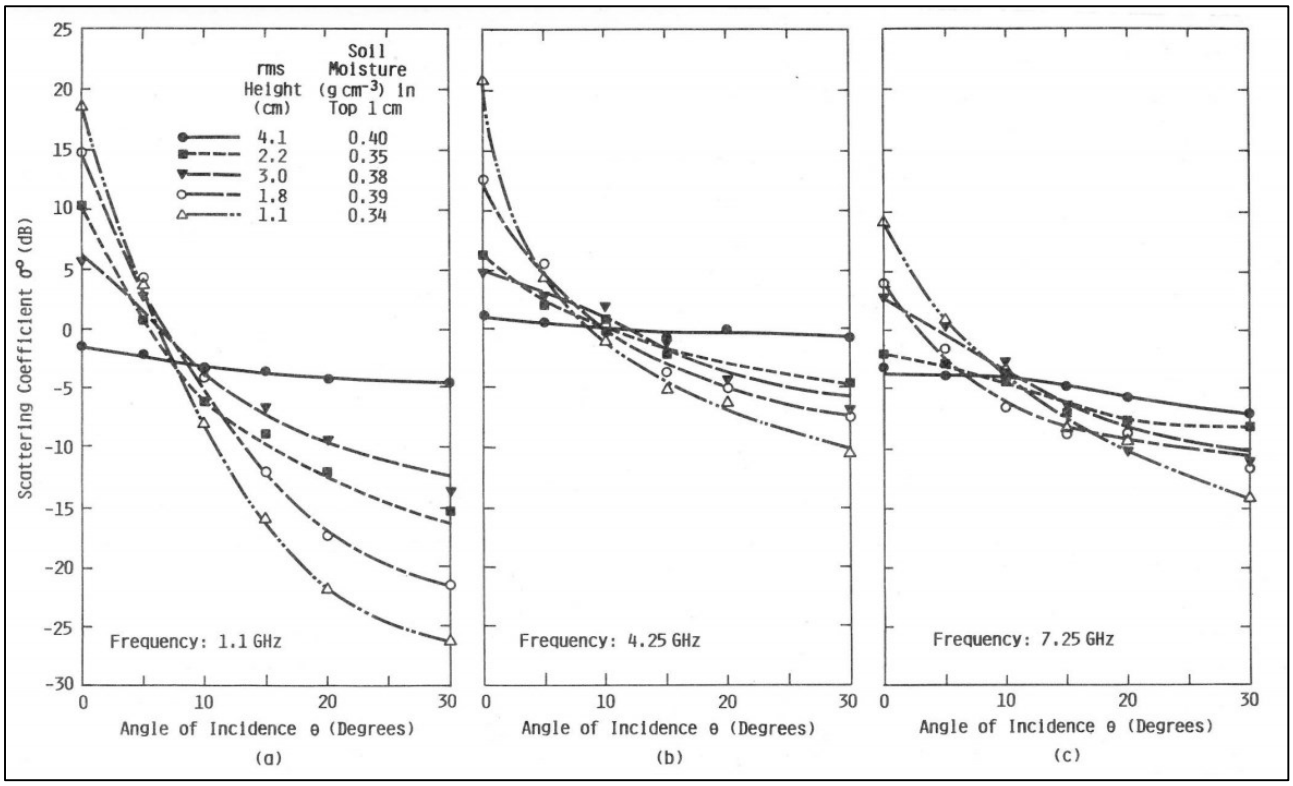

Figure 2.3: The effect of incidence angle and surface roughness on the received backscatter for the L-band (a), C-band (b) and the X-band (c).

Figure 2.3 illustrates how the backscatter return changes depending on the surface roughness and incidence angle for the L-band, C-band and X-band in Figure 2.3a, Figure 2.3b and Figure 2.3c respectively. As wavelength decreases from The L-band to the X-band, the effect of the incidence angle on the backscatter becomes less pronounced. The sensitivity to surface roughness decreases as the wavelength decreases. For a given surface roughness, the change in backscatter is also greater for the longer the longer L-band than and becomes less exaggerated with as the wavelength decreases from Figure 2.3a to Figure 2.3c.

2.5.2.5 Double bounce

Apart from the surface roughness, the geometric configuration of objects can cause brighter return signals than expected. This happens because the radar return signal is enhanced by intersecting specular surfaces, or corner reflectors, thereby generating double bounce reflectance (ESA 2014). Corner reflectors are commonly found in urban areas because many features with complex angular shapes are found there, but can also be found in rural areas (Campbell & Wynne 2011).

2.5.2.6 Dielectric properties

The dielectric properties of a material (ϵ) are used as a measure of the reflectivity and conductivity of a substance (Woodhouse 2006). It is a complex value, consisting of a real component (ϵ') and an imaginary component (ϵ'') and is expressed using the following equation:

Equation 2.5

$$\epsilon = \epsilon' - i\epsilon''$$

The real component, ϵ' represents the permittivity of the material (Ulaby, Moore & Fung 1986) and is referred to as the dielectric constant. The imaginary component, ϵ'', designates losses of the dielectric constant (Ulaby, Moore & Fung 1986; Raney 1998). The dielectric constant of a target measures its ability to conduct electrical energy. This value is strongly affected by moisture, consequently the presence of moisture in both soil and vegetation has a significant impact on radar backscatter (Campbell & Wynne 2011). An increase in moisture leads to an increase in backscatter. The radar signal is sensitive to the presence of moisture in the soil and vegetative tissue. An increase in moisture leads to a significant increase in radar reflectivity. The effect of this sensitivity seems to be most pronounced at steep depression angles.

2.5.3 Pre-processing of SAR imagery

SAR images are subject to severe geometric distortions such as layover, foreshortening and shadow, as well as radiometric distortions, especially in regions with high and variable relief (Campbell & Wynne 2011). The radiometric and geometric properties of an image are significantly influenced by the regional terrain (Lillesand, Kiefer & Chipman 2008). Images must therefore be corrected before they can be used for surface mapping and change detection.

2.5.3.1 Terrain correction and geocoding

Variations in the topography of a SAR scene have a strong impact on the backscatter return. Changes in the geometry of the surface lead to variations in the backscatter signal, thereby complicating interpretation of information such as surface roughness and dielectric properties present in the backscattered signal (Wivell et al. 1992). In order to put SAR images to full use, these effects caused by terrain must be removed (Wivell et al. 1992).

Due to the side-looking geometry of SAR images, they are subject to distortions caused by differences in height in the range (across-track) direction (Lillesand, Kiefer & Chipman 2008). These geometric distortions can be corrected by geocoding the SAR image (Wivell et al. 1992). When an image is geocoded, each pixel in the original image is transformed to a reference map geometry (Holecz et al. 1994). The Range-Doppler algorithm (used in this study for geocoding) is

an inverse transformation model, whereby a digital elevation model (DEM), position and velocity vectors and the Doppler frequencies and pulse transit times are required as input and the pixel location of the SAR image is returned (Wivell et al. 1992; ESA 2014).

2.5.3.2 Radiometric calibration

Raw SAR images are usually not radiometrically corrected and significant radiometric bias are present within images. Uncalibrated SAR images are appropriate for qualitative use, but for quantitative image analysis SAR images need to be calibrated (El-Darymli et al. 2014). Radiometric calibration is also required for comparison of SAR images which were either acquired by different SAR sensors or images acquired from the same sensor but at different times, in different modes or processed by different image processors (El-Darymli et al. 2014).

During radiometric calibration, local incidence angle correction and image replica power adjustments are performed (Freeman 1992; Kellndorfer Dobson & Ulaby 1996) and topographic distortions are therefore corrected for each pixel (Small et al. 1997). The backscatter signal is converted to the normalised radar cross section (σ^0), a normalised, unitless entity which represents the strength of the returned SAR signal and is normally expressed in decibels (dB) (Lillesand, Kiefer & Chipman 2008).

2.5.3.3 Speckle

All radar images are subject to a certain degree of speckle, which is a seemingly random pattern of brighter and darker in the image, giving the image a salt-and-pepper look. This phenomenon is because radar pulses are transmitted coherently such that the waves oscillate in phase with one another. The multiple scattering returns are modified by constructive and destructive interference within each resolution cell, causing speckle (Lillesand, Kiefer & Chipman 2008). Speckle in an image will generally increase with signal intensity (Masoomi, Hamzehyan & Shirazi 2012; Nezry 2014). Speckle can be minimised using different techniques such as multiple look-processing or filtering techniques (Raney 1998).

For this study, Frost filtering was used as method for speckle filtering. Frost speckle filtering is well suited for delineating flood extent as it preserves the edges and texture of the original image but it increases image contrast and speckle noise (Zhou et al. 2000). Frost filtering operates on the basic concept of minimising the mean square error based on the assumption that an image is degraded by multiplicative noise (Frost et al. 1982; Ozdarici, & Akyurek 2010). The value of the filtered pixel of interest depends on the weighted sum of the kernel and the weighting factor decreases as distance from the pixel of interest increases (Wang Ge & Li 2012). The filter adapts based on changes in the local mean and standard deviation within homogeneous areas while also

preserving the edges (Frost et al. 1982). A damping factor is also required: a larger damping value will preserve the edges more accurately, but pixel values are smoothed less (Wang Ge & Li 2012).

2.6 SAR INTERACTION WITH FLOODED LANDSCAPES

2.6.1 Open water

At radar wavelengths, open water is generally smooth and considered to be a specular reflector. The incident microwave radiation is directed away from the SAR system by water, yielding low backscatter values. The surrounding terrain is assumed to be rougher and act as a diffuse reflector and the backscatter values are generally higher than those of open water (Solbø & Solheim 2004). The contrast between open water areas and the surrounding terrain is mostly dependent on the incidence angle, wavelength and polarisation of the SAR system (Henderson 1995; Solbø & Solheim 2004).

As the incidence angle increases, the contrast between water and land areas generally increases and are therefore more easily separable (Solbø & Solheim 2004). However, an increase in incidence angle may also lead to more shadowing effects, especially in areas of steeper terrain and high resolution imagery (Henderson 1995). These areas could therefore be incorrectly interpreted as water (Henderson 1995). Steeper incidence angles can also lead to layover, which can lead to loss of information when classifying slim water bodies constrained by high trees or banks (Henderson 1995). Additionally, water surfaces are also more sensitive to surface roughness at steeper incidence angles (Töyrä & Pietroniro 2005). Longer L-band imagery is most suitable to delineate the water-land boundaries, followed by the shorter wavelengths such as C-band and X-band, since longer wavelengths are less sensitive to small-scale surface roughness such as wind and waves over water surfaces (Alsdorf, Rodríguez & Lettenmaier 2007; Bartsch et al. 2012). Surfaces appear rougher at shorter wavelengths leading to higher backscatter values over water, thereby lowering the contrast between water and surrounding land (Ulaby, Moore & Fung 1986; Bartsch et al. 2012). The L-band has also been found to be better suited to distinguish between several roughness classes than the C-band or the X-band (Ulaby, Moore & Fung 1986). Martinis (2010), however, argues that X-band may be better suited to distinguish between water and land despite the relative increase in backscatter over smooth water surfaces. Fewer features will have a smooth surface and tone similar to water and therefore a higher contrast ratio between water and terrestrial surfaces exists (Drake & Shuchman 1974).

When the general statistics were taken into account, Henry et al. (2006) observed secondary peaks in the like-polarized images concluded that like-polarised data are better than cross-polarised data

for flooded area identification. HH-polarisation in particular is well suited for discrimination between water and the surrounding land, and usually has the best radiometric dynamic range, which suggests better differentiation between classes (Henry et al. 2006). The horizontal component of the signal exhibits lower scattering from open water surfaces (Henry et al. 2006; Martinis, Twele & Voigt 2009). Cross-polarisation contributes information regarding the characteristics of the landscape, distinguishing forested areas from bare soil areas and thereby providing more information for delineating flood extent. Cross-polarised imagery is also less sensitive to surface conditions such as surface roughness caused by wind. However, the radiometric dynamics are usually lower than like-polarisations, which could cause lower class separability (Henry et al. 2006).

If surface water roughness increases due to wind, waves or streams, backscattering of water areas can increase, causing difficulties in identifying flooded areas, leading to lower class separability (Brivio et al 2002; Horritt, Mason & Luckman 2001). The contrast between open water and the surrounding land will decrease with an increase in wind speeds. VV-polarised imagery is the most sensitive to waves and ripples and cross-polarisation usually outperforms VV-polarised images for open water surfaces (Henry et al. 2006; Matgen et al. 2007).

2.6.2 Flooded vegetation

Complex vegetation cover with different structural layers affects the radar backscatter. For flooded vegetation, three important backscattering mechanisms are involved when considering backscatter received from flooded vegetation: "scattering from the canopy, specular scattering from the water surface, and double reflection between the water surface and the emergent vegetation" (Horritt et al. 2003: 271). These backscattering mechanisms can further be expanded using Equation 2.6 and Equation 2.7 as discussed later on in this section. However, the backscatter from flooded vegetation is intricate and multifaceted, and depends on the vegetation cover, as well as wavelength, incidence angle and polarisation of the SAR (Bourgeau-Chavez et al. 2009). In this section, the effect of forest as well as non-woody, herbaceous vegetation cover on the identification of flooded area with SAR imagery, will be discussed.

A forested area has three distinct layers: The ground layer; the trunk layer – made up of trunks and large branches; and the canopy layer, which comprises of foliage and small twigs (Kasischke & Bourgeau-Chavez 1997). The total backscatter received from forested vegetation is a result of these components: the total backscatter received from forested areas can be attributed to backscatter from the surface, backscatter from the canopy layer, backscatter from the tree trunks,

double bounce backscatter from the tree trunk-ground and the ground and multiple path backscatter between the canopy and ground (Kasischke & Bourgeau-Chavez 1997). These components can be seen in Figure 2.4 below:

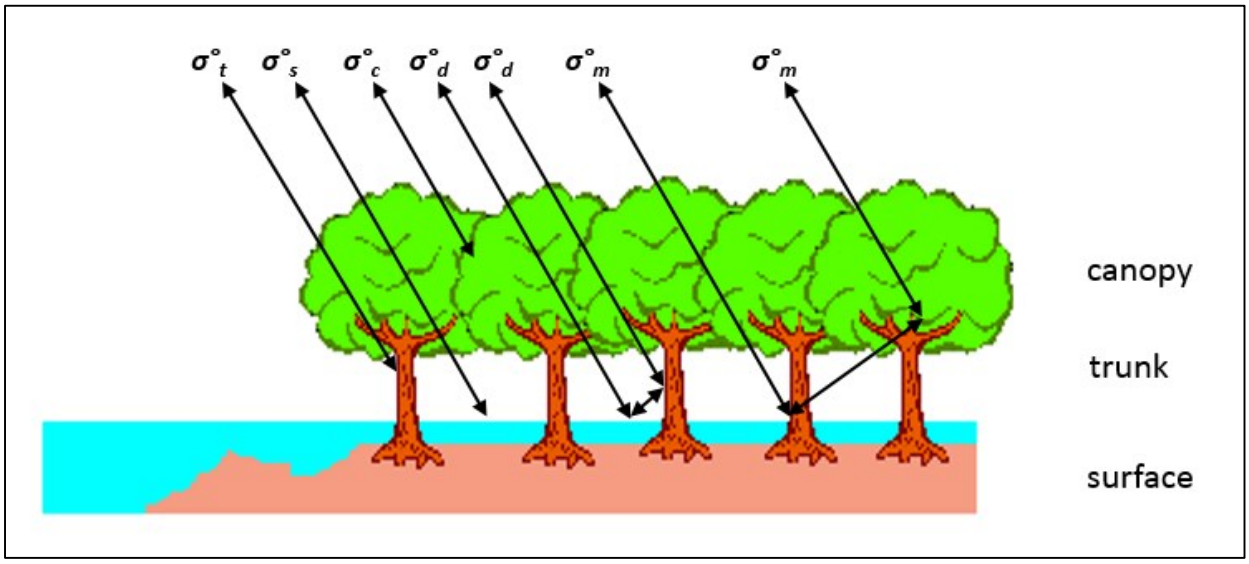

Adapted from Kasischke & Bourgeau-Chavez (1997)

Figure 2.4: The major sources of backscatter from flooded woody vegetation: surface backscatter (σ_s), canopy backscatter (σ_c), tree trunk backscatter (σ_t), ground-trunk backscatter (σ_d) and multiple path backscatter (σ_m)

The relationship between these variables can expressed using the following formula (Dobson et al. 1995):

$$\sigma^\circ_{tw} = \sigma^\circ_c + \tau_c^2 \tau_t^2 \left(\sigma^\circ_m + \sigma^\circ_t + \sigma^\circ_s + \sigma^\circ_d\right) \qquad \text{Equation 2.6}$$

where

σ°_{tw}	is the total backscatter
σ°_s	is the surface backscatter
τ_c	is the transmission coefficient of the vegetation canopy
τ_t	is transmission coefficient of the trunk layer,
σ°_c	is the backscattering from the canopy layer;
σ°_m	is the multiple path scattering between canopy and ground;
σ°_t	is scattering from the tree trunk; and
σ°_d	is the double bounce backscatter from the trunk and the ground.

When surface roughness (relative to wavelength) is present, backscatter returned from the surface (σ°_s) is higher, while multipath energy (σ°_m) and double bounce energy (σ°_d) decreases (Kasischke & Bourgeau-Chavez 1997). When the surface is flooded, the surface roughness is therefore

removed and the ground-trunk ($\sigma°_d$) and ground-canopy ($\sigma°_m$) interaction is higher (Hess, Melack & Simonett 1990; Kasischke & Bourgeau-Chavez 1997). This is illustrated Figure 2.5. A flooded forested area will therefore have higher backscatter return than the same area during dry conditions, due to this double bounce between the water surface and the forest stems. Townsend (2002) found that the double bounce interaction ($\sigma°_d$) has the highest influence on the total backscatter received from flooded forest.

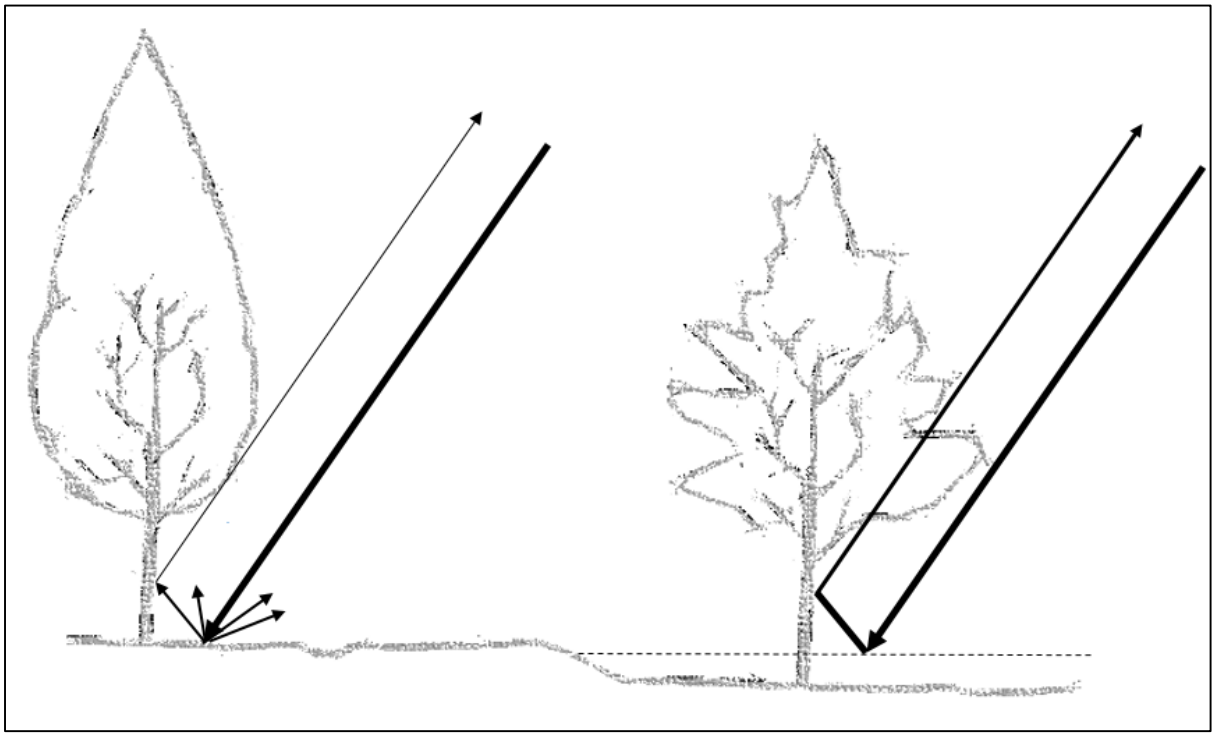

Adapted from Hess, Melack & Simonett (1990)

Figure 2.5: SAR signal interaction with trunks in non-flooded conditions (left) and flooded conditions (right). Signal return is higher in flooded conditions because of less surface scattering

The dielectric constant is also an important factor, were an increase in the dielectric constant results in higher backscatter from the surface ($\sigma°_s$), multipath energy ($\sigma°_m$) and double bounce energy ($\sigma°_d$) (Kasischke & Bourgeau-Chavez 1997). Detecting flooded area beneath the forest layer also depends on the transmission coefficients of the trunk (τ_t) and the canopy layer (τ_c) higher transmission will lead to higher returns from the surface ($\sigma°_s$), multipath energy ($\sigma°_m$), double bounce energy ($\sigma°_d$) and tree trunk ($\sigma°_d$) (Townsend 2002). The transmissivity is influenced by the biomass of the forested vegetation, and a higher biomass will decrease both transmissivity coefficients, thereby decreasing the total backscatter (Dobson et al. 1995).

Non-woody, herbaceous vegetation only consists of two layers, the canopy layer and the surface layer, as seen in Figure 2.6 (Kasischke & Bourgeau-Chavez 1997). The total backscatter for these

vegetation types ($\sigma°_{th}$) can be determined by removing the trunk layer and its variables from the equation, thereby simplifying the formula to the following:

$$\sigma^{\circ}_{th} = \sigma^{\circ}_{c} + \tau_c^2(\sigma^{\circ}_{m} + \sigma^{\circ}_{s})$$

Equation 2.7

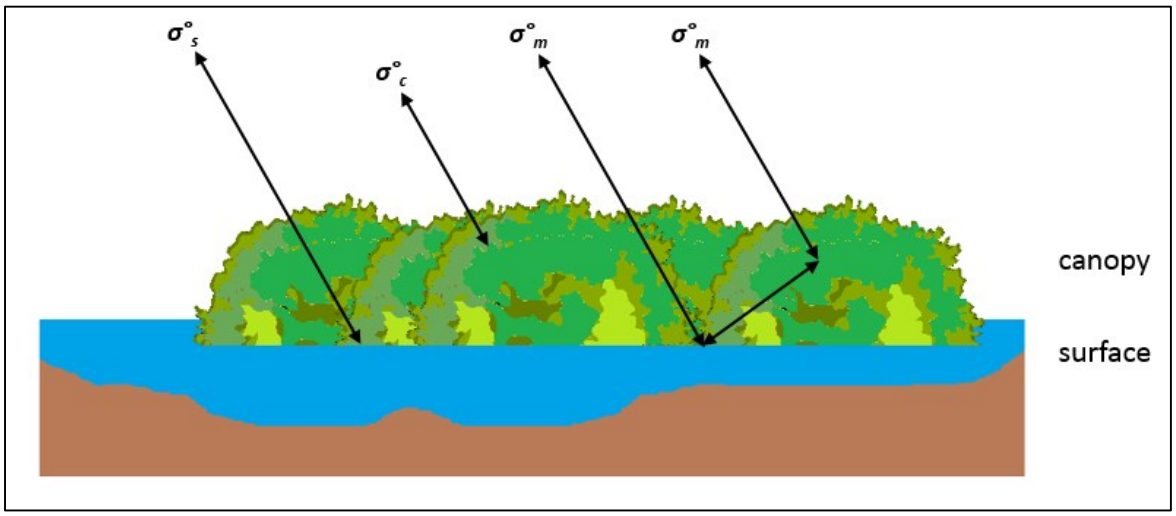

Adapted from Kasischke & Bourgeau-Chavez (1997)

Figure 2.6: The major sources of backscatter from flooded herbaceous vegetation: surface backscatter (σs), canopy backscatter (σc) and multiple path backscatter (σm).

For forest areas, the transmissivity coefficients of the trunk (τ_t) and the canopy layer (τ_c) depend on the wavelength of the SAR signal. Longer wavelengths such as the L-band are more suited for flood detection in forested areas due to the higher transmissivity coefficients and double bounce being more pronounced (Hess, Melack & Simonett 1990). If the wavelength is longer than the leaf size then the canopy layer has almost no effect on the backscatter received by the sensor (Wang et al. 1995). Shorter wavelengths, such as the C-band and the X-band, have lower transmissivity and scattering from the tree canopy is dominant. Double-bounce is therefore not as pronounced as it is with longer wavelengths and total backscatter is lower (Townsend 2001).

C-band imagery, however, has been successful in the mapping of inundation in forested areas, especially during leaf-off conditions and areas with sparse forested vegetation (Townsend 2001; Lang, Townsend & Kasischke 2008). During leaf-on conditions, increased canopy attenuation and volume scattering leads to lower backscatter values than during leaf-off conditions, and the contrast between flooded and non-flooded forest is therefore lower than during leaf-off conditions. The effect of forest density for C-band energy can be illustrated in Figure 2.7. A dense forest scatters the signal at the canopy level and little energy reaches the ground layer. If the forest canopy

is sparse, the signal reaches the ground surface and flood surface or soil moisture conditions can be detected

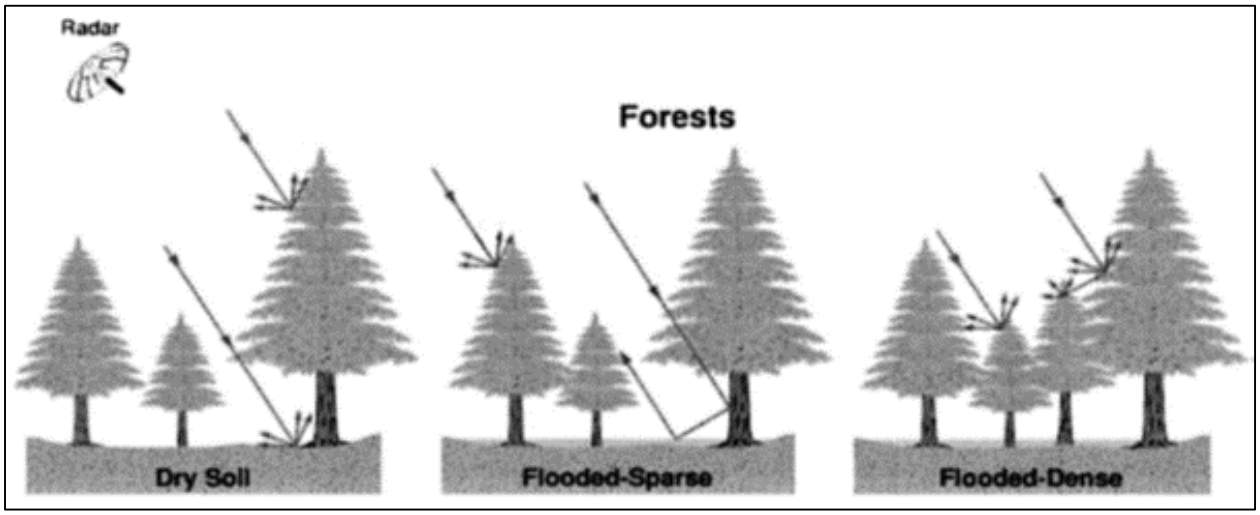

Adapted from Bourgeau-Chavez et al. 2005

Figure 2.7: Theoretical scattering mechanisms of C-band energy from flooded versus non-flooded conditions in forested areas

Horritt, Mason & Luckman (2001), however, found that for C-band images, some unflooded vegetation regions had low backscatter values (comparable to open water) and were likely to be misclassified as water. This was likely due to enhanced backscatter, expected from wet soils in the area, being reduced by dense vegetation canopy cover. For X-band imagery, Henderson (1995) found that higher signal return due to double bounce was present at the edges of flooded forests, since volume scattering from the canopy is not of importance.

For herbaceous vegetation, longer wavelengths, such as the L-band do not interact with the vegetation, thus generating low backscatter such as that expected of water (Horritt et al. 2003). The shorter C-band and X-band data experience higher signal returns in marshlands because of double bounce from the canopy layer (Ormsby, Blanchard & Blanchard 1985; Horritt, Mason & Luckman 2001; Horritt et al. 2003). The water level or soil moisture content for herbaceous wetlands are, however, important to consider when interpreting signal return as illustrated for areas of dry soil, wet soil and inundated conditions in Figure 2.8 for C-band energy. If the soil is dry the signal return is low because of diffuse scattering from the canopy and the ground. With an increase in moisture comes an increase in the dielectric constant and possibly some double bounce scattering from the ground-stem interaction. When water levels increase and the ground as well as the vegetation are flooded, energy is scattered forward in a specular fashion causing a lower signal return than that of dry soil (Bourgeau-Chavez et al. 2005).

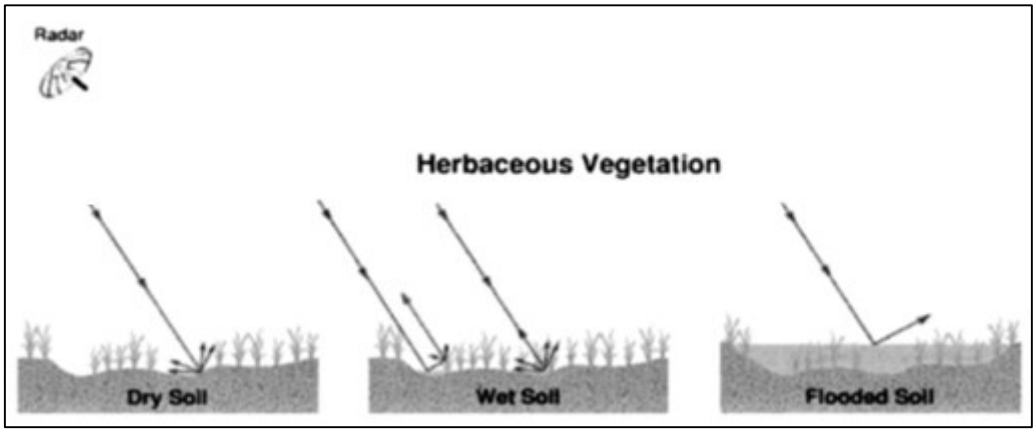

Adapted from Bourgeau-Chavez et al. (2005)

Figure 2.8: Theoretical scattering mechanisms of C-band energy flooded versus non-flooded conditions for herbaceous vegetation areas

Incidence angle also has an impact on signal return from flooded vegetation. For both forested and non-woody vegetation, steeper incidence angles (less than 35°) are preferred for flood detection. For steeper incidence angles, the path length of the radiation between travels through the canopy layer is shorter than that of shallower incidence angles. The attenuation and the volumetric scattering from the canopy layer is therefore less and double bounce is greater (Hess, Melack & Simonett 1990; Wang et al. 1995). The effect of the incidence angle, however, is dependent on forest type and structure (Towensend 2001).

In the Amazon wetlands, for example, for all flooded vegetation types, there is an almost linear decrease in backscatter response as incidence angles become shallower, until about 34° (Tiner, Lang & Klemas 2015). After this, the linear decrease continues for grass and forested areas, but there is not a substantial decrease for shrubs (Tiner, Lang & Klemas 2015). For low biomass emergent vegetation, backscatter decreases until about 39°, and starts to increase at about 46°, since only signals at very shallow incidence angles will interact with these vegetation types with short vertical profiles (Tiner, Lang & Klemas 2015).

Lang, Townsend & Kasischke (2008) however found that backscatter generally decreased with an increase in incidence angle for flooded and non-flooded conditions, but the distinction between flooded and non-flooded regions did non decline as severely with increase incidence angle. The detection of flooded conditions under forests at steeper incidence angles was also less than

expected, but greater than expected at shallower incidence angles (Lang, Townsend & Kasischke 2008).

Backscatter from flooded vegetation is also dependent on polarisation. Like-polarised data are preferred to identify flooded forested areas, but HH-polarised imagery is preferred over VV-polarisation, mostly because the difference between flooded and non-flooded forested area is most pronounced in HH-polarised images (Kasischke & Bourgeau-Chavez 1997). The double bounce backscatter return from the surface-trunk interaction is much less pronounced for VV-polarisation than for HH-polarisation due to greater canopy volume scattering of VV-polarisation. Wang et al. (1995) found that backscatter returns from HV-polarised energy for C- L- and P-wavelengths are mostly from the tree crown layer and returns are about the same for flooded forest as for non-flooded forested areas.

HV-polarised data is however best for discrimination between herbaceous and woody vegetation in wetlands, since they are most sensitive to biomass (Bourgeau-Chavez et al. 2001). Pope et al. (1997) found that L-band HH-polarised data and C-band HH- and VV-polarised data can detect flooded conditions for dense marshlands (where herbaceous vegetation is dominant), but C-band VV-polarised data was better for detection in marshlands with lower percentage vegetation cover.

2.6.3 Flooded urban areas

Flood delineation in urban areas using SAR imagery has been met with limited success. Buildings which act as corner reflectors and metal surfaces cause enhanced scattering as seen in Figure 2.9a. This enhanced scattering effect is also perceived during flooded conditions (seen in Figure 2.9b) and no changes are apparent when compared to non-flooded conditions (Giacomelli, Mancini & Rosso 1995; Oberstadler, Hönch & Huth 1997; Solbø & Solheim 2004).

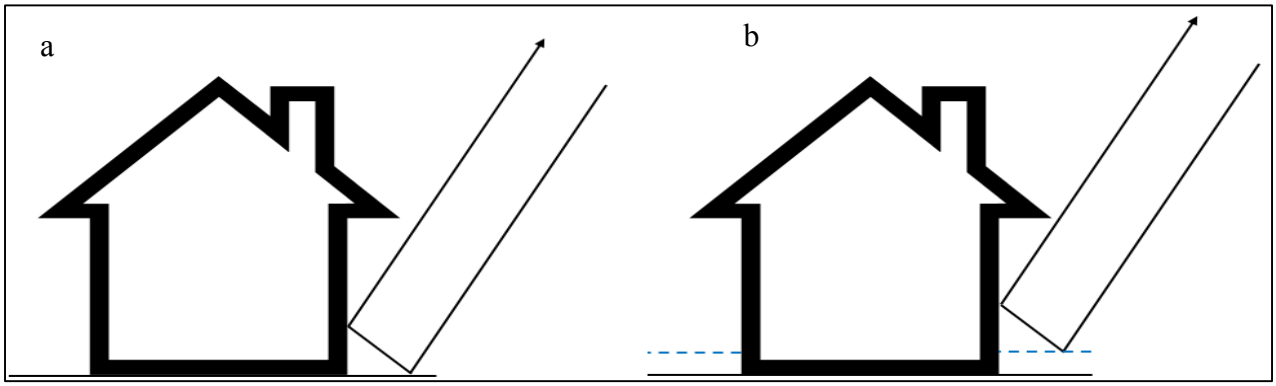

Adapted from Solbø & Solheim (2004)

Figure 2.9: Urban areas during non-flooded conditions (a) and flooded conditions (b). Changes are not apparent in urban areas

The side-looking nature of SAR systems may also affect flood-detection in urban areas. Some areas such as regions with steep terrain and regions with tall buildings (e.g. urban areas) may be hidden because of shadow and foreshortening effects, and land use information cannot be extracted (Oberstadler, Hönch & Huth 1997; Mason et al. 2010) Smooth surfaces such as roads may appear dark on SAR imagery because of specular reflection and can wrongly be classified as flooded area (Oberstadler Hönch & Huth, 1997).

Flood detection can be enhanced in all areas, including urban terrain, when interferometric coherence information is used in combination with radar backscatter (Stabel & Löffler 2003). Repeat pass interferometry has been found to be a more challenging approach for flood delineation because of long repeat times and a high chance of the occurrence of temporal de-correlation (Solbø & Solheim 2004). Kemp (2010), however, found that interferometric coherence is a suitable tool for flood extent delineation in Réunion Island and L-band data, in particular, worked well for flood extent delineation if the repeat times are not too long.

2.7 APPROACHES TO FLOOD EXTENT DELINEATION USING SAR IMAGERY

In this section a brief overview of methods for flood mapping with the use of SAR imagery is provided. An overview of the widely-used approaches to flood delineation using SAR imagery will first be given, followed by a more in-depth discussion of the two selected methods for flood extent delineation used in this study, namely thresholds and ACMs.

2.7.1 General overview

A very simple and commonly used technique for estimation of water extent on SAR imagery is visual interpretation (e.g. Oberstadler, Hönch & Huth 1997). However, since only a restricted number of grey-levels are discernible with the human eye, visual interpretation of a single SAR image is difficult. Some backscatter values are also not characteristic of water and can only be detected using more than one image (Oberstadler, Hönch & Huth 1997). Additionally, since this is a manual process involving digitising of the boundary between land and water, it is time consuming. Results are also subjective, making repeatability of results difficult (Martinis 2010).

Another (and frequently used approach) to flood mapping is the separation of flooded and non-flooded areas using thresholding (Voigt et al. 2008). A threshold value is determined to separate the flooded areas with low backscatter from the non-flooded areas with higher backscatter values. The selected threshold depends on the study area and the distribution of the backscatter intensity

(Sanyal & Lu 2004). Thresholds can either be determined manually (e.g. Malnes, Guneriussen & Høgda 2002; Solbø & Solheim 2004; Henry et al. 2006; Manjusree et al. 2012; Long, Fatoyinbo & Policelli 2014), or automatically (e.g. Bazi, Bruzzone & Melgani 2005). A disadvantage of using thresholds is that the values will depend on the SAR instrument and respective image and when thresholds are manually selected the results can lack objectivity and traceability (Kussul, Shelestov & Skakun 2008). A more in-depth look at thresholds can be found in section 2.7.2.

Supervised classification has also been applied to flood mapping using SAR imagery. De Roo et al. (1999) digitised flooded and non-flooded areas on ERS-1 and -2 images. These areas were used as training areas and image classification was performed using a maximum likelihood classification. The assumption was made that data approximate a normal distribution of the flooded and non-flooded areas. Townsend (2001) classified RADARSAT images of the forests of the Roanoke River floodplain into flooded and non-flooded areas in using a binary recursive classifier after collecting suitable training areas.

A disadvantage of the extensively employed approaches to flood mapping discussed above is that a characteristic backscattering coefficient value must be selected to be able to distinguish between flooded and non-flooded regions of a SAR image. The result can therefore be subjective and random if unsupported by in-situ reference data. Because of these drawbacks, active contour models have received more widespread attention, since incomplete and noisy images can be classified using this technique (e.g. Horritt, Mason & Luckman 2001; Matgen et al. 2007). A more in-depth look at active contours can be found in section 2.7.3.

Multitemporal approaches to flood mapping have generally been found to be superior to single-date approaches (Voigt et al. 2008). The principle involves change detection by comparing conditions before and after a flooding event has occurred. Different approaches using change detection for flood mapping include amplitude based techniques (e.g. Heremans et al. 2003; Long, Fatoyinbo & Policelli 2014) and interferometric or coherence-based techniques (e.g. Nico et al. 2000; Horritt, Mason & Luckman 2001). For the amplitude-based techniques, the flooded area will experience a change in backscatter value between the reference image and the flooded image, while the regions with similar backscatter value in both areas are assumed to have no change.

In studies using interferometry, flooded areas can therefore be identified as areas with low coherence between two SAR images covering the same area. Problems arise when other regions apart from flooded areas have low coherence. Corr, Keyte & Whitehouse (1995) found that

coherence was high for fields with a 3-day-repeat cycle, whereas forested areas had lower coherence because of volume scattering. Horritt, Mason & Luckman (2001) found that coherence for vegetation was also much lower because of the 35 day interval between the acquisitions of the ERS-1 images and, thus, limited the use of coherence mapping. Refice et al. (2014) used high-resolution, X-band, stripmap COSMO/SkyMed data for flood monitoring in the Southern Basilicata region, Italy by using RGB composites and cluster analysis of the multi-temporal images and found that coherence information from SAR images could greatly benefit flood identification. Nico et al. (2000) found that information extracted from amplitude as well as coherence was the best approach. Amplitude was used to extract most of the flooded area and regions with high coherence were then eliminated, which resulted in more homogeneous flooded regions with fewer artefacts.

Several studies extract information from remotely sensed images following pixel-based image classification, where a single pixel is considered as the most basic geometric component (Voigt et al. 2008). Region-based image analysis, where the neighbouring values are taken into account has however been garnering considerable attention for remote sensing applications, including flood mapping. Matgen et al. (2011) applied region growth based on radiometric thresholding for flood estimation. Seeds are placed at the core of the initial water bodies extracted from thresholds and enlarged until the backscatter in the regions is homogeneous. Mason et al. (2010) manually identified water and non-water training sites in urban areas and mapped inundation in urban areas using a region growing method.

Object-based image analysis has garnered considerable attention for image analysis (e.g. Heremans et al. 2003; Pulvirenti et al. 2011). Object-based image analysis is based on the theory that image analysis can be performed on homogeneous objects and not necessarily single pixels (Benz et al. 2004). Homogeneous, non-overlapping objects usually correlate with real features on the surface of the earth. Images are segmented based on similar spectral or textural properties; contextual information, such as texture and geometric properties provide additional parameters for image classification and potentially improve accuracy (Benz et al. 2004).

Image segmentation is increasing in popularity in the field of remote sensing, particularly because of an increase in the spatial resolution of imagery (Voigt et al. 2008). Higher spatial resolution of data increases within-class variance and this leads to high spectral confusion within classes (Gong et al. 1992) which could be overcome with object-based image analysis (Blaschke 2010). A disadvantage of the object-based approaches to image analysis is the high processing demand of

segmentation (Voigt et al. 2008). Heremans et al. (2003) segmented both a flooded image and a non-flooded reference image using eCognition. Dark-toned objects were extracted in a classification run. In a second classification all dark objects from the first classification whose values decreased by a set threshold value were finally classified as flooded areas. Pulvirenti et al. (2011) segmented high resolution COSMO-SkyMed images and the mean multi-temporal radar signatures were extracted per region in each image. Segments were classified as flooded or non-flooded using assumed reference multi-temporal backscattering trends, thereby generating a map of the flood evolution.

2.7.2 Thresholds

Thresholding is a widely used method to distinguish between flooded and non-flooded areas in SAR images (e.g. Malnes, Guneriussen & Høgda 2002; Solbø & Solheim 2004; Henry et al. 2006). It is an effective flood detection method in non-forested, open areas (Solbø & Solheim 2004). In these areas, elements of the SAR image are generally classified as flooded when the intensity is below a certain threshold, while non-flooded and dry areas are above this threshold (Solbø & Solheim 2004; Voigt et al 2008). The simplest method to classify flooded and non-flooded areas is therefore to consider the distribution of intensity values of the SAR image (e.g. Solbø & Solheim 2004; Henry et al. 2006).

Generally, when examining the histogram of a SAR image, intensity peaks in the high value range and in the low intensity range, the latter one caused by water (Henry et al. 2006). The threshold is then placed at the local minimum between the two peaks (or modes) as can be seen in Figure 2.10. The selected threshold will depend on the contrast between the land and water. Generally it needs to be set for each individual SAR scene individually (Solbø & Solheim 2004).

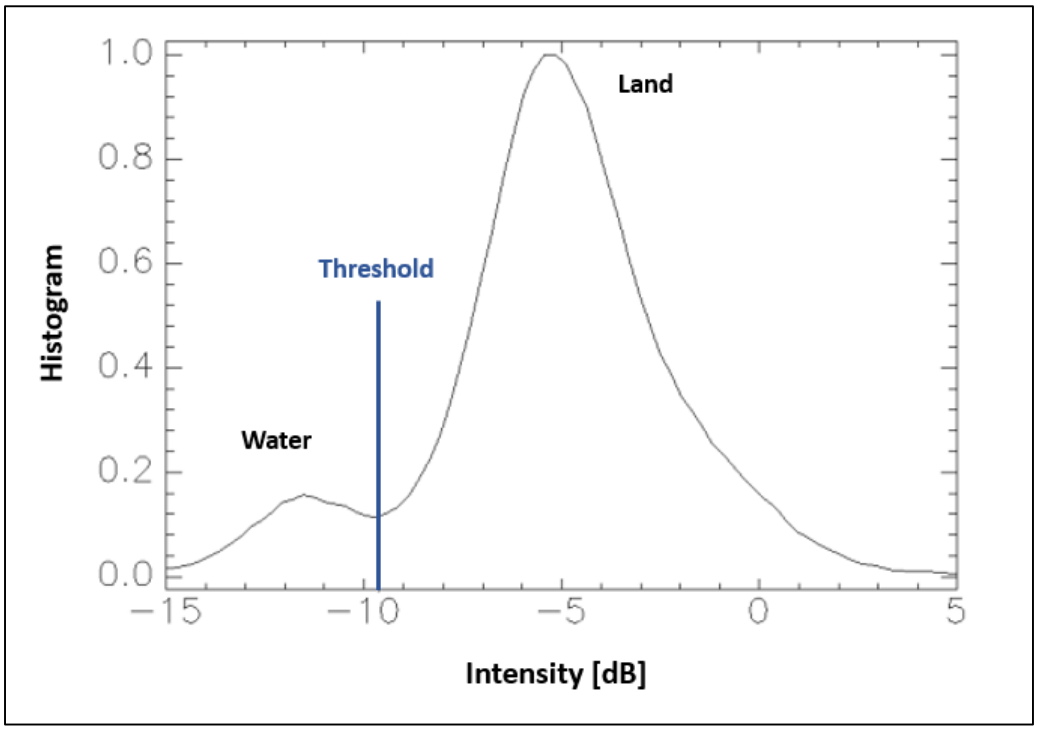

Adapted from Solbø & Solheim (2004)

Figure 2.10: Histogram showing the intensity distribution of a SAR image during flooded conditions. The low intensity range is the water, while the higher intensity range is the surrounding non-flooded land. The threshold is set at the local minimum between the two peaks.

Factors which determine the contrast between flooded and non-flooded areas for open water as discussed in more detail in section 2.6.1, are wavelength, incidence angle and polarisation of the SAR image (Bartsch et al. 2012; Solbø & Solheim 2004). Longer wavelengths are less sensitive to surface roughness. Shallower incidence angles, water and land areas are more easily separable (Solbø & Solheim 2004). Generally VV-polarisation seems to have the lower contrast between the flooded and the non-flooded classes (Solbø & Solheim 2004).

The advantage of using thresholds is that it is not computationally very demanding and therefore appropriate for rapid flood delineation. Results are generally reliable and steadfast and the majority of the extent of the flooded regions can be identified (Voigt et al. 2008). A disadvantage is that roughening of the water surface (e.g. due to wind, waves or streams) usually increases the backscatter values of the water, thereby decreasing the contrast between water and non-water surfaces. This can have an impact on the threshold selection since either a higher threshold would be selected, thereby leading to overestimation of flooded area, or a low threshold selection could cause flooded areas to be undetected (Matgen et al. 2007).

Manjusree et al. (2012) determined optimal threshold ranges for all polarisations with incidence angles ranging between 20° and 49°. This was done by drawing transect lines within different types of water surfaces, and analysing the backscatter response within the different water bodies and then determining an average backscatter range for the different water feature types. For near to far ranges the optimum thresholds for flooded water surfaces were found to be between -8 and -12 dB for HH-polarisation, -15 to -24 dB for HV- and VH-polarisations and -6 to -15 dB for VV-polarisation. The average backscatter values for the different were established and are summarised in Table 2.2 below.

Table 2.2: Average backscatter (dB) threshold values in different water features

Water feature type	**Threshold Backscatter for each polarisation**			
	HH	**HV**	**VH**	**VV**
Flood Water	-8 to -12	-15 to -24	-15 to -24	-6 to -15
River Water	-16 to -30	-24 to -36	-24 to -36	-19 to -32
Tank Water	-13 to -26	-22 to -40	-22 to -40	-16 to -28
Oxbow Lake	-16 to -24	-21 to -32	-21 to -32	-24 to -32
Partially Submerged Features	-18 to -30	-24 to -34	-24 to -34	-8 to -18

Source: Manjusree et al. (2012: 118)

The average backscatter for all other water feature types was found to be lower than that of flooded water bodies. This could be due to the fact that the other water surfaces are generally calmer than expansive flooded water areas (Manjusree et al. 2012).

Long, Fatoyinbo & Policelli (2014) estimated flood extent using a multi-temporal approach in combination with thresholds. The flood extent in the Zambezi Region, Namibia was determined using a non-flooded reference image and an image captured during the flood event. The difference between the absolute values of the two images was calculated. The flooded areas in the difference image were then identified according to dark or very bright values based on the determined thresholds and the large flooded areas were then grouped.

2.7.3 Active contour model

The purpose of an ACM is to perform image segmentation and subdividing the image into its basic features. As can be seen in Figure 2.11 below, this is achieved by drawing an initial contour i.e. an initial boundary which is in close approximation to the object of interest. This contour is deformable and is then steered towards the actual contours of the objects (Kass et al. 1988; Chan & Vese 2001). This is done through the use of energy minimisation functions based on image properties which steer the contour towards features of interest. The final contour is then wrapped

around the object of interest and the image is then segmented into its foreground objects and the surrounding background. In the context of flood mapping using satellite imagery, this would involve setting up an initial contour close to the boundaries of the water. The contour then moves towards the flooded regions. The image is then segmented into its foreground objects, the flooded regions of interest, and the background, which would be the non-flooded regions.

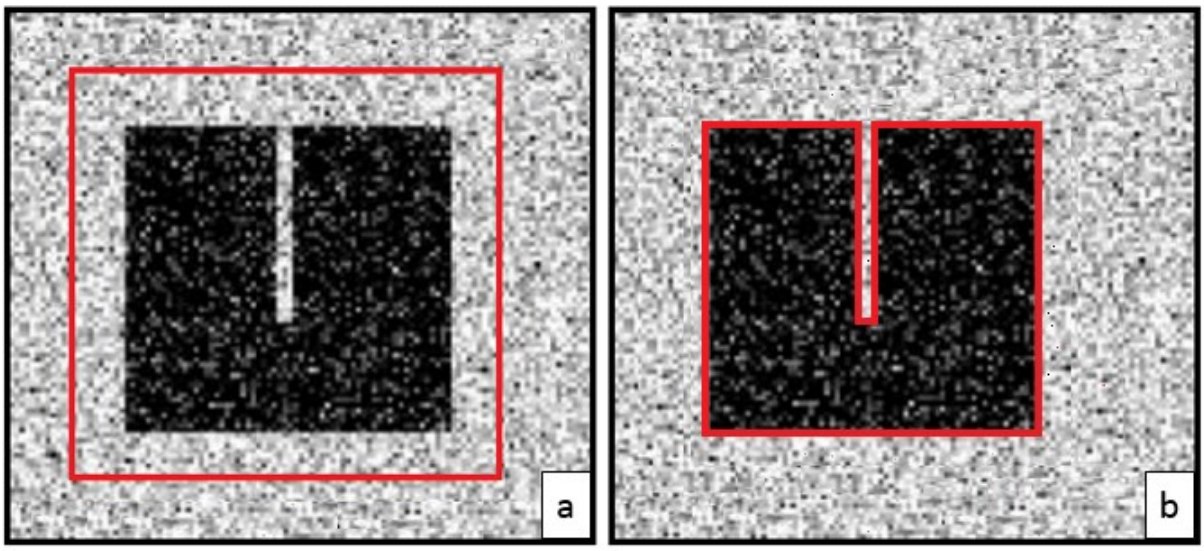

Adapted from Zhang et al. (2010)

Figure 2.11: In (a), the initial contour can be seen, while in (b), the contour settled along the edges of the desired object.

ACMs can either be categorised according to their initial contour or according to their energy functions. Based on curve representation, ACMs in literature can be either be classified as parametric (e.g. Kass et al. 1988) or geometric active contours (e.g. Caselles et al. 1993). Parametric active contours represent contours explicitly in parametric form as splines, which is a polynomial or set of polynomials used to estimate a surface or a curve. A main drawback is that transformations in the topology (the division or joining) of the changing contour cannot be handled and contours can therefore not automatically divide or merge. This complicates the segmentation of multiple objects (Xu, Yezzi & Prince 2000).

For flood extent delineation this would mean that if an initial boundary is drawn around two distinct flooded regions, the contour will not be able to divide and segment both flooded regions as separate objects. Similarly, if multiple contours are used as input and move towards a single flooded object, the final contours will not effectively merge when they move towards the flooded area of interest. Additionally, a random parameterisation of the curves is employed and therefore not effectively using the geometric information of the objects for segmentation (Xu, Yezzi & Prince 2000).

Geometric active contours address the most important limitations of parametric active contours and make use of curve evolution as well as level set methods. Level sets are sets of points at a given cross section of a curve when the curve is taken and built into a surface (Sethian 2006). This is illustrated in Figure 2.12:

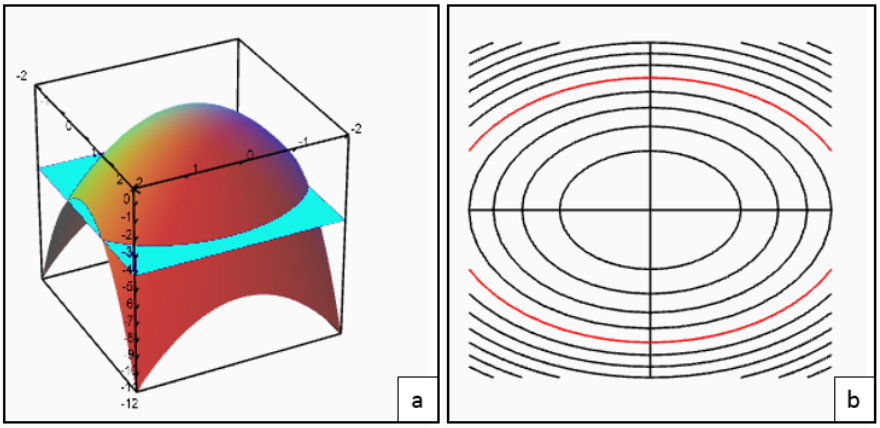

Adapted from Nykamp (2015)

Figure 2.12: An illustration of level sets. Original curve seen in (a), while in (b) the curve is represented as contours. The blue plane in (a) is the red level set in (b).

To some extent, the curve evolves as a gradient descent towards and increasingly better final boundary, as can be seen Figure 2.13. Using this approach, curves and surfaces can change shape using geometric processes, and evolution is independent from parametrisation. Therefore, one or multiple contours are implicitly formulated as level sets of a 2-dimensional scalar function. Parameterisations are calculated after the deformation has commenced, which allows for automated reparameterisation and topological change control (Xu, Yezzi & Prince 2000).

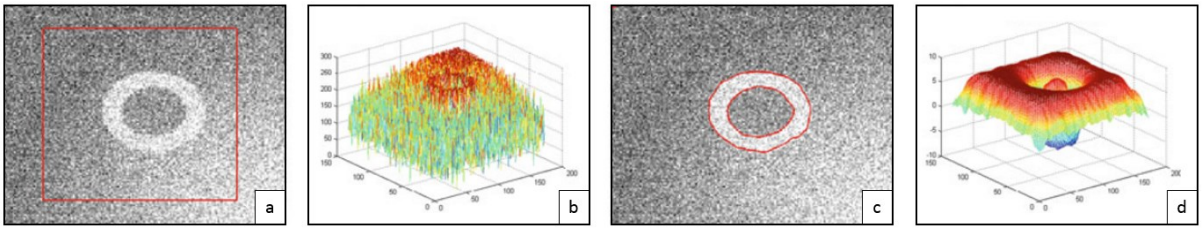

Adapted from Tian et al. (2013)

Figure 2.13: The initial contour is seen in (a) and in figure (b) it is displayed in three dimensions. Figure (c) is shows the final contour and (d) shows the final level set function.

Based on energy, ACMs can be categorised as either edge based or region based models (e.g. Chan & Vese 2001). Edge based models make use of image gradients to detect the object boundaries (Li

et al. 2007). This approach is sensitive to noise and also very reliant on the where the initial contour is placed (Chan & Vese 2001; Vikram & Yezzi 2012). Edge based segmentation, however, is more precise along the edges of object boundaries (Appia & Yezzi 2011). If this method is therefore employed for the identification of flooded areas, the boundaries between flooded and non-flooded regions have to be very distinct and very little noise can be present in a SAR image for results to be viable.

Region based models use the statistical information of the objects and the background regions find an energy optimum where the model fits the image best for identification of objects. Region based models do not use the image gradient, and are therefore better equipped to segment images with very weak object boundaries (Liu, Wang & Zhu 2015). Region based models are also less sensitive to the position of the initial boundary (Appia & Yezzi 2011). Therefore flooded objects can still be identified using satellite imagery, even if images are subject to noise and boundaries between flooded and the surrounding non-flooded regions are not necessarily that distinct.

The Chan-Vese algorithm (used in this study), is a geometric, region based ACM (2001). The segmentation boundary is implicitly denoted using a level set function, which handles topological changes during the segmentation process more easily than parametric methods. Since this is a region based model, information within the region and not only at the boundaries of objects is considered. The initial image, even if noisy, also does not have to be smoothed and boundaries are therefore preserved. Objects which do not necessarily have boundaries distinctly defined by the image gradient or objects which do not necessarily have smooth boundaries can also be detected. Since it is also a geometric model, many objects can be identified using only one initial curve. The location of the initial curve can be anywhere in the image, and it does not have to surround the objects to be detected (Chan & Vese 2001). This would therefore be an appropriate active contour for flood extent mapping for this study.

When using active contours, an initial contour is required as input. This can be done manually, but requires much user input which can be a tedious process, especially for areas which have many individual flooded areas. Approaches to approximate the flooded areas using more automatic procedures and then transferring these areas as initial polygons therefore seem to be more promising approach in order to circumvent the manual setup of the polygon (Voigt et al. 2008).

This study, however, attempted to use the Canny edge detector to estimate the edges. This particular edge detector was selected since not only are edges detected, but the algorithm also

computes the strength of these edges. Weak edges caused by noise can therefore be discarded (Canny 1986). The Canny edge detector is an edge detection algorithm where the edges of a greyscale input image are identified by detecting the location of intensity discontinuities in the output image (Fisher et al. 2003). The identified edges should be as close to the real edges as possible and an actual edge should also not have more than one detected edge (Moeslund 2009). An example of a segmented image can be seen in Figure 2.14 below:

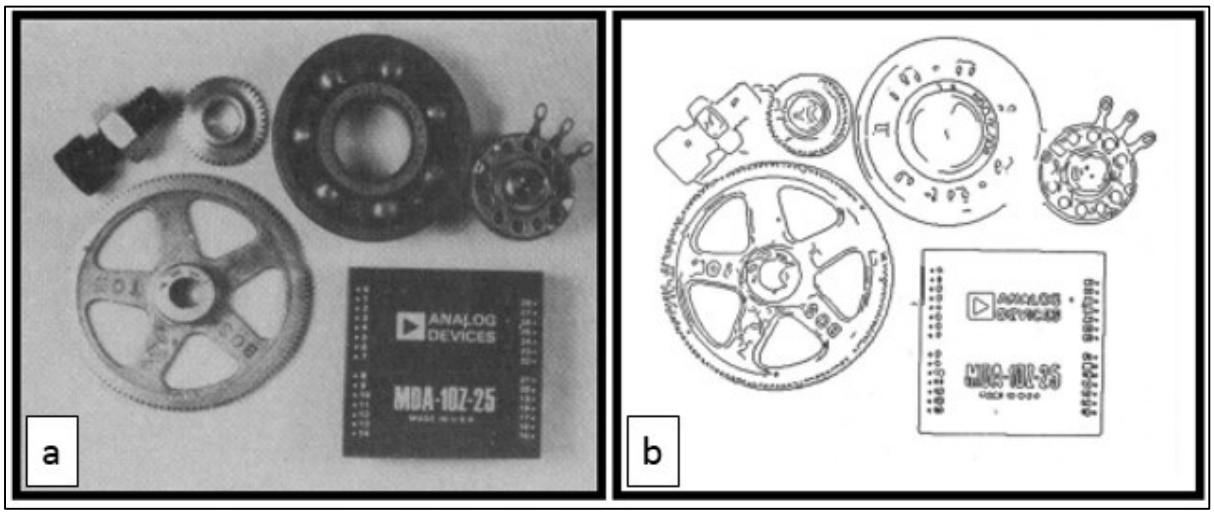

Adapted from Canny (1986)

Figure 2.14: Original image shown in (a), while the edge map as identified by the Canny algorithm is seen in (b).

The edge detection algorithm is a five-stage process. The image is first smoothed using a Gaussian filter (Canny 1986). Then, areas where the greyscale intensity changes the most are identified by calculating image gradients (Moeslund 2009). The next step, non-maximum suppression, converts the blurry, thick edges of the gradient magnitude image to potential sharp edges (Canny 1986; Moeslund 2009). A high and a low threshold is then specified. Finally edge tracking by hysteresis generates the final contour using the two thresholds. Strong edges remain as edges. Weak edges and intermediate edges not attached to strong edges are discarded. (Mordvintsev & Rahman 2014).

Several studies have applied active contours for the identification of flooded areas in SAR imagery. A geometric, statistical ACM developed by Horitt (1999) was applied for flood mapping by Horitt, Mason & Luckmann (2001), Horitt et al. (2003) and Hahmann & Wessel (2010) for flood extent delineation. Horitt, Mason & Luckmann (2001) classified two SAR images of the Thames River to assess the performance of this algorithm and compared it to flood extent delineation obtained from aerial photography. Problem areas were flooded hedgerows which gave high returns and non-flooded vegetation regions which gave similar signal returns to water. Despite the encountered difficulties, 75% of the shoreline area was correctly classified. 70% of the shoreline coincided with

the ground data to within 20m. This study recommended that these areas can be identified using a multi-temporal approach and comparing pre- and post-flood conditions on imagery.

Horritt et al. (2003) used this algorithm in a salt marsh environment and mapped open water as well as non-flooded vegetation, leaving the emergent vegetation. This was done to start the contour in known water regions and dry land regions and no previous knowledge of flooded vegetation is required. Results were then validated using a waterline obtained from LiDAR topography and tidal elevation. It was found that including flooded vegetation in waterline location reduces error in flood mapping by a factor of about 2, which translates to a decline in location error of the waterline from 120 m to 70 m.

Hahmann & Wessel (2010) used a parametric active contour and a geometric active contour model to delineate flood boundaries and results were then visually compared to differential global positioning system (DGPS) reference data and good agreement for both methods were observed. The parametric active contour model, however had some inaccuracies, which was probably due to difficulties with parameter adjustment. The parametric active contour model worked well with smooth and rough water bodies, but topology changes were not possible with this method. Geometric active contours had good results for smooth water bodies, but rougher water bodies were, however, not as successfully extracted with this method.

CHAPTER 3 RESEARCH METHODS

Chapter 3 provides an outline of methods used in this research. A brief description of data selection is given followed by a description of the pre-processing methods performed to prepare data for analysis. The areas of interest for classification are then highlighted, followed by a description of the classification methods, where the flooded areas are classified using the SAR imagery. Finally, the obtained results are statistically and visually compared to Landsat data. The statistical comparison will be in the form of accuracy assessment statistics.

3.1 DATA COLLECTION

The 2009 flood in the Zambezi Region was selected for flood delineation using SAR in this study, since this was a particularly wet year and floods reached record levels as described in section 1.5 and multiple SAR images covering this flooding period were available for analysis. The footprints, metadata and preview of different SAR scenes were examined using ESA's Earth Observation Link (EOLi-SA) software to select appropriate images covering the flood period.

Multiple SAR images from two different sensors were acquired: wide swath mode (WSM) images from the Advanced Synthetic Aperture Radar (ASAR) sensor, carried by the Environmental satellite (ENVISAT), and fully polarimetric (PLR) images from the Phased Array L-band Synthetic Aperture Radar (PALSAR) sensor, carried by the Advanced Land Observing Satellite (ALOS). The collection of multiple images from two different sensors allows for the determination of the impact of different system parameters (wavelength, polarisation and incidence angle) on classification results.

Ten HH-polarised, C-band ENVISAT ASAR WSM images were downloaded from ESA's Earth Observation portal (ESA 2013). Incidence angles of the subsets covering the study ranged between 5° and 66°. Three ALOS PALSAR PLR image sets, each consisting of four images (HH-, HV-, VH- and VV-polarised) with incidence angles ranging between 12° and 37° were acquired by sending a research proposal to ESA. Details of the two SAR systems and the image acquisition modes of relevance in this study are specified in Table 3.1 below.

Table 3.1: SAR image and sensor specifications of relevance in this study

Sensor	Acquisition mode	Band	Polarisation	Spatial resolution	Incidence angle	Swath
ENVISAT ASAR (2002-2012)	WSM	C 5.6 cm	HH	75 m	5° - 66°	400 km
ALOS PALSAR (2006 - 2011)	PLR	L (1270 MHz) 23.6 cm	HH+HV+VH+VV	30 m	12° -37°	30 km

ASAR image acquisition dates were between 17 March 2009 and 30 May 2009, while the PALSAR images were captured on 19 March 2009 and 5 April 2009. These dates cover the main period of the flood, which increased sharply around 20 March 2009, peaking around 26 March 2009, after which waters slowly receded (De Groeve & Riva 2009) as discussed in section 1.5. Acquisition dates of the SAR images can be found in Table 3.2.

Table 3.2: Acquisition dates of SAR imagery and corresponding Landsat reference imagery

SAR images			Landsat image		Interval between acquisition dates of SAR and Landsat image
SAR sensor	Acquisition date	Incidence angle	Landsat sensor	Acquisition date	
Envisat ASAR (WSM)	2009-03-17	16° - 38°	Landsat TM	2009-03-19	2
Envisat ASAR (WSM)	2009-03-20	11° - 48°	Landsat TM	2009-03-19	1
Envisat ASAR (WSM)	2009-03-23	35° - 57°	Landsat ETM+	2009-03-27	4
Envisat ASAR (WSM)	2009-03-24	5° - 53°	Landsat ETM+	2009-03-27	3
Envisat ASAR (WSM)	2009-04-25	14° - 62°	Landsat ETM+	2009-04-28	3
Envisat ASAR (WSM)	2009-05-10	6° - 43°	Landsat TM	2009-05-06	4
Envisat ASAR (WSM)	2009-05-11	18° - 66°	Landsat TM	2009-05-06	5
Envisat ASAR (WSM)	2009-05-14	9° - 57°	Landsat TM	2009-05-06	8
Envisat ASAR (WSM)	2009-05-29	11° - 48°	Landsat TM	2009-05-22	7
Envisat ASAR (WSM)	2009-05-30	13° - 62°	Landsat TM	2009-05-22	8
PALSAR (PLR)	2009-03-19 (1)	14° - 37°	Landsat TM	2009-03-19	0
PALSAR (PLR)	2009-03-19 (2)	20° -30°	Landsat TM	2009-03-19	0
PALSAR (PLR)	2009-04-05	12° - 31°	Landsat ETM+	2009-04-12	7

The footprint of the ASAR subsets and the PALSAR images used for this study can be seen in Figure 3.1. The extent of all ASAR image subsets is outlined in red. Two of the three PALSAR sets were captured on 19 March 2009, but they have different extents. Throughout the remainder of this study, the PALSAR set with the extent outlined in yellow will be referred to as the first set of PALSAR images captured on 19 March 2009 and listed in tables and figures as 2009-03-19 (1), while the PALSAR with the extent outlined in purple will be referred to as the second set of

PALSAR images captured on 19 March 2009 and listed in tables and figures as 2009-03-19 (2). The PALSAR image set captured on 5 April 2009 is outlined in blue.

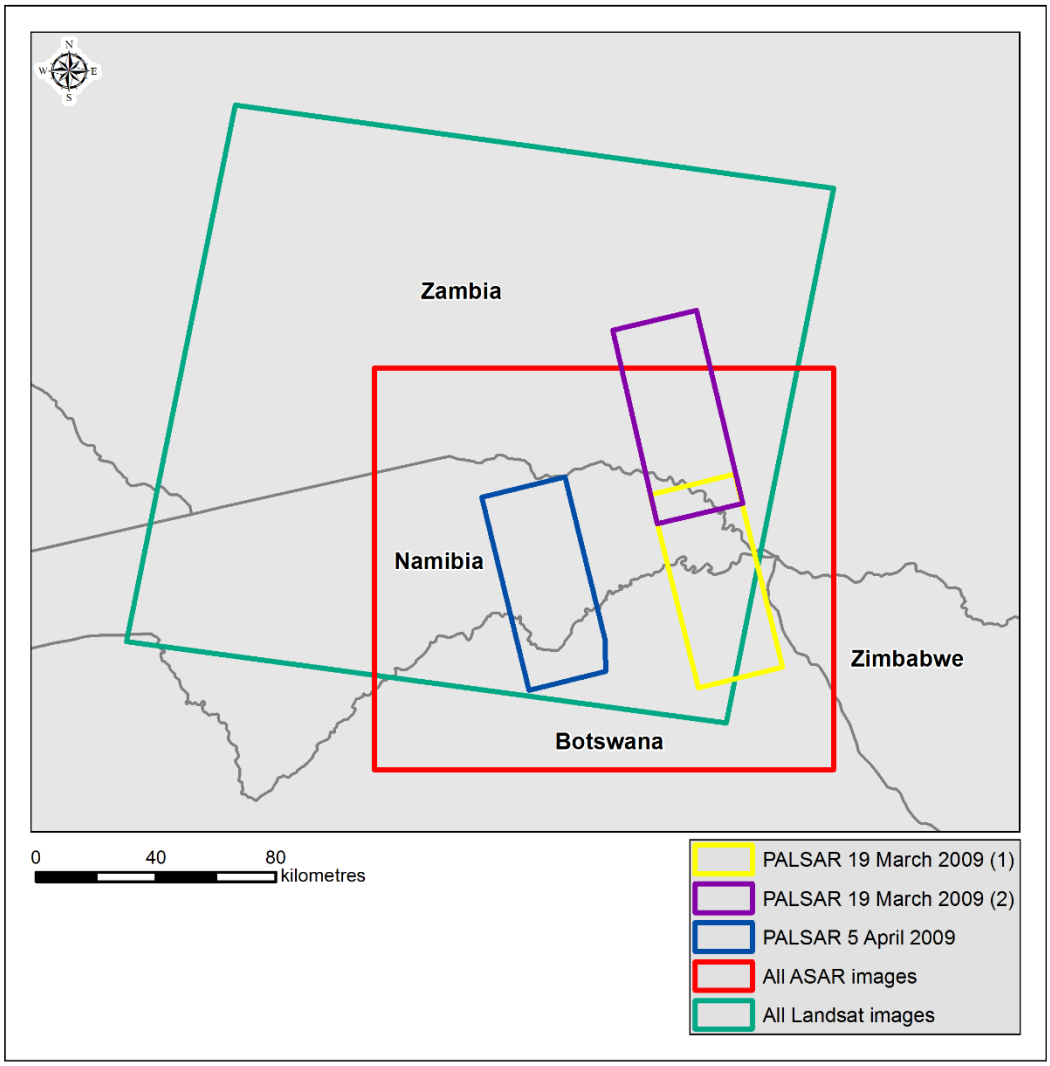

Figure 3.1: Extents of the SAR and Landsat images

Since no reference ground data were available to determine the accuracy of the classified SAR images, it was decided that six Landsat 5 (TM) and Landsat 7 (ETM+) images would be used as substitute reference data. Six Landsat images with acquisition dates ranging from 19 March 2009 to 22 May 2009 were acquired from the USGS Earth Explorer to validate results from the classified SAR images through visual and statistical comparisons described in section 3.4. The extent of the Landsat images is shown in green in Figure 3.1 and details of Landsat imagery can be found in Appendix A.

3.2 PRE-PROCESSING

Satellite imagery contains radiometric and geometric distortions which need to be accounted for and corrected. For image and quantitative analyses to commence, these errors need to be fixed. Therefore, image pre-processing needs to be performed on the acquired satellite imagery before principal image analysis can commence. This section describes the pre-processing steps which the data underwent prior to commencing with main image analysis.

3.2.1 Landsat imagery

Landsat is subject to atmospheric attenuation (described in Appendix A). Radiometric corrections are performed on the Landsat images in order to correct radiometric distortions by the sensor, to compensate for atmospheric attenuation and to convert the images to surface reflectance. Atmospheric corrections were performed on the Landsat 5 and Landsat 7 images using the ATCOR 2 module in PCI Geomatica 2013. ATCOR 2 was selected since this module does not require detailed terrain data and the Zambezi Region is an extremely flat area. Topographic effects are therefore expected to have minimal impact on the study area.

3.2.2 SAR imagery

3.2.2.1 Terrain correction and geocoding

SAR images for this study were geometrically corrected using the Range Doppler Terrain Correction operator in the Next ESA SAR Toolbox. This operator uses the Range Doppler orthorectification method to geocode SAR images by using the available orbit state vector information in the metadata, the radar timing annotations, the slant to ground range conversion parameters and a digital elevation model (DEM) to produce a geocoded image (NEST 2013).

3.2.2.2 Calibration

Raw SAR images are usually not radiometrically corrected and significant radiometric bias is present in the images. The digital numbers (DNs) of SAR images were therefore converted to the backscatter value through the process of calibration. SAR images were calibrated in NEST using the calibration operator, and the DN values of the pixels were converted to normalised radar cross section (σ^0) values (NEST 2013).

3.2.2.3 Speckle filtering

Since SAR images are instrinsically subject to speckle, the frost filtering algorithm as described in 2.5.3.3 was applied to the SAR images in NEST. This algorithm was selected since it is well suited for flood extent mapping, for speckle is reduced and image contrast is increased, but the edges and texture of the original image is preserved (Zhou et al. 2000).

3.3 CLASSIFICATION OF THE OPEN WATER BODIES

In this section, the process of image analysis is described. The areas of interest for classification are first established. The classification of the corrected SAR images into flooded and non-flooded regions using thresholds will then be described. Flooded regions considered for classification are open water areas. This will be followed by a description of the classification of the corrected SAR image into flooded and non-flooded regions using ACMs.

3.3.1 Areas of interest for classification

This study focused on the classification of open waterbodies within SAR images. For these waterbodies, backscatter return is low, such as those shown by the red arrows in Figure 3.2.

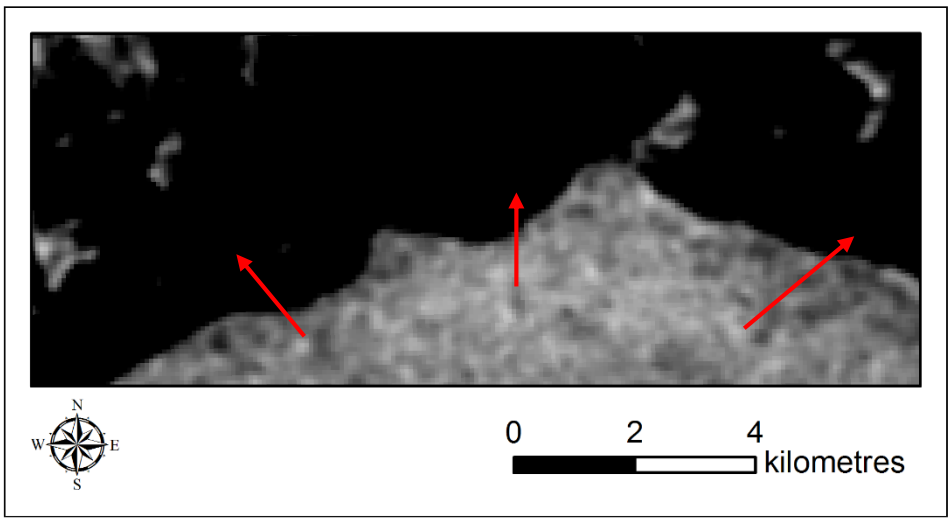

Figure 3.2: ASAR image of Open waterbodies of interest for classification (shown by the red arrows). Backscatter is very low.

Areas where flooded vegetation caused higher backscatter return, due to double bounce from flooded surface and trunk interaction, were not considered for classification for this research study. The reason for this is that different regions with high backscatter returns on the SAR images related to different spectral signatures on the corresponding Landsat images. This is illustrated in Figure 3.3 and Figure 3.5 respectively, while signatures are those extracted from the points shown in Figure 3.4 and Figure 3.6 respectively.

In the region at Lake Liambezi (Figure 3.3) for example, classes are easily discernible. On the ASAR image of 25 April 2009 (Figure 3.3a), the areas with high backscatter correspond to a mixed signal between vegetation and water on the Landsat image of 20 April 2009 (Figure 3.3b) as shown by the spectral signatures of the points (Figure 3.4). The dark open water regions corresponded to open water spectral signatures while the non-flooded vegetation corresponds to vegetation signature on the Landsat image.

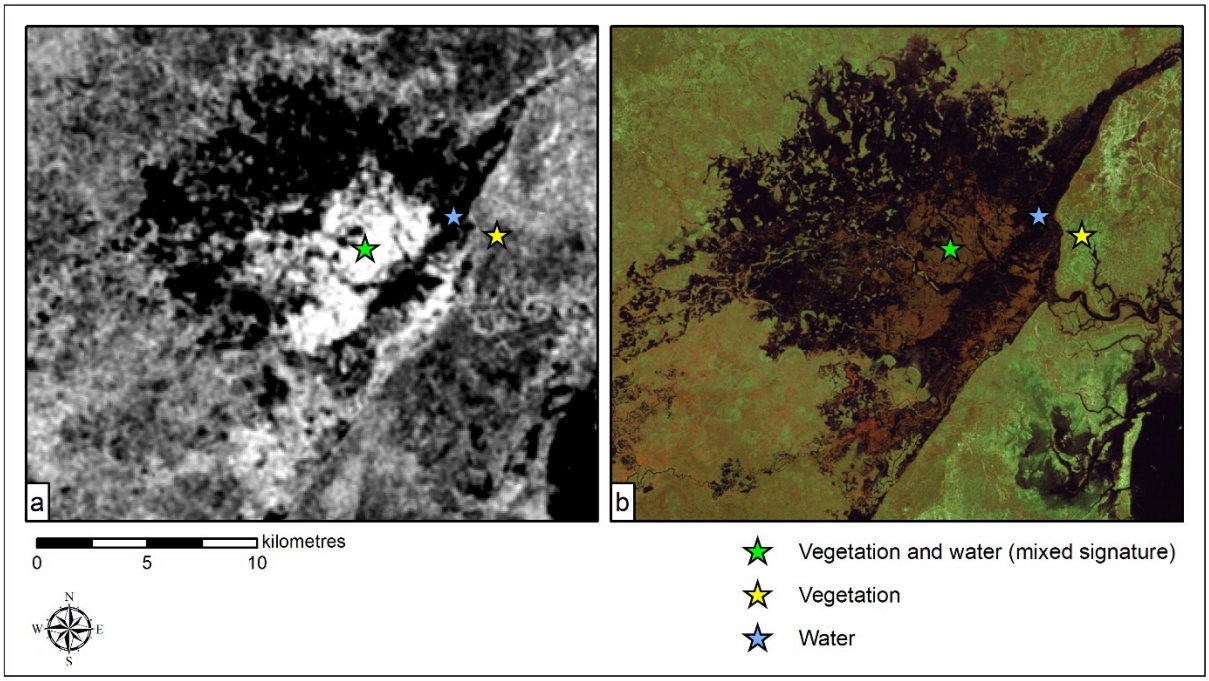

Figure 3.3: Lake Liambezi. ASAR image of 25 April 2009 is shown in (a), while (b) shows the Landsat image of 20 April 2009. Points show different land cover classes.

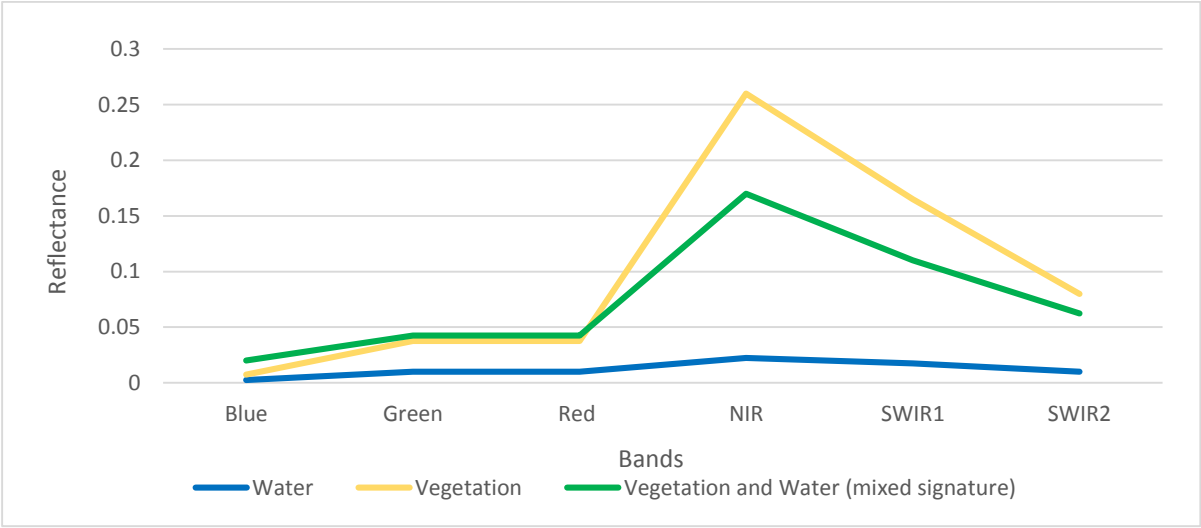

Figure 3.4: Spectral signatures extracted from points shown in Figure 3.3.

For other regions, however, such as the subset of the Zambezi River, where the dominant vegetation is grassland, uncertainty arose. The areas with bright backscatter return on the same ASAR image (Figure 3.5a), corresponded to areas in the Landsat image (Figure 3.5a) that had pure vegetation signatures (Figure 3.6) more vibrant than the woody vegetation signatures in Figure 3.4. This could either indicate that the area is not flooded, or that the area beneath canopy is flooded but does not appear on the image due to the vegetation cover. The non-flooded area on the ASAR images corresponded to bare soil or a mixture between bare soil and vegetation on the Landsat images.

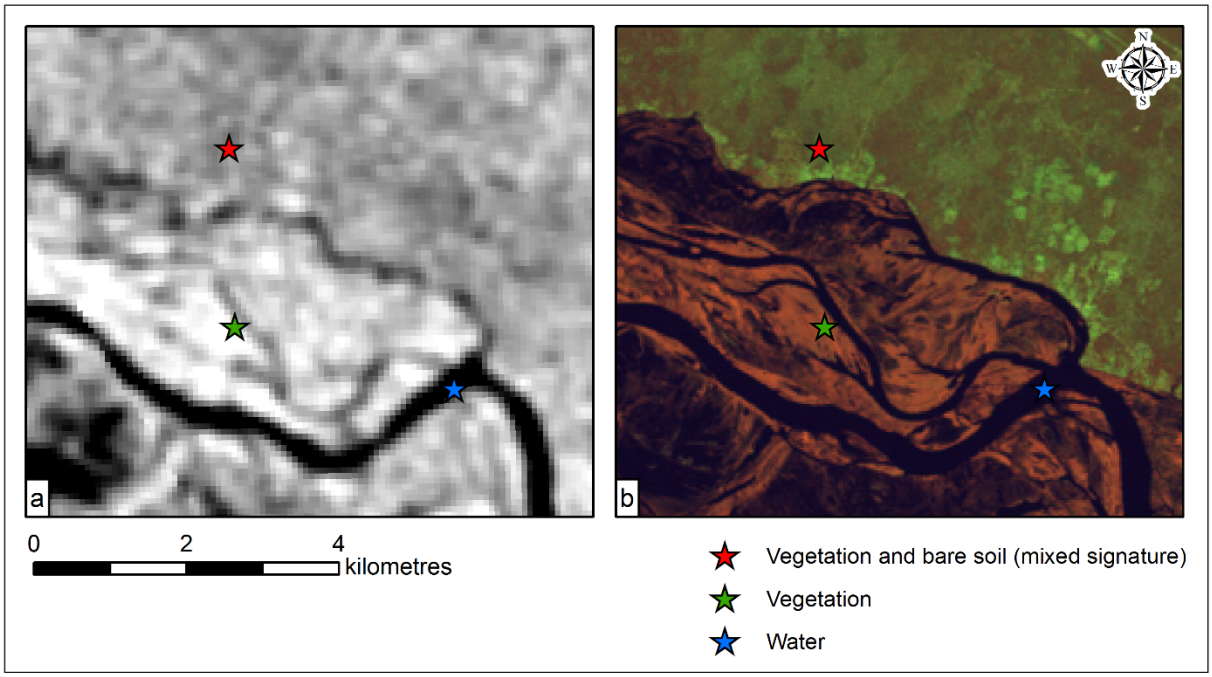

Figure 3.5: Region at the Zambezi River. ASAR image of 25 April 2009 is shown in (a), while (b) shows the Landsat image of 20 April 2009. Points show different land cover classes

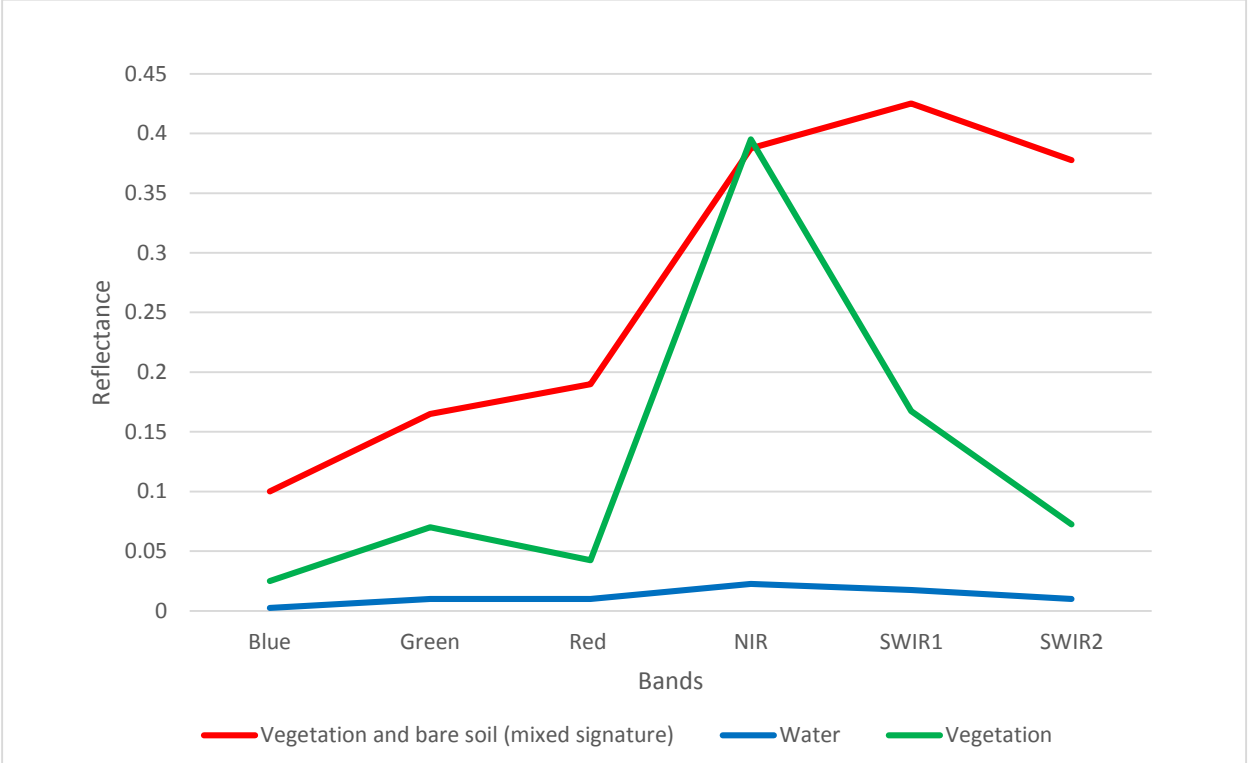

Figure 3.6: Spectral signatures extracted from points shown in Figure 3.5

These flooded vegetation areas which had high backscatter return were therefore disregarded due to the uncertainty regarding their flooded or non-flooded status when using Landsat as reference. Therefore, the classification focuses on identifying open water flooded regions. Classification

accuracies should, however, not be severely affected since the area covered is relatively small and extracted points for accuracy assessment were mostly located in open water areas.

3.3.2 Thresholds

For this section, the properties of the histograms of the SAR images and thresholding were used to distinguish between flooded and non-flooded areas. The histogram of the SAR image represents the distribution of the backscatter intensity (measured in dB). When the histograms of the SAR images were analysed, two discernible peaks were observed for all the SAR image histograms as seen in Figure 3.7. A high backscatter intensity peak and lower secondary backscatter intensity peak. The assumption is made that the high backscatter intensity peak represents non-flooded regions, while the lower secondary backscatter intensity peak represents water or flooded regions and the backscatter threshold value that separates these two classes is located at the local minimum between these two peaks (e.g. Solbø & Solheim 2004).

For this study, however, when employing the use of thresholds for the identification of flooded water bodies, a range of backscatter intensities were extracted to determine at which point the optimal threshold for each image is located based on comparison with Landsat images and to determine how the overall accuracy changes with a change in the threshold value. The steps involved for image classification were threefold: extracting the histogram; determining the upper and lower thresholds as well as the slices in between; classifying the SAR image into flooded and non-flooded regions at each threshold, thereby creating multiple binary images from each SAR image.

Firstly, the histogram of the distribution of backscatter intensities for each image was extracted in Matlab. Histograms were constructed using bin sizes of 0.1 dB. The next step was to determine the range of threshold slices. For this study, the selected lower threshold was situated at the local minimum between the two intensity peaks, while the selected upper threshold was an estimate of the inflection point between the local minimum and the higher backscatter intensity peak. Thresholds were then varied between these two values in increments of 0.5 dB. The extracted histograms for each SAR image as well as the location and number of thresholds per image can be found in Appendix B. An example for the ASAR WSM image acquired on 20 March 2009 can be seen in Figure 3.7 below, where the threshold values ranged between -13.5 and -9 dB.

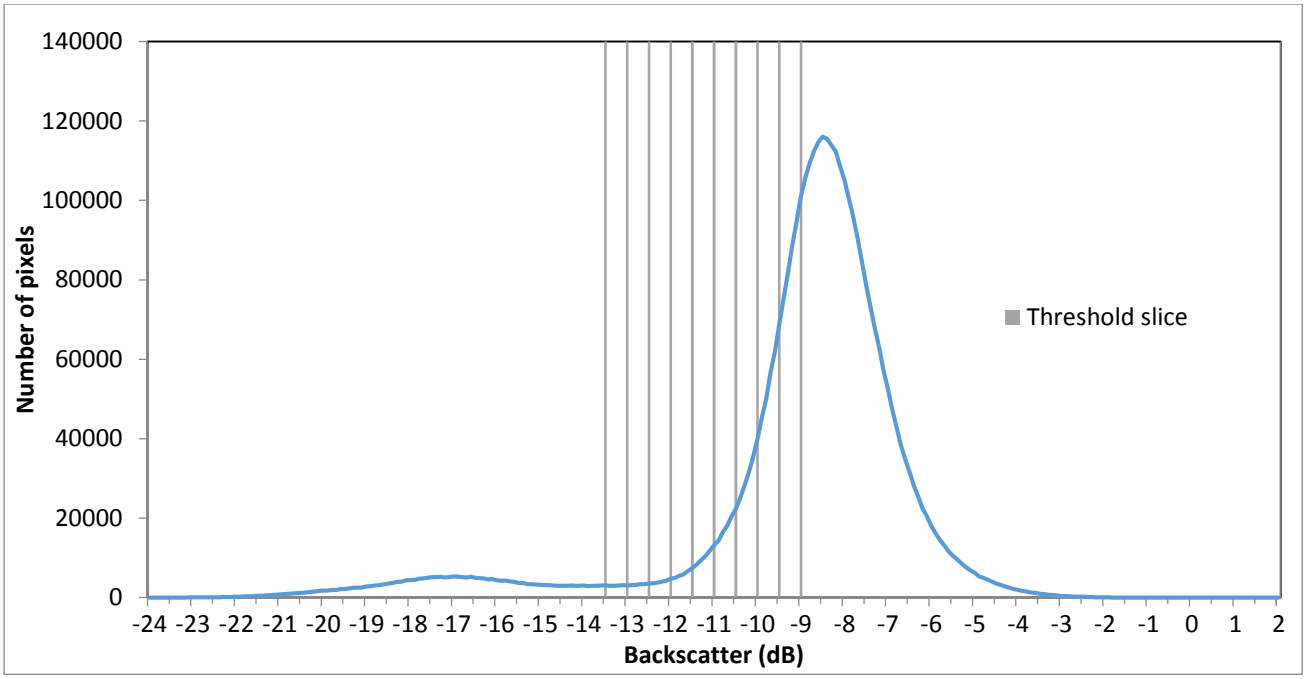

Figure 3.7: Threshold slices for the ASAR image captured on 20 March 2009.

The number of increments varied for each SAR image based on the histogram properties. All threshold values for each of the ASAR images are summarised in Table 3.3 while all threshold values for each of the PALSAR images are summarised in Table 3.4.

Table 3.3: All thresholds summarised for each ASAR image (dB)

2009-03-17	**2009-03-20**	**2009-03-23**	**2009-03-24**	**2009-04-25**	**2009-05-10**	**2009-05-11**	**2009-05-14**	**2009-05-29**	**2009-05-30**
-11	-13.5	-18	-13	-16	-13.5	-17	-15	-14.5	-16.5
-10.5	-13	-17.5	-12.5	-15.5	-13	-16.5	-14.5	-14	-16
-10	-12.5	-17	-12	-15	-12.5	-16	-14	-13.5	-15.5
-9.5	-12	-16.5	-11.5	-14.5	-12	-15.5	-13.5	-13	-15
-9	-11.5	-16	-11	-14	-11.5	-15	-13	-12.5	-14.5
-8.5	-11	-15.5	-10.5	-13.5	-11	-14.5	-12.5	-12	-14
	-10.5	-15	-10	-13	-10.5	-14	-12	-11.5	-13.5
	-10	-14.5		-12.5		-13.5	-11.5		-13
	-9.5	-14		-12		-13			-12.5
	-9	-13.5		-11.5		-12.5			
		-13				-12			
		-12.5							
		-12							
		-11.5							

Table 3.4: All thresholds summarised for each PALSAR image (dB)

2009-03-19 (1) (HH)	2009-03-19 (1) (HV)	2009-03-19 (1) (VH)	2009-03-19 (1) (VV)	2009-03-19 (2) (HH)	2009-03-19 (2) (HV)	2009-03-19 (2) (VH)	2009-03-19 (2) (VV)	2009-04-05 (HH)	2009-04-05 (HV)	2009-04-05 (VH)	2009-04-05 (VV)
-21	-28.5	-28	-22.5	-22.5	-28	-27.5	-24.5	-22	-27.5	-27.5	-22.5
-20.5	-28	-27.5	-22	-22	-27.5	-27	-24	-21.5	-27	-27	-22
-20	-27.5	-27	-21.5	-21.5	-27	-26.5	-23.5	-21	-26.5	-26.5	-21.5
-19.5	-27	-26.5	-21	-21	-26.5	-26	-23	-20.5	-26	-26	-21
-19	-26.5	-26	-20.5	-20.5	-26	-25.5	-22.5	-20	-25.5	-25.5	-20.5
-18.5	-26		-20	-20	-25.5	-25	-22	-19.5	-25	-25	-20
-18			-19.5	-19.5	-25	-24.5	-21.5	-19	-24.5	-24.5	-19.5
-17.5			-19	-19	-24.5	-24	-21	-18.5	-24	-24	-19
-17			-18.5	-18.5	-24	-23.5	-20.5	-18	-23.5		-18.5
			-18	-18	-23.5		-20	-17.5			-18
			-17.5	-17.5	-23		-19.5	-17			
				-17			-19	-16.5			
				-16.5			-18.5	-16			
				-16			-18				
				-15.5			-17.5				
				-15			-17				
				-14.5			-16.5				
							-16				

The local minimum was approximated in Matlab using the extrema function. Extrema values are the largest and smallest values of functions, either within a subset of a range or a global range. The histogram was plotted in excel and the calculated extrema were plotted on the histogram to determine the location of the desired local minimum.

To estimate the upper threshold, the histograms had to be smoothed to remove any sharp local edges in the noisy histogram. The SAR histograms were smoothed in R using the locally weighted scatter plot smooth (LOESS) method which creates a smooth line from the original data through the use of locally weighted regression. The neighbouring data points, referred to as span or bandwidth, determine the new smoothed value (Cleveland 1979). The span was set to 0.1. The smoothed histogram was then plotted in Excel where the inflection points were then determined by determining the locations where the second derivative is (or approximates) zero.

3.3.3 Active contour models

Using ACMs for flood extent delineation in this study involved two steps: setting up an initial deformable contour, which moves toward object boundaries, and then segmenting the image into flooded and non-flooded regions. One drawback when using ACMs is the manual setup of the initial contour for water areas, thereby requiring a fair amount of user input for flood extraction

(Voigt et al. 2008). To overcome this setback, an initial contour for each calibrated, geocoded SAR image was determined using the Canny edge detector in Matlab, which requires the SAR image, the upper and lower thresholds during the hysteresis process and optionally, the standard deviation of the Gaussian filter (Matlab 2013a). See section 2.7.3 for a description of the Canny edge detection process. The upper and lower thresholds were specified using a scalar value, where the scalar values represent the higher threshold and the lower threshold value is 0.4 times the high threshold (Matlab 2013a). Through trial and error, the Canny scalar value for ASAR images which yielded the most favourable edge based on visual assessment was between 0.2 and 0.4 (see Table 3.5 for the scalar value for each ASAR image) and for all PALSAR images 0.3. The standard deviation of the Gaussian filter was left at its default value, the square root of two. In the output image, values of 1 represent edge pixels and values of 0 represent other areas (Matlab 2013a).

Table 3.5: Scalar value to determine the upper and lower thresholds for the Canny edge for the ACM segmentation process for each ASAR image. Number of iterations the ACM ran for was 1000 for all ASAR images.

ASAR image acquisition date	**Canny scalar value for thresholds**
17-03-09	0.2
20-03-09	0.3
23-03-09	0.3
24-03-09	0.4
25-04-09	0.3
10-05-09	0.3
11-05-09	0.3
14-05-09	0.3
29-05-09	0.3
30-05-09	0.3

The next step involved segmenting each individual SAR image into its flooded and non-flooded areas in Matlab using the Chan-Vese ACM. Three parameters were required as input: the input image, the mask image and the maximum number of iterations. The input image is the image to be segmented, which were the individual SAR images in this study (Matlab 2013b). The mask image defines the initial contour, which is the output Canny images for each SAR image generated in the previous step (Matlab 2013b). The maximum number of iterations is a scalar number which specifies the maximum number of times the initial contour can evolve (Matlab 2013b).

The number of times a model is set to run varies extensively in literature, ranging from a few iterations to a few 1000 iterations (e.g. Chan & Vese 2001; Lie, Lysaker, & Tai 2006) The model was therefore set to run for a maximum of 1000 iterations for all ASAR images, which yielded strong results. The PALSAR images were however more sensitive to the number of iterations and

the number of increments which yielded acceptable classification results selected through trial and error. The number of iterations for each PALSAR image is summarised in Table 3.6 below.

Table 3.6: The number of iterations for the ACM segmentation process for each PALSAR image. Canny scalar value was 0.3 for all PALSAR images

SAR Date	**Number of iterations**
19-03-2009 (1) (HH)	200
19-03-2009 (1) (HV)	300
19-03-2009 (1) (VH)	1000
19-03-2009 (1) (VV)	500
19-03-2009 (2) (HH)	200
19-03-2009 (2) (HV)	200
19-03-2009 (2) (VH)	200
19-03-2009 (2) (VV)	200
05-04-2009 (HH)	100
05-04-2009 (HV)	700
05-04-2009 (VH)	200
05-04-2009 (VV)	100

3.4 EVALUATION OF FLOOD MAPS

An accuracy assessment was performed on each classified SAR image to provide some measure of reliability of the classifications. No ground reference data is available in this study, therefore reference points from respective Landsat images with acquisition dates close to each SAR image were used. Confusion matrices and the standard error measures (overall accuracy, user's accuracy, producer's accuracy and kappa) were calculated to quantitatively assess the accuracy of each classified image.

A number of points were manually created and labelled for each Landsat image in regions which are also within the SAR images and not affected by cloud cover obscuring the satellite image or missing scan lines. The flooded points were definite open water bodies on the Landsat image. Points labelled as non-flooded were labelled as such according to visual interpretation. However, water could be present beneath vegetation canopy, and could therefore influence the accuracy. This should, however occur at a minimum, since non-flooded points were mostly collected away from the greater water bodies. The labelled points were then used to perform accuracy assessments on the ASAR images. Table 3.7 below summarises the total number of points and the number of points per class from each Landsat image for the respective ASAR images.

Table 3.7: Number of collected points from the Landsat images and the ASAR images for which the points will be used.

Landsat sensor	Acquisition date	Total number of extracted points	Number of points: flooded class	Number of points: non-flooded class	ASAR images using extracted Landsat points for accuracy assessment
Landsat TM	2009-03-19	134	70	64	2009-03-17
					2009-03-20
Landsat ETM+	2009-03-27	308	193	115	2009-03-23
					2009-03-24
Landsat ETM+	2009-04-28	327	232	95	2009-04-25
Landsat TM	2009-05-06	155	78	77	2009-05-10
					2009-05-11
					2009-05-14
Landsat TM	2009-05-22	142	73	69	2009-05-30

To perform an accuracy assessment on the PALSAR images, a subset of the labelled points which fell within the extent of the respective PALSAR image was extracted. An exception was the Landsat image of 20 April 2009, which were only used for PALSAR images and not ASAR images. For 20 April 2009, points were manually extracted for PALSAR images. Table 3.8 below summarises the total number of points and the number of points per class for each Landsat image for the respective PALSAR sets.

Table 3.8: Number of collected points from the Landsat images and the PALSAR images for which the points will be used.

Landsat sensor	Acquisition date	Total number of extracted points	Number of points: flooded class	Number of points: non-flooded class	PALSAR images on which accuracy assessment will be performed using extracted points
Landsat TM	2009-03-19	118	55	63	2009-03-19 (1)
Landsat TM	2009-03-19	91	45	46	2009-03-19 (2)
Landsat ETM+	2009-04-20	120	70	50	2009-04-25

From Table 3.7 and Table 3.8 it can be seen the number of points for each class are markedly uneven for some Landsat images. This is where the kappa statistic would be advantageous for accuracy assessment purposes, since it not only accounts for chance agreement, but is also not affected by the uneven distribution of points within classes (Silcocks 1983; Emmert-Streib 2009). A commonly used scale for the interpretation of kappa values is listed in Table 3.9 below. These

divisions are arbitrary, but are useful benchmarks for purposes of interpretation (Landis & Koch 1977).

Table 3.9: Interpretation of Kappa values

Kappa value	**Interpretation**
<0.00	Less than chance agreement
0.00-0.2	Slight agreement
0.21-0.4	Fair agreement
0.41-0.6	Moderate agreement
0.61-0.8	Substantial agreement
0.81-1	Almost perfect agreement

Source: Landis & Koch (1997)

Additionally, the user's and producer's accuracy will reveal the error within different classes and it will therefore be possible to evaluate the distribution of error within the flooded and non-flooded classes (Campbell & Wynne 2011).

Images were also qualitatively assessed by discussing general problems using the two selected classification approaches when visually assessing classification results as well as discussing the impact of sensor properties such as wavelength, incidence angle and polarisation on classification accuracies.

CHAPTER 4 RESULTS AND DISCUSSION

In this chapter, section 4.1 summarises results obtained from the classification and accuracy of the ASAR images, followed by the PALSAR images. Section 4.2 compares results obtained from thresholds with those obtained from ACMs. The general problems encountered when using the two classifiers are also addressed. Finally, the influence of wavelength, incidence angle and polarisation is addressed. While the aim of this study is to classify open water bodies, regions of flooded vegetation, which generated high backscatter and also corresponded to definite flooded areas on the Landsat images, were present in this study area and their significance for flood mapping is also discussed.

4.1 RESULTS

4.1.1 ASAR

4.1.1.1 Thresholds

An example of obtained classification results is depicted in Figure 4.1 for the ASAR WSM image captured on 20 March 2009. Figure 4.1a shows the original unclassified image. Figure 4.1b depicts the flood extent that yielded the highest overall accuracy, at -12 dB. Figure 4.1c depicts all the threshold slices on a single map and in this example, threshold intensities range between -9 and -13.5 dB. As the threshold value is increased, higher intensities are classified as flooded area and the classified flooded region expands, as can be seen more clearly in the inserted image in Figure 4.1c, outlined in red.

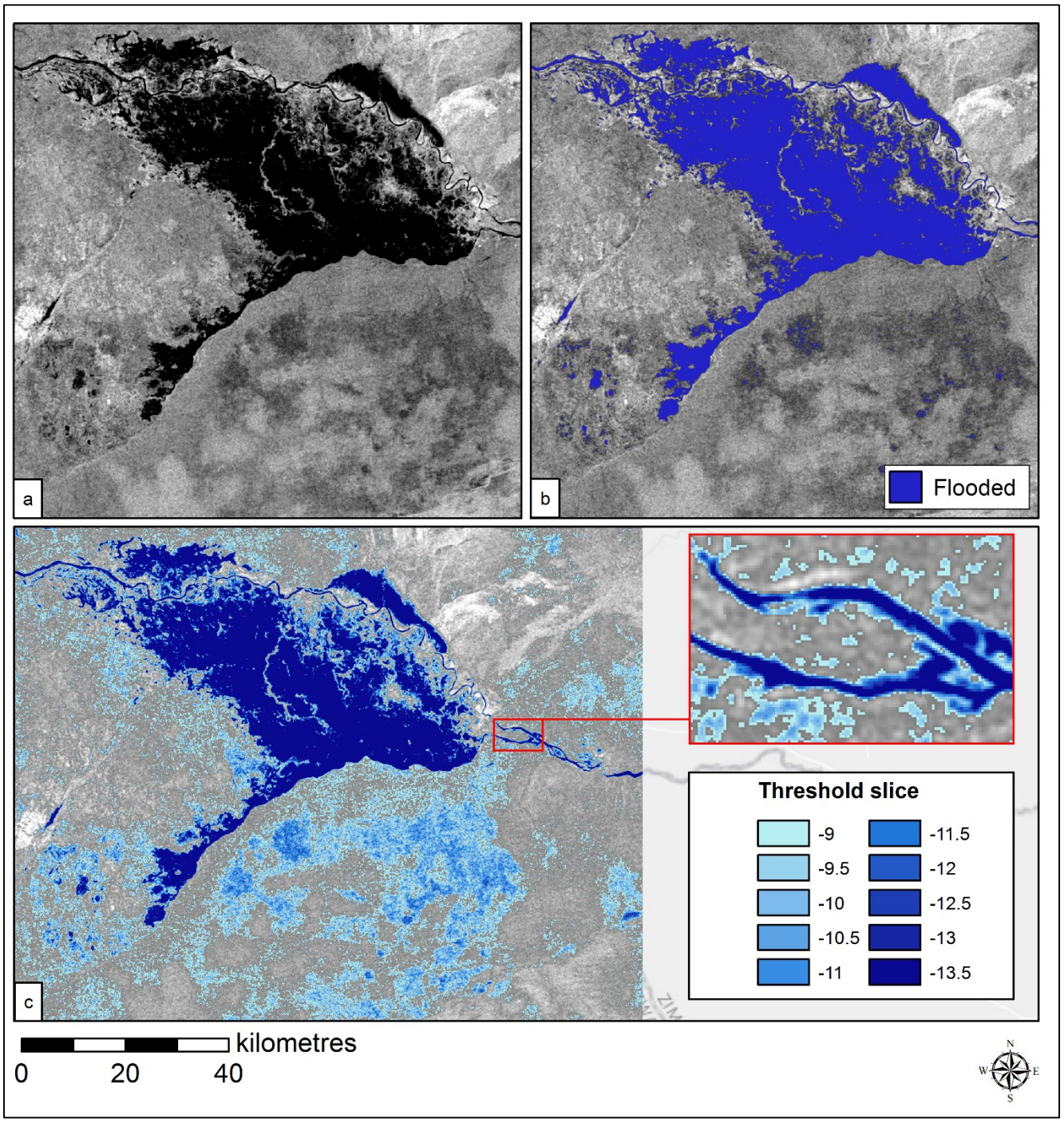

Figure 4.1: The original ASAR WSM image, captured on 20 March 2009 (a), the classified image with a threshold of -12 dB (b), which had the highest overall accuracy, and the stacked threshold levels with threshold values ranging from -9 to -13.5 dB (c). The area classified as flooded increases with an increase in threshold as seen in the inset on (c).

For each threshold value of each ASAR image a confusion matrix was created and the error metrics calculated. Error metrics for all threshold values for every ASAR image can be found in Appendix C.

Figure 4.2 shows the overall accuracy per threshold value for each ASAR image, while Figure 4.3 shows the corresponding kappa statistics for these images. For each trend line, the first point is the overall accuracy of the lowest threshold located at the local minimum between the two peaks, the last point is the overall accuracy for the inflection point and the points in between are the overall accuracies of the threshold values in between the upper and lower threshold varied in increments of 0.5 dB, as discussed in section 3.3.2. For all the ASAR images, the threshold value with the highest overall accuracy and kappa value is not located at the local minimum, but is between 1.5 dB and 6 dB higher than the local minimum. In both these figures there is a general upward trend as the threshold value increases. Overall accuracy peaks between -14.5 and -8.5. Exceptions are the two images captured on 20 March 2009 and 29 May 2009. The accuracies seem to stay level and then show a general downward trend. Additionally, for 11 May 2009 and 30 May 2009, after the upward trend, the overall accuracy seems to stay level, followed by a downward trend.

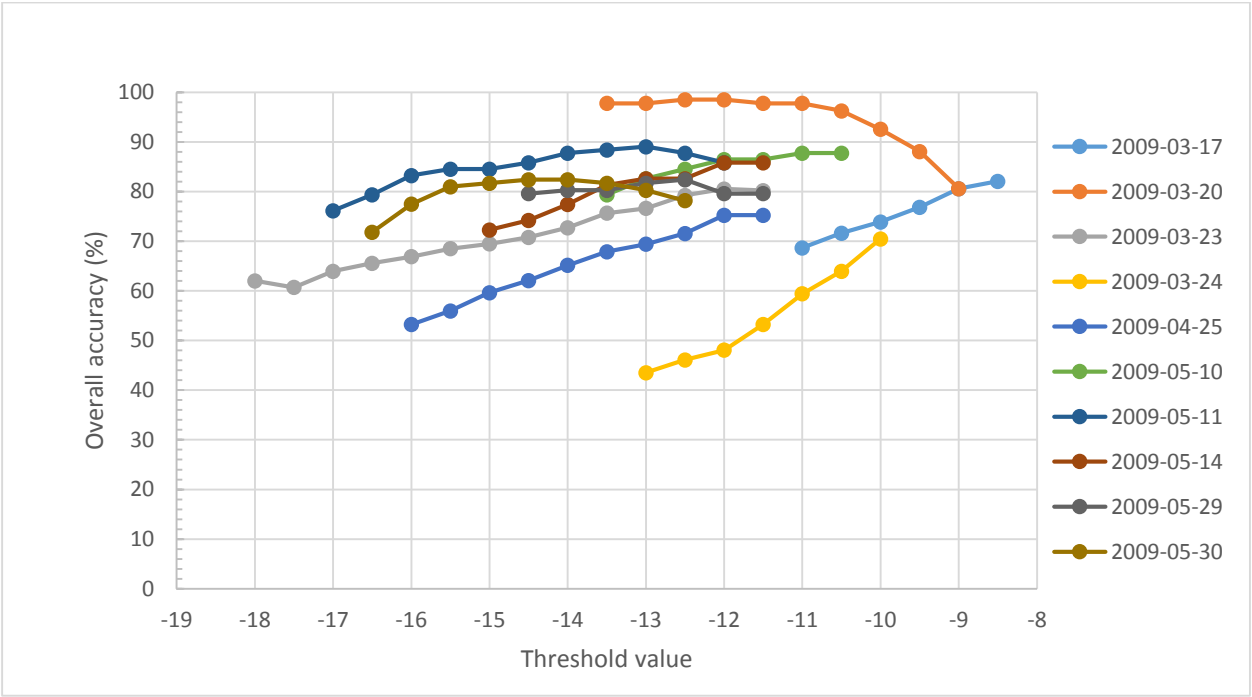

Figure 4.2: Overall Accuracy for each threshold value for all ASAR WSM images

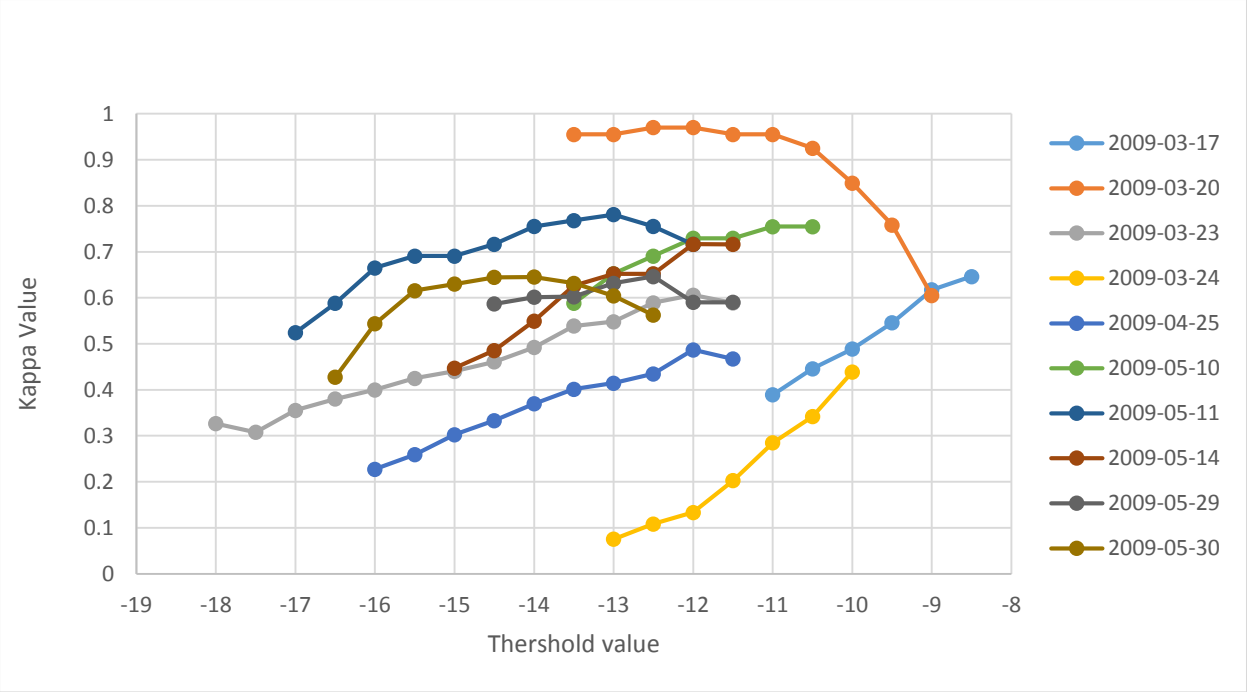

Figure 4.3: Kappa statistic for each threshold value for all ASAR WSM image

The threshold values which yielded the highest overall accuracy for each respective ASAR image is summarised in Table 4.1 below (while the confusion matrices for these threshold values that yielded the highest overall accuracy for each ASAR image can be found in Appendix D). The threshold values range between -14 and -8.5 dB, while the overall accuracy ranges between 70% and 99%. The user's and producer's accuracy for the flooded class range between 87% and 100%, and 58% and 97% respectively, while the user's and producer's accuracy for the non-flooded class range between 55% and 97%, and 86% and 100% respectively. The kappa statistic ranges between 0.44 and 0.97.

Table 4.1: Confusion matrix results for best threshold slices for the ASAR WSM images

SAR Date	Best Threshold	Overall Accuracy	User's accuracy flooded	Producer's accuracy flooded	User's accuracy non-flooded	Producer's accuracy non-flooded	Kappa
2009-03-17	-8.5	82	98	67	73	98	0.65
2009-03-20	-12	99	100	97	97	100	0.97
2009-03-23	-12	81	91	76	69	88	0.61
2009-03-24	-10	70	92	58	56	91	0.44
2009-04-25	-12	75	93	71	55	86	0.49
2009-05-10	-10.5	88	87	88	88	87	0.75
2009-05-11	-13	89	98	79	83	99	0.78
2009-05-14	-12	86	91	79	82	92	0.72
2009-05-29	-12.5	82	88	74	79	90	0.65
2009-05-30	-14	82	92	70	77	95	0.65

Despite the large range of overall accuracy and kappa values for the ASAR images, most classified images for thresholds listed in Table 4.1 had good overall accuracies, above 80%, and kappa values above 0.6 which indicates substantial agreement between classified image and reference points according to Table 3.9. Exceptions are 24 March 2009 and 25 April 2009, yielding overall accuracies of 70% and 75% respectively, and kappa values were low, scoring 0.44 and 0.49 respectively. These images had low accuracies most likely due to large portions of higher backscatter return, either caused by disturbances over the open water surfaces, or interaction with the flooded vegetation.

4.1.1.2 Active contours

For each ASAR image, the Canny edge detector was used to determine the initial contour when using active contours as the image classifier. An example for the ASAR image captured on 23 March 2009 can be seen in Figure 4.4. Figure 4.4a shows the initial contour in light blue. The inserted image gives a closer view of the initial contour in the area shown in red. The final segmented image showing the flooded area can be seen in Figure 4.4b.

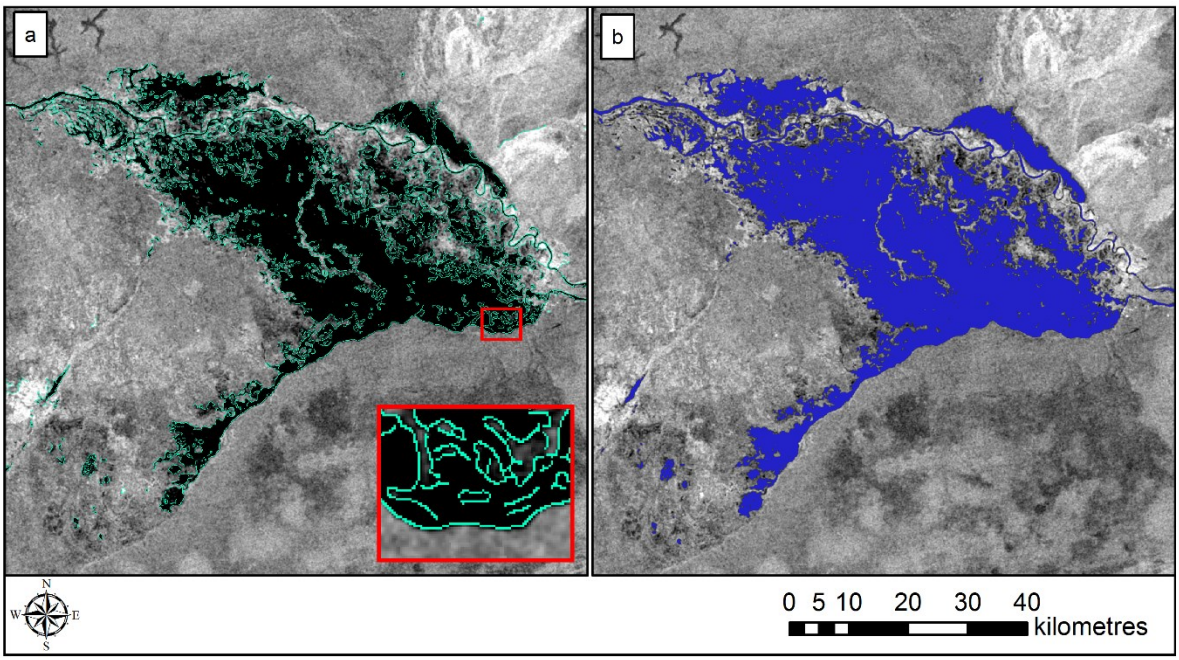

Figure 4.4: ASAR image of 23 March 2009. The Canny edge in light blue can be seen in (a). The inserted image in (a) outlined in red gives a close-up view of the edge. The segmented flooded region as identified by the ACM is shown in (b)

Table 4.2 below summarises the error metrics of the ACM classification for each ASAR image. The overall accuracy ranges between 58% and 98%. The user's and producer's accuracy for the flooded class range between 74% and 100%, and 34% and 100% respectively. The user's and

producer's accuracy for the non-flooded class range between 47% and 100%, and 64% and 100% respectively. The kappa statistic ranges between 0.27 and 0.96. The confusion matrices for the ACM classified ASAR images can be found in Appendix D.

Table 4.2: Confusion matrix results for active contours for the ASAR WSM images

SAR Date	Overall Accuracy	User's accuracy flooded	Producer's accuracy flooded	User's accuracy non-flooded	Producer's accuracy non-flooded	Kappa
2009-03-17	87	98	77	80	98	0.75
2009-03-20	98	100	96	96	100	0.96
2009-03-23	71	100	54	56	100	0.47
2009-03-24	58	97	34	47	98	0.27
2009-04-25	67	98	54	47	98	0.39
2009-05-10	85	77	100	100	71	0.70
2009-05-11	85	100	71	77	100	0.70
2009-05-14	82	98	65	74	99	0.64
2009-05-29	80	74	96	94	64	0.60
2009-05-30	82	76	97	96	67	0.64

ACMs also produced a large range of overall accuracy and kappa values for the ASAR images, but most classified images had good overall accuracies, above 80% and kappa values above 0.6. Exceptions are 23 March 2009, 24 March 2009 and 25 April 2009, yielding overall accuracies of 71% and 58% and 67% respectively, and kappa values were low, scoring 0.47, 0.27 and 0.39 respectively.

4.1.2 PALSAR

4.1.2.1 Thresholds

An example of classification results obtained from PALSAR imagery captured on 19 March 2009 can be seen in Figure 4.5. The original unclassified HV-polarised image is shown in Figure 4.5a. Figure 4.5b illustrates the flood extent that yielded the highest overall accuracy, at -27 dB. In Figure 4.5c the stacked threshold slices are shown, ranging between -28.5 and -26 dB. With an increase in the threshold, the classified region expands, which is clearer in the inserted image in Figure 4.5c outlined in red. However, the area expanding with an increase in threshold value is not as pronounced as in the ASAR WSM images.

For each threshold value of each PALSAR image a confusion matrix was created and the error metrics calculated. Error metrics for all threshold values for every PALSAR image can be found

in Appendix C. The confusion matrices for the threshold values that yielded the highest overall accuracy for each PALSAR images can be found in Appendix D.

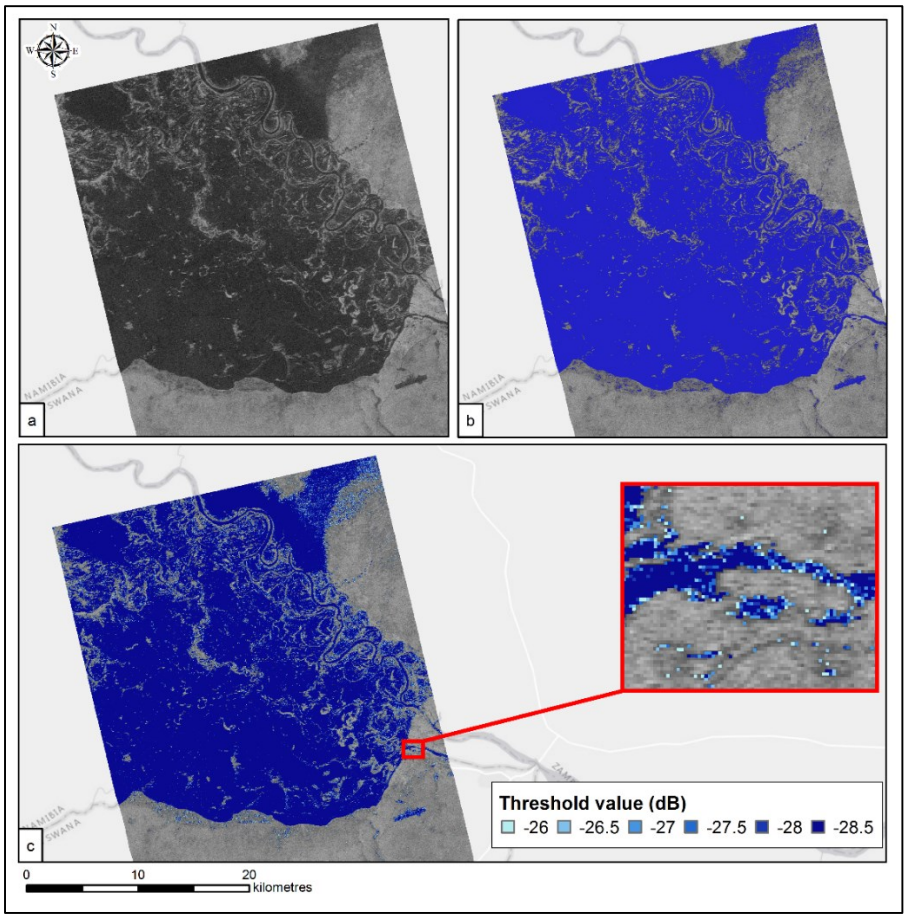

Figure 4.5: PALSAR HV-polarised image of 19 March 2009. The original PALSAR image captured on 19 March 2009 (a), the classified image with a threshold value of -27 (b) which had the highest overall accuracy, and the stacked threshold values ranging from -26 to -28.5 dB (c). The area classified as flooded increases with an increase in threshold as seen in the inset on (c). © ESA.

Figure 4.6 shows the overall accuracy per threshold value for each PALSAR image compared to while Figure 4.7 shows the corresponding Kappa for these images. Overall accuracy peaked between -27.5 and -17 dB. In both these figures the overall accuracy remains level followed by a gradual downward trend with an increase in the threshold for all but four images. For the HH-polarised image from the first set of PALSAR images captured on 19 March 2009, as well as the HH-, VV- and VH- polarised PALSAR images captured on 5 April 2009, there is a modest upward trend. Overall accuracy therefore stays relatively constant.

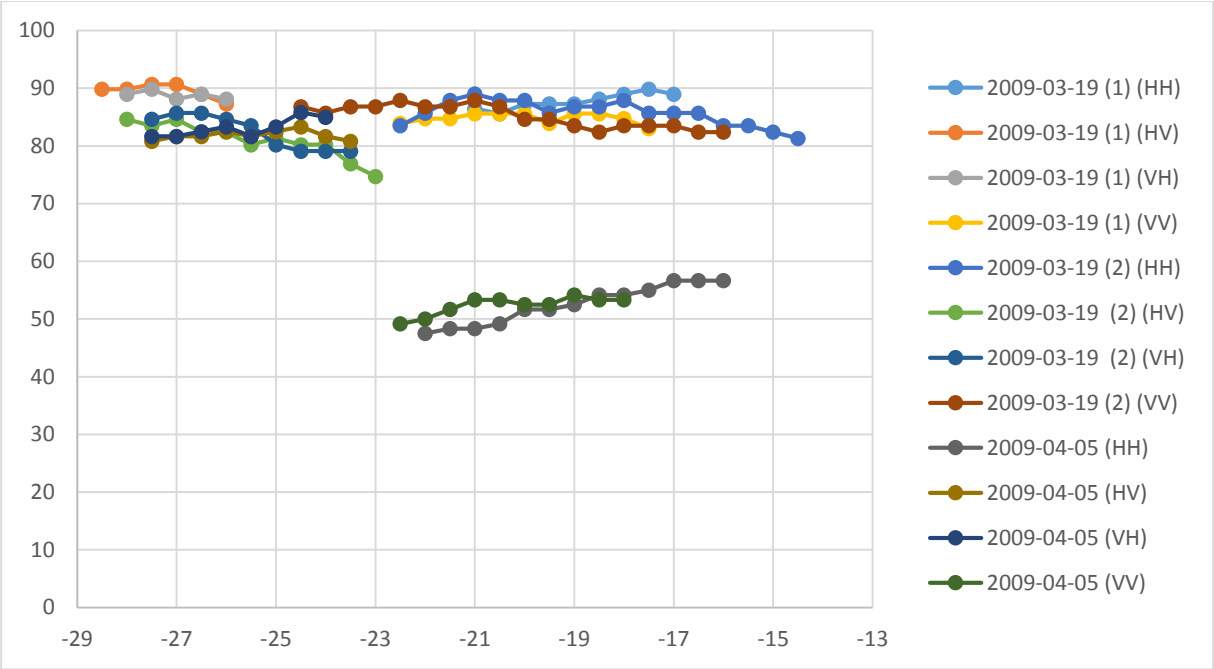

Figure 4.6: Overall Accuracy for each threshold value for all PALSAR PLR images

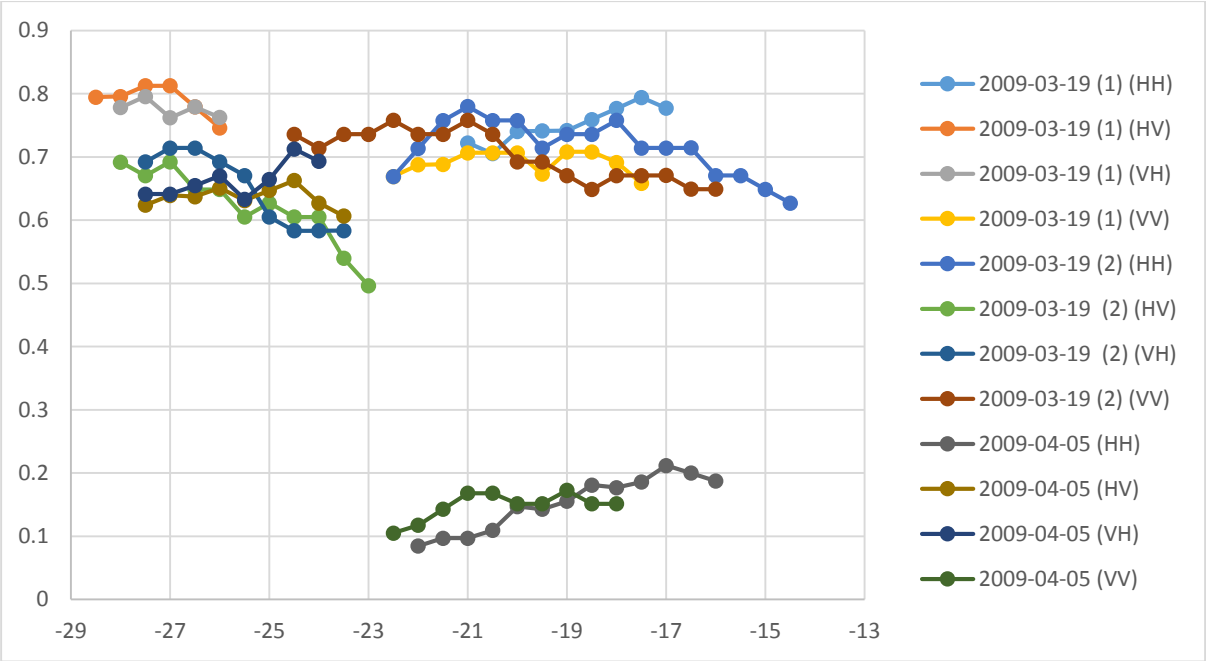

Figure 4.7: Kappa statistic for each threshold value for all PALSAR PLR images

Table 4.3 below summarises threshold values for each image which delivered the highest overall accuracy when compared to the sample points derived from the Landsat images. The threshold values range between -21 and -17 for the HH-polarised images, -27 and -24.5 for the HV-polarised images, -27.5 and -24.5 for the VH-polarised images and -21 and -19 for the VV-polarised images. The overall accuracy for all images range between 54% and 91%. The user's and producer's accuracy for the flooded class range between 82% and 97% and 26% and 91% respectively, while the user's and producer's accuracy for the non-flooded class range between 47% and 92% and 80% and 98% respectively. The kappa statistic varied between 0.17 and 0.81.

Table 4.3: Confusion matrix results for best threshold slices for the PALSAR PLR images

SAR Date	Threshold	Overall Accuracy	User's accuracy flooded	Producer's Accuracy flooded	User's accuracy non-flooded	Producer's accuracy non-flooded	Kappa
2009-03-19 (1) (HH)	-17.5	90	94	84	87	95	0.79
2009-03-19 (1) (HV)	-27	91	89	91	92	90	0.81
2009-03-19 (1) (VH)	-27.5	90	89	89	90	90	0.80
2009-03-19 (1) (VV)	-19	86	90	78	83	92	0.71
2009-03-19 (2) (HH)	-21	89	97	80	83	98	0.78
2009-03-19 (2) (HV)	-27	85	82	89	88	80	0.69
2009-03-19 (2) (VH)	-27	86	85	87	87	85	0.71
2009-03-19 (2) (VV)	-21	88	89	87	87	89	0.76
2009-05-04 (HH)	-17	57	88	30	49	94	0.21
2009-05-04 (HV)	-24.5	83	89	81	77	86	0.66
2009-05-04 (VH)	-24.5	86	91	84	80	88	0.71
2009-05-04 (VV)	-19	54	86	26	47	94	0.17

The overall accuracy and kappa values for most PALSAR images, however, are high with overall accuracies above 80% and kappa values of 0.66 and above, which means agreement between classified image and reference points is substantial to almost perfect (see Table 3.9). Exceptions are the HH- and VV-polarised images of 5 April 2009 with overall accuracies of 57% and 54% respectively, and kappa values of 0.21 and 0.17 respectively indicating only slight agreement.

4.1.2.2 Active contours

Similar to the ASAR images, the initial contour for each PALSAR image was determined using the Canny edge detector. An example for the HV-polarised PALSAR image from the first set captured on 19 March 2009 can be seen in Figure 4.8. In Figure 4.8a, the initial contour is seen in light blue. The inset image in Figure 4.8a shows a closer view of the initial contour in the area shown in red. The segmented image showing the flooded area can be seen in Figure 4.8b.

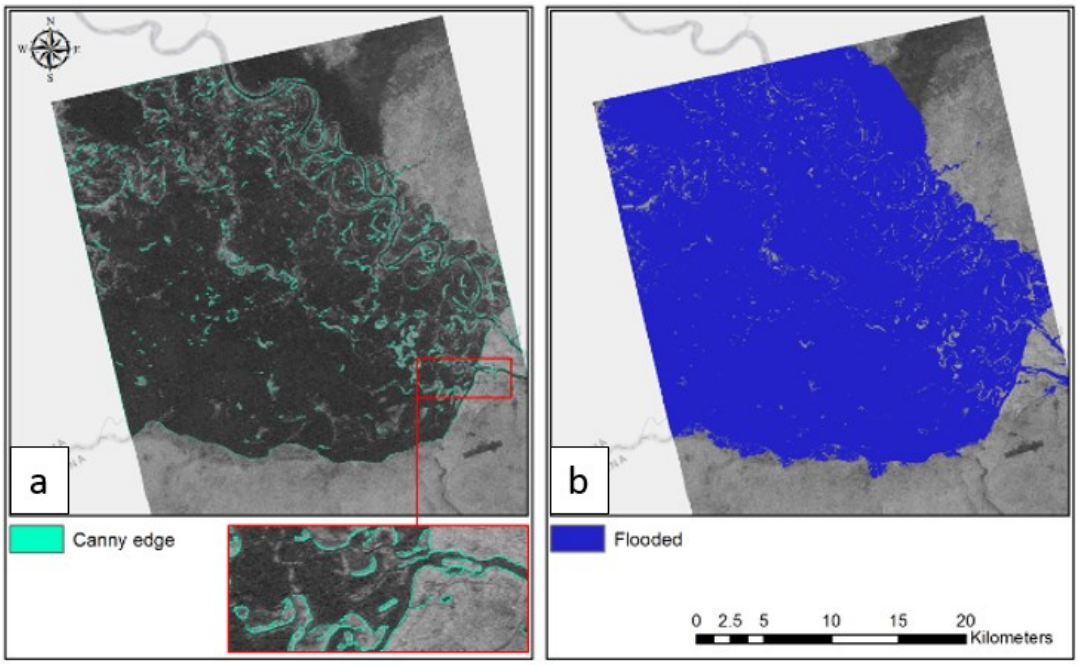

Figure 4.8: PALSAR HV-polarised image of 19 March 2009. Canny edge in light blue as can be seen on the left in (a). The inserted image outlined in red gives a close-up view of the edge. (b) shows the segmented flooded region as identified by ACMs. © ESA.

Table 4.4 below summarises the error metrics for ACMs for PALSAR images. The overall accuracy ranges between 60% and 96%. The user's and producer's accuracy for the flooded class range between 82% and 96%, and 34% and 96% respectively, while the user's and producer's accuracy for the non-flooded class range between 51% and 95%, and 80% and 97% respectively. The kappa statistic range between 0.27 and 0.91. The confusion matrices for the ACM classified PALSAR images can be found in Appendix D.

Table 4.4: Confusion matrix results for active contours for the PALSAR PLR images

SAR Date	Overall accuracy	User's accuracy flooded	Producer's Accuracy flooded	User's accuracy non-flooded	Producer's accuracy non-flooded	Kappa
2009-03-19 (1) (HH)	92	96	87	90	97	0.85
2009-03-19 (1) (HV)	96	96	95	95	97	0.91
2009-03-19 (1) (VH)	89	84	95	95	84	0.78
2009-03-19 (1) (VV)	89	96	80	85	97	0.78
2009-03-19 (2) (HH)	88	85	91	91	85	0.76
2009-03-19 (2) (HV)	88	83	96	95	80	0.76
2009-03-19 (2) (VH)	89	84	96	95	83	0.78
2009-03-19 (2) (VV)	87	82	93	93	80	0.74
2009-05-04 (HH)	60	92	34	51	96	0.27
2009-05-04 (HV)	86	96	79	76	96	0.72
2009-05-04 (VH)	88	92	87	83	90	0.76
2009-05-04 (VV)	60	92	34	51	96	0.27

The overall accuracy and kappa values for most PALSAR images are, however, also high for ACMs, with overall accuracies above 80% and kappa values of 0.66 and above, which means agreement between classified image and reference points is substantial (see Table 3.9) is substantial to almost perfect. Exceptions are the HH- and VV-polarised images of 5 April 2009 with overall accuracies of 57% and 54% respectively, and kappa values of 0.21 and 0.17 respectively indicating only slight agreement for these two images.

4.2 DISCUSSION

A general finding for thresholds was that the best threshold values (as determined by the highest overall accuracy) were not necessarily located at the local minimum, but between 1.5 and 6 dB higher. This is most likely due to the fact that the histogram was extracted over the entire region, which causes backscatter to be convoluted between the two classes if the incidence angle is not taken into account. This could be remedied by segmenting the image into strips along the azimuth direction, extract the histogram for each of these subsets and then use the local minima for each subset for classification. Additionally, the overall accuracy for the PALSAR images did not vary as much with each threshold value as was the case for the ASAR images, indicating that results are more robust for PALSAR images.

4.2.1 Active contours versus thresholds

Figure 4.9 and Figure 4.10 below show the comparison of the overall accuracy and kappa values respectively for the optimal thresholds (as determined by maximum overall accuracy) and the ACMs for the ASAR imagery. When comparing the accuracy results of the best threshold and the ACMs used for flood mapping for each image, thresholds seem to yield higher overall accuracies and kappa values in all instances except for one ASAR image (17 March 2009).

To further substantiate this finding, a one-tailed paired t-test (with a confidence interval of 95%) was performed on the overall accuracy and kappa respectively to determine if there is a significant directional difference in the accuracy results of the threshold and ACMs, or if one mean is consistently greater than the other. Results show that a directional difference in the means of the overall accuracy and kappa statistic for the two classification methods is present ($p<0.05$). However, the difference is marginal, and the average difference between the overall accuracy of the two classification methods is 3.8%. The average difference between the kappa values for the two methods amounts to 0.05.

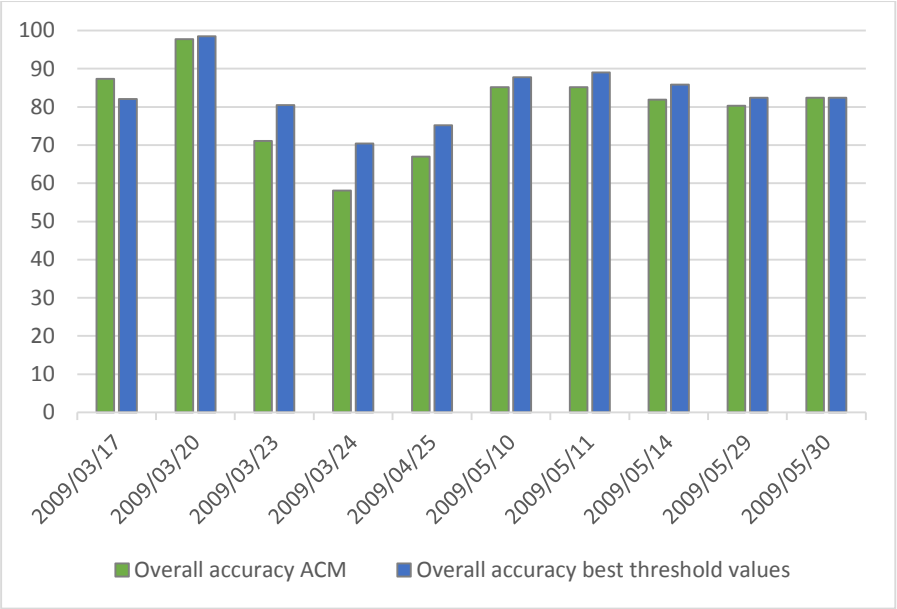

Figure 4.9: Comparison of the overall accuracy percentages for ACMs versus thresholds for ASAR images

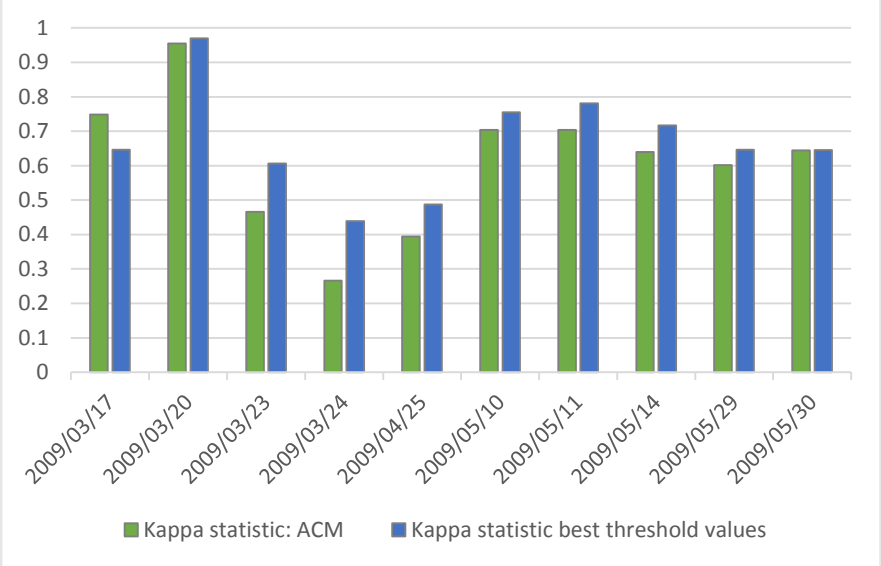

Figure 4.10: Comparison of the kappa statistic for ACMs versus thresholds for ASAR images

However, greater differences arise in the individual flooded and non-flooded classes, which become apparent when comparing the user's and producer's accuracy of the flooded and the non-flooded classes for each method. Figure 4.11 below shows the relationship between the user's and producer's accuracy for the flooded and non-flooded classes of thresholds and ACMs classification methods for the ASAR images. A classification would ideally match the validation data well and will have high producer's accuracy which corresponds to a low error of omission, as well as high user's accuracy, which corresponds to a low error of commission. Points will therefore ideally be located at the top right of the graph if the percentage of producer's and user's accuracy is high.

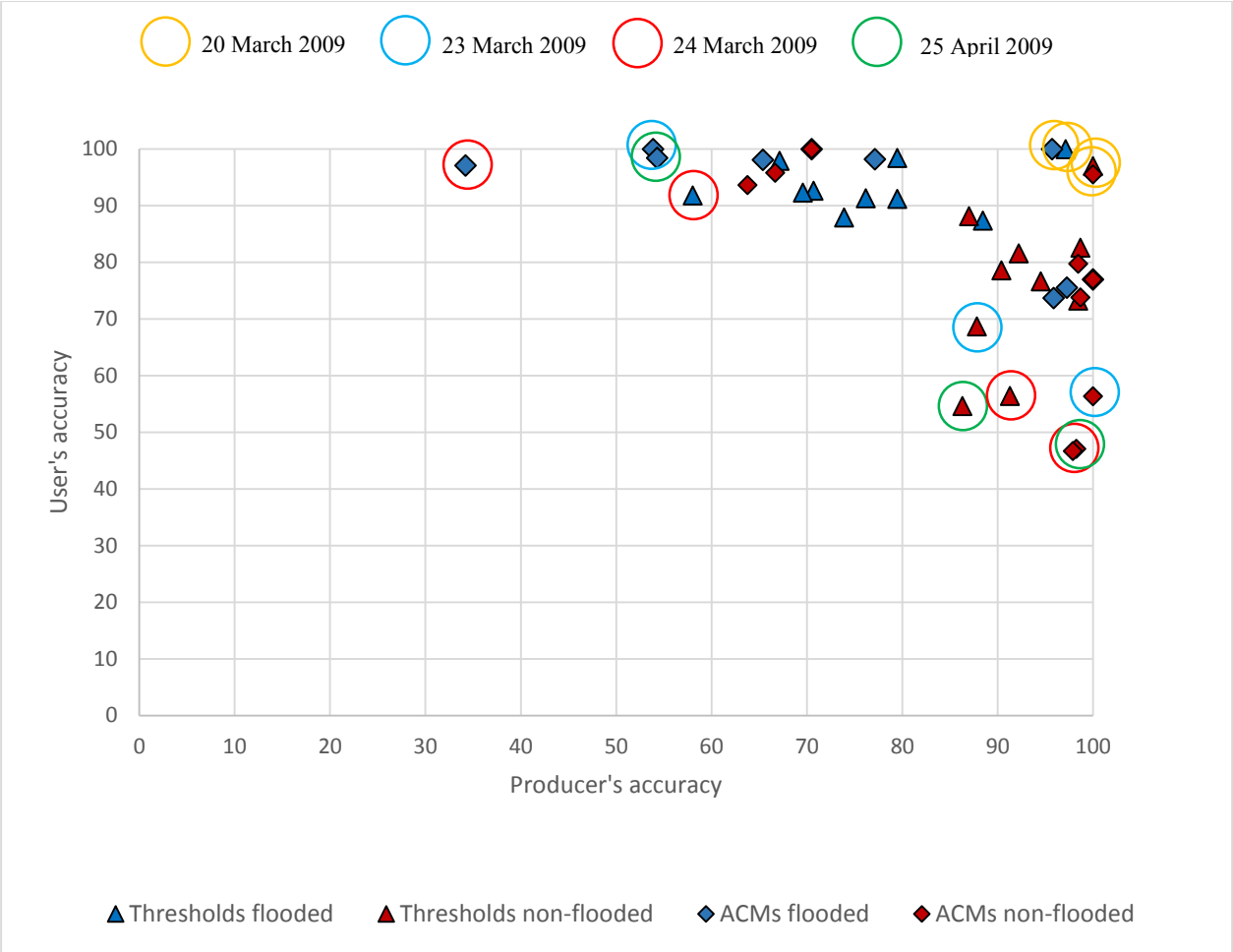

Figure 4.11: Relationship between the producer's and the user's accuracy for the flooded and non-flooded classes for thresholds and ACMs for the ASAR images.

While there is high variability within the different classes, the producer's and user's accuracies are generally high for the ASAR images. The threshold images seem to be slightly more clustered and there is more variability in the user's and producer's accuracy of the ACM classifiers, which suggests that the flood maps obtained from the ACM classifier are slightly less consistent than for the threshold classifier. This could possibly be due to the placement of the initial contour, which would be different for each of the ASAR images. The variation in backscatter would yield different initial contours based on the backscatter, which in turn in influenced by the incidence angle of the images.

A few outliers were also present and highlighted on the graph. The ASAR image of 20 March 2009 (outlined in yellow) had consistently high user's and producer's accuracy for both threshold and ACM classification methods. This image was ideal for open water classification, since water surfaces were calm and contrasts between flooded and non-flooded regions were high.

The points with low producer's accuracy for the flooded class and low user's accuracy for the non-flooded class are those of 23 March 2009 (outlined in blue), 24 March 2009 (outlined in red) and 25 April 2009 (outlined in green). For 24 March and 25 April 2009, a large portion of the water had high backscatter return, either due to disturbances over the open water surfaces, or interaction with the flooded vegetation, causing higher backscatter return over all large portion of the flooded areas. Subsequently flooded regions were incorrectly classified as non-flooded regions, thereby increasing the error of omission for the flooded class and the error of commission for the non-flooded class.

For 23 March 2009, however, the reason for the lower than expected user's accuracy for the flooded class and producer's accuracy for the non-flooded class was possibly due to the number of days between the reference Landsat images (27 March 2009) and the ASAR image. Certain points selected along water edges on the Landsat image, were not yet flooded on the ASAR image of 23 March 2009. As stated earlier in sections 1.5 and 3.1, floodwaters increased sharply around 20 March and peaked around 26 March. This was therefore a crucial period in which floods progressed more rapidly in a lateral direction and change was more drastic than for other image dates. Therefore, despite the good agreement based on visual inspection (see maps in Appendix E), a lot of flooded reference points, especially along the edges were non-flooded points on the ASAR image, caused a high error of omission for the flooded class and a high error of commission for the non-flooded class. Therefore classification results would not be as accurate for the image of 23 March 2009 since flood extents were so different.

Figure 4.12 and Figure 4.13 below show the comparison of the overall accuracy and kappa values respectively for the optimal thresholds (as determined by maximum overall accuracy) and the ACMs for the PALSAR images. When comparing the best threshold and ACMs for the PALSAR images, ACMs mostly outperformed the threshold slice, albeit only marginally, with the exceptions of the VV-polarised data for the first PALSAR set of 19 March 2009, the HH- and VV-polarised data for the second PALSAR set of 19 March 2009 and the HV-polarised image of 5 April 2009.

To substantiate this finding, a one-tailed paired t-test (with a confidence interval of 95%) was also performed on the overall accuracy and kappa statistic results for the PALSAR images to determine if there is a significant directional difference in the mean accuracy results of the two classification methods. Results once again show that a directional differences in the means of the overall accuracy and kappa statistic for the two classification methods is present ($p<0.05$). Differences are

however marginal and the average difference between overall accuracy of the two methods is 2.9%, while the average difference between the kappa values of the two methods is 0.05 for the PALSAR images.

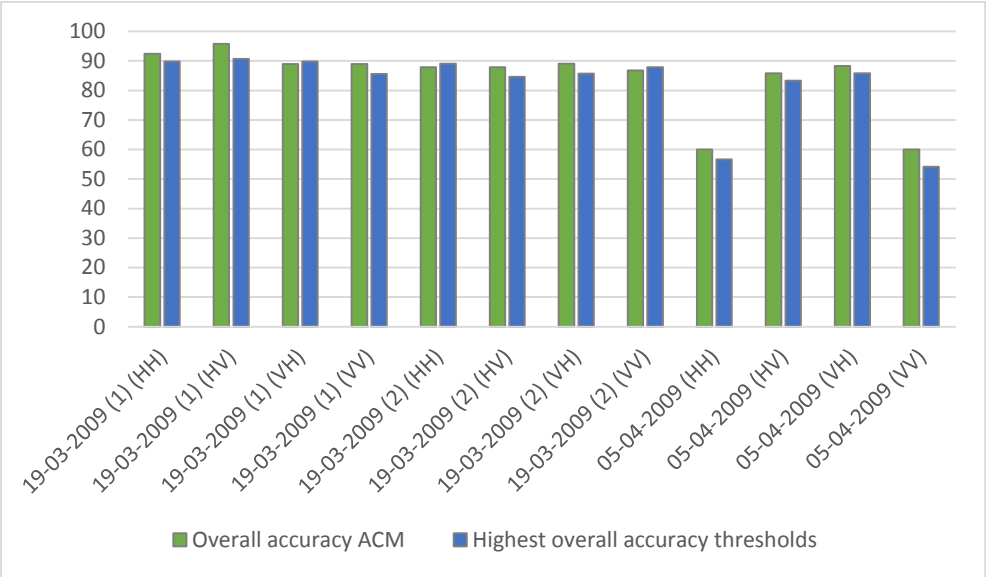

Figure 4.12: Comparison of the overall accuracy percentages for ACMs versus thresholds for PALSAR images

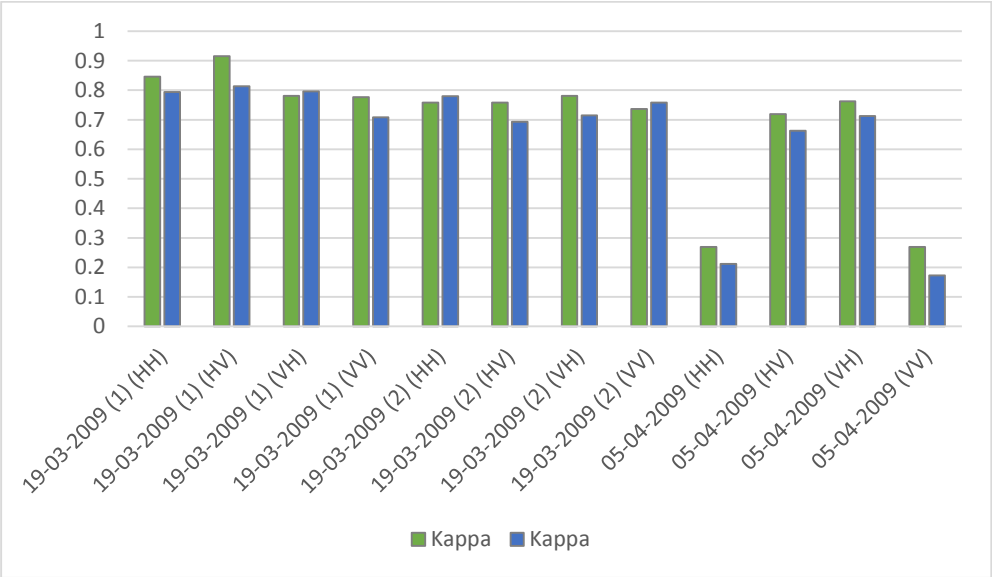

Figure 4.13: Comparison of the kappa statistic for ACMs versus thresholds for PALSAR images

Figure 4.14 below shows the relationship between the user's and producer's accuracy for the flooded and non-flooded classes of threshold and ACM classification methods for the PALSAR images. Accuracy values are clustered at the top right of the graph for both the thresholds and ACM classifications, indicating high producer's and user's accuracy and hence low error of omission and low error of commission for both classes of both classifiers.

Figure 4.14: Relationship between the producer's and the user's accuracy for the flooded and non-flooded classes for thresholds and ACMs for the PALSAR images

The outliers were the HH- (outlined in red) and VV-polarised images (outlined in blue) of 5 April 2009. These two images were subject to severe surface roughness over a large extent of the flooded region (see Figure 4.21), which would lead to a lower producer's accuracy (and hence a higher error of omission) for the flooded classes. This will be addressed in section 4.2.4.

There were some general problems encountered for thresholds for both ASAR and PALSAR images. When surfaces were rougher, contrast between flooded and non-flooded area were lower and threshold could potentially be set too high. For the ASAR image of 24 March 2009 for example, the threshold value was -10 dB. This threshold value yielded the highest overall accuracy, but flooded area can be overestimated, or error of commission is higher, which corresponds to lower user's accuracy. Most ASAR images were affected in this way (see Appendix E for maps), but a large portion of the overestimated areas do not fall within the Zambezi Region and can therefore be masked out using he using the borders of Namibia as the boundary. Another approach would be to create subsets of the images along the azimuth direction to account for the changes in

backscatter due to changes in the incidence angles. The histograms for each subset should then be extracted the local minima used for classification.

Another issue with thresholds is that other non-water features with very low backscatter will be included in the flooded class. An example would be the Kasane airport in Botswana and the roads west of the airport, as shown on the second set of the HH-polarised PALSAR images captured on 19 March 2009 (Figure 4.15). This could be remedied using urban masks to remove these areas from the final product.

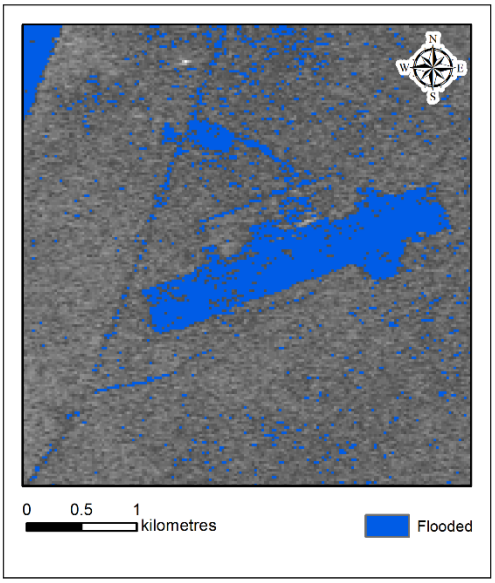

Figure 4.15: PALSAR image of 19 March 2009 (second set). Kasane airport and a road to its left misclassified as flooded region due to low backscatter. © ESA.

Additionally, isolated noisy pixels with low backscatter were classified as flooded area when using thresholds, giving classified images a grainy appearance. This could potentially be corrected with post-classification filtering to remove noise.

Problems were also encountered with the active contour approach. Certain smaller regions with low backscatter return were not segmented into the flooded class as indicated by the red arrows in Figure 4.16. This is likely because the model assumes that the backscatter intensities are homogeneous throughout the entire region. However, if flooded backscatter intensities are dissimilar throughout the entire region, certain areas will not be included in the final flooded region (Wang, De-Huang & Xu 2010). Sensitivity of the initial contour could also potentially be an issue, and if the initial contour is not placed close to the flood boundaries flooded areas could potentially not be identified (Wang, De-Huang & Xu 2010). This could possibly be corrected by using a

water mask of the existing water bodies as initial polygon which would be a good estimate of the boundaries (Voigt et al. 2008). The ACM algorithm would then move the boundary to include the flooded region

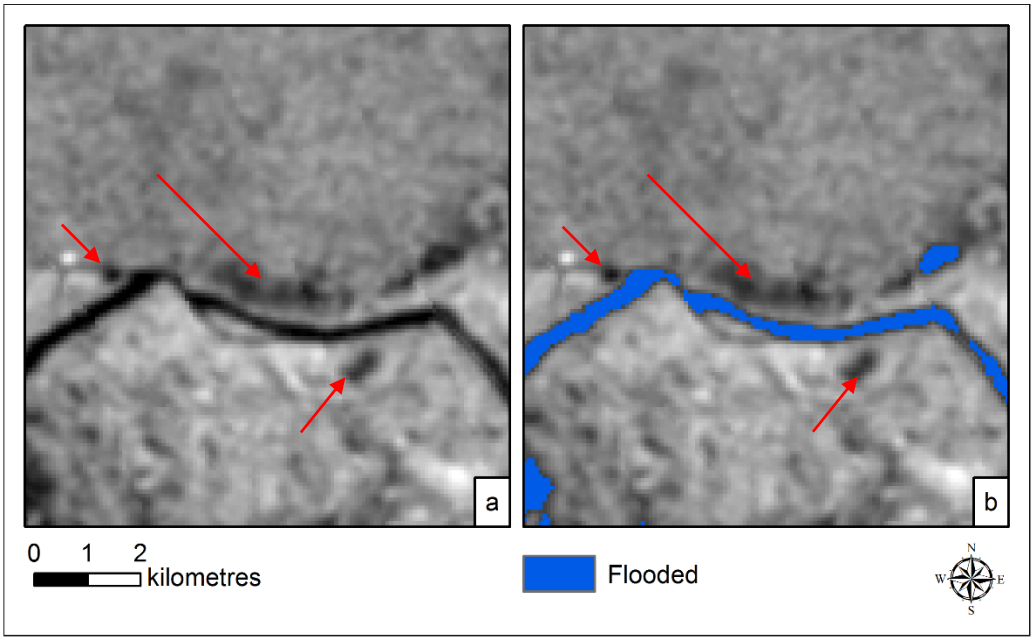

Figure 4.16: ASAR image, captured on 23 March 2009, showing a segment of the Zambezi River. Some flooded areas, such as the dark areas around the river (shown by the red arrows), were not segmented into flooded regions by the ACM classifier.

Another problem encountered for some of the PALSAR images is some non-water areas close to the water regions, with slightly darker backscatter values than the other surrounding (non-flooded) areas, were classified as flooded areas. An example would be the area located within the red region in Figure 4.17 on the HV-polarised PALSAR image from the first set captured in 19 March 2009. This is likely because of sensitivity to the initial contour (Wang, De-Huang & Xu 2010). During the evolution of the initial contour, the flooded region continued to grow to include these non-flooded regions due to the lower backscatter values before the segmentation process terminated.

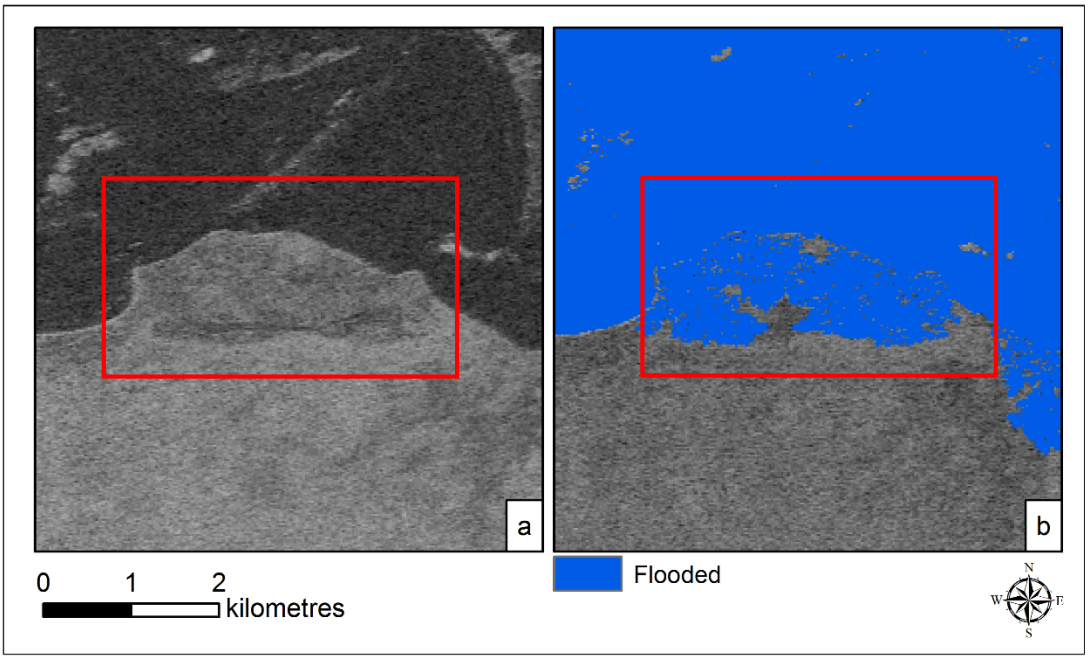

Figure 4.17: HV-polarised PALSAR image (second set). Some non-flooded areas close to water (Figure 4.17a) were also incorrectly classified as flooded region (Figure 4.17b) © ESA.

When assessing overall performance, both methods yield acceptable results. When using simple thresholds, the process can be tedious when done manually. This is because of the initial data preparation such as the smoothing of curves and the fact that the threshold slice yielding the highest result is not a constant value for all images, but depends on the image and its properties. However, it is one of the simplest methods to follow. Furthermore, the threshold values which yielded viable results in this study for open water are within the range suggested by Manjusree et al. (2012) in section 2.7.2, so using the properties of distribution of the backscatter seems to be a good approach for estimation of the threshold value.

Using ACM for image segmentation can be difficult due to the sensitivity of the initial contour and flooded regions with non-homogeneous backscatter intensities. However, the advantage is that it is a region based approach and therefore takes neighbouring values into account, and results are less noisy. It can also be used to identify water areas with rough surfaces if an initial contour is set for such areas. Since using thresholds operates on a per-pixel basis, it would be more difficult to isolate such areas.

Both have merits and drawbacks as discussed, but overall the ACM yielded slightly higher overall accuracy for PALSAR, while thresholds yielded slightly higher overall accuracy for ASAR images when compared to points derived from Landsat. Despite the variation in the user's and producer's accuracy for the classifiers for ASAR as well as the PALSAR images, both methods yielded good

results if images were not severely affected by surface disturbances. Therefore, it would seem that the SAR sensor and image properties take precedence over the method of classification which will be addressed in sections 4.2.2, 4.2.3 and 4.2.4.

4.2.2 Wavelength

Wavelength has a clear impact on signal return from flooded regions. This becomes apparent when comparing certain areas on PALSAR images (L-band) and ASAR images (C-band) to Landsat images. Figure 4.18 below shows an area near the Zambezi River, located west from the Impalila Woodlands and illustrates the differences in backscatter returns.

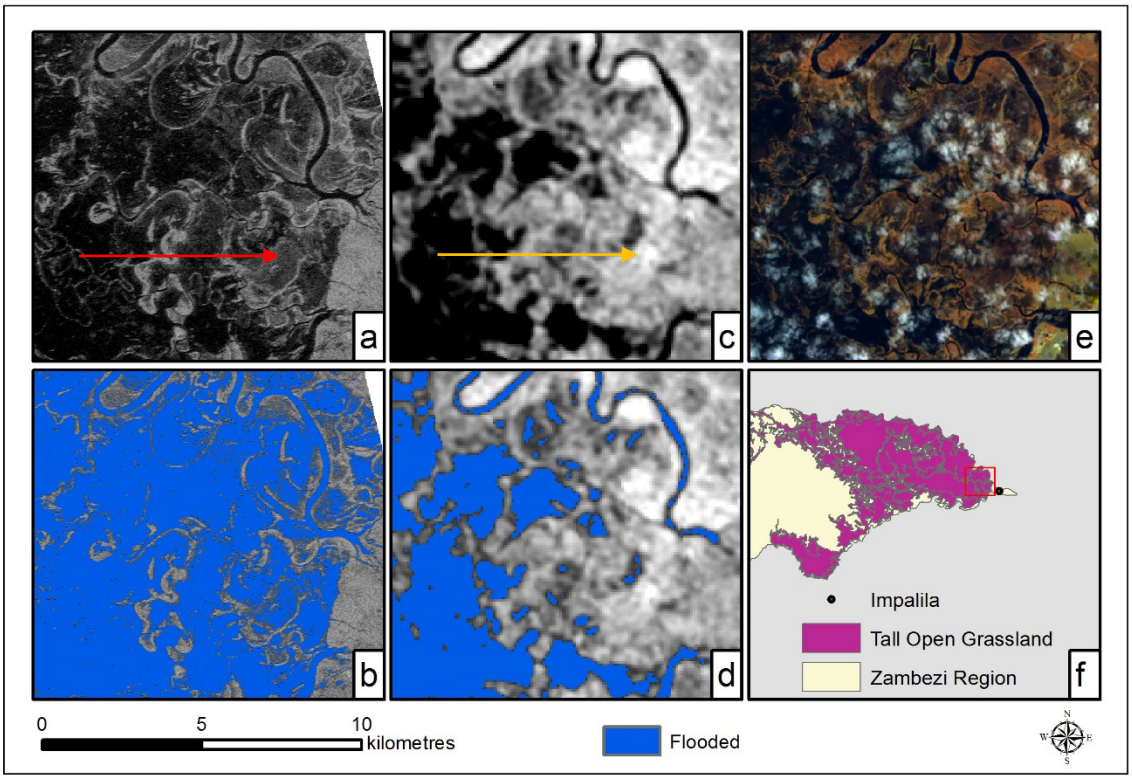

Figure 4.18: Differences in backscatter return based on wavelengths. The HH-polarised PALSAR image of 19 March 2009 is shown in (a) and the classified regions for this image is shown in (b). The ASAR image of 20 March 2009 is shown in (c) and the classified regions for this image is shown in (d). Red and yellow arrows in (a) and (c) are examples where differences arise due to different wavelength. The Landsat image of 19 March 2009 is shown in (e). The vegetation structure of the region is mostly tall open grassland (f).

On the HH-polarised PALSAR image (Figure 4.18a), captured on 19 March 2009, where the signal return is lower than the surroundings, it is subsequently classified as a flooded region, such as the area highlighted by the red arrow Figure 4.18b. For the HH-polarised ASAR image captured one day later on 20 March 2009 (Figure 4.18c), some of the areas had low backscatter returns and were classified as flooded (Figure 4.18d), while other regions (highlighted by the yellow arrow) had higher backscatter returns than the PALSAR images and were subsequently not classified flooded

regions. When compared to the Landsat 5 image captured 19 March 2009 (Figure 4.18e), it can be seen that these areas are however flooded. The main vegetation structure found in this region, according Mendelsohn & Roberts (1997), is tall open grassland (Figure 4.18f). Therefore more flooded grassland areas have lower backscatter returns resembling that of open water on the PALSAR image with the longer wavelength therefore than the ASAR image with the shorter wavelength.

Figure 4.19 below shows the vegetation structure found at the Bukalo Channel. The main vegetation structure found in the area according to Mendelsohn & Roberts (1997), is tall closed woodland (Figure 4.19a). Figure 4.19b is a close-up of the region near the Bukalo channel. Upon closer inspection, when looking at higher resolution imagery such as those on Google Earth captured between 20 June 2006 and 26 October 2013, as well as the satellite and high-resolution aerial base map from ArcGIS (shown in Figure 4.19c), the vegetation structure the along the banks of the Bukalo channel within the red borders in Figure 4.19b is predominantly cultivated and/or other herbaceous vegetation. This is shown by the closer view in Figure 4.19c. Farther from the banks of the channel as well as near the northern regions of the channel (outside the red outlined area in Figure 4.19b), the more dominant vegetation structure is woody vegetation, shown in Figure 4.19d.

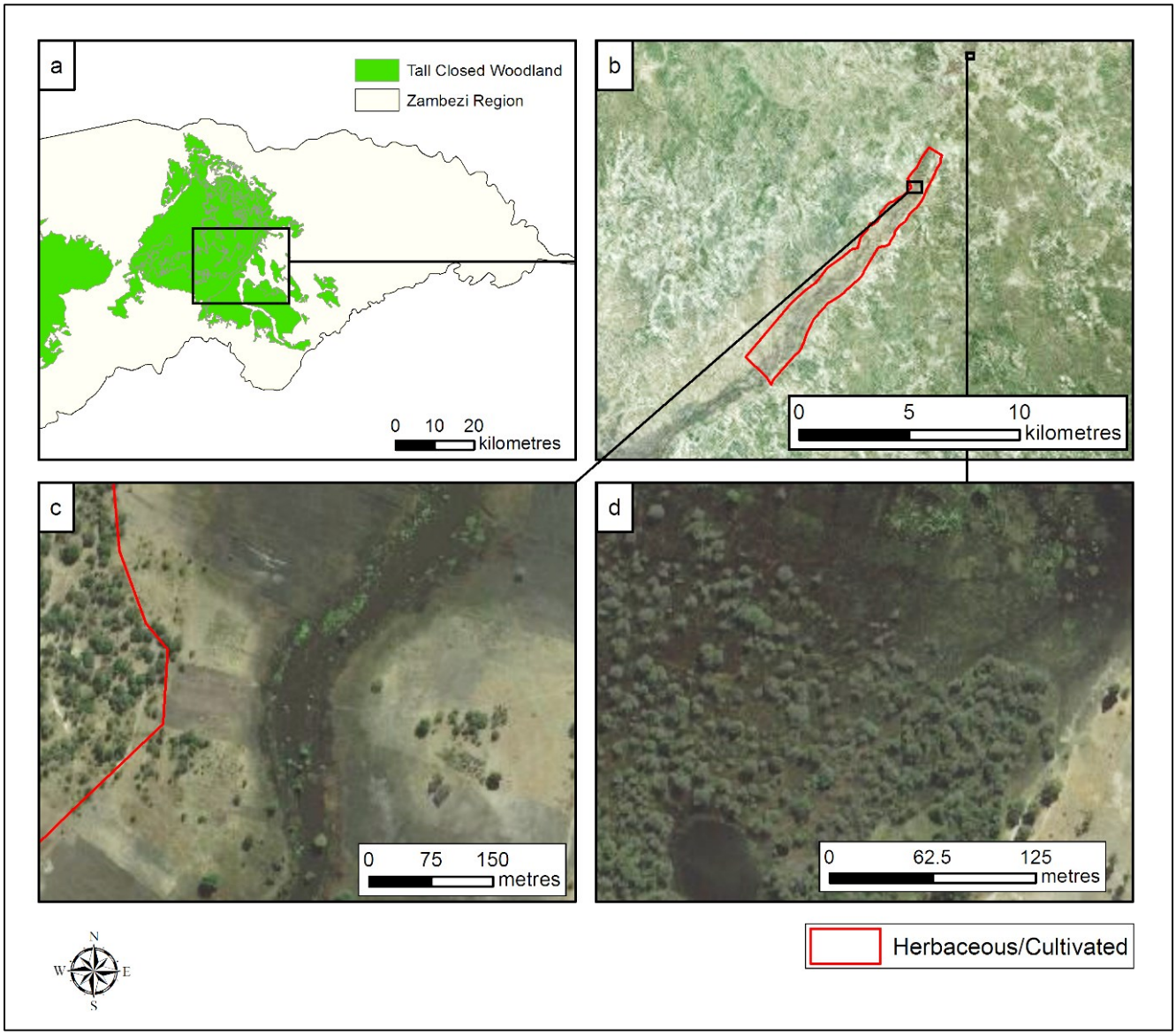

Figure 4.19: The dominant vegetation structure near the Bukalo channel is woody vegetation (a), but along the banks of the channel within the region outlined in red (b), the dominant vegetation structure is herbaceous and cultivated areas (c). Outside the region, the dominant vegetation structure is woody vegetation as can be seen in (d).

Figure 4.20 shows the Bukalo channel and the impact different wavelengths have on classification results.

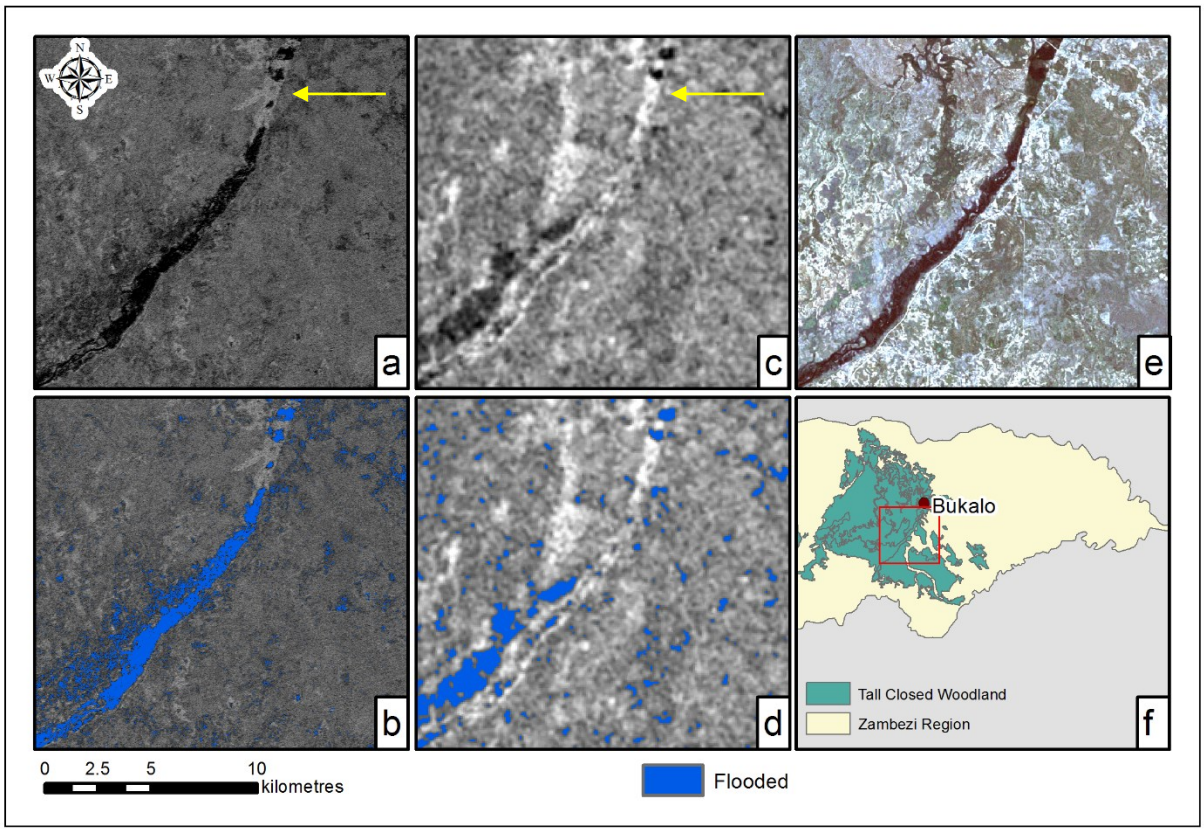

Figure 4.20: The Bukalo channel. The HH-polarised PALSAR image of 5 April 2009 is shown in (a) and the classified regions for this image is shown in (b). The ASAR image captured on 25 April 2009 is shown in (c) and the classified regions for this image is shown in (d). The channel is flooded as can be seen from the Landsat image of 20 April 2009 (e). Dominant vegetation structure is tall closed woodland (f) but herbaceous vegetation is present along the banks of the channel (see Figure 4.19). Yellow arrows in (a) and (c) show the northern regions of the channel where the flooded woodland causes high backscatter return for both the ASAR and the PALSAR images. © ESA.

The HH-polarised PALSAR image, captured on 5 April 2009 is shown in Figure 4.20a. The channel mostly has darker backscatter returns than the surrounding area along the channel banks where the herbaceous vegetation (as illustrated in Figure 4.19) is found. However, the northern regions of the channel, where woody vegetation is found (shown by the yellow arrow in Figure 4.20a and Figure 4.20c), had higher backscatter returns. The regions with dark backscatter returns regions were subsequently classified as flooded regions, but the areas with high backscatter returns were not included in these regions (Figure 4.20b). There are, however, differences between the different polarisations of the PALSAR images, which will be addressed in section 4.2.4.

For the ASAR image captured on 25 April 2009 (Figure 4.20c), the flooded regions for both herbaceous and woody vegetation areas generally had higher backscatter returns. The dark regions

were classified as flooded, but there were fewer open water body regions with lower backscatter return than for the PALSAR image.

This difference between C- and L-band backscatter return from the more herbaceous vegetation such as the cultivated regions at Bukalo channel and the flooded grassland areas in Figure 4.18 and Figure 4.20 is consistent with findings in literature as discussed in section 2.6.2. For herbaceous vegetation, the longer wavelengths (e.g. L-band) do not interact with the canopy layer and lower backscatter values due to specular reflection from water surfaces, but the shorter wavelengths (e.g. C-band) have higher signal return because of double bounce (Ormsby, Blanchard & Blanchard 1985; Ulaby, Moore & Fung 1986; Horritt, Mason & Luckman 2001; Horritt et al. 2003; Bourgeau-Chavez et al. 2005; Bartsch et al. 2012). This means that the longer L-band is more suitable to detect open water surfaces due to minimal interaction with the herbaceous vegetation.

Also consistent with literature, flooded forest regions received higher backscatter returns than during dry conditions for both wavelengths due to the double bounce (σ_d) between horizontal water layer and the forest trunk layers as described in section 2.6.2 (Hess, Melack & Simonett 1990; Kasischke & Bourgeau-Chavez 1997; Townsend 2002).

Figure 4.21 shows the different polarisations of PALSAR images captured on 5 April 2009 situated at the floodplains near the Chobe River.

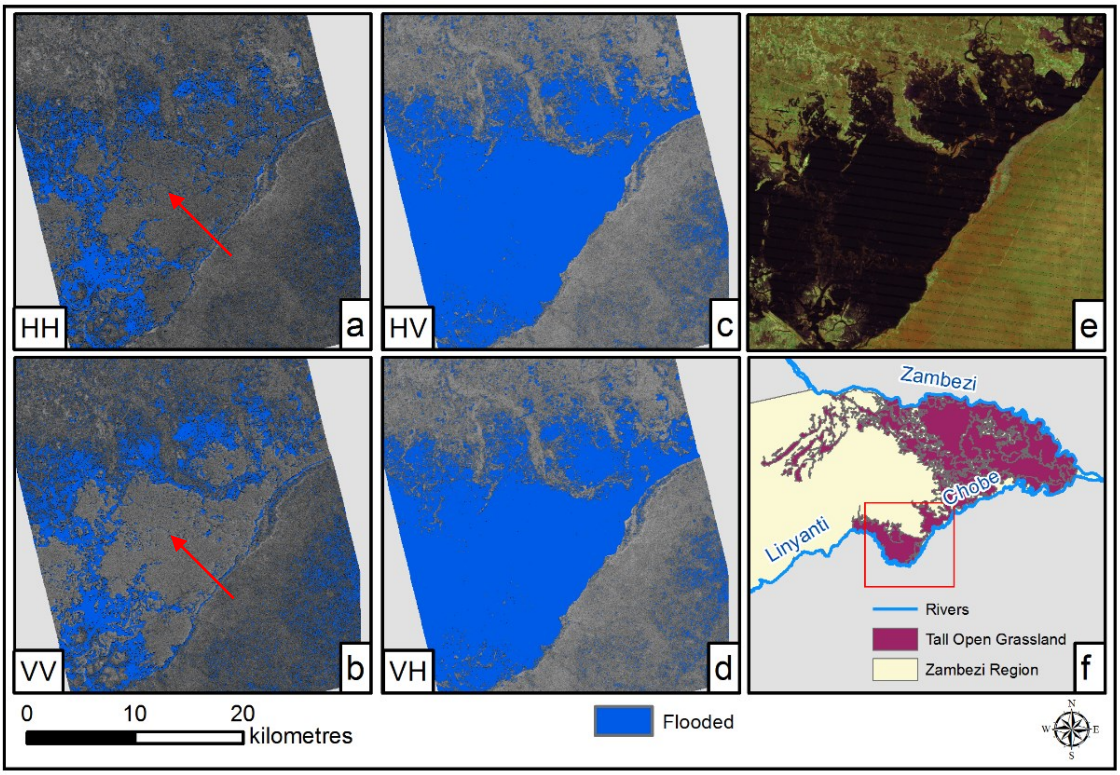

Figure 4.21: Classified flooded regions of HH-polarised (a), VV-polarised (b), HV-polarised (c) and VH-polarised (d) images of 5 April 2009. On both like-polarised images, a large area (indicated by the red arrows) which is actually flooded when compared to the Landsat image of 12 April 2009 (e) remained unclassified. Dominant vegetation structure in this area is grassland (f). © ESA.

The backscatter return from the HH- and the VV-polarised images (Figure 4.21a and Figure 4.21b respectively) in the regions such as those highlighted by the red arrows are higher than expected for the flooded areas at L-band wavelengths in grassland areas. This also occurs on the first set of HH- and VV-polarised images captured on 19 March 2009 (see Appendix E for classified maps). This higher backscatter is not seen on the HV-and the VH-polarised images (Figure 4.21c and Figure 4.21d respectively) but it is flooded when examining the Landsat images of 12 April 2009 (Figure 4.21e). The dominant vegetation structure in these images is grassland according to Mendelsohn & Roberts (1997), as seen in Figure 4.21f. Therefore, the area mostly consists of flooded grassland or open water bodies.

The higher backscatter could either because of the dominant vegetation structure of the area, but this is unlikely since other areas in the HH- and VV-polarised images which have similar grassland vegetation structures do not experience the same effect. Higher backscatter is therefore likely due to the roughening of the water surface, possibly because of wind or turbulence. The differences in polarisation will be addressed in section 4.2.4. Important to note here however is that despite PALSAR images having a longer wavelength, supposed to be less sensitive to small-scale surface roughness over water bodies such as wind and ripples according to Alsdorf, Rodríguez & Lettenmaier (2007) and Bartsch et al. (2012), these images still captured higher backscatter returns than expected for flooded grassland and open water areas.

4.2.3 Incidence angle

For the ASAR images, backscatter responses vary significantly with incidence angle. The effect that incidence angle has on the signal return is dependent on vegetation type. Clear differences emerge when comparing the images of 20 March 2009 and 23 March 2009 in Figure 4.22.

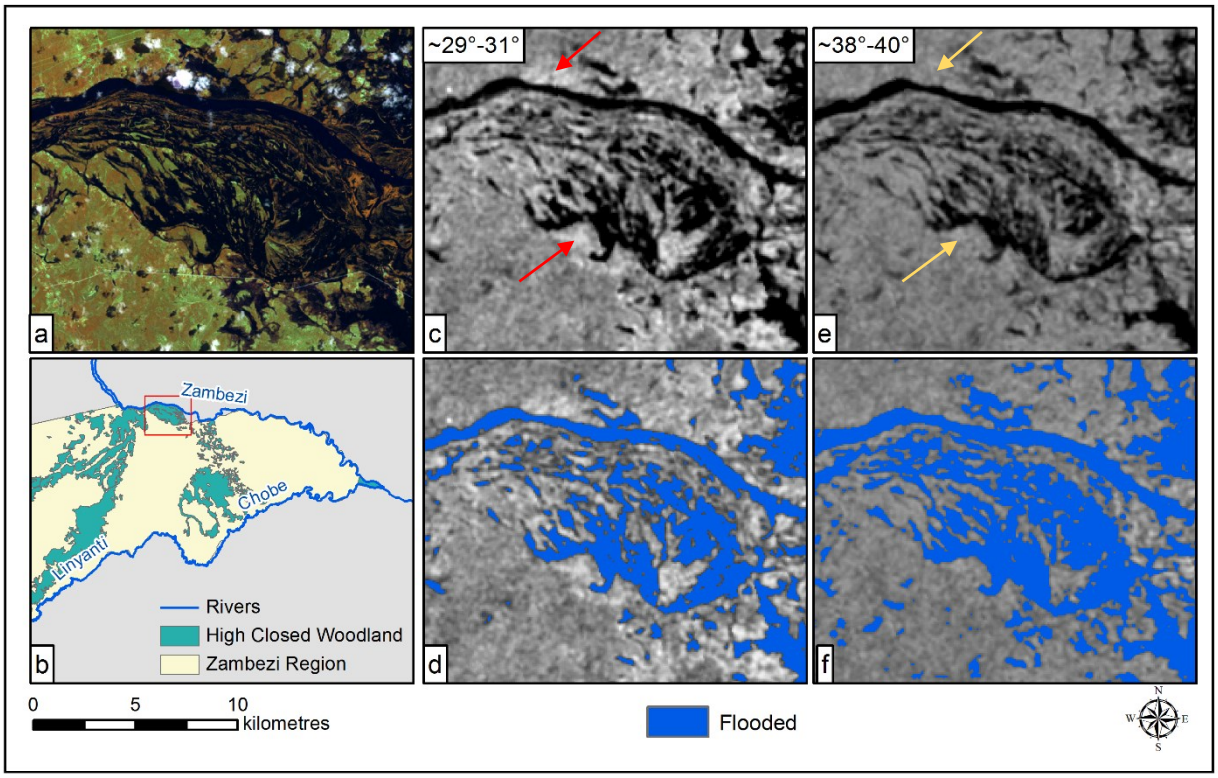

Figure 4.22: The Landsat image subset of 19 March 2009 is shown in (a). Dominant vegetation structure in this region is high closed woodland (b). The ASAR image subset of 20 March 2009 is shown in (c) and the classified regions for this image is shown in (d). The ASAR image subset of 23 March 2009 is shown in (e) and the classified regions for this image is shown in (f). Incidence angles for the subsets are shown in (c) and (e). Red and yellow arrows in (c) and (e) highlight examples of differences in backscatter return at different incidence angles for flooded woody vegetation.

On the Landsat 5 subset of 19 March 2009 the dark flooded regions can be seen (Figure 4.22a). The dominant vegetation structure in this region is high closed woodland (Figure 4.22b). For the

subset of the 20 March 2009 image shown in Figure 4.22c, the incidence angle ranged between 29° and 31°. Regions such as those indicated by the red arrows in Figure 4.22c had high backscatter return. This suggests interaction with the flooded surface and the trunk, thereby causing higher backscatter return due to double bounce. Low backscatter was classified as flooded, while the areas with higher backscatter, which suggests flooded woodland, were not classified as flooded (Figure 4.22d).

The incidence angle for the same subset on the 23 March 2009 image (Figure 4.22e) ranged between 38° and 40°. For flooded regions in the image of 23 March 2009, however, water regions either had low backscatter return, which were classified as flooded area (Figure 4.22f), or backscatter resembled non-flooded vegetation (such as those areas highlighted by the yellow arrows in Figure 4.22e), likely due to scattering from the canopy and subsequently were not classified as flooded. A greater extent was correctly classified as flooded than for 20 March 2009 in this region because of the dark backscatter return. Incidence angles for this image ranged between about 29° and 34°, which seems to be a favourable angle range for open water bodies. This is because it is not too steep, and contrast between flooded and non-flooded is therefore adequate. It is also not too shallow and severely affected by vegetation.

The same effect can be observed when comparing the same high closed woodland area (Figure 4.23b) for the images of 10 May 2009 and 11 May 2009 in Figure 4.23.

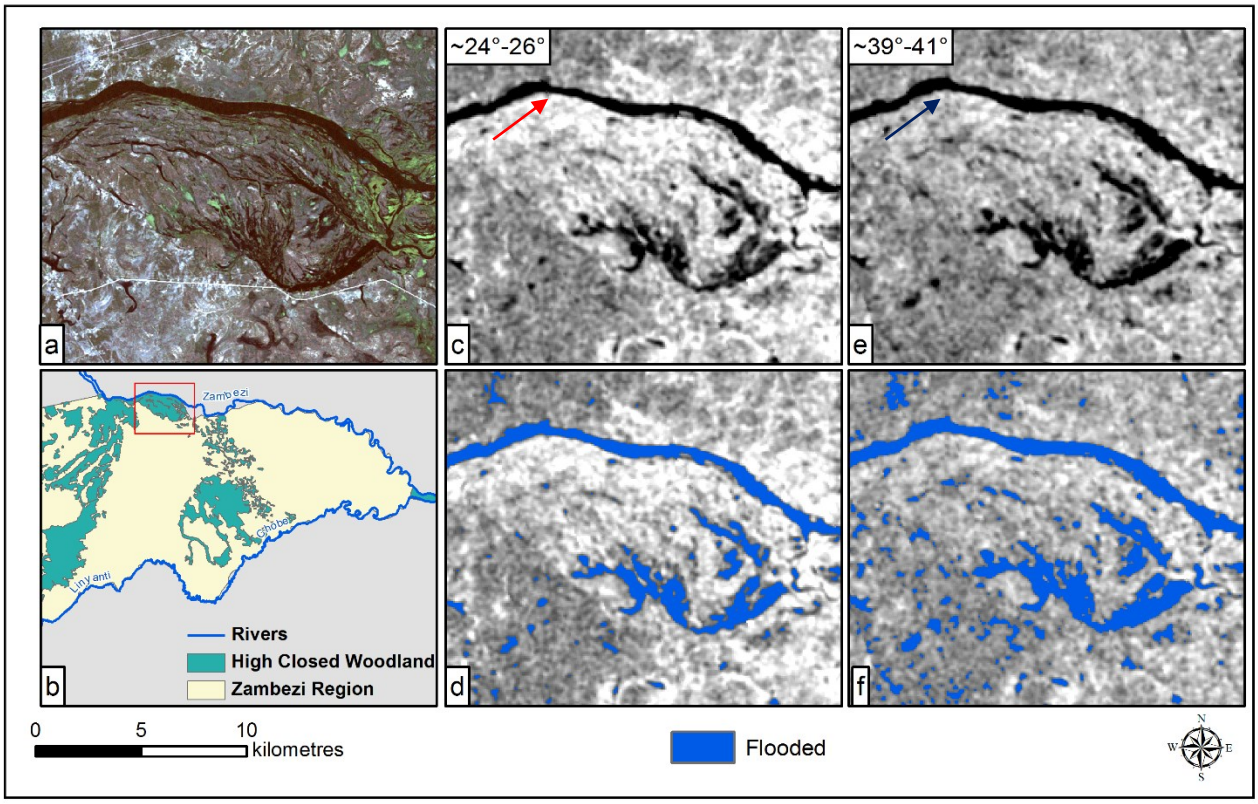

Figure 4.23: The Landsat image subset of 6 May 2009 is shown in (a). Dominant vegetation structure in this region is high closed woodland (b). The ASAR image subset of 10 May 2009 is shown in (c) and the classified regions for this image is shown in (d). The ASAR image subset of 11 May 2009 is shown (e), and the classified regions for this image is shown in (f). Incidence angles for the subsets are shown in (c) and (e). Red and dark blue arrows in (c) and (e) highlight examples of differences in backscatter return at different incidence angles for flooded woodland.

On the Landsat image of 6 May 2009, the dark flooded regions can be seen (Figure 4.23a). The incidence angle for the 10 May 2009 (Figure 4.23c) subset is between 24° and 26°. Dark open water with low backscatter returns were classified as flooded, but other areas, such as those shown by the red arrow, had higher backscatter due to the double bounce causes by the flooded surface-trunk interaction and were not classified as flooded areas (Figure 4.23d). For 11 May 2009 (Figure 4.23e), with shallower incidence angles ranging between 39° and 41°, dark open waters were classified as flooded areas (Figure 4.23f) but fewer areas had high backscatter return resembling flooded vegetation than that of 10 May 2009. Backscatter returns such as those indicated by the dark blue arrow in Figure 4.23e resembled the surrounding non-flooded vegetated areas, suggesting volumetric scattering from the canopy.

At the Bukalo channel, for the SAR images of 10 May 2009 and 11 May 2009, notable differences can also be seen as illustrated in Figure 4.24.

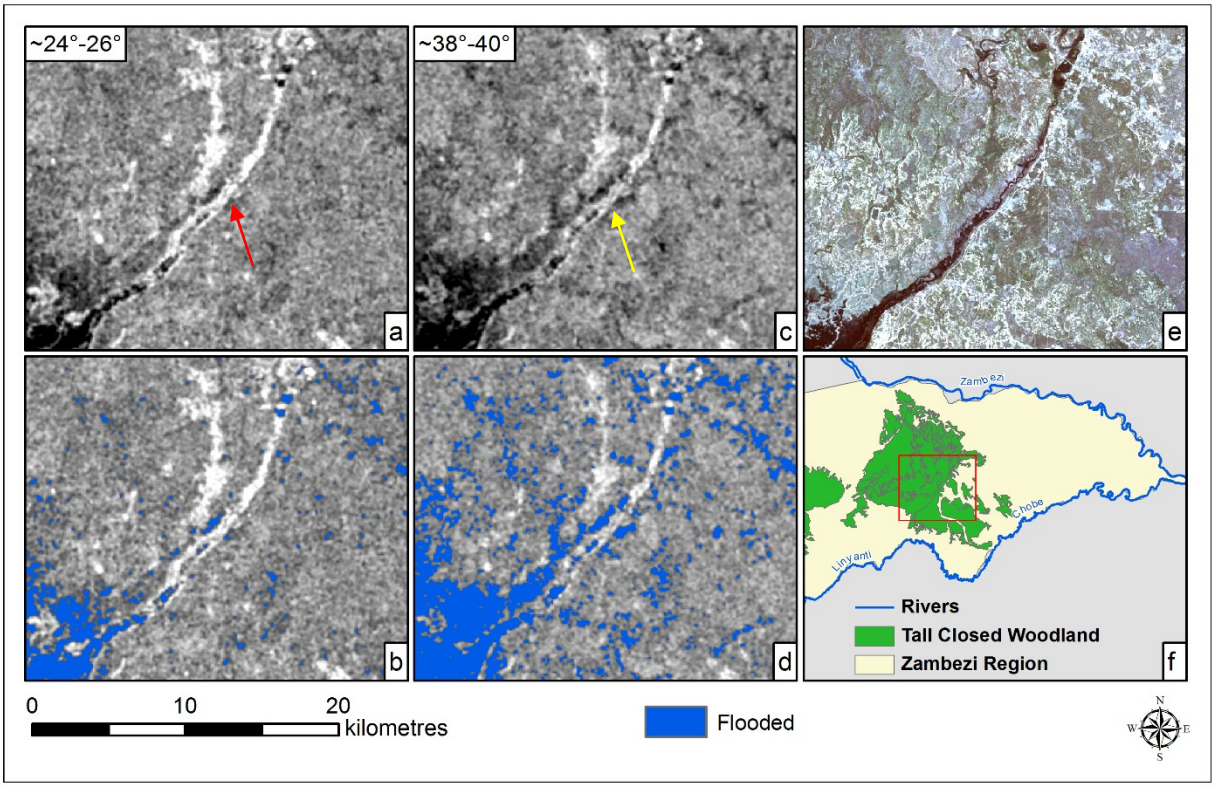

Figure 4.24: The Bukalo channel. The ASAR image subset of 10 May 2009 shown in (a) and the classified regions for this image is shown in (b). The ASAR image subset of 11 May 2009 is seen in (c), and the classified regions for this image is shown in (d). The Landsat 5 image of 6 May 2009 where low spectral signatures indicate flooded areas can be seen in (e). Dominant vegetation in the area is tall closed woodland (f), however herbaceous vegetation is found along the channel banks (see Figure 4.19). Incidence angles for the subsets are shown in (a) and (c). Red and yellow arrows in (a) and (c) highlight examples of differences in backscatter return at different incidence angles.

The incidence angle of the 10 May 2009 image subset (Figure 4.24a) ranges between 24° and 26°. The open water areas with dark backscatter returns were classified as flooded regions (Figure 4.24b). The incidence angle of the 11 May 2009 image subset (Figure 4.24c) ranges between 38 and 40°. A greater extent of the area had dark backscatter returns than 10 May 2009 which were subsequently classified as flooded regions (Figure 4.24d). On the Landsat 5 image of 6 May 2009, the dark flooded regions can be seen (Figure 4.24e). The dominant vegetation structure (tall closed woodland) is shown in Figure 4.24f, but varies and herbaceous vegetation is present closer to the banks of the channel as established in Figure 4.19. The image with the shallower incidence angle therefore had a greater area recognised as open water than the steeper incidence angle.

The areas with high backscatter returns on the ASAR images correspond to the dark flooded regions on the Landsat image and are therefore ‘flooded vegetation’. For both the herbaceous and the woody areas, the incidence angle impacts the backscatter return received in the areas. If it can be assumed that the effect of differences in water level between the image acquisition dates are negligible, the incidence angle impacts the backscatter return received in the areas.

The backscatter return for the flooded vegetation regions in the 10 May 2009 image (with steeper incidence angles) is generally higher for such areas shown by the red arrow in Figure 4.24a than for 11 May 2009 (with shallower incidence angles), as shown by the dark yellow arrow in Figure 4.24c, indicating more double bounce backscatter on the 10 May 2009 subset due to water surface-trunk or water surface-stem interaction.

The findings from Figure 4.22, Figure 4.23 and Figure 4.24 are consistent with the findings in literature. For the dark open water regions, it was found that shallower incidence angles lead to better separability between flooded and non-flooded regions (Solbø & Solheim 2004; Henry et al. 2006). For flooded vegetation, however, with steeper incidence angles the path that the SAR signal travels through the vegetation canopy is shorter and there is more interaction with the stems and water surface for herbaceous vegetation, as well as the trunks and water surface for forested areas, thereby reducing canopy volume scattering. Therefore backscatter returns are higher than during dry conditions (Hess, Melack & Simonett 1990; Wang et al. 1995; Bourgeau-Chavez et al. 2005).

For areas dominated by tall grassland vegetation, the backscatter return was more difficult to analyse. Figure 4.25 illustrates the differences in backscatter return for 20 March 2009 and 23 March 2009 in a region where tall open grassland is the dominant vegetation structure.

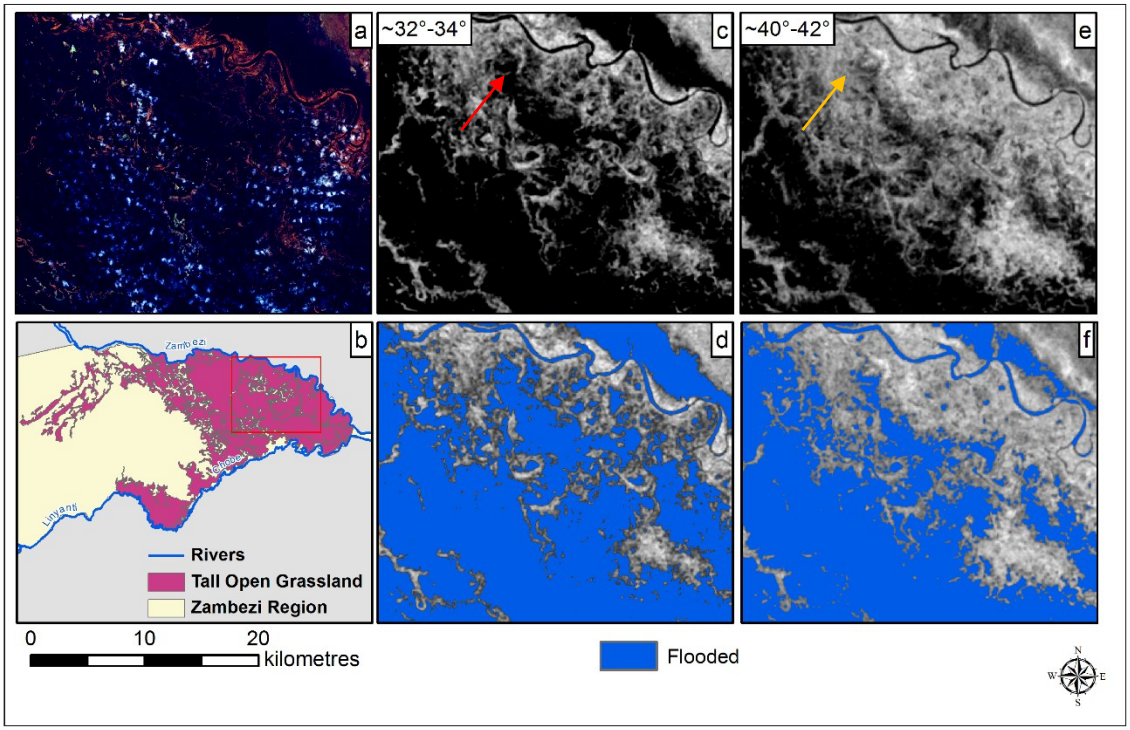

Figure 4.25: Landsat image of 19 March 2009 is shown in (a), while (b) shows the dominant vegetation structure in the region to be tall open grassland. The ASAR subset of 20 March 2009 is shown in (c), and the classified flooded regions for this image is shown in (d). The ASAR subset of 23 March 2009 is shown in (e), and the classified flooded regions for this image is shown in (f). Incidence angles for the subsets are shown in (c) and (e). Red and yellow arrows in (c) and (e) are examples where differences arise due to different incidence angles.

The dark areas on the Landsat image of 19 March 2009 shows the flooded extent of the region (Figure 4.25a), while Figure 4.25b shows the dominant vegetation structure, tall open grassland, in the area. The incidence angle for the 20 March 2009 subset ranges between 32° and 34° (Figure 4.25c). For 20 March 2009 a larger extent had low backscatter return and was subsequently classified as flooded area (Figure 4.25d). The incidence angle for the 23 March 2009 subset ranges between 40° and 42° (Figure 4.25e). When comparing the area shown by the red arrow in Figure 4.25c and the yellow arrow in Figure 4.25e, the backscatter is slightly higher for 23 March 2009 than for 20 March 2009. A similar effect can be seen when comparing 10 May 2009 and 11 May 2009 (Figure 4.26).

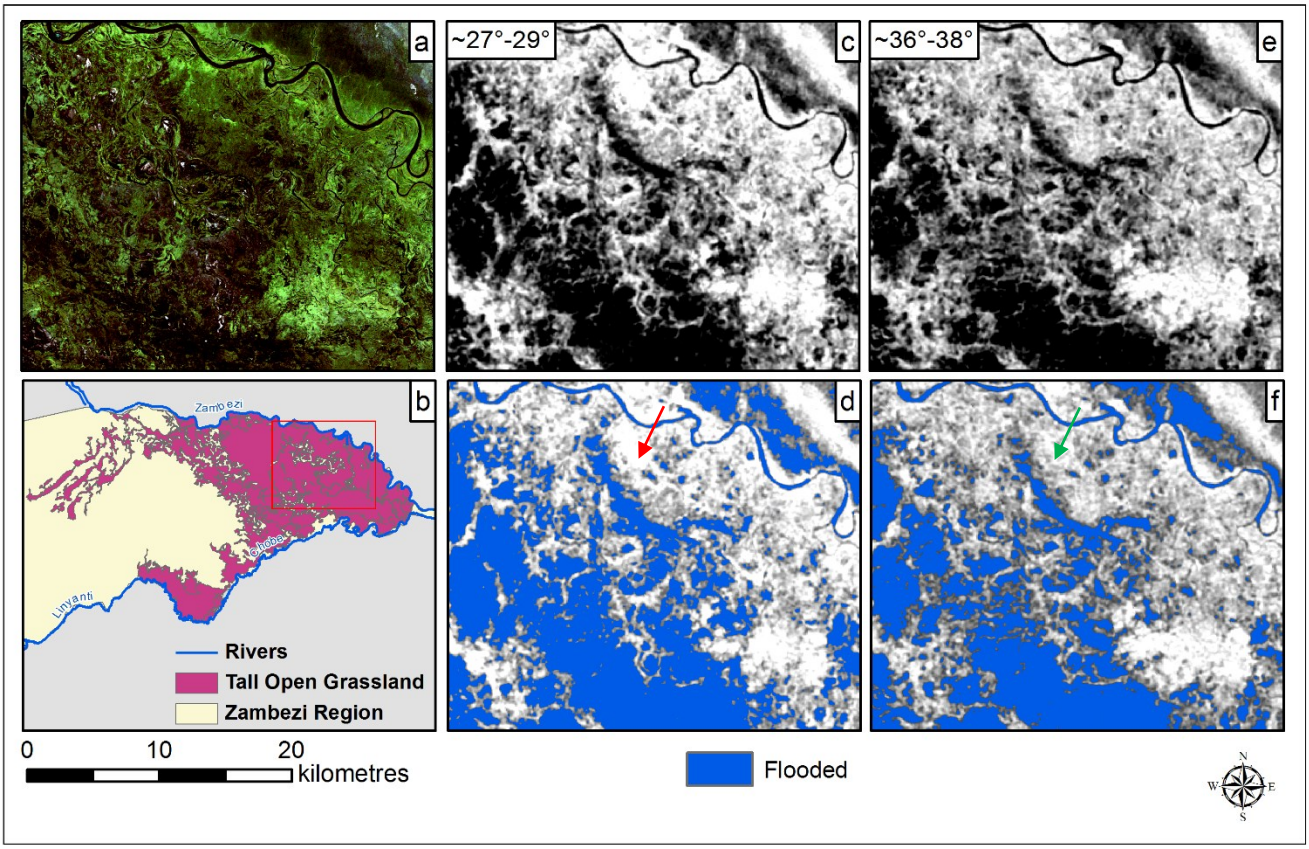

Figure 4.26: Landsat image of 6 May 2009 is shown in (a), while (b) shows the dominant vegetation structure in the region to be tall open grassland. The ASAR subset of 10 May 2009 is shown in (c), and the classified flooded regions for this image is shown in (d). The ASAR subset of 11 May 2009 is shown in (e), and the classified flooded regions for this image is shown in (f). Incidence angles for the subsets are shown in (c) and (e). Red and green arrows in (d) and (f) are examples where classification are different due to different incidence angles.

The dark regions on the Landsat subset of 6 May 2009 (Figure 4.26a) show the flooded extent. The dominant vegetation structure is tall open grassland, shown in Figure 4.26b. For the subset of 10 May 2009 the incidence angle ranges between 27° and 29° (Figure 4.26c). The areas with low backscatter were classified as flooded (Figure 4.26d). For the 11 May 2009 subset the incidence angle ranged between 36° and 38° and fewer areas had low backscatter corresponding to open water (Figure 4.26e). Therefore a slightly smaller extent was classified as flooded (Figure 4.26f). Additionally, for 10 May 2009, areas such as shown by the red arrow in Figure 4.26d had high backscatter return than the corresponding areas in 11 May 2009, shown by the green arrow in Figure 4.26f. This indicates that double bounce interaction between the flooded surface and stems is dominant for these areas in the 10 May 2009 subset, while volumetric scattering from the canopy layer is dominant for the same areas on the 11 May 2009 image.

The backscatter returns discussed in Figure 4.25 and Figure 4.26 could either be due to differences in the water levels as the flood progressed over the days, or the differences in incidence angle between the two image sets. If the main influence is the difference in water levels, the interactions can be explained by the increase in moisture (Bourgeau-Chavez et al. 2005). If the moisture increases, double-bounce scattering increases because of the ground-stem interaction for herbaceous vegetation (Bourgeau-Chavez et al. 2005). Yet if the vegetation is submerged by water, open water, specular reflection occurs over the water surface occurs and backscatter is low (Bourgeau-Chavez et al. 2005).

If the water level change is, however, negligible, as assumed to be in this section, incidence angle would have an impact on the received backscatter from the flooded regions. From Figure 4.25 and Figure 4.26, for steeper incidence angles, less interaction with the grassland and more interaction with the water is evident. Larger areas will therefore have low signal returns for the steeper incidence angles. The regions where the signal did interact with vegetation had higher backscatter for the steeper incidence angles than that of areas with shallower incidence angles, likely due to double bounce from the ground-stem interaction with the grasslands (Bourgeau-Chavez et al. 2005). When the incidence angles were shallower, a larger extent of the region had backscatter values resembling non-flooded vegetation, indicating diffuse reflection due to interaction with vegetation and not water (Hess, Melack & Simonett 1990).

Incidence angle also has an effect on flooded open water bodies that experience some form of disturbance over the water causing surface roughening, which in turn increases backscatter. Waterbodies will then be incorrectly classified as unflooded regions. The ASAR image of 24 March 2009 (Figure 4.27), for example, experienced severe surface roughness over a major portion of the flooded areas and was also one of the images with the poorest accuracy assessment results. The incidence angle for the areas which were most severely affected, was very low, ranging between 5° and 26°.

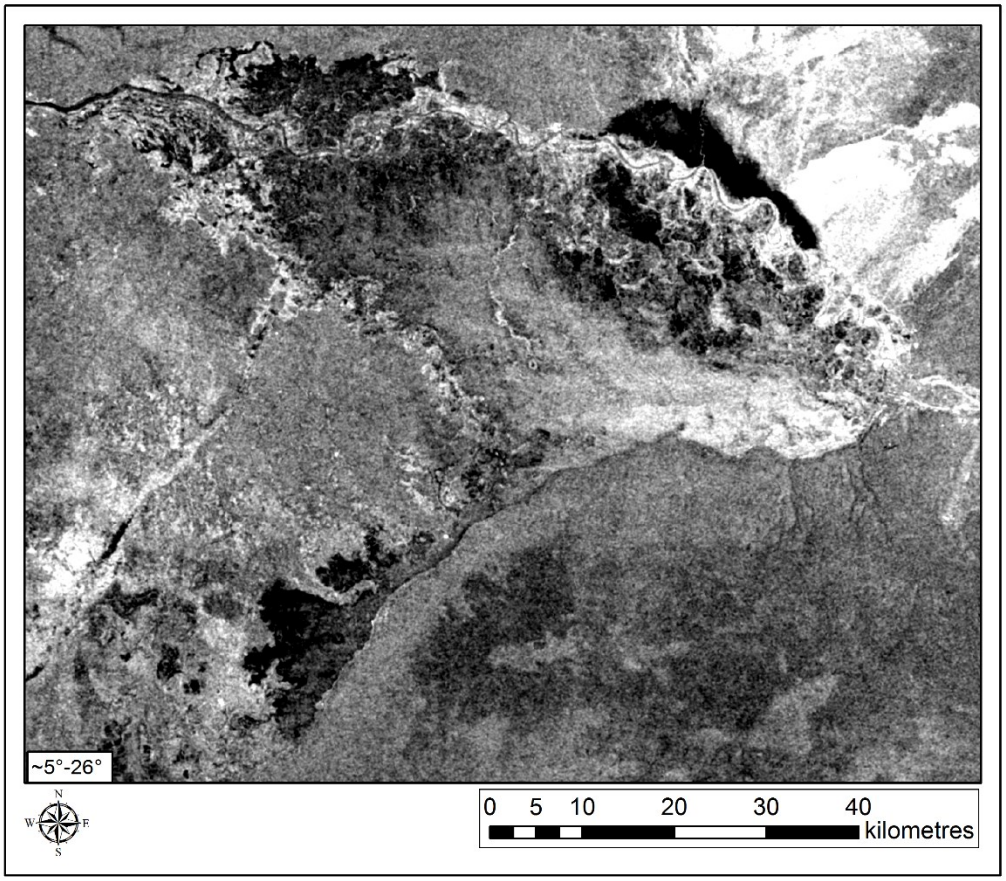

Figure 4.27: 24 March 2009, with steep incidence angles and severe surface attenuation had poor contrast between flooded and non-flooded areas.

The image of 17 March 2009 (Figure 4.28) also experienced surface roughness over open water areas, albeit not to the same severe extent as that of 24 March 2009. The incidence angle for the 17 March 2009 subset shown in Figure 4.28a ranged between 18° and 21° over open water body areas experiencing surface roughness. The region shown by the yellow arrow in the Landsat image (Figure 4.28b) is clearly flooded, while the same region on the ASAR image subset (shown by the red arrow in Figure 4.28a) has slightly higher backscatter than expected from open water due to the effect of disturbances over the open waters on the SAR image can be seen - despite the excessive cloud cover on the Landsat image.

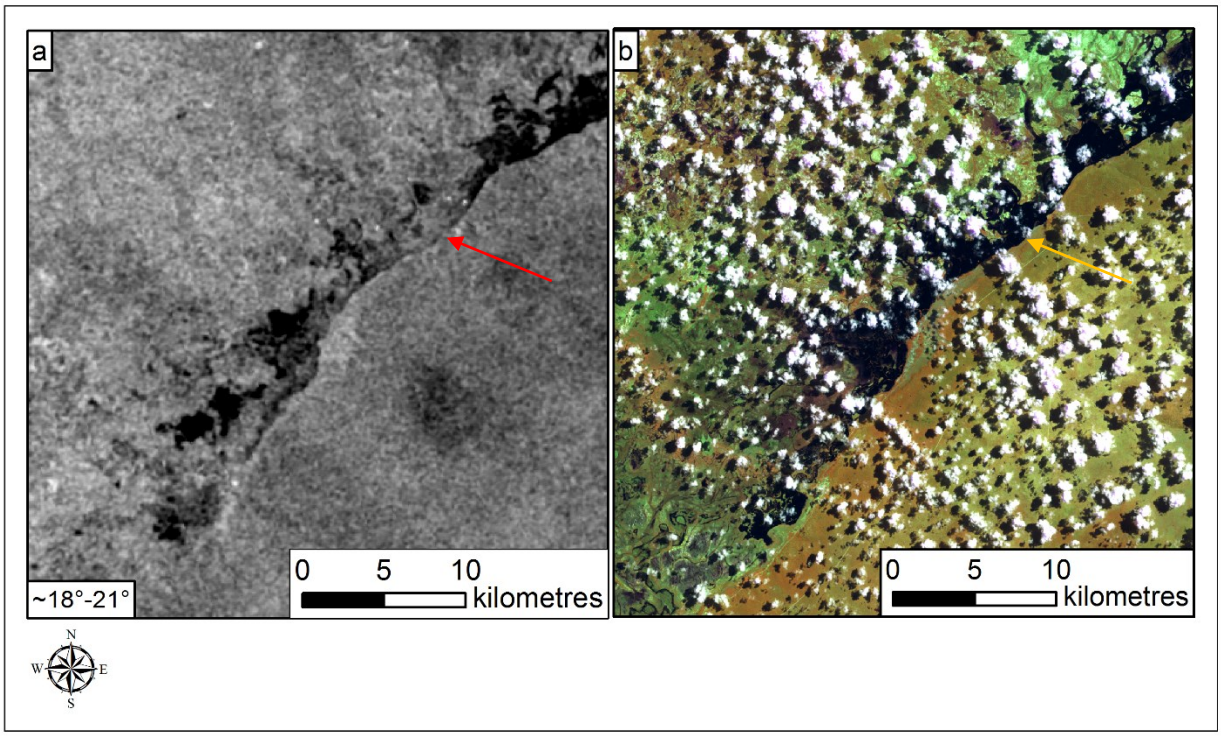

Figure 4.28: ASAR image of 17 March 2009 (a). When the flooded regions such as the area shown by the red arrow is compared to the Landsat image (such as the region shown by the yellow arrow) of 19 March 2009 (b). These areas had steep incidence angles and were sensitive to surface roughness.

A similar effect can be seen in Figure 4.29. For the ASAR image of 10 May 2009 (Figure 4.29a) some open water areas (as shown by the red arrow) had higher backscatter return than expected for open water due to surface roughness when compared to the Landsat image of 6 May 2009 in Figure 4.29b (as shown by the yellow arrow). The incidence angles for this subset ranged between 23° and 26°. The findings of Figure 4.27, Figure 4.28 and Figure 4.29 are consistent with the findings of Töyrä & Pietroniro (2005) – that steeper incidence angles are more sensitive to disturbances such as waves on water surfaces.

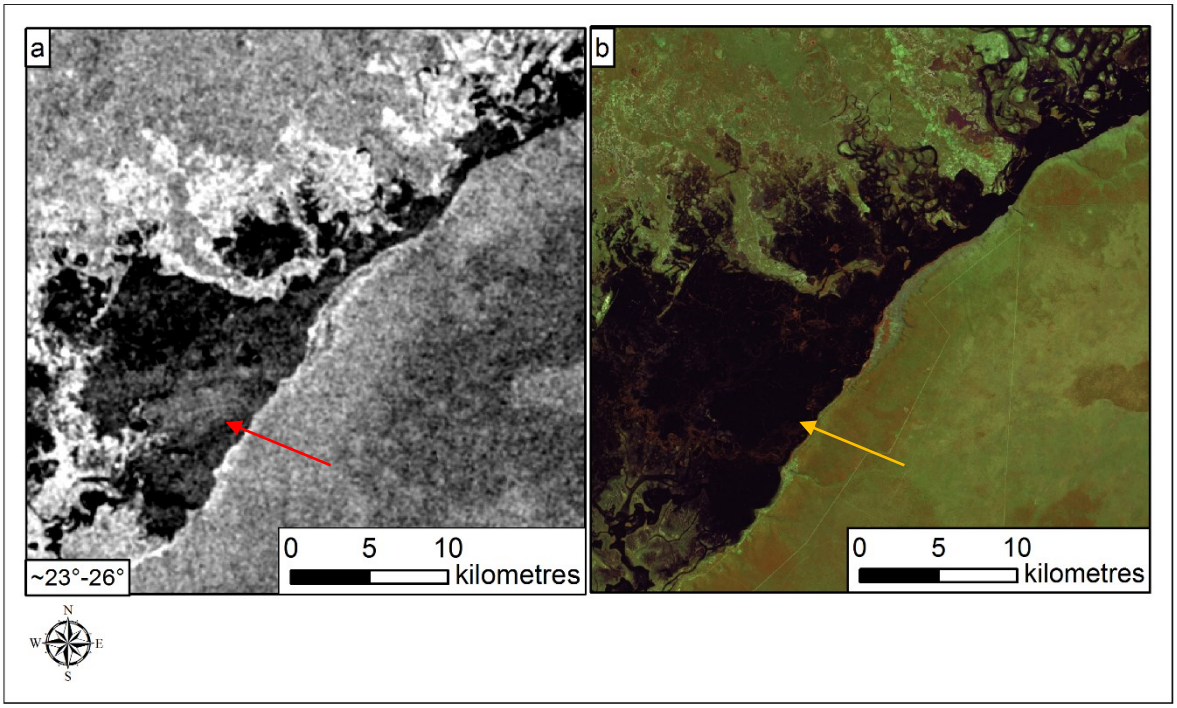

Figure 4.29: ASAR image of 10 May 2009 (a). When the flooded regions such as the area shown by the red arrow is compared to compared to the Landsat image of 6 May 2009 (b). These areas had steep incidence angles and were sensitive to surface roughness.

The PALSAR images cannot be compared in the same manner as that of the ASAR images, since all three sets of 2009 images have rather steep incidence angles ranging between 11° and 37°, and the incidence angles over the flooded areas do not change significantly enough to make justifiable comparisons about the differences between the three PALSAR sets. The effect of steep incidence angles, however, seems to be in agreement with prevailing literature. In the tall, closed woodland areas backscatter return is higher (see Figure 4.35a) due to greater interaction with the forest stems and water surface causing double bounce, and less canopy volume scattering (Hess, Melack & Simonett 1990; Wang et al. 1995).

In the tall, open grassland areas and the open water areas, specular reflection is prevalent and backscatter is low, indicating minimal interaction with vegetation. There are however noticeable differences at those areas based on polarisation, which will be discussed in section 4.2.4.

4.2.4 Polarisation

The PALSAR images are fully polarimetric and therefore the influence of polarisation on backscatter returns over flooded areas for these images can be assessed. Figure 4.30 and Figure 4.31 show the overall accuracy and kappa statistic for the different polarisations of the PALSAR image sets using thresholds; Figure 4.32 and Figure 4.33 show the overall accuracy and kappa statistic results of the different polarisations of the PALSAR image sets using ACMs.

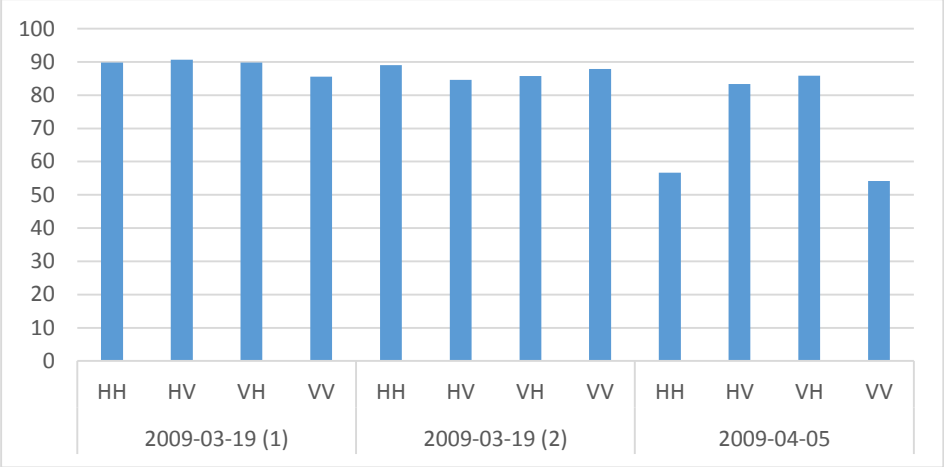

Figure 4.30: Overall accuracy for the different polarisations of each set of PALSAR images for the threshold classification method

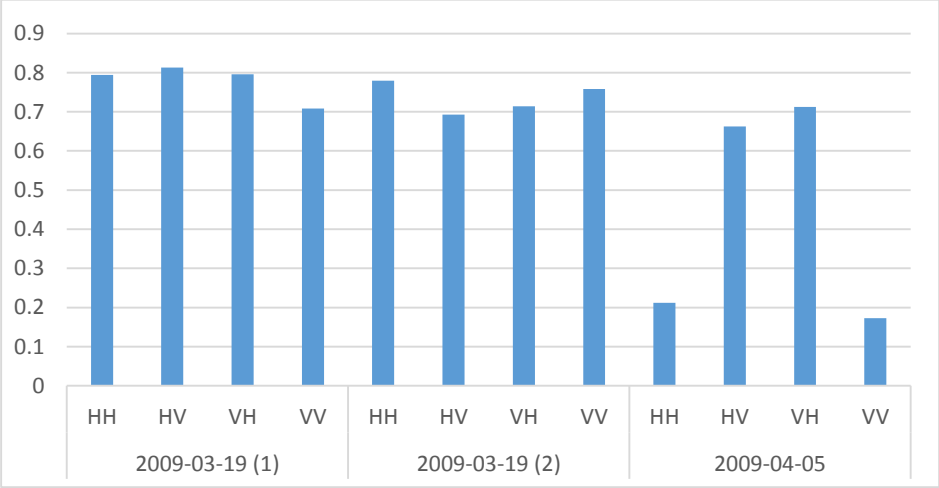

Figure 4.31: Kappa statistic for the different polarisations of each set of PALSAR images for the threshold classification method

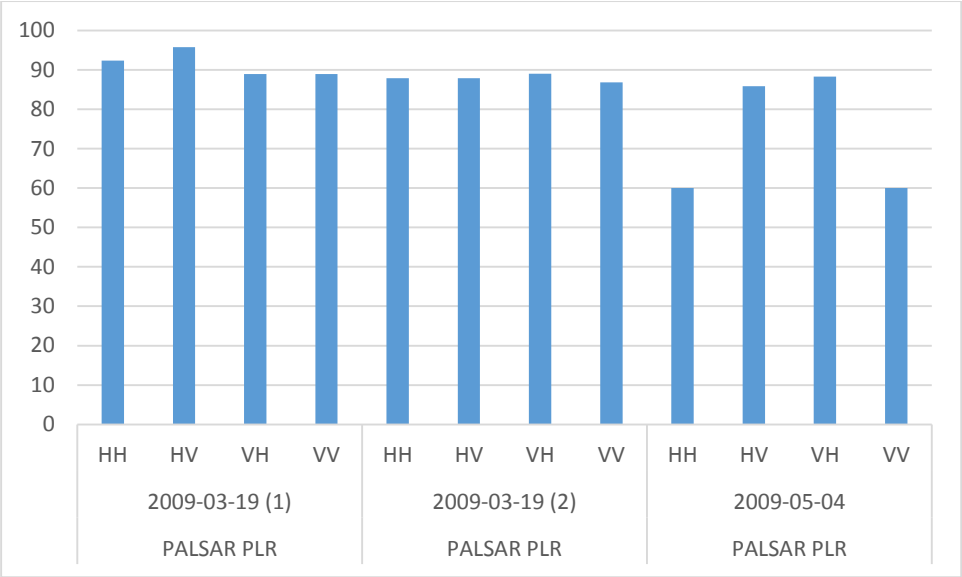

Figure 4.32: Overall accuracy for the different polarisations of each set of PALSAR images for the ACM classification method

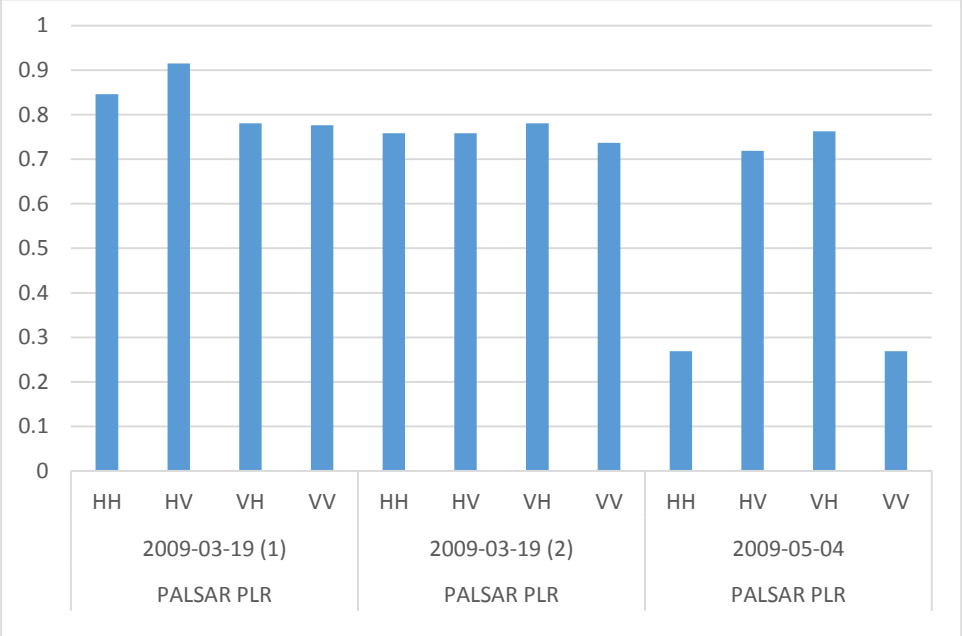

Figure 4.33: Kappa statistic for the different polarisations of each set of PALSAR images for the ACM classification method

When assessing the overall accuracy and kappa statistic results for both ACMs and thresholds, the classified HH-polarised and the VV-polarised images from 5 April have much lower overall accuracies and kappa values than the other images. The image set captured on 5 April 2009 was shown earlier in Figure 4.21 in section 4.2.2, where it was seen that a high backscatter return was received over a large portion of the flooded area for the like-polarised images. The main vegetation structure found in this area, as previously stated, is tall open grassland, and the flooded regions are therefore mostly flooded grasslands and open water areas.

The cross-polarised images showed no sensitivity to surface roughness over these areas, returning low backscatter values which were subsequently classified as flooded areas. The higher backscatter return was also found on the HH- and VV-polarised image from the first PALSAR image set captured on 19 March 2009 (see Appendix E for these maps). However, the affected flooded extent was no as large as that of the HH- and VV-polarised images of 5 April 2009 and the overall accuracy and kappa statistics was therefore not noticeably lower than those of the corresponding cross-polarised images.

This is consistent with the findings of Henry et al. (2006) that cross-polarised data are less sensitive to surface conditions such as surface roughness. Despite radiometric dynamics generally found to be lower for cross-polarisation (e.g. Henry et al. 2006) which usually leads to lower class separability, cross-polarised data can contribute to flood mapping information because of the lower sensitivity to surface roughness as seen from this study.

VV-polarisation exhibited highest sensitivity to surface roughness of all the polarisations, and experienced higher than expected backscatter returns over open waters, such as the Zambezi River, where the HH-polarised image had low signal returns (Figure 4.34). This is consistent with the findings of Henry et al. (2006) and Matgen et al. (2007) stating that VV-polarisation is the most sensitive polarisation mode to waves and ripples.

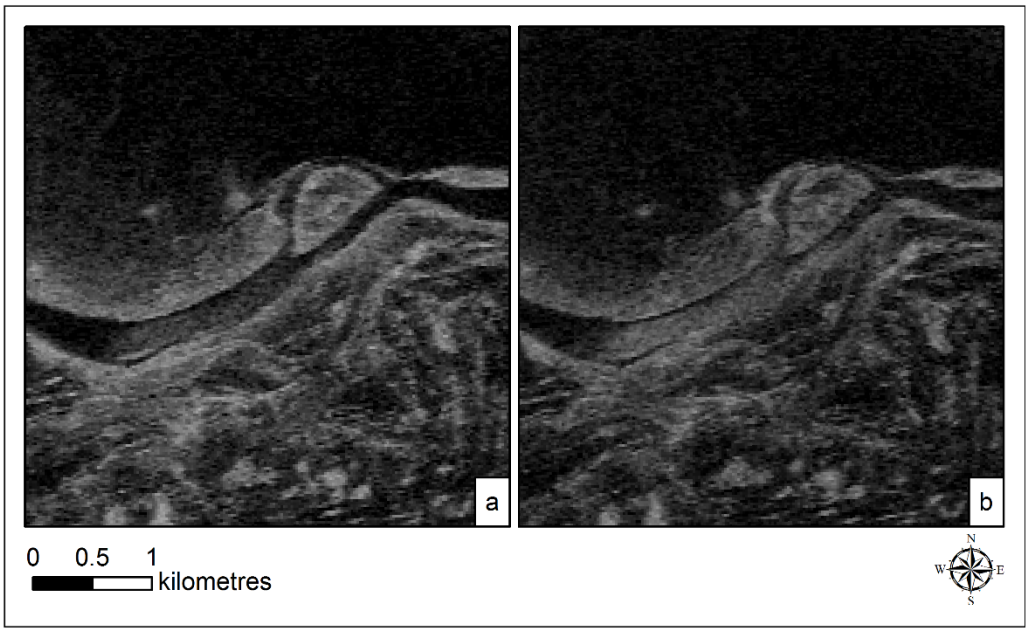

Figure 4.34: PALSAR image of 19 March 2009 (first set). The HH-polarised image (a) and VV-polarised image (b) shows a section of the Zambezi River. On the VV-polarised image, a slightly larger extent of the river has higher backscatter returns than the other polarisations, such as the HH-polarisation shown. VV-polarised images was the most sensitive to surface roughness. © ESA.

On the second set of PALSAR images captured on 19 March 2009, it appeared that there were not any higher returns over flooded water areas caused by surface roughness (See Appendix E for maps). On these images, the like-polarised images seemed to yield better results than cross-polarised images for the threshold classification, with HH-polarisation yielding the highest overall accuracy (89%). This substantiates literature arguing that HH-polarisation is well suited for discrimination between water and the surrounding land because of its better radiometric dynamic range and since the horizontal component of the signal receives lower backscatter values from the open water surface (Henry et al. 2006; Martinis, Twele & Voigt 2009).

For ACMs, however, the VH- polarised image (89%) had the highest overall accuracy, followed by the HH-polarised image (88%), but the difference of 1% between these two images is negligible and both like- and cross-polarisation images are useful for flood mapping.

Figure 4.35 below shows a subset of the PALSAR images captured on 5 April 2009 in HH-polarisation (Figure 4.35a), VV-polarisation (Figure 4.35b), HV-polarisation (Figure 4.35c) and VH-polarisation (Figure 4.35d). On the Landsat image (Figure 4.35e) flooded regions are the dark areas with low spectral signatures. The area is north of the Bukalo channel and the dominant vegetation structure is tall closed woodland (Figure 4.35f).

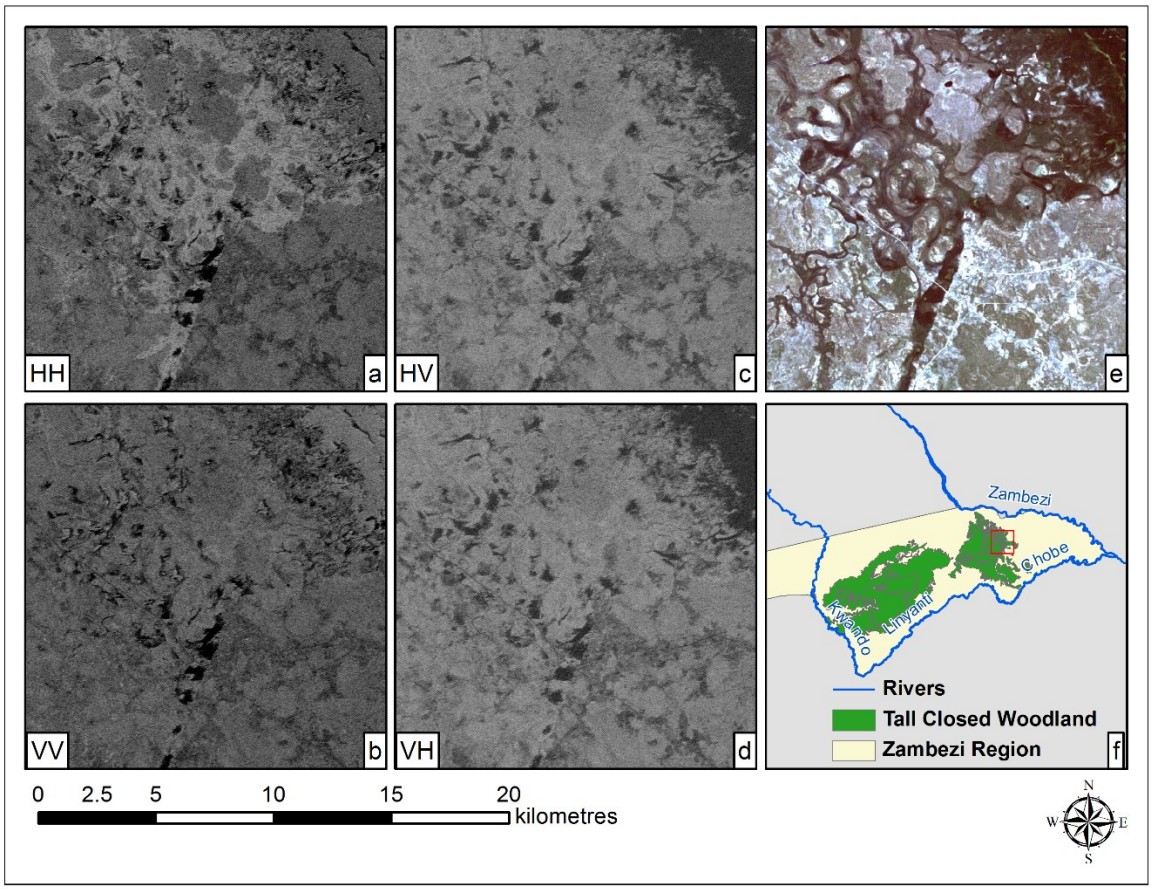

Figure 4.35: Area to the north of the Bukalo channel. HH-polarised image (Figure 4.35a), VV-polarised image (b), HV-polarised image (c) and VH-polarised image (d) captured on 5 April 2009. On the Landsat image of 20 April 2009 (e) dark areas are flooded. Dominant vegetation structure is tall closed woodland (f). © ESA.

Flooded vegetation in this area yielded high backscatter values areas and was therefore not classified as flooded area. The HH-polarised image (Figure 4.35a) is however the only polarisation where the contrast between flooded vegetation and non-flooded vegetation is markedly different and the flooded vegetation yields higher backscatter returns than the surrounding non-flooded vegetation. These high signal returns match the dark, flooded areas on the Landsat image of 20 April 2009 (Figure 4.35e). For all the other polarisations (VV-, HV- and VH- polarised images in Figure 4.35b, Figure 4.35c and Figure 4.35d) the flooded vegetation blends in too well with the surrounding non-flooded vegetation.

This means that if the methods employed in this study are refined to identify flooded forest flooded areas with higher signal return than the surrounding non-flooded regions, HH-polarisation would be best suited to identify those areas. This is consistent with Kasischke, Melack & Dobson (1997) that like-polarised data are preferred for mapping to identify flooded forested areas and HH-

polarisation is particularly well suited for flooded vegetated areas, since the difference between flooded and non-flooded forested area is most pronounced in HH-polarised images.

From this section it can be concluded that like-polarised images for L-band imagery are best suited for flood mapping purposes over dark water body surfaces with little or no disturbances which could lead to surface roughness, with HH-polarisation yielding the best results. However, The HV-polarised images yield better results when there are disturbances over open water surfaces, since it showed much less sensitivity towards surface roughness. HH-polarised images are also better for the identification of flooded woodland areas, since these areas have a much higher signal return than the surrounding non-flooded area, while no differences between these two classes are perceived in the other polarisations.

Therefore HH- and HV- polarisations should provide sufficient discriminatory power required for open water as well as flooded vegetation regions. For example, Sentinel-1 captures imagery in single polarisation (HH or VV) or dual polarisation (HH+HV or VV+VH). The recommended acquisition mode best suited for flood mapping of would therefore be the HH+HV dual polarisation mode. The methods would however need to be adapted to include flooded vegetation. This would mean including a high upper threshold value for the high signal returns when using thresholds, or an initial contour which identifies the high signal returns when using ACMs.

CHAPTER 5 CONCLUSION

In this chapter the main conclusions drawn from the study are summarised, the aim and objectives are revisited, the limitations of the study are discussed and recommendations are made for future research on flood extent classification in Zambezi Region.

5.1 REVISITING THE OBJECTIVES

The aim of this study was to evaluate the use of ENVISAT ASAR and ALOS PALSAR imagery to estimate open water flood boundaries in the Zambezi Region using two different classification algorithms on the SAR imagery, thereby dividing the image into flooded and non-flooded regions: ACMs and thresholds. This aim was to be achieved by setting and realising five research objectives. In this section, each objective is revisited and the findings of the previous chapters are summarised to determine if the objectives were attained.

Objective 1: Derive the flood extent from the SAR images using thresholds and ACMs

To achieve this objective, ASAR WSM and PALSAR PLR images captured during the 2009 floods in the eastern Zambezi Region were obtained. These images were subject to geometric and radiometric distortions and, subsequently, geometric and radiometric corrections as well as speckle filtering were performed to remove distortions during the pre-processing phase. The images were then classified, firstly using thresholds as classification method and then using ACMs as classification method. For thresholds, a number of threshold values were selected based on the histogram of each SAR images. For ACMs an initial contour for each SAR was derived using the Canny edge detector. The images were then segmented into flooded and non-flooded regions using the Chan-Vese ACM model in Matlab.

Objective 2: Qualitatively assess classified images obtained from thresholds and ACMs

For this objective the classified images were examined to determine if certain classification errors or trends for the classified SAR images were noticeable for each of the two different classification methods. While both methods yielded acceptable results when classifying open water bodies, there were some noticeable errors. It was found that on the PALSAR images, there were regions north of the Zambezi River which had low backscatter returns, resembling flooded open water regions. The spectral signatures of these regions, however, resembled vegetation on the reference Landsat

imagery and it was uncertain if these areas were flooded beneath the canopy. Field data or higher resolution imagery such as SPOT or aerial photographs could potentially clarify these areas.

When using thresholds for classification, features such as roads and airports were also classified as flooded areas due to their low backscatter. The threshold classification also included isolated noisy pixels from the SAR images into the flooded open water class. These pixels could however be removed if the methods were expanded to include a post-classification filtering to remove noise.

When using ACMs for the classification of flooded areas, some open water bodies with low backscatter returns were not segmented as flooded regions, possibly due to sensitivity to the placement of the initial contour or non-homogeneous backscatter intensities among the flooded regions. Other areas which were not open water areas but located near open water bodies and had slightly lower backscatter values than the surroundings were classified as non-flooded regions. This was probably due to the evolution of the initial contour which included these areas because of the slightly lower backscatter values before the segmentation process terminated. These errors could potentially be addressed through the selection of a better initial contour (such as an existing polygon of permanent water bodies) and fewer iterations.

Objective 3: Determine the accuracies of the two classification methods when compared to Landsat imagery

To achieve this objective, accuracy assessments were performed on the classified SAR images by extracting points from Landsat images with acquisition dates close to each SAR image. The overall accuracy, user's accuracy, producer's accuracy and kappa were then calculated to quantitatively assess the accuracy of each classified image. It was found that for threshold, highest overall accuracies were usually not attained at the local minimum, but 1.5 dB to 6 dB higher, most likely due to backscatter convolution between the two classes due to incidence angle not being taken into account. Results could be improved by segmenting the image into strips along the azimuth direction, extract the histogram and local minima for each of these subsets for classification purposes.

For the ASAR images, the best performing thresholds for each image ranged between -14 and -8.5 dB. The overall accuracy ranged between 70% and 99%. The user's and producer's accuracy for the flooded open water class ranged between 87% and 100%, and 58% and 97% respectively, while the user's and producer's accuracy for the non-flooded class ranged between

55% and 97% and 86% and 100% respectively. The kappa statistic varied between 0.44 and 0.97. When the active contour classification method was used for the classification of the ASAR images, overall accuracy ranged between 58% and 98%. The user's accuracy and producer's accuracy for the flooded class ranged between 74% and 100%, and 34% and 100% respectively, the user's accuracy and producer's accuracy for the non-flooded class between 47% and 100%, and 64% and 100% respectively. The kappa statistic varied between 0.27 and 0.96.

For PALSAR images, the best performing thresholds for each image ranged between -21 and -17 dB for the HH-polarised images, -27 and -24.5 dB for the HV-polarised image, -27.5 and -24.5 dB for the VH-polarised images and -21 and -19 dB for the VV-polarised image. The overall accuracy for all images ranged between 54% and 91%. The user's and producer's accuracy for the flooded open water class ranged between 82% and 97% and 26% and 91% respectively, while the user's and producer's accuracy for the non-flooded class ranged between 47% and 92% and 80% and 98% respectively. The kappa statistic varied between 0.17 and 0.81. When the active contour method was used for the classification of the PALSAR images, overall accuracy ranged between 60% and 96%.The user's and producer's accuracy for the flooded class ranged between 82% and 96%, and 34% and 96% respectively, while the user's accuracy and producer's accuracy for the non-flooded class fell between 51% and 95%, and 80% and 97% respectively. The kappa statistic varied between 0.27 and 0.91.

Accuracies were generally acceptable apart from a few images attenuated by surface roughness. From the assessment of the overall accuracy results, it can be concluded that the threshold classification method performed slightly better for ASAR images, while the ACM classification method performed slightly better for the PALSAR images, but differences were marginal. Despite the large amount of variation in the user's and producer's accuracies, both methods of classification yield acceptable accuracies for flood extent delineation of open water bodies. Ultimately, the sensor properties such as wavelength, polarisation and incidence angle, are more important than the method of classification in this study.

Objective 4: Determine the impact of sensor parameters on classification results

To reach this objective, the results were qualitatively assessed by comparing different SAR images to each other and to Landsat images to determine whether any differences in backscatter could be detected based on wavelength, incidence angle and polarisation.

It was found that the longer wavelengths were better suited for open water detection than the shorter C-band. In the areas with more herbaceous vegetation, such as grassland regions or cultivated lands seen in this study, the PALSAR image with L-band wavelength, interacted less with the vegetation in the area and backscatter returns were low because of specular reflection. The ASAR images had high backscatter return because of interaction with the vegetation. For the woodland areas both ASAR and PALSAR images had high backscatter returns. The methods employed in this study therefore need to be extended to include flooded vegetation.

Incidence also had an impact on flood extent delineation in this region. For the open water bodies, shallower incidence angles yielded better classification results. For grassland areas, if differences in water level are negligible between the two acquisition dates of the ASAR images, dark backscatter returns were more prevalent at steeper incidence angles, indicating more interaction with water and less interaction with vegetation. At shallower incidence angles, backscatter was higher, indicating interaction with vegetation and not water. Therefore, steeper incidence angles are preferred for classification of flooded grassland regions if dark water bodies are to be identified.

For the flooded woodland areas, backscatter return was higher than during dry conditions. The methods therefore need to be adapted to classify these areas. Steeper incidence angles would then be better suited to include these areas since the path length of the signal is shorter and the attenuation and volumetric scattering from the canopy layer is therefore less and double bounce between the water surface and the trunk is more prevalent. At shallower incidence angles, there is more volumetric scattering because of interaction with the canopy and not the flooded surface, making flooded-woodland less distinguishable from non-flooded woodland.

When polarisations were compared, HH-polarised was the best polarisation to distinguish between flooded and non-flooded regions when there was no disturbance over the flooded area. For flooded woodland areas, HH-polarisation was the only polarisation where a higher backscatter return than the surrounding non-flooded area was recorded, while little difference between these two classes was perceived in the other polarisations. However, HV-polarisation was better suited for flood extent delineation in the open water areas when surface roughness was present. VV-polarisation was found to be the most sensitive polarisation mode to waves and ripples. A combination of HH- and HV- polarisations should provide sufficient discriminatory power required for open water as well as flooded vegetation regions but the methods would however need to be adapted to include flooded vegetation.

Objective 5: Synthesize the results and assess the suitability of SAR-based flood mapping using the techniques and sensors employed

Despite the problems encountered, SAR yielded high overall accuracies for both classification methods when identifying open water. SAR images, with the unique ability to operate day and night, not being severely attenuated by inclement weather and the ability to detect inundation between forest canopies provide advantages for flooded extent delineation in a complex area such as the Zambezi Region. Although the sensor parameters had a significant impact on classification results, images from both SAR systems could be used to adequately map inundated areas. It was found that the method of classification used in this study was less important than the sensor parameters. It was found for open water areas: longer wavelengths and shallower incidence angles yielded the best results. For flooded vegetation: steeper incidence angles yielded more contrast between flooded and non-flooded areas due to an increase in double bounce.

5.2 LIMITATIONS AND RECOMMENDATIONS

It is necessary to highlight certain limitations of the study, particularly regarding the impact of vegetation in the study area, the selected methods of classification, and the selected method of accuracy assessment.

For this research, the assumption was that the SAR images can be divided into two classes only, namely flooded and non-flooded regions. This assumption works well if the only flooded regions are open water bodies with low backscatter return and contrast between dry areas with higher backscatter. The Zambezi Region, however, is a complex area with different vegetation structures, ranging from grassland to woodland areas, which had an impact on the backscatter return depending on the wavelength, incidence angle and polarisation. For the PALSAR images, flooded woodland areas had higher backscatter return during dry conditions, while backscatter return for both flooded grassland and flooded woodland areas was higher than during non-flooded regions for the ASAR image.

Discerning these areas from other non-flooded areas with high backscatter using Landsat images, however, proved to be difficult. The spectral signature from the Landsat images was a mixture between vegetation and water for some regions, but for other areas with high backscatter returns

on the SAR images, the spectral signatures on the Landsat images matched only vegetation. This does not necessarily mean that water is not present. It could be that water signatures were not captured since they are below the vegetation canopy. For these areas, the Landsat images were therefore not well-suited for validation purposes. Optical sensors with higher spatial resolution could potentially be better suited to determine whether these areas are flooded or not, or field observations could potentially be better suited for validation data.

Additionally, in this study only backscatter properties were used to determine flooded regions, which not only caused difficulties with the flooded vegetation, but also some non-flooded areas with low backscatter. The non-flooded areas with low backscatter were erroneously included in the flooded class. Additional measures therefore be taken to improve classification accuracies. Either a combination of properties of optical and SAR images can be used for differentiation or a multi-temporal approach to classification can be followed to identify areas which underwent a net increase or decrease in backscatter return.

The number of days between the acquisition dates of the ASAR 23 March 2009 images and the reference Landsat image of 27 2009 March was also a limitation since floodwaters along the boundaries led to a high error of omission for the flooded class and a high error of commission for the non-flooded class. Possible solutions would be to obtain different imagery closer to the capture date of the ASAR image.

Another limitation was the selection of the initial contour for ACMs. The contours showed much sensitivity to their initial states and not all waterbodies were always segmented into the flooded class. The Canny edge detector is therefore not an ideal initial contour and it is therefore recommended that that a water mask, as suggested by Voigt et al. (2008) is used. The Canny edge detector did however yield good results and would be effective if no water mask is available.

5.3 CONCLUDING REMARKS

This research was undertaken to assess the suitability of using SAR imagery for flood extent delineation. The aim was to evaluate the use of ENVISAT ASAR and ALOS PALSAR imagery to estimate open water flood boundaries in the Zambezi Region using both thresholds and ACMs classification algorithms on the SAR imagery, thereby dividing the image into flooded and non-flooded regions. The aim was realised by setting five main objectives which were realised through the methods employed. It was found that despite the limitations addressed in this chapter, SAR images can effectively delineate flooded open water bodies with the two selected methods. It is

especially advantageous during inclement weather when cloud cover proves problematic for optical images. However, wavelength, polarisation and incidence angle of SAR images are important variables which impact classification results.

This study found that longer wavelengths, shallower incidence angles and HH- and HV-polarisations would generally yield best results for the classification of open water bodies, when using only backscatter information. When flooded vegetation regions are also present, steeper incidence angles will be better to increase separability between flooded and non-flooded vegetation. The combination of wavelength, incidence angle and polarisation which would yield the most robust classification results for open water detection would therefore be L-band images, with shallower incidence angles between about 30° and 40° and a combination of HH- and HV-polarisation. While both methods yield good results, thresholds would be a better choice for rapid flood extent delineation since it yields robust results. It is a relatively simple method to use and is not computationally demanding. While ACMs yielded good results, it was done in Matlab and would depend on the software availability.

It is recommended that future research undertakes either a multi-temporal approach, whereby an image during flooded conditions as well as a non-flooded reference image is incorporated to detect change in backscatter returns during flooded conditions, or a combination of SAR and optical imagery be used for flood estimation. The combination of these two image types will make use the advantages of both methods while the limitations of these two approaches will be minimised.

[31856 words]

REFERENCES

Adelekan, IO 2010. Vulnerability of poor urban coastal communities to flooding in Lagos, Nigeria. *Environment & Urbanization*. 22, 2: 433–450.

Ahern M, Kovats RS, Wilkinson P, Few R & Matthies F 2005. Global health impacts of floods: epidemiologic evidence. *Epidemiologic reviews* 27, 1: 36-46.

Aguilar E, Peterson TC, Obando PR, Frutos R, Retana JA, Solera M, Soley J, García IG, Araujo RM, Santos AR & Valle VE 2005. Changes in precipitation and temperature extremes in Central America and northern South America, 1961–2003. J*ournal of Geophysical Research: Atmospheres (1984–2012)* 110, D23.

Allaby M 2003. *Floods*. New York: Facts on File.

Alsdorf DE, Rodríguez E & Lettenmaier DP 2007. Measuring surface water from space. *Reviews of Geophysics* 45, 2.

Anyamba A, Chretien JP, Small J, Tucker CJ & Linthicum KJ 2006. Developing global climate anomalies suggest potential disease risks for 2006–2007. International journal of health geographics 5, 1: 60.

Appia V & Yezzi A 2011. *Active geodesics: Region-based active contour segmentation with a global edge-based constraint*. Proceedings of the IEEE International Conference on Communications held 5-9 June 2011. Kyoto: IEEE.

Bartsch A, Trofaier AM, Hayman G, Sabel D, Schlaffer S Clark DB & Blyth E 2012. Detection of open water dynamics with ENVISAT ASAR in support of land surface modelling at high latitudes. *Biogeosciences* 9, 2: 703-714.

Bates, BC, Kundzewicz ZW, Wu S & Palutikof JP (eds) 2008. Climate change and water. Technical paper of the Intergovernmental Panel on Climate Change. Geneva: IPCC Secretariat

Bazi Y, Bruzzone L & Melgani F 2005. An unsupervised approach based on the generalized Gaussian model to automatic change detection in multitemporal SAR images. *IEEE Transactions on Geoscience and Remote Sensing,* 43, 4: 874-887.

Beilfuss R 2012. A risky climate for southern African hydro: assessing hydrological risks and consequences for Zambezi River Basin dams. Berkeley (CA): International Rivers.

Bell FG 2004. *Engineering Geology and Construction*. New York: Spoon Press.

Benz UC, Hofmann P, Willhauck G, Lingenfelder I & Heynen M 2004. Multi-resolution, object-oriented fuzzy analysis of remote sensing data for GIS-ready information. *ISPRS Journal of Photogrammetry and Remote Sensing* 58, 3: 239-258.

Blaschke T 2010. Object based image analysis for remote sensing. *ISPRS Journal of Photogrammetry and Remote Sensing* 65, 1: 2-16.

Bourgeau-Chavez LL, Smith KB, Brunzell SM, Kasischke ES, Romanowicz EA & Richardson CJ 2005. Remote monitoring of regional inundation patterns and hydroperiod in the Greater Everglades using Synthetic aperture radar. *Wetlands* 25, 1: 176-191.

Bourgeau-Chavez LL, Riordan K, Powell R, Miller N & Nowels M 2009. Improving Wetland Characterization with Multi-Sensor, Multi-Temporal SAR and Optical/Infrared Data Fusion. In Jedlovec G (ed) Advances in geoscience and remote sensing, 679-708 Vukovar: InTech.

Bouwer LM, Crompton RP, Faust E, Höppe P & Pielke Jr RA 2007. Confronting disaster losses. Science, 318, 5851: 753.

Bouwer, LM 2011. Have disaster losses increased due to anthropogenic climate change? *Bulletin of the American Meteorological Society* 92, 1: 39-46.

Bradshaw CJ, Sodhi NS, Peh KSH & Brook BW 2007. Global evidence that deforestation amplifies flood risk and severity in the developing world. *Global Change Biology* 13, 11: 2379-2395.

Brauch HG 2003. Urbanization and Natural Disasters in the Mediterranean: Population Growth and Climate Change in the 21st Century. In Kreimer A, Arnold M & Carlin A (eds) *Building safer cities: the future of disaster risk*. Washington DC: World Bank Publications

Brivio PA, Colombo R, Maggi M & Tomasoni R 2002. Integration of remote sensing data and GIS for accurate mapping of flooded areas. *International Journal of Remote Sensing* 23, 3 429-441.

Liu Z, Wang J & Zhu Y 2015. A study of active contour segmentation models based on automatic initial contour. *International Journal of Signal Processing, Image Processing and Pattern Recognition* 8, 4: 201-214.

Campbell JB & Wynne RH 2011. *Introduction to Remote Sensing* 5th ed. New York: The Guilford Press.

Canny J 1986. A computational approach to edge detection. Pattern Analysis and Machine Intelligence. *IEEE Transactions* 6: 679-698.

Carey M 2005. Living and dying with glaciers: people's historical vulnerability to avalanches and outburst floods in Peru. *Global and planetary change* 47, 2: 122-134.

Cavallo EA & Noy I 2009. The economics of natural disasters: a survey [online]. RES Working Papers 4649, Inter-American Development Bank, Research Department. Available from: https://ideas.repec.org/p/idb/wpaper/4649.html [Accessed 8 July 2015].

Chan TF & Vese L 2001. Active contours without edges. *IEEE transactions on image processing* 10, 2: 266-277.

Chase MJ & Griffin CR 2009. Elephants caught in the middle: impacts of war, fences and people on the elephant distribution and abundance in the Caprivi Strip, Namibia. *African Journal of Ecology* 472: 223-233.

Cleveland WS 1979. Robust locally weighted regression and smoothing scatterplots. *Journal of the American statistical association* 74,368: 829-836.

Collins M, Knutti R, Arblaster J, Dufresne JL, Fichefet T, Friedlingstein P, Gao X, Gutowski WJ, Johns T, Krinner G, Shongwe M, Tebaldi C, Weaver AJ & Wehner M 2013: Long-term climate change: Projections, commitments and irreversibility. In Stocker T, Qin D, Plattner GK, Tignor M, Allen SK, Boschung J, Nauels A, Xia Y, Bex V, Midgley PM (eds) *Climate Change 2013: The Physical Science Basis. Contribution of Working Group I to the Fifth Assessment Report of the Intergovernmental Panel on Climate Change*. Cambridge University Press.

Dallemand JF, Lichtenegger J, Raney RK, & Schumann R 1993. Radar imagery: theory and interpretation. Lecture notes. RSC Series: FAO.

Darby SE 1999. Effect of riparian vegetation on flow resistance and flood potential. *Journal of Hydraulic* Engineering 125, 5: 443-454.

De Groeve T & Riva P 2009. *Global real-time detection of major floods using passive microwave remote sensing*. Proceedings of the 33rd International Symposium on Remote Sensing of Environment held 4-8 May 2009 Stresa: International Center for Remote Sensing of Environment and the Joint Research Centre of the European Commission

De Roo A, Van Der Knijff J, Horritt M, Schmuck G and De Jong SM 1999. *Assessing flood damages of the 1997 Oder flood and the 1995 M euse flood*. Proceedings of the Second International ITC Symposium on Operationalization of Remote Sensing held 16-20 August 1999. Enschede: International Institute for Aerospace Survey and Earth Sciences (ITC) - Division of Applied Geomorphological Surveys.

Di Baldassarre G, Montanari A, Lins H, Koutsoyiannis D, Brandimarte L & Blöschl G 2010. Flood fatalities in Africa: from diagnosis to mitigation. *Geophysical Research Letters* 37, 22: L22402.

Diallo A Ndam NT, Moussiliou A, Dos Santos S, Ndonky A, Borderon M, Oliveau S, Lalou R & Le Hesran JY 2012. Asymptomatic carriage of Plasmodium in urban Dakar: the risk of malaria should not be underestimated. *PLoS One* 7, 2.

Dietrich JC, Bunya S, Westerink JJ, Ebersole BA, Smith JM, Atkinson JH, Jensen R, Resio DT, Luettich RA, Dawson C, Cardone VJ, Cox AT, Westering HJ & Roberts HJ 2010. A high-resolution coupled riverine flow, tide, wind, wind wave, and storm surge model for southern Louisiana and Mississippi. Part II: Synoptic description and analysis of Hurricanes Katrina and Rita. *Monthly Weather Review* 138, 2: 378-404.

Dobson MC, Ulaby FT, Pierce LE, Sharik, TL, Bergen KM, Kellndorfer J & Siqueira P 1995. Estimation of forest biophysical characteristics in northern Michigan with SIR-C/X-SAR. *IEEE Transactions on Geoscience and Remote Sensing* 33, 4: 877-895.

Doocy S, Daniels A, Murray S & Kirsch TD 2013. The Human Impact of Floods: a Historical Review of Events 1980-2009 and Systematic Literature Review. *PLOS Currents* 5.

Douglas I, Alam K, Maghenda M, Mcdonnell Y, McLean L, & Campbell J 2008. Unjust waters: climate change, flooding and the urban poor in Africa. *Environment and Urbanization* 20, 1: 187-205.

Drake B & Shuchman RA 1974. *Feasibility of Using Multiplexed SLAR Imagery for Water Resources Management and Mapping Vegetation Communities*. Proceedings of the 9th International Symposium on Remote Sensing of Environment held 15-19 April. Michigan: Environmental Research Institute of Michigan.

Dunne T & Leopold LB 1978. *Water in environmental planning*. San Francisco: WH Freeman

Dussaillant A, Benito G, Buytaert W, Carling P, Meier C & Espinoza F 2010. Repeated glacial-lake outburst floods in Patagonia: an increasing hazard? Natural hazards 54, 2: 469-481.

ECLAC (Economic Commission for Latin America and the Caribbean) 2003. *Handbook for estimating the socio-economic and environmental effects of disaster*. Mexico City: ECLAC [online]. Available from: http: //www.eclac.org/publicaciones/xml/4/12774/lcmexg5i_VOLUME_Ia. pdf [Accessed 5 June 2015].

El-Darymli K, Mcguire P, Gill E, Power E & Moloney C. *Understanding the significance of radiometric calibration for synthetic aperture radar imagery*. Proceedings of the IEEE Canadian Conference on Electrical and Computer Engineering (CCECE) held 4. 4-7 May. Toronto: IEEE Canada.

Embleton C & Embleton-Hamann C 1997. *Geomorphological hazards of Europe*. Amsterdam, New York: Elsevier.

Emmert-Streib F 2009. *Information theory and statistical learning*. New York; London: Springer

ESA (European Space Agency) 2013. Eoportal (Earth Observation portal) [online]. Available from: http://services.eoportal.org/web/guest/sse-services [Accessed August – September 2013].

ESA (European Space Agency) 2014. RADAR and SAR Glossary [online]. Available from: https://earth.esa.int/handbooks/asar/CNTR5-2.html#eph.asar.gloss.radsar:CORNER_REFLECT [Accessed 7 January 2015].

Espinoza JC, Ronchail J, Guyot JL, Junquas C, Drapeau G, Martinez JM, Santini W, Vauchel P, Lavado W, Ordoñez J & Espinoza R 2012. From drought to flooding: understanding the abrupt

2010–11 hydrological annual cycle in the Amazonas River and tributaries. Environmental Research Letters 7: 1-7.

European Commission 2007. Directive 2007/60/EC of the European Parliament and of the council of 23 October 2007 on the assessment and management of flood risks [online]. Available from: http://eurlex.europa.eu/LexUriServ/LexUriServ.do?uri=OJ:L:2007:288:0027:0034:EN:PDF [Accessed 20 November 2015].

Euripidou, E & Murray V 2004. Public health impacts of floods and chemical contamination. *Journal of Public Health*, 26, 4: 376-383.

Field CB (ed) 2012. *Managing the risks of extreme events and disasters to advance climate change adaptation: special report of the intergovernmental panel on climate change*. Cambridge University Press.

Fisher R, Perkins S, Walker A and Wolfart E 2003. Canny Edge Detector [online]. Available from: http://homepages.inf.ed.ac.uk/rbf/HIPR2/canny.htm [Accessed 4 October 2014].

Freeman A 1992. SAR calibration: An overview. Geoscience and Remote Sensing, *IEEE Transactions on* 30, 6: 1107-1121.

Gautam KP & van der Hoek EE 2003. *Literature study on environmental impact of floods*. Delft Cluster.

Giacomelli A, Mancini M, & Rosso R. 1995. Assessment of flooded areas from ERS-1 PRI data: An application to the 1994 flood in Northern Italy. *Physics and Chemistry of the Earth* 20, 5: 469-474.

Giorgi F 2006. Climate change hot-spots. *Geophysical research letters* 33, 8.

Gong P, Marceau DJ and Howarth PJ 1992. A comparison of spatial feature extraction algorithms for land-use classification with SPOT HRV data. *Remote sensing of environment* 40, 2: 137-151.

Hahmann T & Wessel B 2010. *Surface water body detection in high-resolution TerraSAR-X data using active contour models*. Proceedings of the 8th European Conference on Synthetic Aperture Radar held 7-10 June 2010. Aachen: Association for Electrical, Electronic &Information Technologie VDE.

Haylock MR, Peterson TC, Alves LM, Ambrizzi T, Anunciação YM, Baez J, Barros VR, Berlato MA, Bidegain M, Coronel G & Corradi V 2006. Trends in total and extreme South American rainfall in 1960-2000 and links with sea surface temperature. Journal of climate 19, 8: 1490-1512.

Henderson, FM 1995. Environmental factors and the detection of open surface water areas with X-band radar imagery. *International Journal of Remote Sensing* 16, 13: 2423-2437.

Henry JB, Chastanet P, Fellah K & Desnos YL 2006. Envisat multi-polarized ASAR data for flood mapping. *International Journal of Remote Sensing* 27, 10: 1921-1929.

Heremans R, Willekens A, Borghys D, Verbeeck B, Valckenborgh J, Acheroy M & Perneel C 2003. *Automatic detection of flooded areas on ENVISAT/ASAR images using an object-oriented classification technique and an active contour algorithm*. Proceedings of the IEEE Conference on Recent Advances in Space Technologies held 20-22 November 2003, Istanbul: IEEE.

Hess LL, Melack JM, & Simonett DS 1990. Radar detection of flooding beneath the forest canopy: a review. *International Journal of Remote Sensing* 11, 7: 1313-1325.

Holden J 2012. *An introduction to physical geography and the environment* 3rd ed. Halrow: Pearson Education

Holecz F, Meier E, Piesbergen J, Wegmüller U & Nüesch D 1994. *Radiometric calibration of airborne SAR imagery*. Proceedings of the International Geoscience and Remote Sensing Symposium (IGARSS'94). Surface and Atmospheric Remote Sensing: Technologies, Data Analysis and Interpretation held 8-12 August 1994. Pasadena: IEEE.

Holloway A, Chasi V, de Waal J, Drimie S, Fortune G, Mafuleka G, Morojele M, Penicela Nhambiu B, Randrianalijaona M, Vogel C and Zweig P 2013. *Humanitarian Trends in Southern Africa: Challenges and Opportunities*. Southern Africa: Regional Interagency Standing Committee (RIASCO).

Horritt, MS 1999. A statistical active contour model for SAR image segmentation. *Image and Vision Computing* 17: 213–224.

Horritt MS, Mason DC & Luckman AJ 2001. Flood boundary delineation from synthetic aperture radar imagery using a statistical active contour model. *International Journal of Remote Sensing* 22, 13: 2489-2507.

Horritt MS, Mason DC, Cobby DM, Davenport IJ & Bates PD 2003. Waterline mapping in flooded vegetation from airborne SAR imagery. *Remote Sensing of Environment* 85 271-281.

Huntington TG 2006. Evidence for intensification of the global water cycle: review and synthesis. *Journal of Hydrology* 319, 1: 83-95.

Ivers LC & Ryan ET 2006. Infectious diseases of severe weather-related and flood-related natural disasters. *Current opinion in infectious diseases* 19, 5: 408-414.

Isunju JB, Orach CG & Kemp J (in press). Hazards and vulnerabilities among informal wetland communities in Kampala, Uganda. Environment & Urbanization.

Jha AK, Bloch R & Lamond J 2012. *Cities and flooding: a guide to integrated urban flood risk management for the 21st century*. Washington DC: World Bank Publications.

Jongman B, Ward PJ & Aerts JC 2012. Global exposure to river and coastal flooding: Long term trends and changes. *Global Environmental Change* 22, 4: 823-835.

Jonkman SN 2005. Global perspectives on loss of human life caused by floods. *Natural Hazards* 34, 2: 151-175.

Kasischke ES & Bourgeau-Chavez LL 1997. Monitoring South Florida wetlands using ERS-1 SAR imagery. *Photogrammetric Engineering and Remote Sensing* 63, 3: 281-291

Kasischke ES, Melack JM & Dobson MC 1997. The use of imaging radars for ecological applications: A review. *Remote Sensing of Environment* 59: 141-156.

Kass M, Witkin A, & Terzopoulos D 1988. Snakes: Active contour models. *International journal of computer vision* 1, 4: 321-3.

Kellndorfer JM, Dobson MC & Ulaby FT 1996. *Geocoding for classification of ERS/JERS-1 SAR composites*. Proceedings of the International Geoscience and Remote Sensing Symposium (IGARSS '96) held 31 May 1996. Lincoln: IEEE.

Kemp JN 2010. The application of multi-source remote sensing for sediment transport mapping in an intertropical context (La Réunion Island and South Africa). Doctoral dissertation. Réunion: University of La Réunion.

Kundzewicz ZW, Mata LJ, Arnell NW, Döll P, Jiménez B, Miller K, Oki T, Şen Z & Shiklomanov I 2007. Freshwater resources and their management. In Parry ML, Canziani OF, Palutikof JP, van der Linden PJ & Hanson CE (eds) *Climate Change 2007: Impacts, Adaptation and Vulnerability. Contribution of Working Group II to the Fourth Assessment Report of the Intergovernmental Panel on Climate Change*. Cambridge: Cambridge University Press.

Kundzewicz ZW, Mata LJ, Arnell NW, Döll P, Jimenez B, Miller K, Oki T, Şen Z & Shiklomanov I 2008. The implications of projected climate change for freshwater resources and their management. *Hydrological Sciences Journal* 53, 1: 3-10.

Kundzewicz, ZW 2011. Nonstationarity in Water Resources–Central European Perspective. *Journal of the American Water Resources Association* 47, 3: 550–562.

Kundzewicz ZW, Plate EJ, Rodda HJE, Rodda JC, Schellnhuber HJ & Strupczewski WG 2012. Changes in Flood Risk – Setting the Stage. In Kundzewicz ZW (ed) *Changes in Flood Risk in Europe* 11-26. Wallingford: IAHS Press.

Kundzewicz ZW, Kanae S, Seneviratne SI, Handmer J, Nicholls N, Peduzzi P. Reinhard Mechler R, Bouwer LM, Arnell N, Mach, K, Muir-Wood, R, Brakenridge, GR, Kron W, Benito G,

Honda Y, Takahashi K & Sherstyukov B 2014. Flood risk and climate change: global and regional perspectives. *Hydrological Sciences Journal* 59, 1: 1-28.

Kussul N, Shelestov A and Skakun S 2008. Grid system for flood extent extraction from satellite images. *Earth Science Informatics* 1:3-4: 105-117.

Landis JR & Koch GG 1977. The measurement of observer agreement for categorical data. *Biometrics* 33: 159-174.

Lang MW, Townsend PA & Kasischke ES 2008. Influence of incidence angle on detecting flooded forests using C-HH syntheticaperture radar data. *Remote Sensing of Environment* 112: 3898-3907.

Leopold LB 1994. *A View of the River*. Cambridge: Harvard University Press.

Lie J, Lysaker M & Tai XC 2006. A binary level set model and some applications to Mumford-Shah image segmentation. *Image Processing, IEEE Transactions on* 15,5: 1171-1181.

Lillesand, Kiefer & Chipman 2008. *Remote sensing and image interpretation* 6th ed. Hoboken: John Wiley & Sons.

Long S, Fatoyinbo TE & Policelli F 2014. Flood extent mapping for Namibia using change detection and thresholding with SAR. *Environmental Research Letters 9*, 3: 035002.

Malnes E, Guneriussen T & Høgda KA 2002. *Mapping of flood-area by Radarsat in Vannsjø, Norway*. Proceedings of the International Symposium on Remote Sensing of Environment held 8-12 April 2001. Buenos Aires: Northern Research Institute (Norut).

Manjusree P, Kumar LP, Bhatt CM, Rao GS & Bhanumurthy V 2012. Optimization of threshold ranges for rapid flood inundation mapping by evaluating backscatter profiles of high incidence angle SAR images. *International Journal of Disaster Risk Science* 3, 2: 113-122.

Marengo JA, Borma LS, Rodriguez DA, Pinho P, Soares WR & Alves LM 2013a. Recent extremes of drought and flooding in Amazonia: vulnerabilities and human adaptation. American Journal of Climate Change 2: 87-96

Marengo JA, Alves LM, Soares WR, Rodriguez DA, Camargo H, Riveros MP & Pabló AD 2013b. Two contrasting severe seasonal extremes in tropical South America in 2012: flood in Amazonia and drought in northeast Brazil. Journal of Climate 26, 22: 9137-9154.

Martinis S, Twele A & Voigt S 2009. Towards operational near real-time flood detection using a split-based automatic thresholding procedure on high resolution TerraSAR-X data. *Natural Hazards and Earth System Science* 9, 2: 303-314.

Martinis S 2010. Automatic near real-time flood detection in high resolution X-band synthetic aperture radar satellite data using context-based classification on irregular graphs. Doctoral dissertation. Ludwig Maximilian University of Munich, Faculty of Earth Sciences.

Mason DC, Speck R, Devereux B, Schumann GJ, Neal JC & Bates PD 2010. Flood detection in urban areas using TerraSAR-X. *Geoscience and Remote Sensing, IEEE Transactions on 48*, 2: 882-894.

Masoomi A, Hamzehyan R & Shirazi, NC 2012. Speckle reduction approach for SAR image in satellite communication. *International Journal of Machine Learning and Computing*, 2, 1: 62.

Mather PM 2004. *Computer processing of remotely-sensed images* 3rd ed. Chicester, West Sussex: Wiley.

Matgen P, Schumann G, Henry, JB, Hoffmann L & Pfister L 2007. Integration of SAR-derived river inundation areas, high-precision topographic data and a river flow model toward near real-time flood management. *International Journal of Applied Earth Observation and Geoinformation* 9, 3: 247-263.

Matgen P, Hostache R, Schumann G, Pfister L, Hoffmann L & Savenije HHG 2011. Towards an automated SAR-based flood monitoring system: Lessons learned from two case studies. *Physics and Chemistry of the Earth, Parts A/B/C 36*, 7: 241-252.

Matlab 2013a. Matlab R2013a. Mathworks. [online help]. Online Available: http://www.mathworks.com/discovery/edge-detection.html.

Matlab 2013b. Matlab R2013a. Mathworks. [online help]. Online Available: http://www.mathworks.com/help/images/ref/activecontour.html.

May W 2004. Simulation of the variability and extremes of daily rainfall during the Indian summer monsoon for present and future times in a global time-slice experiment. *Climate Dynamics* 22, 2-3: 183-204.

Mendelsohn J & Roberts C 1997. *An environmental profile and atlas of Caprivi*. Windhoek: Gamsberg Macmillan Publishers.

Mendelsohn J, Jarvis A, Roberts C & Robertson T. 2002. *Atlas of Namibia: a portrait of the land and its people*. Cape Town: New Africa Books (Pty) Ltd.

Mendelsohn J 2007. A digest of information on key aspects of Caprivi's geography. Raison [online]. Available from: http://www.raison.com.na/Namibia,%20Caprivi%20region%20-%20a%20digest%20of%20key%20information.pdf [Accessed 15 June 2014].

Milly PCD, Wetherald RT, Dunne KA & Delworth TL 2002. Increasing risk of great floods in a changing climate. *Nature* 415, 6871: 514-517.

Mimura N, Yasuhara K, Kawagoe S, Yokoki H & Kazama S 2011. Damage from the Great East Japan Earthquake and Tsunami-a quick report. *Mitigation and Adaptation Strategies for Global Change*, 16, 7: 803-818.

Mirza MMQ 2002. Global warming and changes in the probability of occurrence of floods in Bangladesh and implications. *Global environmental change* 12, 2: 127-138

Moeslund TB 2009. Canny Edge detection [online]. Available from: http://www.cse.iitd.ernet.in/~pkalra/csl783/canny.pdf [Accessed 1 October 2014]

Moore AE, Cotterill FPD, Main MPL & Williams HB 2007. The Zambezi River. In Gupta A (ed) Large Rivers: Geomorphology and Management, 311-332. Chichester: Wiley.

Moore AE, Cotterill FPD & Eckardt F 2012. The evolution and ages of Makgadikgadi palaeo-lakes: Consilient evidence from Kalahari drainage evolution south-central Africa. *South African Journal of Geology* 115, 3: 385-413.

Moore S, Eng E & Daniel M 2003. International NGOs and the role of network centrality in humanitarian aid operations: a case study of coordination during the 2000 Mozambique floods. Disasters 27, 4: 305-318.

Mordvintsev A & Rahman A 2014. Canny Edge Detection [online]. Available from: http://opencv-python-tutroals.readthedocs.org/en/latest/py_tutorials/py_imgproc/py_canny/py_canny.html. [Accessed 6 October 2014].

Namibia (Republic of) 2011. *Namibia 2011 population and housing census main report*. Windhoek: Namibia Statistics Agency.

Namibia Meteorological Service 2015. Tabulation of Climate Statistics for Selected Stations in Namibia [online]. Avaiable from http://www.meteona.com/attachments/035_Namibia_Long-term_Climate_Statistics_for_Specified_Places[1].pdf [Accessed 12 May 2014]

Nadal NC, Zapata RE, Pagan I, López R & Agudelo J 2009. Building damage due to riverine and coastal flood. *Journal of Water Resources Planning and Management* 136, 3: 327-336.

NASA (National Aeronautics and Space Administration) 2015a. Landsat 5. NASA Landsat Science [online]. Available from: http://landsat.gsfc.nasa.gov/?p=3180 [Accessed 12 October 2015].

NASA (National Aeronautics and Space Administration) 2015b. Landsat 7. NASA Landsat Science [online]. Available from: http://landsat.gsfc.nasa.gov/?p=3180 [Accessed 12 October 2015].

Nchito WS 2007. Flood risk in unplanned settlements in Lusaka. *Environment and Urbanization* 19, 2: 539-551.

NEST (Next ESA SAR Toolbox) 2013. NEST Overview. ESA (European Space Agency) [Online Help]. Online available: http://corp.array.ca/nest-web/help/index.html

Nezry E 2014. Adaptive Speckle Filtering in Radar Imagery. In Closson D (ed) *Land Applications of Radar Remote Sensing*. InTech: Available from: http://www.intechopen.com/books/land-applications-of-radar-remote-sensing/adaptive-speckle-filtering-in-radar-imagery.

Nicholls RJ, Hoozemans FM & Marchand M 1999. Increasing flood risk and wetland losses due to global sea-level rise: regional and global analyses. *Global Environmental Change* 9: S69-S87.

Nicholls RJ, Marinova N, Lowe JA, Brown S, Vellinga P, De Gusmao D, Hinkel J & Tol RS 2010. Sea-level rise and its possible impacts given a 'beyond 4 C world' in the twenty-first century. *Philosophical Transactions of the Royal Society of London A: Mathematical, Physical and Engineering Sciences 369*, 1934: 161-181.

Nico G, Pappalepore M, Pasquariello G, Refice A & Samarelli S 2000. Comparison of SAR amplitude vs. coherence flood detection methods-a GIS application. *International Journal of Remote Sensing* 21, 8: 1619-1631.

Nykamp DQ 2015. Level sets. Math Insight [online]. Available from: http://mathinsight.org/level_sets [Accessed 20 November 2015]

Oberstadler R Hönsch H & Huth D 1997. Assessment of the mapping capabilities of ERS-1 SAR data for flood mapping: a case study in Germany *Hydrological processes 11,* 10: 1415-1425.

Ormsby JP, Blanchard BJ & Blanchard AJ 1985. Detection of lowland flooding using active microwave systems. *Photogrammetric Engineering and Remote Sensing*, 51, 3: 317-329.

Ozdarici A & Akyurek, Z 2010. *A comparison of SAR filtering techniques on agricultural area identification.* Proceedings of the ASPRS 2010 Annual Conference held 26-30 April 2010, San Diego: American Society for Photogrammetry and Remote Sensing

Pachauri RK & Meyer L (eds) 2014. Climate Change 2014: Synthesis Report. Contribution of Working Groups I, II and III to the Fifth Assessment Report of the Intergovernmental Panel on Climate Change. Geneva: IPCC.

Pallard B, Castellarin A & Montanari, A 2009. A look at the links between drainage density and flood statistics. *Hydrology and Earth System Sciences* 13, 7: 1019-1029.

PDNA (Post-Disaster Needs Assessment) 2009. A Report Prepared by the Government of the Republic of Namibia, with support from the International Community [online]. Available from: http://www.recoveryplatform.org/assets/publication/PDNA/Namibia%20PDNA.pdf [Accessed 18 March 2014].

Peake WH & Oliver, TL 1971. *The response of terrestrial surfaces at microwave frequencies*. Ohio State University Electroscience Lab Technical Report AFAL-TR-70-301. Columbus: Ohio State University Electroscience Lab.

Petersen 2001. Impacts of flash floods. In Gruntfest E & Handmer JW (eds) *Coping with flash floods* 11-18. Dordrecht, Boston: Kluwer Academic Publishers.

Pope KO, Rejmankova E, Paris JF & Woodruff R 1997. Detecting seasonal flooding cycles in marshes of the Yucatan Peninsula with SIR-C polarimetric radar imagery. *Remote Sensing of environment* 59, 2: 157-166.

Pulvirenti L, Chini M, Pierdicca N, Guerriero L & Ferrazzoli P 2011. Flood monitoring using multi-temporal COSMO-SkyMed data: Image segmentation and signature interpretation. *Remote Sensing of Environment 115*, 4: 990-1002.

Rajeevan M, Bhate J & Jaswal AK 2008. Analysis of variability and trends of extreme rainfall events over India using 104 years of gridded daily rainfall data. Geophysical research letters 35, 18

Raney RK 1998: Radar fundamentals: Technical perspective. In Henderson FM & Lewis AJ (eds) *Manual of remote sensing: Principles and applications of imaging radar* 3rd ed. 9-130. New York: John Wiley & Sons.

Reason CJC & Keibel A 2004. Tropical cyclone Eline and its unusual penetration and impacts over the southern African mainland. Weather and forecasting 19, 5: 789-805.

Refice A, Capolongo D, Pasquariello G, D'Addabbo A, Bovenga F, Nutricato R, Lovergine FP & Pietranera L 2014. SAR and InSAR for flood monitoring: examples with COSMO-SkyMed data. *Selected Topics in Applied Earth Observations and Remote Sensing, IEEE Journal of* 7, 7: 2711-2722.

Richter R & Schläpfer D 2015. Atmospheric / Topographic Correction for Satellite Imagery. German Aerospace Centre.

Richards JA, Woodgate PW & Skidmore AK 1987: An explanation of enhanced radar backscattering from flooded forests. *International Journal of Remote Sensing* 8, 7: 1093-1100.

Riebeek H & van Langenhove G 2010. Zambezi Flood Plain, Namibia: Image of the Day. NASA [online]. Available from: http://earthobservatory.nasa.gov/IOTD/view.php?id=44132 [Accessed 13 September 2015].

Reed DW 2002. Reinforcing flood–risk estimation. *Philosophical Transactions of the Royal Society of London A: Mathematical, Physical and Engineering Sciences* 360, 1796: 1373-1387.

Rossi G, Harmanciogammalu NB & Yevjevich V (eds) 1994. *Coping with floods Volume 257* 3-9. Springer Science & Business Media.

Samimi C, Fink AH & Paeth H 2012. The 2007 flood in the Sahel: causes, characteristics and its presentation in the media and FEWS NET. *Natural Hazards and Earth System Sciences* 12, 2: 313-325.

Sanyal J & Lu XX 2004. Application of remote sensing in flood management with special reference to monsoon Asia: a review. *Natural Hazards 33*, 2: 283-301.

Sarachik ES & Cane MA 2010. *The El Niño-Southern Oscillation Phenomenon*. Cambridge; New York: Cambridge University Press

Schumann AH 2011. Introduction – Hydrological Aspects of Risk Management. In Schumann AH (ed) *Flood risk assessment and management: how to specify hydrological loads, their consequences and uncertainties*, 1-10. Berlin, Heidelberg, New York: Springer.

Sethian JA 2006. Level Set Methods: An initial value formulation. University of Berkley Mathematics [online]. Available from: https://math.berkeley.edu/~sethian/2006/Explanations/level_set_explain.html.

Shahid S 2011. Trends in extreme rainfall events of Bangladesh. Theoretical and Applied Climatology 104:3-4: 489-499.

Silcocks, P. B. (1983). Measuring repeatability and validity of histological diagnosis--a brief review with some practical examples. *Journal of clinical pathology* 36,11: 1269-1275.

Small D, Holecz F, Meier E, Nüesch D & Barmettler A 1997. Geometric and radiometric calibration of RADARSAT Images. Proceedings of Geomatics in the Era of RADARSAT held 24–30 May Ottawa, Canada.

Solbø S & Solheim I 2004. *Towards operational flood mapping with satellite SAR*. Proceedings of the ENVISAT/ERS Symposium held 6-10 September 2004. Salzburg: ESA SP-572.

Stabel E & Löffler E 2003. Optimised mapping of flood extent and floodplain structures by radar EO-methods. Proceedings of the FRINGE 2003 Workshop held 1-5 December 2003. Frascati: ESA SP-550.

Tian Y, Duan F, Zhou M & Wu Z 2013. Active contour model combining region and edge information. *Machine Vision and Applications* 24, 1: 47-61.

Tiner RW, Lang MW & Klemas VV 2015. *Remote Sensing of Wetlands: Applications and Advances*. Boca Raton: CRC Press, Taylor & Francis Group

Tockner K & Stanford JA 2002. Riverine flood plains: present state and future trends. *Environmental conservation* 29, 3: 308-330.

Townsend PA 2001. Mapping seasonal flooding in forested wetlands using multi-temporal Radarsat SAR. *Photogrammetric engineering and remote sensing* 67, 7: 857-864.

Townsend PA 2002. Relationships between forest structure and the detection of flood inundation in forested wetlands using C-band SAR. *International Journal of Remote Sensing* 23, 3: 443-460.

Töyrä J & Pietroniro A 2005. Towards operational monitoring of a northern wetland using geomatics-based techniques. *Remote Sensing of Environment* 97, 2: 174-191.

Ulaby FT, Moore RK & Fung, AK 1986. *Microwave remote sensing: active and passive. Volume 3: From theory to applications*. Norwood: Artech House.

UNISDR (United Nations International Strategy for Disaster Reduction) 2011. *Global Assessment Report on Disaster Risk Reduction: Revealing risk, redefining development*. Geneva: UNISDR.

UNOCHA (United Nations Office for the Coordination of Humanitarian Affairs) 2009. West Africa - Flood Affected Population - June to September 2009 (as of 24 Sep 2009). Reliefweb [online]. Available from: http://reliefweb.int/map/benin/west-africa-flood-affected-population-june-september-2009-24-sep-2009 [Accessed 15 December 2015].

UNOCHA (United Nations Office for the Coordination of Humanitarian Affairs) 2011. Southern Africa Flood and Cyclone Situation Update #12. Reliefweb [online]. Available from: http://reliefweb.int/report/lesotho/southern-africa-flood-and-cyclone-situation-update-12 [Accessed 15 December 2015]

Vanneuville W, Kellens W, De Maeyer P, Reniers G & Witlox, F 2011. Is 'flood risk management' identical to 'flood disaster management'? *Earthzine* [online]. Available from: http://earthzine.org/2011/03/21/is-flood-risk-management-identical-to-flood-disaster-management/ [Accessed 11 March 2011].

Vikram A & Yezzi A 2012. Incorporating global information in active contour models. In Di Giamberardino P, Iacoviello D, Tavares JMR & Jorge RN (eds) *Computational Modelling of Objects Represented in Images III: Fundamentals, Methods and Applications*, 53-62. CRC Press.

Voigt S, Martinis S, Zwenzner H, Hahmann T, Twele A and Schneiderhan T 2008. *Extraction of flood masks using satellite based very high resolution SAR data for flood management and modeling*. Proceedings of the 4th International Symposium on Flood Defence held 6-8 May 2008. Toronto: The Institute for Catastrophic Loss Reduction.

Wang Y, Hess L, Solange F & Melack JM 1995. Understanding the radar backscattering from flooded and nonflooded Amazonian forests: results from canopy backscatter modelling. *Remote Sensing of Environment* 54, 3: 324-332.

Wang XF, De-Huang S & Xu H 2010. An efficient local Chan–Vese model for image segmentation. *Pattern Recognition* 43, 3: 603-618.

Wang XG, Ge L& Li X 2012. Evaluation of filters for Envisat ASAR speckle suppression in pasture area. *SPRS Annals of Photogrammetry, Remote Sensing and Spatial Information Sciences* 1: 341-346.

Remote Sensing and Spatial Information Sciences 1: 341–346.

WWAP (World Water Assessment Programme, United Nations) 2009. The United Nations World Water Development Report 3: Water in a Changing World. Paris, London: UNESCO Publishing.

Washington R & Preston A 2006. Extreme wet years over southern Africa: Role of Indian Ocean sea surface temperatures. *Journal of Geophysical Research: Atmospheres (1984–2012)* 111, D15.

Watson D & Adams, M 2010. *Design for Flooding: architecture, landscape, and urban design for resilience to climate change*. John wiley & sons.

Waugh D 1995. *Geography: an integrated approach*. Walton-on-Thames: Nelson

Wivell CE, Steinwand DR, Kelly GG & Meyer DJ 1992. Evaluation of terrain models for the geocoding and terrain correction, of synthetic aperture radar (SAR) images. *IEEE Transactions on Geoscience and Remote Sensing* 30, 6: 1137-1144.

Woodhouse IH 2006. *Introduction to microwave remote sensing*. Boca Raton: Taylor & Francis.

Woodruff JD, Irish JL & Camargo SJ 2013. Coastal flooding by tropical cyclones and sea-level rise. *Nature* 504, 7478: 44-52.

World Bank 2009. *Africa Development Indicators 2008-09: Youth and Employment in Africa – The Potential, the Problem, the Promise.* Washington, DC: World Bank.

Xu C, Yezzi Jr A & Prince, JL 2000. *On the relationship between parametric and geometric active contours*. Proceedings of the Thirty-Fourth Asilomar Conference on Signals, Systems and Computers held 29 October-1 November 2000. Pacific Grove: IEEE

Yevjevich V 1994 Floods and society. In Rossi G, Harmanciogammalu NB & Yevjevich V (eds) *Coping with floods Volume 257* 3-9. Springer Science & Business Media.

Zhang K, Zhang L, Song H & Zhou W 2010. Active contours with selective local or global segmentation: a new formulation and level set method. *Image and Vision computing*, 28, 4: 668-676.

Zhou C, Luo J, Yang C, Li B & Wang S 2000. Flood monitoring using multi-temporal AVHRR and RADARSAT imagery. Photogrammetric engineering and remote sensing 66,5: 633-638.

Zhou T, Song F, Lin R, Chen X & Chen X 2013. The 2012 north china floods: explaining an extreme rainfall event in the context of a longer-term drying tendency. *Bulletin of the American Meteorological Society* 94, 9: S49.

Zwiers FW, Alexander LV, Hegerl GC, Knutson TR, Kossin JP, Naveau, Neville N, Schär C, Seneviratne SI & Zhang X 2013. Climate extremes: challenges in estimating and understanding recent changes in the frequency and intensity of extreme climate and weather events. In Asrar

GR & Hurell JW (eds) *Climate Science for Serving Society* 339-389. Dordrecht Heidelberg New York London: Springer.

APPENDICES

Appendix A	Details of Landsat 5 Thematic Mapper (TM) and Landsat 7, the Enhanced Thematic Mapper Plus (ETM+), and atmospheric correction of these images	
Appendix B	Extracted histograms and location of all thresholds values for ASAR and PALSAR images	
Appendix C	Summaries of error metrics for all threshold values for all SAR images	
Appendix D	Confusion matrices for the best threshold values and the ACMs	
Appendix E	Classified maps of the best threshold values and the ACMs	

APPENDIX A

Details of Landsat 5 Thematic Mapper (TM) and Landsat 7, the Enhanced Thematic Mapper Plus (ETM+), and atmospheric correction of these images

Landsat 5, carrying the Thematic Mapper (TM) was launched on 1 March 1984 (NASA 2015a). TM data are sensed in seven bands, ranging from the visible to mid-infrared spectrum. Details are summarised in Table. Landsat 5 was officially decommisioned in June 2013. Landat 6 was lost at launched and Landsat 5 was therefore succeeded by Landsat 7 and Landsat 8.

Landsat 7, the Enhanced Thematic Mapper Plus (ETM+) was launched on 15 April 1999 and replicates the TM instruments of Landsat 4 and Landsat 5. Additional features included are: a 15m spatial resolution panchromatric band, absolute radiometric calibration accurate within 5%, on-board full aperture solar calibrator, a 60m spatial resolution thermal infrared band and an on-board data-recorder (NASA 2015b).

During 30 May 2003, the Scan Line Corrector (SLC) failed causing wedges of missing data on Landsat 7 images, which increases in magnitude away from nadir. Approximately 22% of the normal scene area is missing (USGS 2013). Details are summarised in Table below. ETM+ scenes used in this study are affected by SLC error as well.

Table A.1: Characteristics of Landsat 4 and 5TM and Landsat 7 ETM+ imagery

Band	**Name**	**Wavelength (µm)**	**Resolution (m)**	**Swath**
1	Blue	0.45-0.52	30	185 km
2	Green	0.52-0.60	30	
3	Red	0.63-0.69	30	
4	Near Infrared (NIR)	0.77-0.90	30	
5	Short-wave Infrared (SWIR1)	1.55-1.75	30	
6	Thermal Infrared	10.40-12.50	60 (ETM+) 120 (TM)	
7	Short-wave Infrared (SWIR2)	2.09-2.35	30	
8	Panchromatic (Landsat 7 only)	0.52-0.90	15	

Adapted from: USGS (2015)

Landsat images are subject to atmospheric attenuation, which occurs because the sensor not only records the brightness values of the Earth's surface of interest for image analysis, but also brightness values from the atmosphere itself, caused by atmospheric scattering (Campbell & Wynne 2011). The recorded digital numbers (DNs) are therefore not an accurate representation of the ground reflectance. When atmospheric correction is performed, the DNs are converted to surface reflectance. ATCOR is a software program used for atmospheric correction of satellite imagery between the solar (0.4-2.5 µm) as well as the thermal (8-14 µm) regions of the electromagnetic spectrum (Richter & Schläpfer 2015).

APPENDIX B

Extracted histograms and location of all thresholds values for ASAR and PALSAR images.

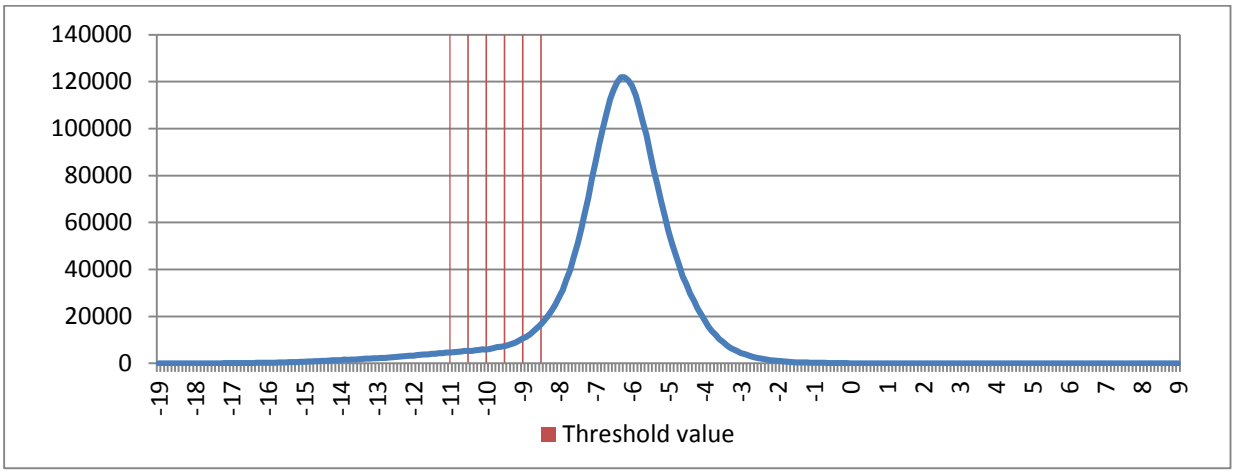

Figure B.1: ASAR WSM 17 March 2009

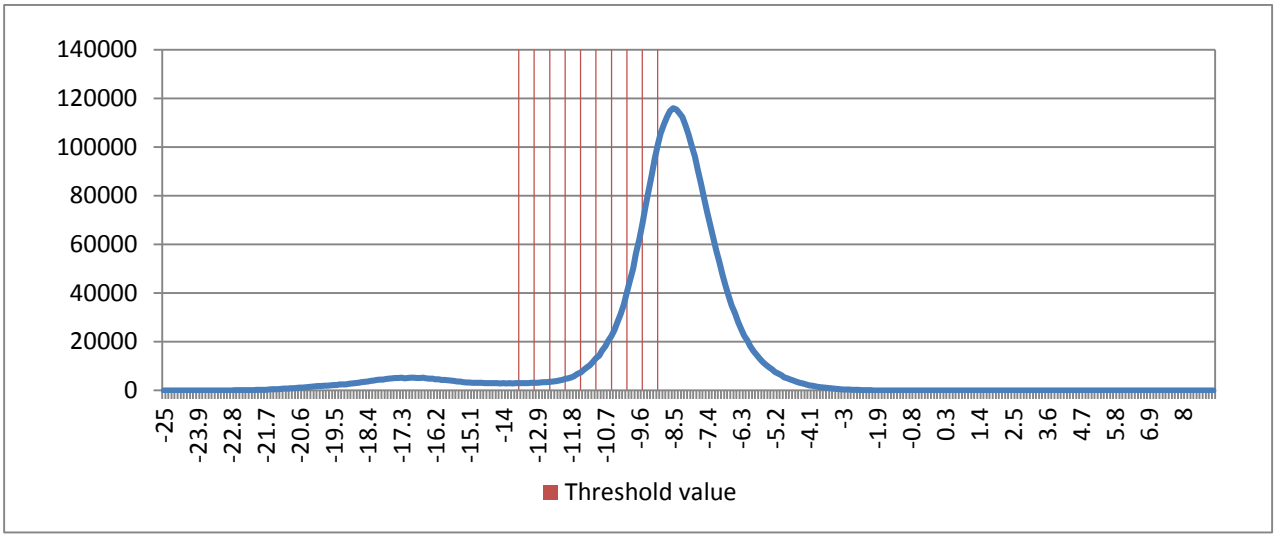

Figure B.2: ASAR WSM 20 March 2009

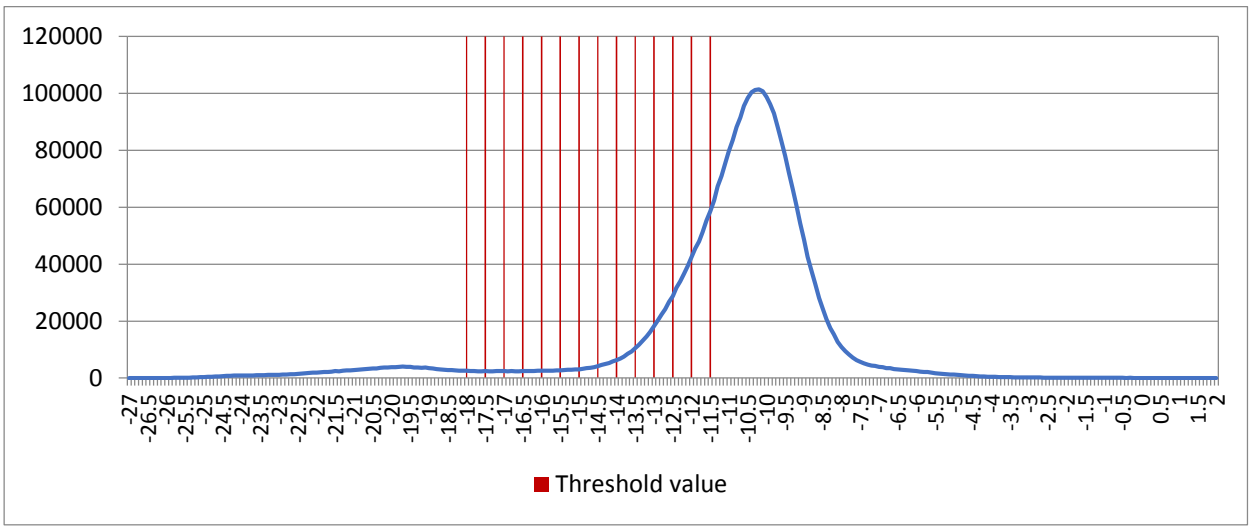

Figure B.3: ASAR WSM 23 March 2009

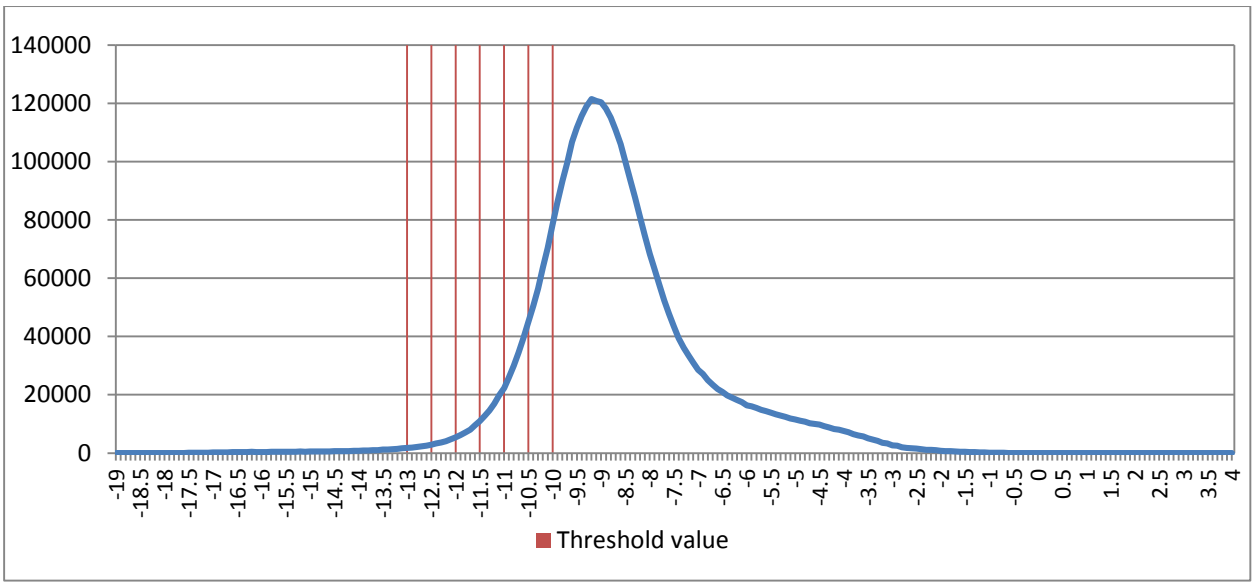

Figure B.4: ASAR WSM 24 March 2009

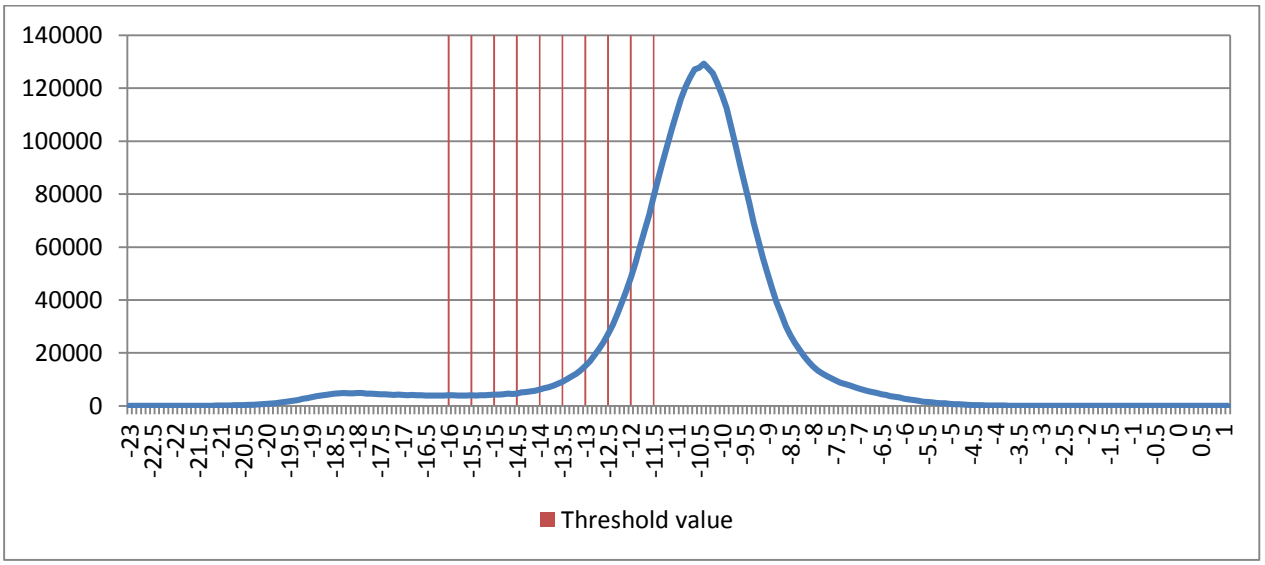

Figure B.5: ASAR WSM 25 April 2009

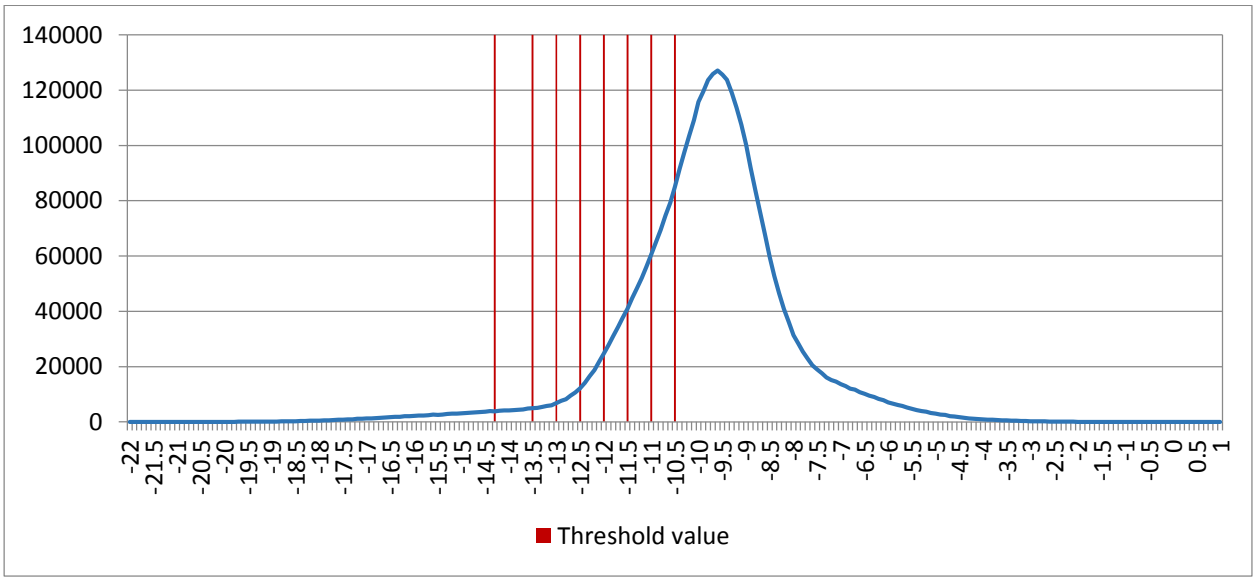

Figure B.6: ASAR WSM 10 May 2009

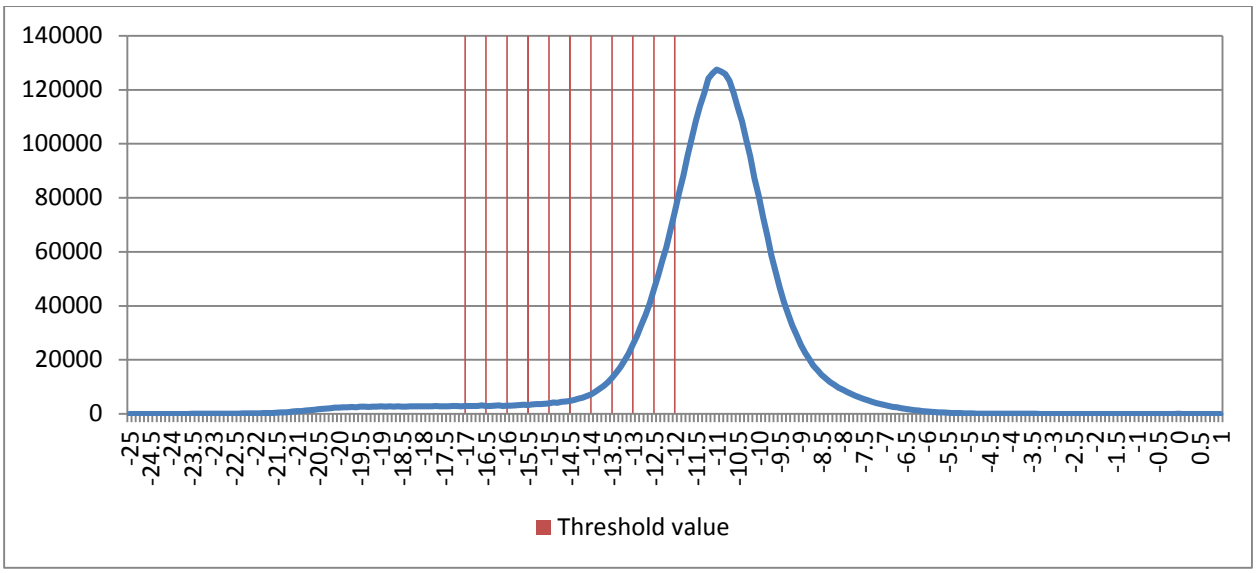

Figure B.7: ASAR WSM 11 May 2009

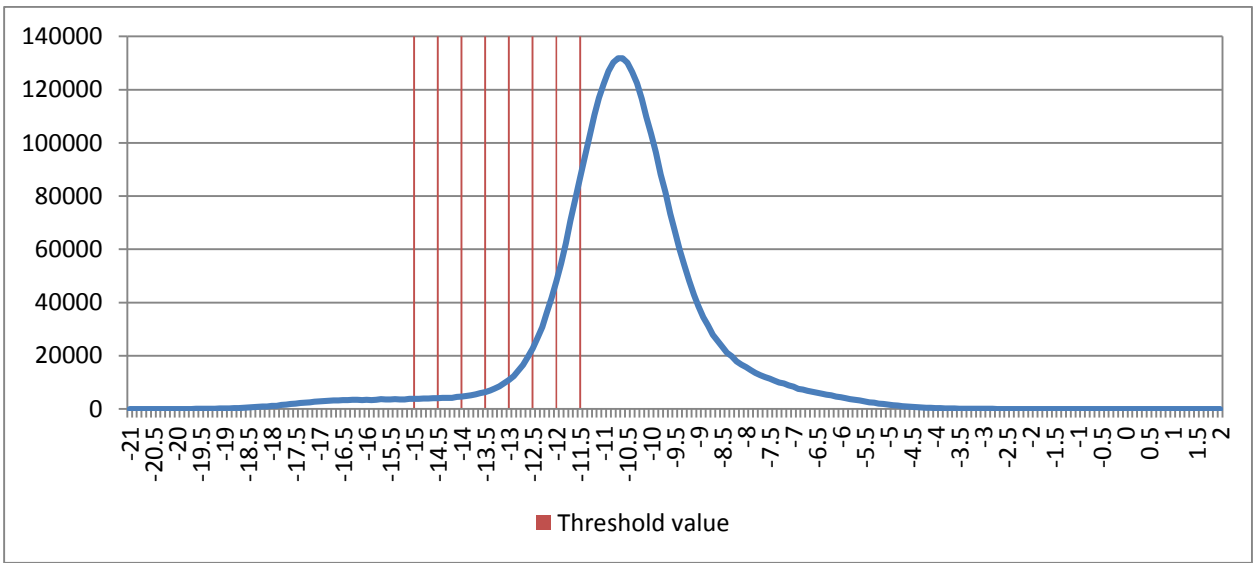

Figure B.8: ASAR WSM 14 May 2009

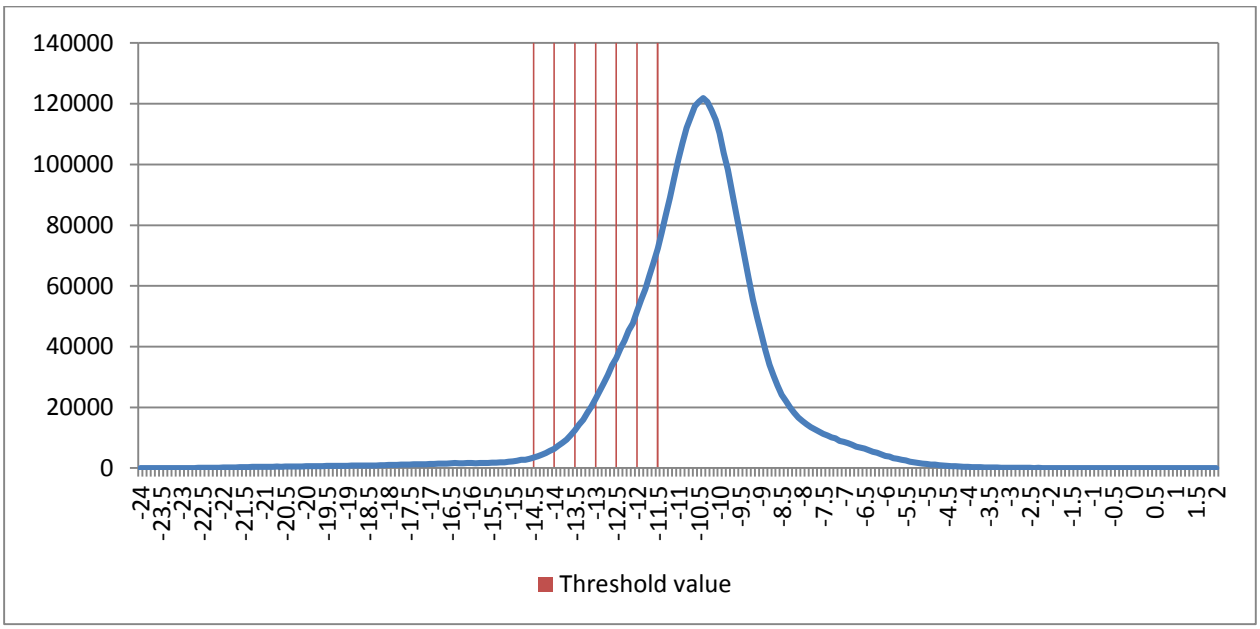

Figure B.9: ASAR WSM 29 May 2009

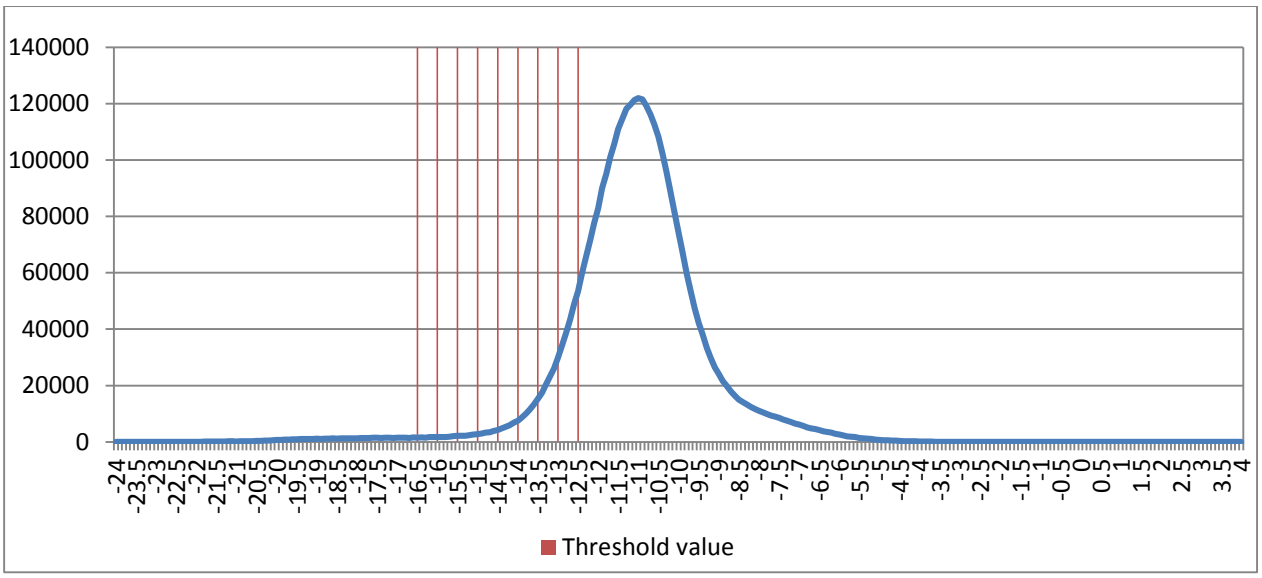

Figure B.10: ASAR WSM 30 May 2009

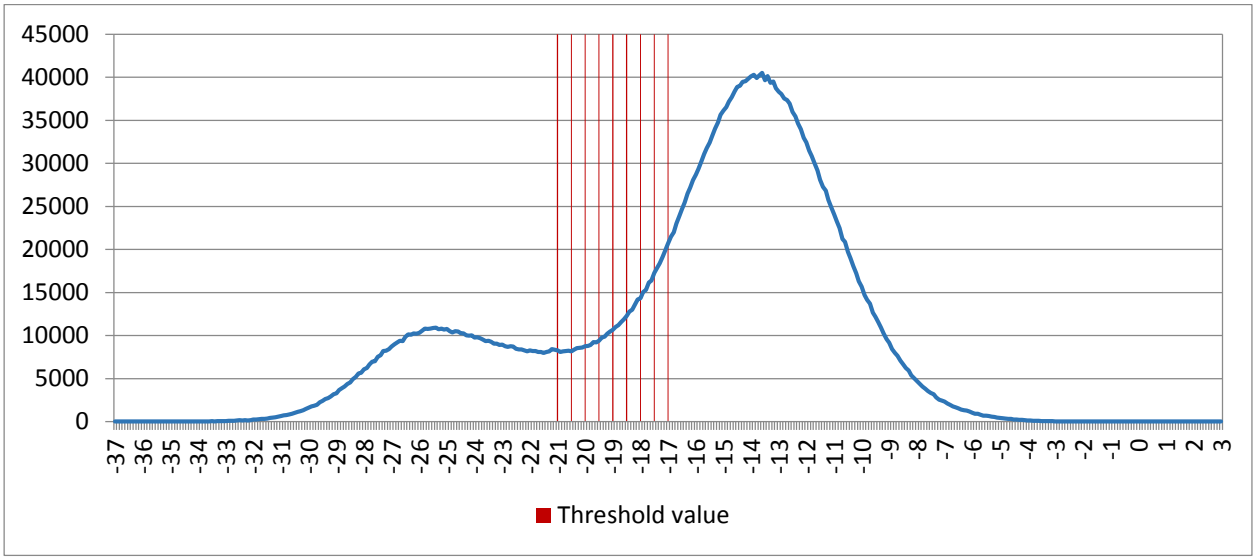

Figure B.11: PALSAR 19 March 2009 (1) – HH-polarisation

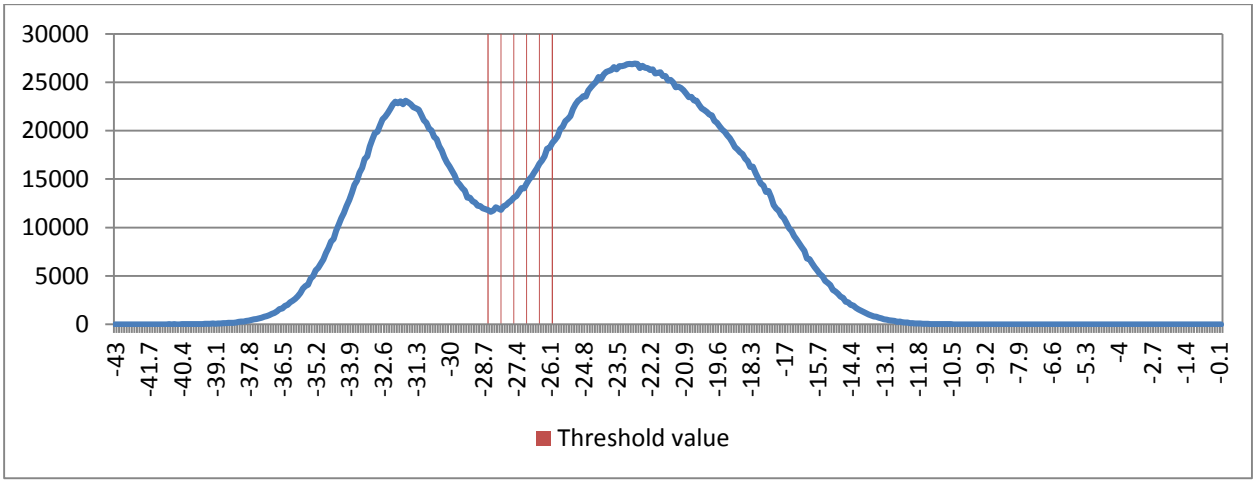

Figure B.12: PALSAR 19 March 2009 (1) – HV-polarisation

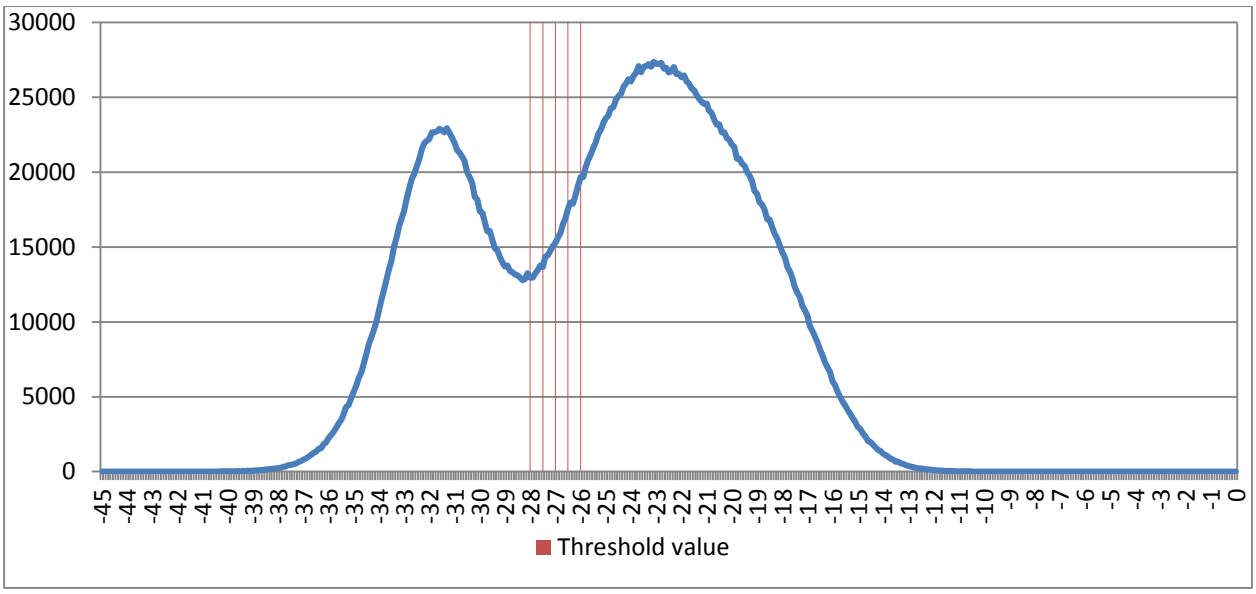

Figure B.13: PALSAR 19 March 2009 (1) – VH-polarisation

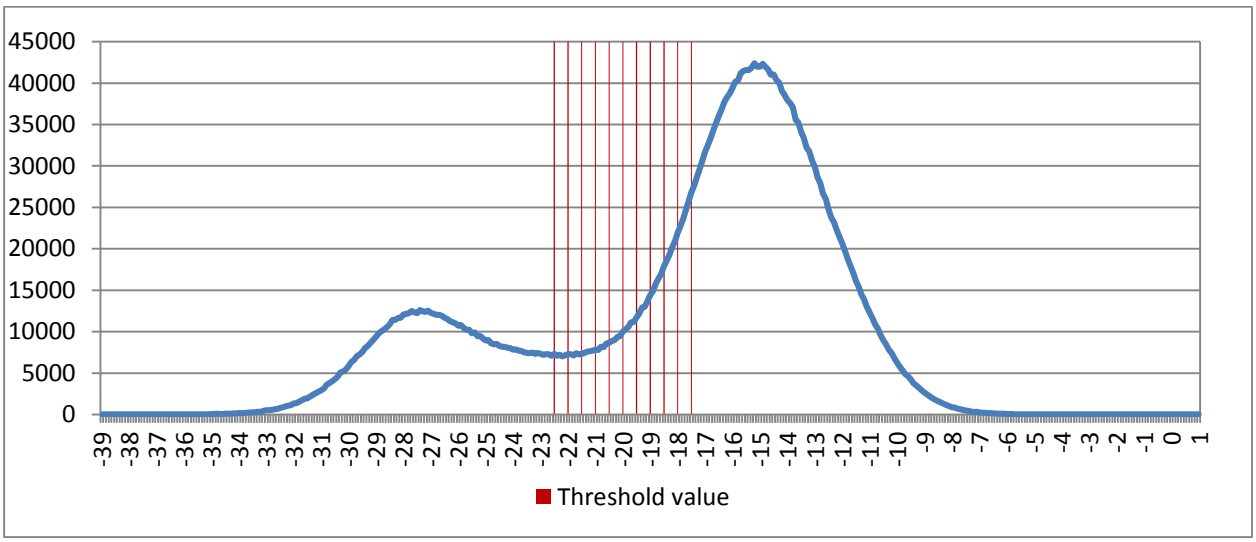

Figure B.14: PALSAR 19 March 2009 (1) – VV-polarisation

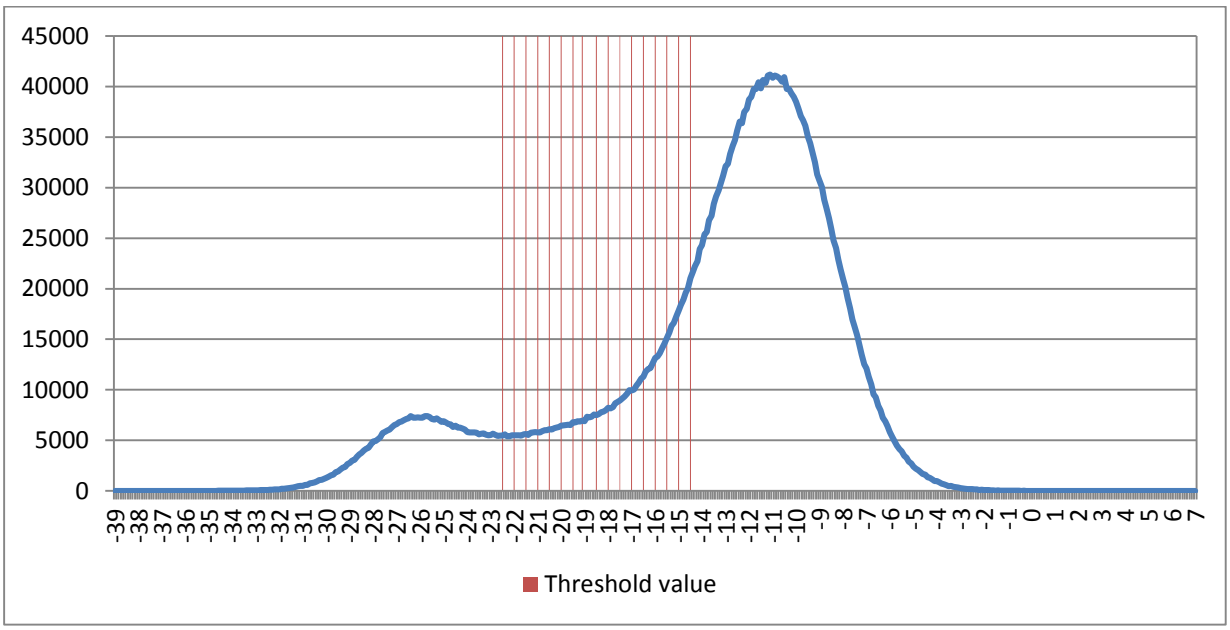

Figure B.15: PALSAR 19 March 2009 (2) – HH-polarisation

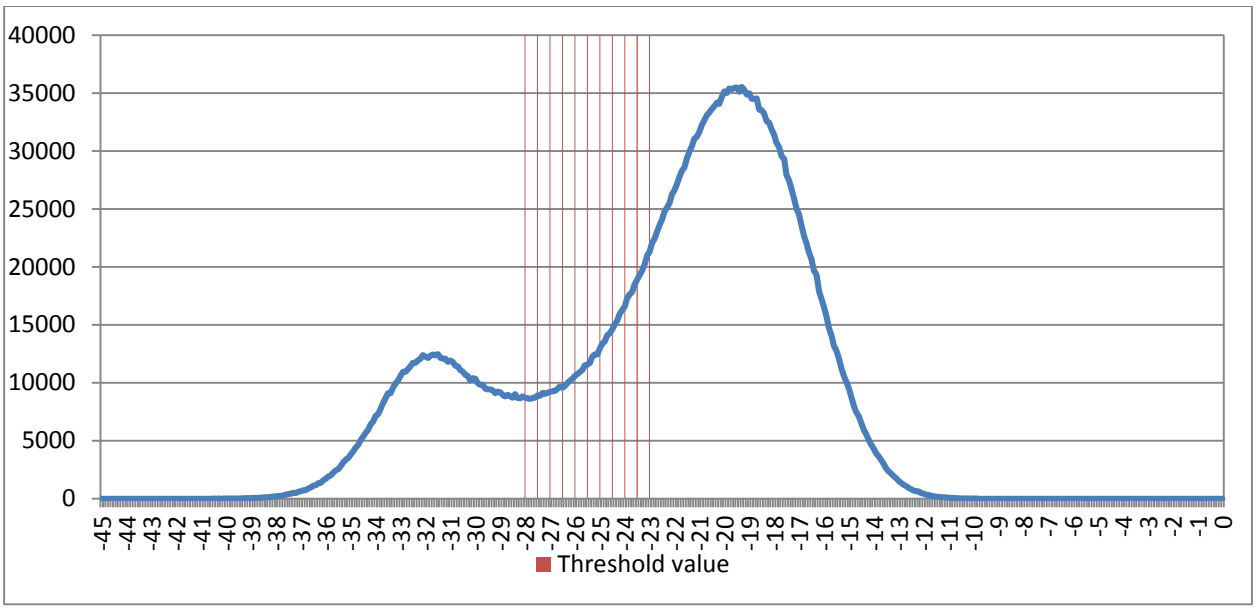

Figure B.16: PALSAR 19 March 2009 (2) – HV-polarisation

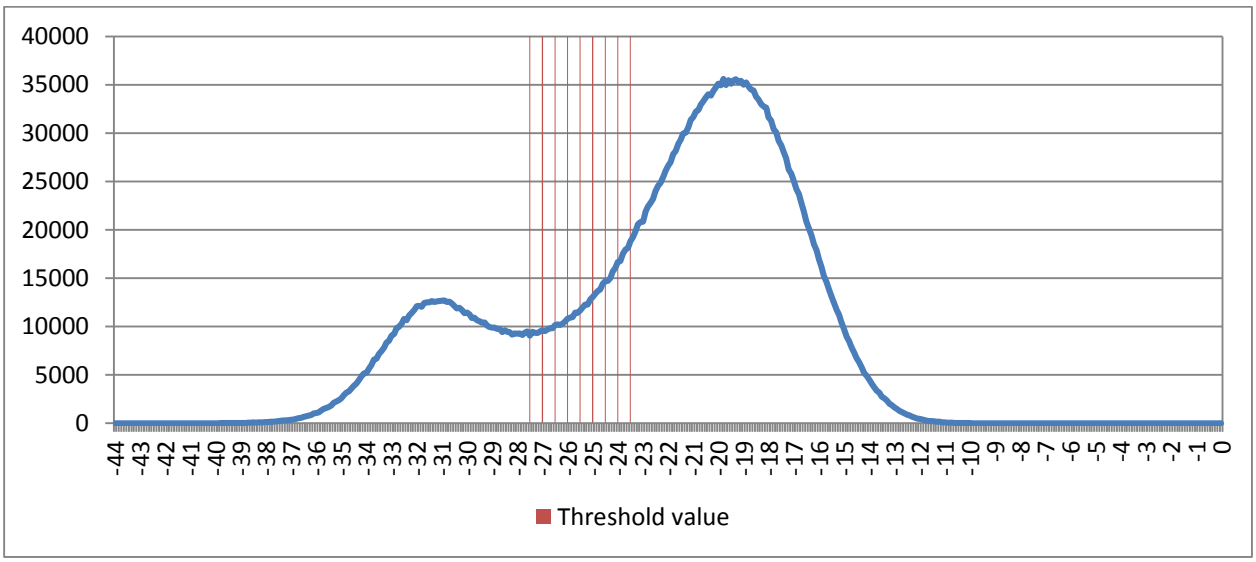

Figure B.17: PALSAR 19 March 2009 (2) – VH-polarisation

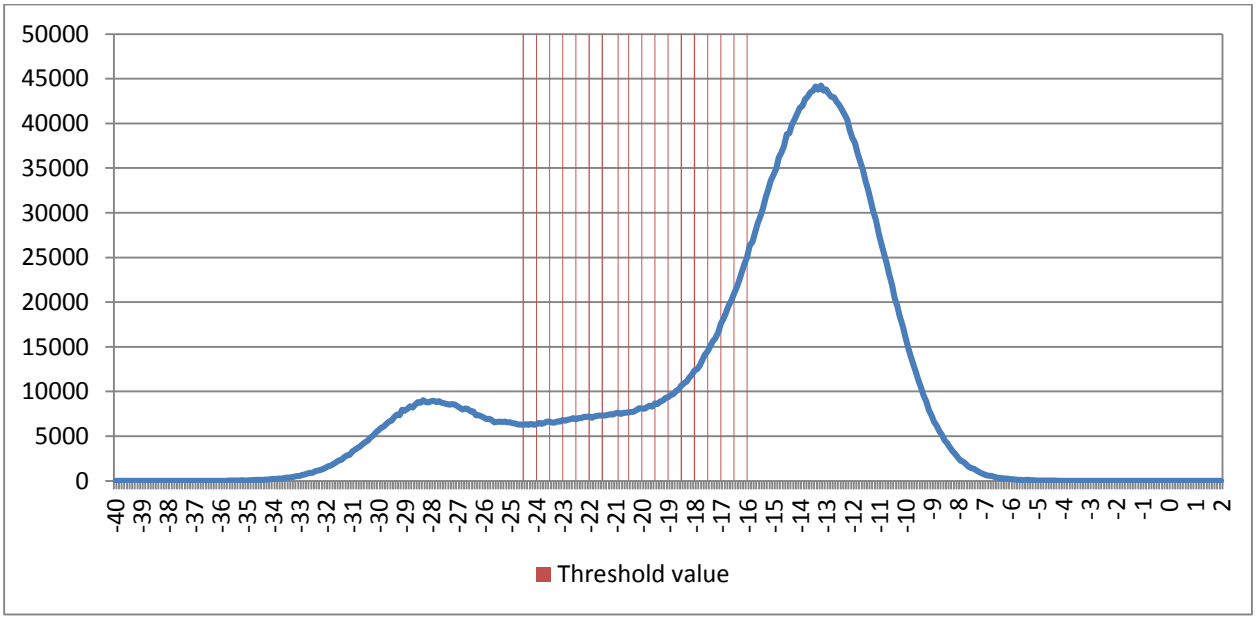

Figure B.18: PALSAR 19 March 2009 (2) – VV-polarisation

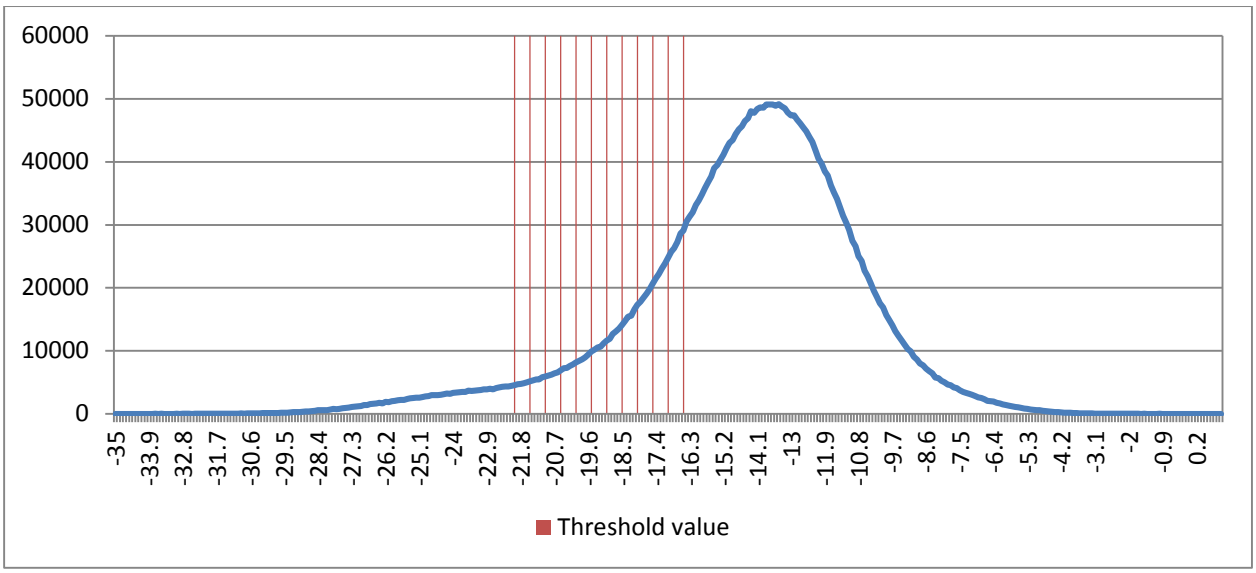

Figure B.19: PALSAR 5 April 2009 – HH-polarisation

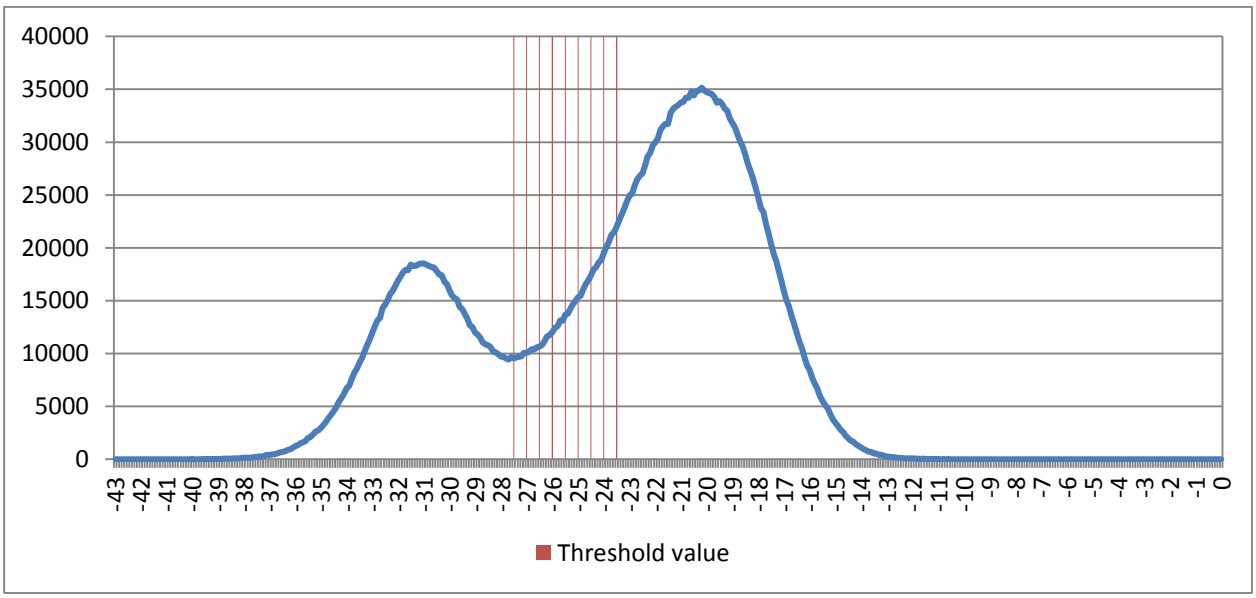

Figure B.20: PALSAR 5 April 2009 – HV- polarisation

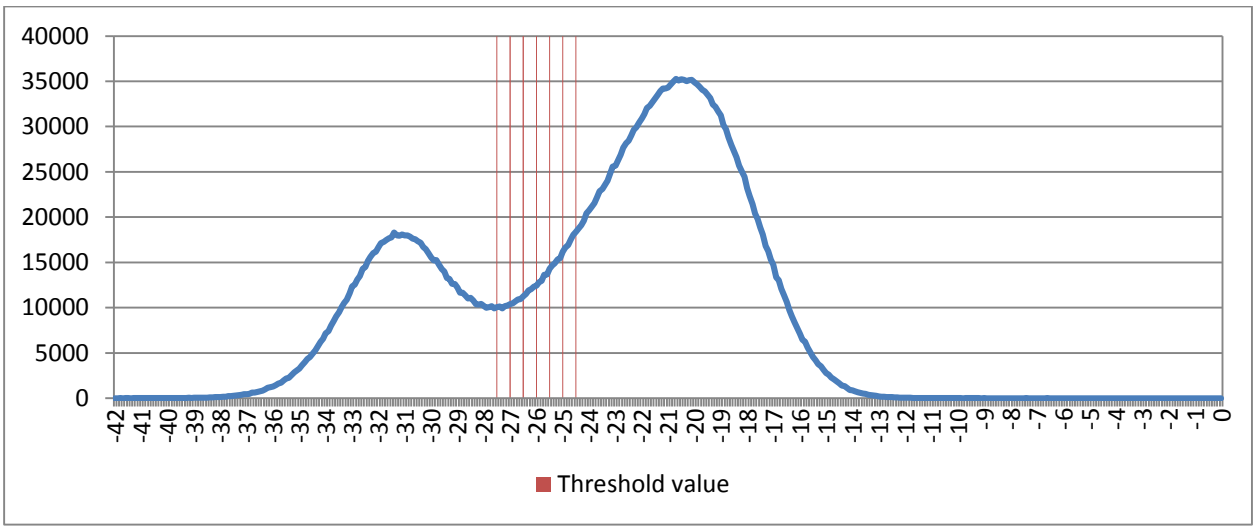

Figure B.21: PALSAR 5 April 2009 – VH- polarisation

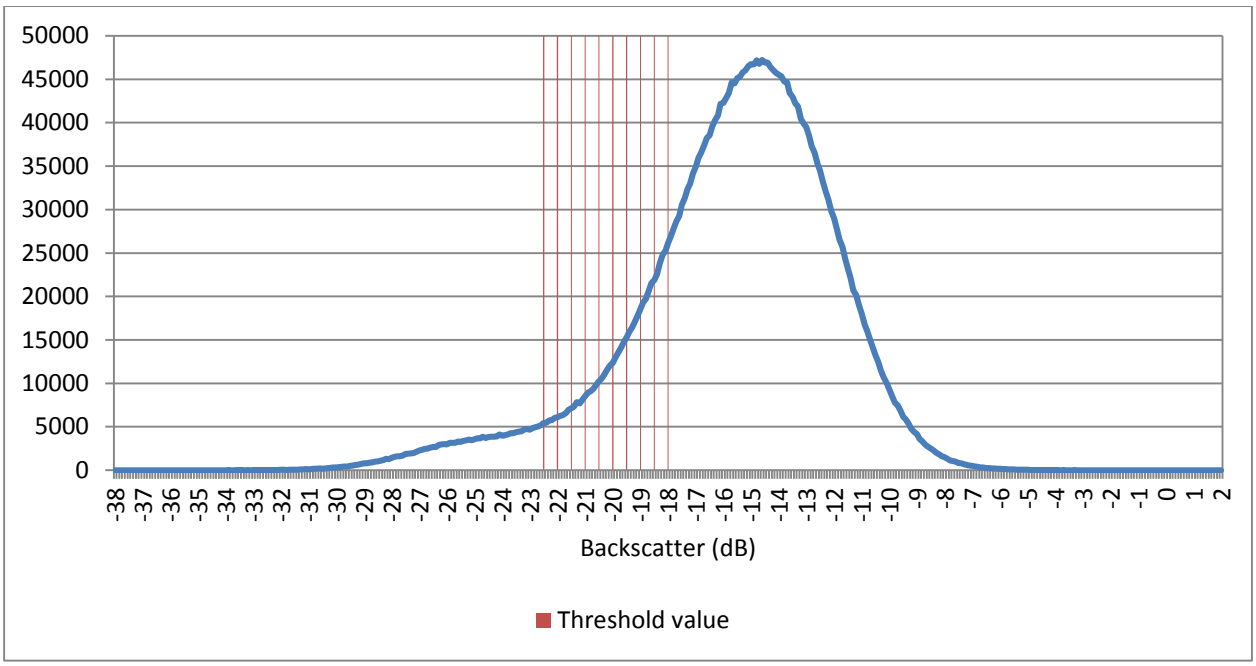

Figure B.22: PALSAR 5 April 2009 – VV- polarisation

APPENDIX C

Summaries of error metrics for all threshold values for all SAR images

Table C.1: ASAR 17 March 2009

Threshold value	Overall Accuracy	User's accuracy flooded	Producer's accuracy flooded	User's accuracy non-flooded	Producer's accuracy non-flooded	Kappa
-11	68.6567	100	40	60.38	100	0.3891
-10.5	71.6418	100	45.71	62.75	100	0.4458
-10	73.8806	100	50	64.65	100	0.4885
-9.5	76.8657	100	55.71	67.37	100	0.5458
-9	80.597	97.83	64.29	71.59	98.44	0.6173
-8.5	82.0896	97.92	67.14	73.26	98.44	0.6463

Table C.2: ASAR 20 March 2009

Threshold value	Overall Accuracy	User's accuracy flooded	Producer's accuracy flooded	User's accuracy non-flooded	Producer's accuracy non-flooded	Kappa
-13.5	97.7612	100	95.71	95.52	100	0.9552
-13	97.7612	100	95.71	95.52	100	0.9552
-12.5	98.5075	100	97.14	96.97	100	0.9701
-12	98.5075	100	97.14	96.97	100	0.9701
-11.5	97.7612	98.55	97.14	96.92	98.44	0.9552
-11	97.7612	98.55	97.14	96.92	98.44	0.9552
-10.5	96.2687	95.77	97.14	96.83	95.31	0.9252
-10	92.5373	98.57	88.46	98.21	85.94	0.8496
-9.5	88.0597	82.14	98.57	98	76.56	0.7584
-9	80.597	73.4	98.57	97.5	60.94	0.6048

Table C.3: ASAR 23 March 2009

Threshold value	Overall Accuracy	User's accuracy flooded	Producer's accuracy flooded	User's accuracy non-flooded	Producer's accuracy non-flooded	Kappa
-18	62.013	100	39.38	49.57	100	0.3266
-17.5	60.7143	100	37.31	48.73	100	0.3076
-17	63.961	100	42.49	50.88	100	0.3555
-16.5	65.5844	100	45.08	52.04	100	0.38
-16	66.8831	100	47.15	53	100	0.3998
-15.5	68.5065	100	49.74	54.25	100	0.425
-15	69.4805	100	51.3	55.02	100	0.4402
-14.5	70.7792	100	53.37	56.1	100	0.4608
-14	72.7273	100	56.48	57.79	100	0.4921
-13.5	75.6494	99.17	61.66	60.64	99.13	0.5388
-13	76.6234	95.49	65.8	62.29	94.78	0.5481
-12.5	79.2208	93.88	71.5	65.84	92.17	0.5891
-12	80.5195	91.3	76.17	68.71	87.83	0.6059
-11.5	80.1948	87.5	79.79	70.45	80.87	0.589

Table C.4: ASAR 24 March 2009

Threshold value	Overall Accuracy	User's accuracy flooded	Producer's accuracy flooded	User's accuracy non-flooded	Producer's accuracy non-flooded	Kappa
-13	43.5065	100	9.84	39.79	100	0.0754
-12.5	46.1039	100	13.99	40.93	100	0.1083
-12	48.0519	100	17.1	41.82	100	0.1335
-11.5	53.2468	100	25.39	44.4	100	0.2026
-11	59.4156	97.22	36.27	47.88	98.26	0.2848
-10.5	63.961	92.71	46.11	50.94	93.91	0.342
-10	70.4545	91.8	58.03	56.45	91.3	0.4386

Table C.5: ASAR 25 April 2009

Threshold value	Overall Accuracy	User's accuracy flooded	Producer's accuracy flooded	User's accuracy non-flooded	Producer's accuracy non-flooded	Kappa
-16	53.211	98.77	34.48	38.21	98.95	0.2275
-15.5	55.9633	98.89	38.36	39.66	98.95	0.2589
-15	59.633	99.02	43.53	41.78	98.95	0.3026
-14.5	62.0795	99.09	46.98	43.32	98.95	0.333
-14	65.1376	98.36	51.72	45.37	97.89	0.3698
-13.5	67.8899	97.04	56.47	47.4	95.79	0.4015
-13	69.419	95.21	59.91	48.62	92.63	0.4146
-12.5	71.5596	93.17	64.66	50.6	88.42	0.4348
-12	75.2294	92.66	70.69	54.67	86.32	0.4868
-11.5	75.2294	89.53	73.71	55.15	78.95	0.467

Table C.6: ASAR 10 May 2009

Threshold value	Overall Accuracy	User's accuracy flooded	Producer's accuracy flooded	User's accuracy non-flooded	Producer's accuracy non-flooded	Kappa
-13.5	79.3548	100	58.97	70.64	100	0.5882
-13	82.5806	100	65.38	74.04	100	0.6524
-12.5	84.5161	100	69.23	76.24	100	0.6909
-12	86.4516	98.31	74.36	79.17	98.7	0.7294
-11.5	86.4516	93.85	78.21	81.11	94.81	0.7293
-11	87.741	90.41	84.62	85.37	90.91	0.7549
-10.5	87.7419	87.34	88.46	88.16	87.01	0.7548

Table C.7: ASAR 11 May 2009

Threshold value	Overall Accuracy	User's accuracy flooded	Producer's accuracy flooded	User's accuracy non-flooded	Producer's accuracy non-flooded	Kappa
-17	76.129	100	52.56	67.54	100	0.524
-16.5	79.3548	100	58.97	70.64	100	0.5882
-16	83.2258	100	66.67	74.76	100	0.6652
-15.5	84.5161	100	69.23	76.24	100	0.6909
-15	84.5161	100	69.23	76.24	100	0.6909
-14.5	85.8065	100	71.79	77.78	100	0.7166
-14	87.7419	100	75.64	80.21	100	0.7552
-13.5	88.3871	100	76.92	81.05	100	0.7681
-13	89.0323	98.41	79.49	82.61	98.7	0.7809
-12.5	87.7419	92.75	82.05	83.72	93.51	0.755
-12	85.8065	86.84	84.62	84.81	87.01	0.7162

Table C.8: ASAR 14 May 2009

Threshold value	Overall Accuracy	User's accuracy flooded	Producer's accuracy flooded	User's accuracy non-flooded	Producer's accuracy non-flooded	Kappa
-15	72.2581	100	44.87	64.17	100	0.4471
-14.5	74.1935	100	48.72	65.81	100	0.4856
-14	77.4194	97.78	56.41	69.09	98.7	0.5496
-13.5	81.2903	98.04	64.1	73.08	98.7	0.6266
-13	82.5806	98.11	66.67	74.51	98.7	0.6523
-12.5	82.5806	94.74	69.23	75.51	96.1	0.6522
-12	85.8065	91.18	79.49	81.61	92.21	0.7164
-11.5	85.8065	85	87.18	86.67	84.42	0.7161

Table C.9: ASAR 29 May 2009

Threshold value	Overall Accuracy	User's accuracy flooded	Producer's accuracy flooded	User's accuracy non-flooded	Producer's accuracy non-flooded	Kappa
-14.5	79.5775	97.62	59.42	72	98.63	0.5868
-14	80.2817	95.56	62.32	73.2	97.26	0.6015
-13.5	80.2817	90.2	66.67	74.73	93.15	0.6025
-13	81.6901	89.09	71.01	77.01	91.78	0.6315
-12.5	82.3944	87.93	73.91	78.57	90.41	0.6461
-12	79.5775	82.26	73.91	77.5	84.93	0.5901
-11.5	79.5775	82.26	73.91	77.5	84.93	0.5901

Table C.10: ASAR 30 May 2009

Threshold value	Overall Accuracy	User's accuracy flooded	Producer's accuracy flooded	User's accuracy non-flooded	Producer's accuracy non-flooded	Kappa
-16.5	71.831	96.77	43.48	64.86	98.63	0.4275
-16	77.4648	97.44	55.07	69.9	98.63	0.5435
-15.5	80.9859	97.73	62.32	73.47	98.63	0.6156
-15	81.6901	97.78	63.77	74.23	98.63	0.63
-14.5	82.3944	97.83	65.22	75	98.63	0.6444
-14	82.3944	92.31	69.57	76.67	94.52	0.6452
-13.5	81.6901	87.72	72.46	77.65	90.41	0.6318
-13	80.2817	83.61	73.91	77.78	86.3	0.6041
-12.5	78.169	78.79	75.36	77.63	80.82	0.5625

Table C.11: PALSAR 19 March 2009 (1) – HH-polarisation

Threshold value	Overall Accuracy	User's accuracy flooded	Producer's accuracy flooded	User's accuracy non-flooded	Producer's accuracy non-flooded	Kappa
-21	86.4407	100	70.91	79.75	100	0.7224
-20.5	85.5932	97.5	70.91	79.49	98.41	0.7054
-20	87.2881	97.62	74.55	81.58	98.41	0.7407
-19.5	87.2881	95.45	76.36	82.43	96.83	0.7413
-19	87.2881	93.48	78.18	83.33	95.24	0.7419
-18.5	88.1356	93.62	80	84.51	95.24	0.7594
-18	88.9831	93.75	81.82	85.71	95.24	0.7768
-17.5	89.8305	93.88	83.64	86.96	95.24	0.7942
-17	88.9831	92	83.64	86.76	93.65	0.7774

Table C.12: PALSAR 19 March 2009 (1) – HV-polarisation

Threshold value	Overall Accuracy	User's accuracy flooded	Producer's accuracy flooded	User's accuracy non-flooded	Producer's accuracy non-flooded	Kappa
-28.5	89.8305	92.16	85.45	88.06	93.65	0.7947
-28	89.8305	89.09	89.09	90.48	90.48	0.7957
-27.5	90.678	89.29	90.91	91.94	90.48	0.8129
-27	90.678	89.29	90.91	91.94	90.48	0.8129
-26.5	88.9831	86.21	90.91	91.67	87.3	0.7794
-26	87.2881	83.33	90.91	91.38	84.13	0.7461

Table C.13: PALSAR 19 March 2009 (1) – VH-polarisation

Threshold value	Overall Accuracy	User's accuracy flooded	Producer's accuracy flooded	User's accuracy non-flooded	Producer's accuracy non-flooded	Kappa
-28	88.9831	88.89	87.27	89.06	90.48	0.7784
-27.5	89.8305	89.09	89.09	90.48	90.48	0.7957
-27	88.1356	85.96	89.09	90.16	87.3	0.7622
-26.5	88.9831	86.21	90.91	91.67	87.3	0.7794
-26	88.1356	84.75	90.91	91.53	85.71	0.7627

Table C.14: PALSAR 19 March 2009 (1) – VV-polarisation

Threshold value	Overall Accuracy	User's accuracy flooded	Producer's accuracy flooded	User's accuracy non-flooded	Producer's accuracy non-flooded	Kappa
-22.5	83.8983	100	65.45	76.83	100	0.6692
-22	84.7458	97.44	69.09	78.48	98.41	0.6877
-21.5	84.7458	95.12	70.91	79.22	96.83	0.6885
-21	85.5932	93.18	74.55	81.08	95.24	0.7068
-20.5	85.5932	93.18	74.55	81.08	95.24	0.7068
-20	85.5932	93.18	74.55	81.08	95.24	0.7068
-19.5	83.8983	89.13	74.55	80.56	92.06	0.6731
-19	85.5932	89.58	78.18	82.86	92.06	0.7082
-18.5	85.5932	89.58	78.18	82.86	92.06	0.7082
-18	84.7458	87.76	78.18	82.61	90.48	0.6914
-17.5	83.0508	83.02	80	83.08	85.71	0.6587

Table C.15: PALSAR 19 March 2009 (2) – HH-polarisation

Threshold value	Overall Accuracy	User's accuracy flooded	Producer's accuracy flooded	User's accuracy non-flooded	Producer's accuracy non-flooded	Kappa
-22.5	83.5165	96.88	68.89	76.27	97.83	0.6693
-22	85.7143	97.06	73.33	78.95	97.83	0.7135
-21.5	87.9121	97.22	77.78	81.82	97.83	0.7577
-21	89.011	97.3	80	83.33	97.83	0.7798
-20.5	87.9121	94.74	80	83.02	95.65	0.7578
-20	87.9121	92.5	82.22	84.31	93.48	0.7579
-19.5	85.7143	88.1	82.22	83.67	89.13	0.714
-19	86.8132	88.37	84.44	85.42	89.13	0.7361
-18.5	86.8132	88.37	84.44	85.42	89.13	0.7361
-18	87.9121	88.64	86.67	87.23	89.13	0.7582
-17.5	85.7143	84.78	86.67	86.67	84.78	0.7143
-17	85.7143	84.78	86.67	86.67	84.78	0.7143
-16.5	85.7143	83.33	88.89	88.37	82.61	0.7145
-16	83.5165	80	88.89	87.8	78.26	0.6707
-15.5	83.5165	80	88.89	87.8	78.26	0.6707
-15	82.4176	78.43	88.89	87.5	76.09	0.6488
-14.5	81.3187	75.93	91.11	89.19	71.74	0.6271

Table C.16: PALSAR 19 March 2009 (2) – HV-polarisation

Threshold value	Overall Accuracy	User's accuracy flooded	Producer's accuracy flooded	User's accuracy non-flooded	Producer's accuracy non-flooded	Kappa
-28	84.6154	86.05	82.22	83.33	86.96	0.6921
-27.5	83.5165	82.61	84.44	84.44	82.61	0.6704
-27	84.6154	81.63	88.89	88.1	80.43	0.6926
-26.5	82.4176	78.43	88.89	87.5	76.09	0.6488
-26	82.4176	78.43	88.89	87.5	76.09	0.6488
-25.5	80.2198	74.55	91.11	88.89	69.57	0.6053
-25	81.3187	75.93	91.11	89.19	71.74	0.6271
-24.5	80.2198	74.55	91.11	88.89	69.57	0.6053
-24	80.2198	74.55	91.11	88.89	69.57	0.6053
-23.5	76.9231	70.69	91.11	87.88	63.04	0.5399
-23	74.7253	68.33	91.11	87.1	58.7	0.4963

Table C.17: PALSAR 19 March 2009 (2) – VH-polarisation

Threshold value	Overall Accuracy	User's accuracy flooded	Producer's accuracy flooded	User's accuracy non-flooded	Producer's accuracy non-flooded	Kappa
-27.5	84.6154	84.44	84.44	84.78	84.78	0.6923
-27	85.7143	84.78	86.67	86.67	84.78	0.7143
-26.5	85.7143	84.78	86.67	86.67	84.78	0.7143
-26	84.6154	81.63	88.89	88.1	80.43	0.6926
-25.5	83.5165	80	88.89	87.8	78.26	0.6707
-25	80.2198	75.47	88.89	86.84	71.74	0.6051
-24.5	79.1209	74.07	88.89	86.49	69.57	0.5833
-24	79.1209	73.21	91.11	88.57	67.39	0.5835
-23.5	79.1209	72.41	93.33	90.91	65.22	0.5837

Table C.18: PALSAR 19 March 2009 (2) – VV-polarisation

Threshold value	Overall Accuracy	User's accuracy flooded	Producer's accuracy flooded	User's accuracy non-flooded	Producer's accuracy non-flooded	Kappa
-24.5	86.8132	92.31	80	82.69	93.48	0.7358
-24	85.7143	90	80	82.35	91.3	0.7139
-23.5	86.8132	90.24	82.22	84	91.3	0.736
-23	86.8132	90.24	82.22	84	91.3	0.736
-22.5	87.9121	90.48	84.44	85.71	91.3	0.758
-22	86.8132	88.37	84.44	85.42	89.13	0.7361
-21.5	86.8132	88.37	84.44	85.42	89.13	0.7361
-21	87.9121	88.64	86.67	87.23	89.13	0.7582
-20.5	86.8132	88.37	84.44	85.42	89.13	0.7361
-20	84.6154	81.63	88.89	88.1	80.43	0.6926
-19.5	84.6154	81.63	88.89	88.1	80.43	0.6926
-19	83.5165	80	88.89	87.8	78.26	0.6707
-18.5	82.4176	78.43	88.89	87.5	76.09	0.6488
-18	83.5165	78.85	91.11	89.74	76.09	0.6708
-17.5	83.5165	78.85	91.11	89.74	76.09	0.6708
-17	83.5165	77.78	93.33	91.89	73.91	0.671
-16.5	82.4176	76.36	93.33	91.67	71.74	0.6492
-16	82.4176	76.36	93.33	91.67	71.74	0.6492

Table C.19: 5 April 2009 – HH-polarisation

Threshold value	Overall Accuracy	User's accuracy flooded	Producer's accuracy flooded	User's accuracy non-flooded	Producer's accuracy non-flooded	Kappa
-22	47.5	100	10	44.25	100	0.0847
-21.5	48.3333	100	11.43	44.64	100	0.0971
-21	48.3333	100	11.43	44.64	100	0.0971
-20.5	49.1667	100	12.86	45.05	100	0.1095
-20	51.6667	100	17.14	46.3	100	0.1471
-19.5	51.6667	92.86	18.57	46.23	98	0.1429
-19	52.5	93.33	20	46.67	98	0.1556
-18.5	54.1667	94.12	22.86	47.57	98	0.1811
-18	54.1667	89.47	24.29	47.52	96	0.1771
-17.5	55	86.36	27.14	47.96	94	0.1859
-17	56.6667	87.5	30	48.96	94	0.2121
-16.5	56.6667	80	34.29	48.89	88	0.2
-16	56.6667	75	38.57	48.81	82	0.1875

: Table C.20 PALSAR 5 April 2009 – HV-polarisation

Threshold value	Overall Accuracy	User's accuracy flooded	Producer's accuracy flooded	User's accuracy non-flooded	Producer's accuracy non-flooded	Kappa
-27.5	80.8333	94.34	71.43	70.15	94	0.624
-27	81.6667	94.44	72.86	71.21	94	0.6393
-26.5	81.6667	92.86	74.29	71.88	92	0.6374
-26	82.5	91.53	77.14	73.77	90	0.651
-25.5	81.6667	88.71	78.57	74.14	86	0.6313
-25	82.5	88.89	80	75.44	86	0.6471
-24.5	83.3333	89.06	81.43	76.79	86	0.6629
-24	81.6667	86.36	81.43	75.93	82	0.6271
-23.5	80.8333	84.06	82.86	76.47	78	0.6068

Table C.21: PALSAR 5 April 2009 – VH-polarisation

Threshold value	Overall Accuracy	User's accuracy flooded	Producer's accuracy flooded	User's accuracy non-flooded	Producer's accuracy non-flooded	Kappa
-27.5	81.6667	96.15	71.43	70.59	96	0.6413
-27	81.6667	96.15	71.43	70.59	96	0.6413
-26.5	82.5	94.55	74.29	72.31	94	0.6548
-26	83.3333	94.64	75.71	73.44	94	0.6703
-25.5	81.6667	90	77.14	73.33	88	0.6333
-25	83.3333	90.32	80	75.86	88	0.6648
-24.5	85.8333	90.77	84.29	80	88	0.7127
-24	85	88.24	85.71	80.77	84	0.6932

Table C.22: PALSAR 5 April 2009 – VV-polarisation

Threshold value	Overall Accuracy	User's accuracy flooded	Producer's accuracy flooded	User's accuracy non-flooded	Producer's accuracy non-flooded	Kappa
-22.5	49.1667	90.91	14.29	44.95	98	0.1051
-22	50	91.67	15.71	45.37	98	0.1176
-21.5	51.6667	92.86	18.57	46.23	98	0.1429
-21	53.3333	93.75	21.43	47.12	98	0.1683
-20.5	53.3333	93.75	21.43	47.12	98	0.1683
-20	52.5	88.24	21.43	46.6	96	0.1514
-19.5	52.5	88.24	21.43	46.6	96	0.1514
-19	54.1667	85.71	25.71	47.47	94	0.1729
-18.5	53.3333	79.17	27.14	46.88	90	0.1515
-18	53.3333	79.17	27.14	46.88	90	0.1515

APPENDIX D

Confusion matrices for the best threshold values and the ACMs

D.1: THRESHOLDS

Table D.1: ASAR WSM 17 March 2009. Threshold – -8.5 dB

		Reference data				
		Non-flooded	**Flooded**	**Totals**	**User's accuracy (%)**	**Error of commission (%)**
Classified image	**Non-flooded**	63	23	86	73	27
	Flooded	1	47	48	98	2
	Totals	64	70	134		
	Producer's accuracy (%)	98	67			
	Error of omission (%)	2	33			
	Overall accuracy (%)	82				
	Kappa	0.65				

Table D.2: ASAR WSM 20 March 2009. Threshold – -12 dB

		Reference data				
		Non-flooded	**Flooded**	**Totals**	**User's accuracy (%)**	**Error of commission (%)**
Classified image	**Non-flooded**	64	2	66	97	3
	Flooded	0	68	68	100	0
	Totals	64	70	134		
	Producer's accuracy (%)	100	97			
	Error of omission (%)	0	3			
	Overall accuracy (%)	99				
	Kappa	0.97				

Table D.3: ASAR WSM 23 March 2009. Threshold – -12 dB

		Reference data				
		Non-flooded	**Flooded**	**Totals**	**User's accuracy (%)**	**Error of commission (%)**
Classified image	**Non-flooded**	101	46	147	69	31
	Flooded	14	147	161	91	9
	Totals	115	193			
	Producer's accuracy (%)	88	76			
	Error of omission (%)	12	24			
	Overall accuracy (%)	81				
	Kappa	0.61				

Table D.4: ASAR WSM 24 March 2009.Threshold – -10 dB

		Reference data				
		Non-flooded	**Flooded**	**Totals**	**User's accuracy (%)**	**Error of commission (%)**
Classified image	**Non-flooded**	105	81	186	56	44
	Flooded	10	112	122	92	8
	Totals	115	193	308		
	Producer's accuracy (%)	91	58			
	Error of omission (%)	9	42			
	Overall accuracy (%)	70				
	Kappa	0.44				

Table D.5: ASAR WSM 25 April 2009. Threshold – -12 dB

		Reference data				
		Non-flooded	**Flooded**	**Totals**	**User's accuracy (%)**	**Error of commission (%)**
Classified image	**Non-flooded**	82	68	150	55	45
	Flooded	13	164	177	93	7
	Totals	95	232	327		
	Producer's accuracy (%)	86	71			
	Error of omission (%)	14	29			
	Overall accuracy (%)	75				
	Kappa	0.49				

Table D.6: ASAR WSM 10 May 2009. Threshold – -10.5 dB

		Reference data				
		Non-flooded	**Flooded**	**Totals**	**User's accuracy (%)**	**Error of commission (%)**
Classified image	**Non-flooded**	67	9	76	88	12
	Flooded	10	69	79	87	13
	Totals	77	78	155		
	Producer's accuracy (%)	87	88			
	Error of omission (%)	13	12			
	Overall accuracy (%)	88				
	Kappa	0.75				

Table D.7: ASAR WSM 11 May 2009. Threshold – -13 dB

		Reference data				
		Non-flooded	**Flooded**	**Totals**	**User's accuracy (%)**	**Error of commission (%)**
Classified image	**Non-flooded**	76	16	92	83	17
	Flooded	1	62	63	98	2
	Totals	77	78	155		
	Producer's accuracy (%)	99	79			
	Error of omission (%)	1	21			
	Overall accuracy (%)	89				
	Kappa	0.78				

Table D.8: ASAR WSM 14 May 2009. Threshold – -12 dB

		Reference data				
		Non-flooded	**Flooded**	**Totals**	**User's accuracy (%)**	**Error of commission (%)**
Classified image	**Non-flooded**	71	16	87	82	18
	Flooded	6	62	68	91	9
	Totals	77	78	155		
	Producer's accuracy (%)	92	79			
	Error of omission (%)	8	21			
	Overall accuracy (%)	86				
	Kappa	0.72				

Table D.9: ASAR WSM 29 May 2009. Threshold – -12.5 dB

		Reference data				
		Non-flooded	**Flooded**	**Totals**	**User's accuracy (%)**	**Error of commission (%)**
Classified image	**Non-flooded**	66	18	84	79	21
	Flooded	7	51	58	88	12
	Totals	73	69	142		
	Producer's accuracy (%)	90	74			
	Error of omission (%)		26			
	Overall accuracy (%)	82				
	Kappa	0.65				

Table D.10: ASAR WSM 30 May 2009. Threshold – -14 dB

		Reference data				
		Non-flooded	**Flooded**	**Totals**	**User's accuracy (%)**	**Error of commission (%)**
Classified image	**Non-flooded**	69	21	90	77	23
	Flooded	4	48	52	92	8
	Totals	73	69	142		
	Producer's accuracy (%)	95	70			
	Error of omission (%)	5	30			
	Overall accuracy (%)	82				
	Kappa	0.65				

Table D.11: PALSAR 19 March 2009 (1) – HH-polarisation. Threshold – -17.5 dB

		Reference data				
		Non-flooded	**Flooded**	**Totals**	**User's accuracy (%)**	**Error of commission (%)**
Classified image	**Non-flooded**	60	9	69	87	13
	Flooded	3	46	47	94	6
	Totals	63	55	118		
	Producer's accuracy (%)	95	84			
	Error of omission (%)	5	16			
	Overall accuracy (%)	90				
	Kappa	0.79				

Table D.12: PALSAR 19 March 2009 (1) – HV-polarisation. Threshold – -27 dB

		Reference data				
		Non-flooded	**Flooded**	**Totals**	**User's accuracy (%)**	**Error of commission (%)**
Classified image	**Non-flooded**	57	5	62	92	8
	Flooded	6	50	56	89	11
	Totals	63	55	118		
	Producer's accuracy (%)	90	91			
	Error of omission (%)	10	9			
	Overall accuracy (%)	91				
	Kappa	0.81				

Table D.13: PALSAR 19 March 2009 (1) – VH-polarisation. Threshold – -27.5 dB

		Reference data				
		Non-flooded	**Flooded**	**Totals**	**User's accuracy (%)**	**Error of commission (%)**
Classified image	**Non-flooded**	57	6	63	90	10
	Flooded	6	49	55	89	11
	Totals	63	55	118		
	Producer's accuracy (%)	90	89			
	Error of omission (%)	10	11			
	Overall accuracy (%)	90				
	Kappa	0.80				

Table D.14: PALSAR 19 March 2009 (1) – VV-polarisation. Threshold – -19 dB

		Reference data				
		Non-flooded	**Flooded**	**Totals**	**User's accuracy (%)**	**Error of commission (%)**
Classified image	**Non-flooded**	58	12	70	83	17
	Flooded	5	43	48	90	10
	Totals	63	55	118		
	Producer's accuracy (%)	92	78			
	Error of omission (%)	8	22			
	Overall accuracy (%)	86				
	Kappa	0.71				

Table D.15: PALSAR 19 March 2009 (2) – HH-polarisation. Threshold – -21 dB

		Reference data				
		Non-flooded	**Flooded**	**Totals**	**User's accuracy (%)**	**Error of commission (%)**
Classified image	**Non-flooded**	45	9	54	83	17
	Flooded	1	36	37	97	3
	Totals	46	45	91		
	Producer's accuracy (%)	98	80			
	Error of omission (%)	2	20			
	Overall accuracy (%)	89				
	Kappa	0.78				

Table D.16: PALSAR 19 March 2009 (2) – HV-polarisation. Threshold – -27 dB

		Reference data				
		Non-flooded	**Flooded**	**Totals**	**User's accuracy (%)**	**Error of commission (%)**
Classified image	**Non-flooded**	37	5	42	88	12
	Flooded	9	40	49	82	18
	Totals	46	45	91		
	Producer's accuracy (%)	80	89			
	Error of omission (%)	20	11			
	Overall accuracy (%)	85				
	Kappa	0.69				

Table D.17: PALSAR 19 March 2009 (2) – VH-polarisation. Threshold – -27 dB

		Reference data				
		Non-flooded	**Flooded**	**Totals**	**User's accuracy (%)**	**Error of commission (%)**
Classified image	**Non-flooded**	39	6	45	87	13
	Flooded	7	39	46	85	15
	Totals	46	45	91		
	Producer's accuracy (%)	85	87			
	Error of omission (%)	15	13			
	Overall accuracy (%)	86				
	Kappa	0.71				

Table D.18: PALSAR 19 March 2009 (2) – VV-polarisation. Threshold – -21 dB

		Reference data				
		Non-flooded	**Flooded**	**Totals**	**User's accuracy (%)**	**Error of commission (%)**
Classified image	**Non-flooded**	41	6	47	87	13
	Flooded	5	39	44	89	11
	Totals	46	45	91		
	Producer's accuracy (%)	89	87			
	Error of omission (%)	11	13			
	Overall accuracy (%)	88				
	Kappa	0.76				

Table D.19: PALSAR 5 April 2009 HH-polarisation. Threshold – -17 dB

		Reference data				
		Non-flooded	**Flooded**	**Totals**	**User's accuracy (%)**	**Error of commission (%)**
Classified image	**Non-flooded**	47	49	96	49	51
	Flooded	3	21	24	88	12
	Totals	50	70	120		
	Producer's accuracy (%)	94	30			
	Error of omission (%)	6	70			
	Overall accuracy (%)	57				
	Kappa	0.21				

Table D.20: PALSAR 5 April 2009 – HV-polarisation. Threshold – -24.5 dB

		Reference data				
		Non-flooded	**Flooded**	**Totals**	**User's accuracy (%)**	**Error of commission (%)**
Classified image	**Non-flooded**	43	13	56	77	23
	Flooded	7	57	64	89	11
	Totals	50	70	120		
	Producer's accuracy (%)	86	81			
	Error of omission (%)	14	19			
	Overall accuracy (%)	83				
	Kappa	0.66				

Table D.21: PALSAR 5 April 2009 – VH-polarisation. Threshold – -24.5 dB

		Reference data				
		Non-flooded	**Flooded**	**Totals**	**User's accuracy (%)**	**Error of commission (%)**
Classified image	**Non-flooded**	44	11	55	80	20
	Flooded	6	59	65	91	9
	Totals	50	70	120		
	Producer's accuracy (%)	88	84			
	Error of omission (%)	12	16			
	Overall accuracy (%)	86				
	Kappa	0.71				

Table D.22: PALSAR 5 April 2009 VV-polarisation. Threshold – -19 dB

		Reference data				
		Non-flooded	**Flooded**	**Totals**	**User's accuracy (%)**	**Error of commission (%)**
Classified image	**Non-flooded**	47	52	99	47	53
	Flooded	3	18	21	86	14
	Totals	50	70	120		
	Producer's accuracy (%)	94	26			
	Error of omission (%)	6	74			
	Overall accuracy (%)	54				
	Kappa	0.17				

D.2: ACTIVE CONTOUR MODELS

Table D.23: ASAR WSM 17 March 2009. Iterations – 1000. Canny scalar –0.2

		Reference data				
		Non-flooded	**Flooded**	**Totals**	**User's accuracy (%)**	**Error of commission (%)**
Classified image	**Non-flooded**	63	16	79	80	20
	Flooded	1	54	55	98	2
	Totals	64	70	134		
	Producer's accuracy (%)	98	77			
	Error of omission (%)	2	23			
	Overall accuracy (%)	87				
	Kappa	0.75				

Table D.24: ASAR WSM 20 March 2009. Iterations – 1000. Canny scalar – 0.3

		Reference data				
		Non-flooded	**Flooded**	**Totals**	**User's accuracy (%)**	**Error of commission (%)**
Classified image	**Non-flooded**	64	3	67	96	4
	Flooded	0	67	67	100	0
	Totals	64	70	134		
	Producer's accuracy (%)	100	96			
	Error of omission (%)	0	4			
	Overall accuracy (%)	98				
	Kappa	0.96				

Table D.25: ASAR WSM 23 March 2009. Iterations – 1000. Canny scalar – 0.3

		Reference data				
		Non-flooded	**Flooded**	**Totals**	**User's accuracy (%)**	**Error of commission (%)**
Classified image	**Non-flooded**	115	89	204	56	44
	Flooded	0	104	104	100	0
	Totals	115	193	308		
	Producer's accuracy (%)	100	54			
	Error of omission (%)	0	46			
	Overall accuracy (%)	71				
	Kappa	0.47				

Table D.26: ASAR WSM 24 March 2009. Iterations – 1000. Canny scalar – 0.4

		Reference data				
		Non-flooded	**Flooded**	**Totals**	**User's accuracy (%)**	**Error of commission (%)**
Classified image	**Non-flooded**	113	127	240	47	53
	Flooded	2	66	68	97	3
	Totals	115	193	308		
	Producer's accuracy (%)	98	34			
	Error of omission (%)	2	66			
	Overall accuracy (%)	58				
	Kappa	0.27				

Table D.27: ASAR WSM 25 April 2009. Iterations – 1000. Canny scalar – 0.3

		Reference data				
		Non-flooded	**Flooded**	**Totals**	**User's accuracy (%)**	**Error of commission (%)**
Classified image	**Non-flooded**	93	106	199	47	53
	Flooded	2	126	128	98	2
	Totals	95	232	327		
	Producer's accuracy (%)	98	54			
	Error of omission (%)	2	46			
	Overall accuracy (%)	67				
	Kappa	0.39				

Table D.28: ASAR WSM 10 May 2009. Iterations – 1000. Canny scalar – 0.3

		Reference data				
		Non-flooded	**Flooded**	**Totals**	**User's accuracy (%)**	**Error of commission (%)**
Classified image	**Non-flooded**	55	0	55	100	0
	Flooded	23	77	100	77	23
	Totals	78	77	155		
	Producer's accuracy (%)	70	100			
	Error of omission (%)	30	0			
	Overall accuracy (%)	85				
	Kappa	0.70				

Table D.29: ASAR WSM 11 May 2009. Iterations – 1000. Canny scalar – 0.3

		Reference data				
		Non-flooded	**Flooded**	**Totals**	**User's accuracy (%)**	**Error of commission (%)**
Classified image	**Non-flooded**	77	23	100	77	23
	Flooded	0	55	55	100	0
	Totals	77	78	155		
	Producer's accuracy (%)	100	71			
	Error of omission (%)	0	29			
	Overall accuracy (%)	85				
	Kappa	0.70				

Table D.30: ASAR WSM 14 May 2009. Iterations – 1000. Canny scalar – 0.3

		Reference data				
		Non-flooded	**Flooded**	**Totals**	**User's accuracy (%)**	**Error of commission (%)**
Classified image	**Non-flooded**	76	27	103	74	26
	Flooded	1	52	52	98	2
	Totals	77	78	155		
	Producer's accuracy (%)	99	65			
	Error of omission (%)	1	35			
	Overall accuracy (%)	82				
	Kappa	0.64				

Table D.31: ASAR WSM 29 May 2009. Iterations – 1000. Canny scalar – 0.3

		Reference data				
		Non-flooded	**Flooded**	**Totals**	**User's accuracy (%)**	**Error of commission (%)**
Classified image	**Non-flooded**	44	3	47	94	6
	Flooded	25	70	95	74	26
	Totals	69	73	142		
	Producer's accuracy (%)	64	96			
	Error of omission (%)	36	4			
	Overall accuracy (%)	80				
	Kappa	0.60				

Table D.32 ASAR WSM 30 May 2009. Iterations – 1000. Canny scalar – 0.3

		Reference data				
		Non-flooded	**Flooded**	**Totals**	**User's accuracy (%)**	**Error of commission (%)**
Classified image	**Non-flooded**	46	2	48	76	4
	Flooded	23	71	94	96	24
	Totals	69	73	142		
	Producer's accuracy (%)	67	97			
	Error of omission (%)	33	3			
	Overall accuracy (%)	82				
	Kappa	0.64				

Table D.33: PALSAR 19 March 2009 (1) – HH-polarisation. Iterations – 200. Canny scalar – 0.3

		Reference data				
		Non-flooded	**Flooded**	**Totals**	**User's accuracy (%)**	**Error of commission (%)**
Classified image	**Non-flooded**	61	7	68	90	10
	Flooded	2	48	50	96	4
	Totals	63	55	118		
	Producer's accuracy (%)	97	87			
	Error of omission (%)	3	13			
	Overall accuracy (%)	92				
	Kappa	0.85				

Table D.34: PALSAR 19 March 2009 (1) – HV-polarisation. Iterations – 300. Canny scalar – 0.3

		Reference data				
		Non-flooded	**Flooded**	**Totals**	**User's accuracy (%)**	**Error of commission (%)**
Classified image	**Non-flooded**	61	3	64	95	5
	Flooded	2	52	54	96	4
	Totals	63	55	118		
	Producer's accuracy (%)	97	95			
	Error of omission (%)	3	5			
	Overall accuracy (%)	96				
	Kappa	0.91				

Table D.35: PALSAR 19 March 2009 (1) – VH-polarisation. Iterations – 1000. Canny scalar – 0.3

		Reference data				
		Non-flooded	**Flooded**	**Totals**	**User's accuracy (%)**	**Error of commission (%)**
Classified image	**Non-flooded**	53	3	56	95	5
	Flooded	10	52	62	84	16
	Totals	63	55	118		
	Producer's accuracy (%)	84	95			
	Error of omission (%)	16	5			
	Overall accuracy (%)	89				
	Kappa	0.78				

Table D.36: PALSAR 19 March 2009 (1) – VV-polarisation. Iterations – 500. Canny scalar – 0.3

		Reference data				
		Non-flooded	**Flooded**	**Totals**	**User's accuracy (%)**	**Error of commission (%)**
Classified image	**Non-flooded**	61	11	72	85	15
	Flooded	2	44	46	96	4
	Totals	63	55	118		
	Producer's accuracy (%)	97	80			
	Error of omission (%)	3	20			
	Overall accuracy (%)	89				
	Kappa	0.78				

Table D.37: PALSAR 19 March 2009 (2) – HH-polarisation. Iterations – 200. Canny scalar – 0.3

		Reference data				
		Non-flooded	**Flooded**	**Totals**	**User's accuracy (%)**	**Error of commission (%)**
Classified image	**Non-flooded**	39	4	43	91	9
	Flooded	7	41	48	85	15
	Totals	46	45	91		
	Producer's accuracy (%)	85	91			
	Error of omission (%)	15	9			
	Overall accuracy (%)	88				
	Kappa	0.76				

Table D.38: PALSAR 19 March 2009 (2) – HV-polarisation. Iterations – 200. Canny scalar – 0.3

		Reference data				
		Non-flooded	**Flooded**	**Totals**	**User's accuracy (%)**	**Error of commission (%)**
Classified image	**Non-flooded**	37	2	39	95	5
	Flooded	9	43	52	83	17
	Totals	46	45	91		
	Producer's accuracy (%)	80	96			
	Error of omission (%)	20	4			
	Overall accuracy (%)	88				
	Kappa	0.76				

Table D.39: PALSAR 19 March 2009 (2) – VH-polarisation. Iterations – 200. Canny scalar – 0.3

		Reference data				
		Non-flooded	**Flooded**	**Totals**	**User's accuracy (%)**	**Error of commission (%)**
Classified image	**Non-flooded**	38	2	40	95	5
	Flooded	8	43	51	84	16
	Totals	46	45	93		
	Producer's accuracy (%)	83	96			
	Error of omission (%)	17	4			
	Overall accuracy (%)	89				
	Kappa	0.78				

Table D.40: PALSAR 19 March 2009 (2) – VV-polarisation. Iterations – 200. Canny scalar – 0.3

		Reference data				
		Non-flooded	**Flooded**	**Totals**	**User's accuracy (%)**	**Error of commission (%)**
Classified image	**Non-flooded**	37	3	40	93	7
	Flooded	9	42	51	82	18
	Totals	46	45	91		
	Producer's accuracy (%)	80	93			
	Error of omission (%)	20	7			
	Overall accuracy (%)	87				
	Kappa	0.74				

Table D.41: PALSAR 5 April 2009 – HH-polarisation. Iterations – 100. Canny scalar – 0.3

		Reference data				
		Non-flooded	**Flooded**	**Totals**	**User's accuracy (%)**	**Error of commission (%)**
Classified image	**Non-flooded**	48	46	94	51	49
	Flooded	2	24	26	92	8
	Totals	50	70			
	Producer's accuracy (%)	96	34			
	Error of omission (%)	4	66			
	Overall accuracy (%)	60				
	Kappa	0.27				

Table D.42: PALSAR 5 April 2009 – HV-polarisation. Iterations – 700

		Reference data				
		Non-flooded	**Flooded**	**Totals**	**User's accuracy (%)**	**Error of commission (%)**
Classified image	**Non-flooded**					
	Flooded					
	Totals					
	Producer's accuracy (%)					
	Error of omission (%)					
	Overall accuracy (%)					
	Kappa					

Table D.43: PALSAR 5 April 2009 – VH-polarisation. Iterations – 200

		Reference data				
		Non-flooded	**Flooded**	**Totals**	**User's accuracy (%)**	**Error of commission (%)**
Classified image	**Non-flooded**	45	9	54	83	17
	Flooded	5	61	66	92	8
	Totals	50	70	120		
	Producer's accuracy (%)	90	87			
	Error of omission (%)	10	13			
	Overall accuracy (%)	88				
	Kappa	0.76				

Table D.44: PALSAR 5 April 2009 VV-polarisation. Iterations – 100

		Reference data				
		Non-flooded	**Flooded**	**Totals**	**User's accuracy (%)**	**Error of commission (%)**
Classified image	**Non-flooded**	48	46	94	51	49
	Flooded	2	24	26	92	8
	Totals	50	70	120		
	Producer's accuracy (%)	94	34			
	Error of omission (%)	4	66			
	Overall accuracy (%)	60				
	Kappa	0.27				

APPENDIX E

Classified maps of the best threshold values and the ACMs

D.1: THRESHOLDS

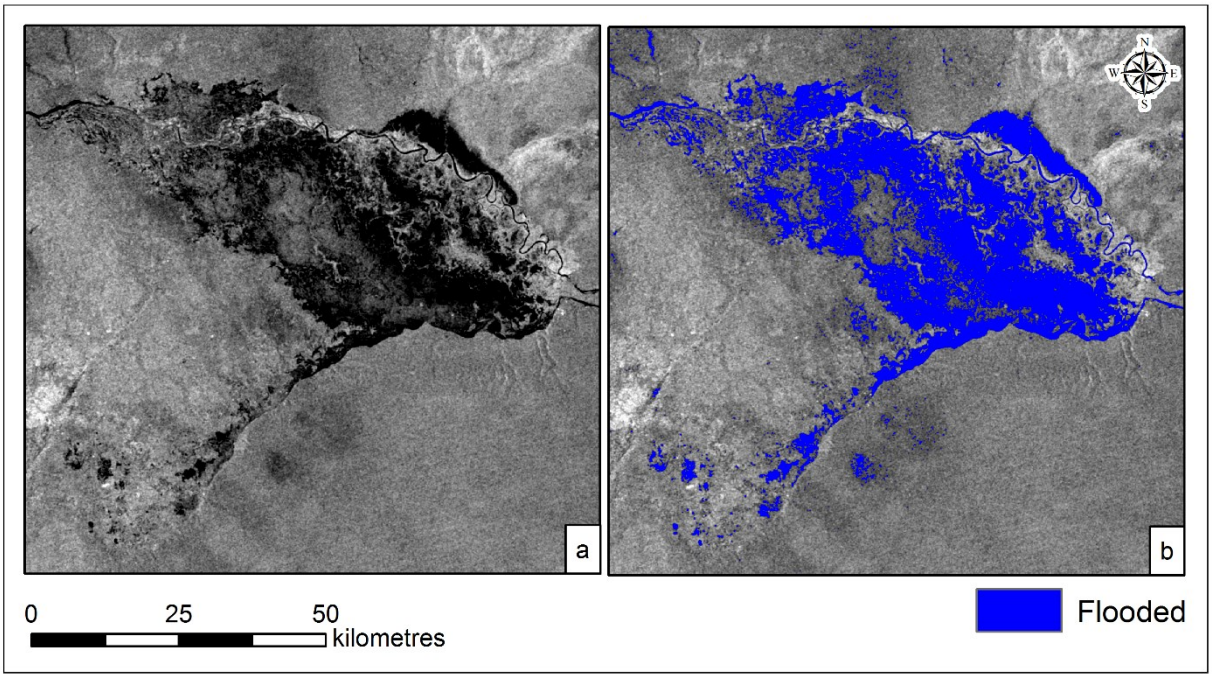

Figure E.1: Unclassified ASAR WSM 17 March 2009 (a). Classified image, threshold – -8.5 dB (b)

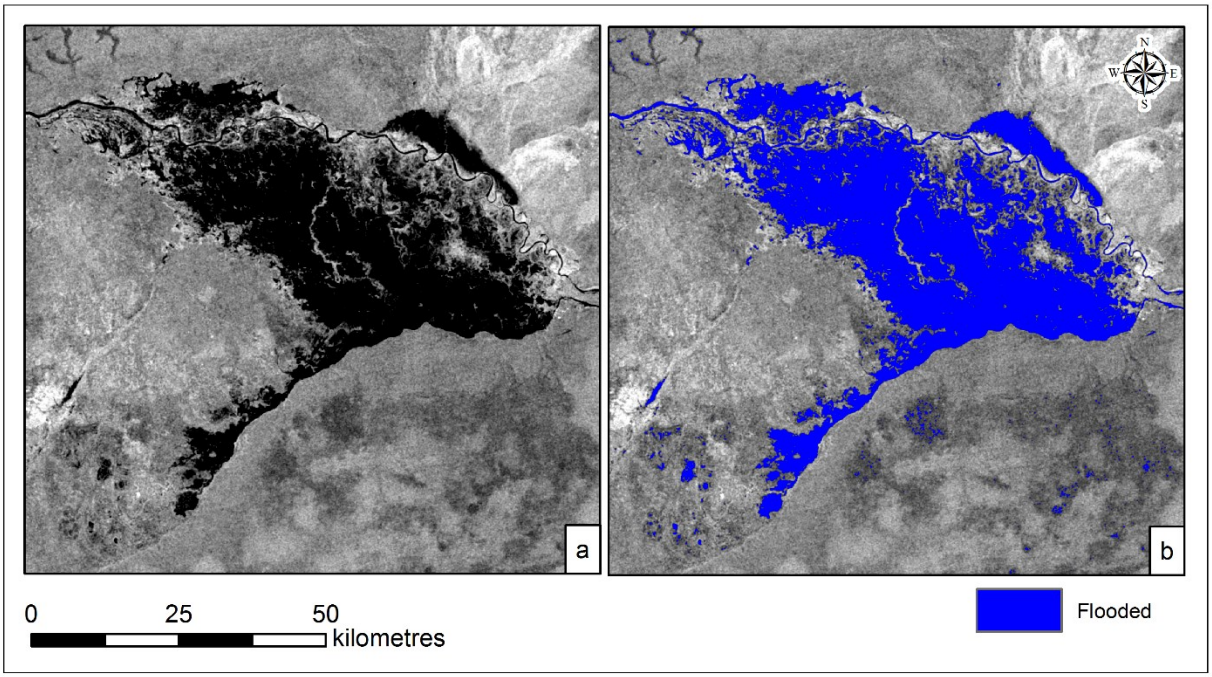

Figure E.2: Unclassified ASAR WSM 20 March 2009 (a). Classified image, threshold – -12 dB (b)

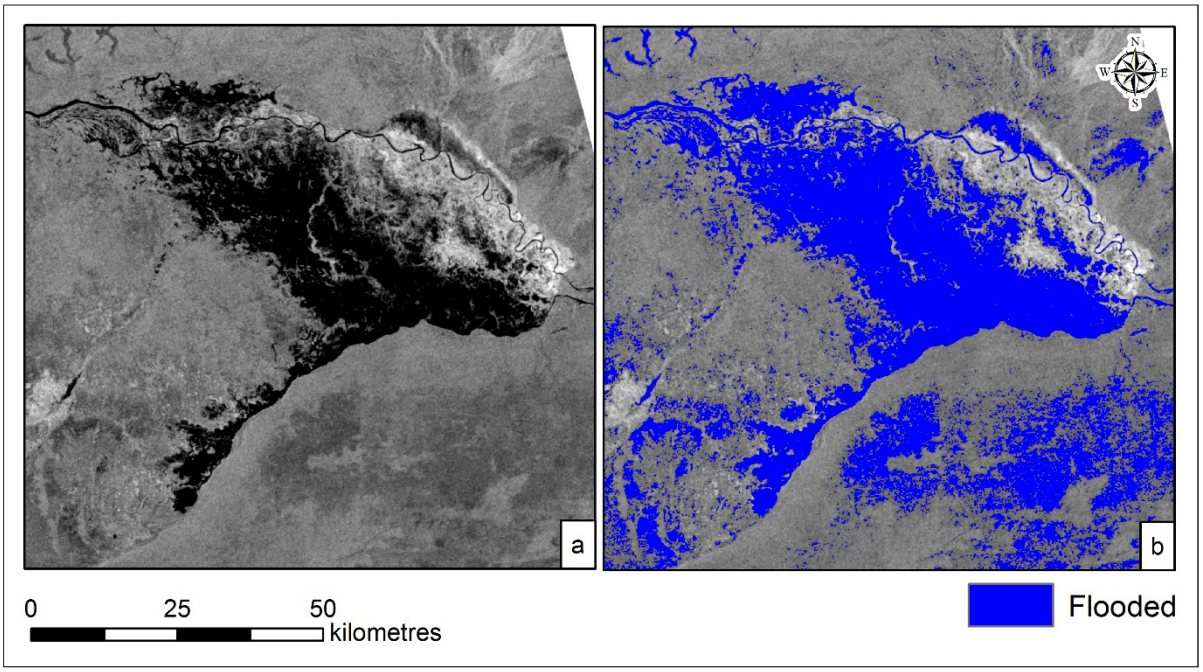

Figure E.3: Unclassified ASAR WSM 23 March 2009 (a). Classified image, threshold – -12 dB (b)

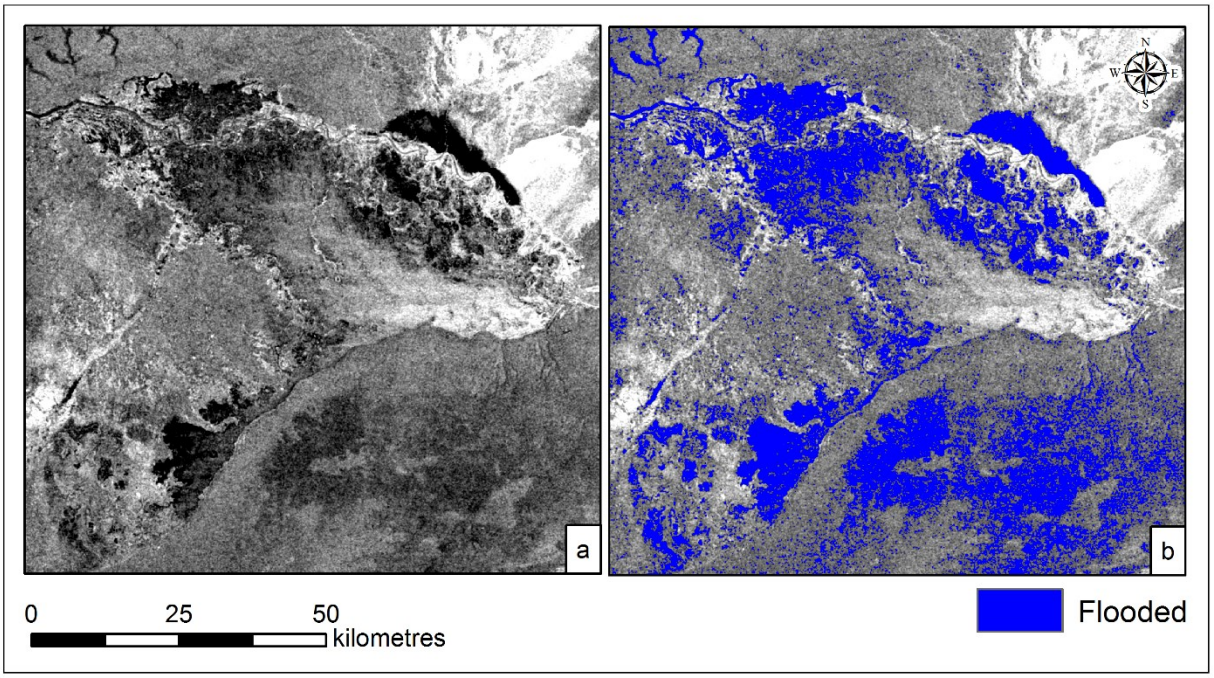

Figure E.4: Unclassified ASAR WSM 24 March 2009 (a). Classified image, threshold – -10 dB (b)

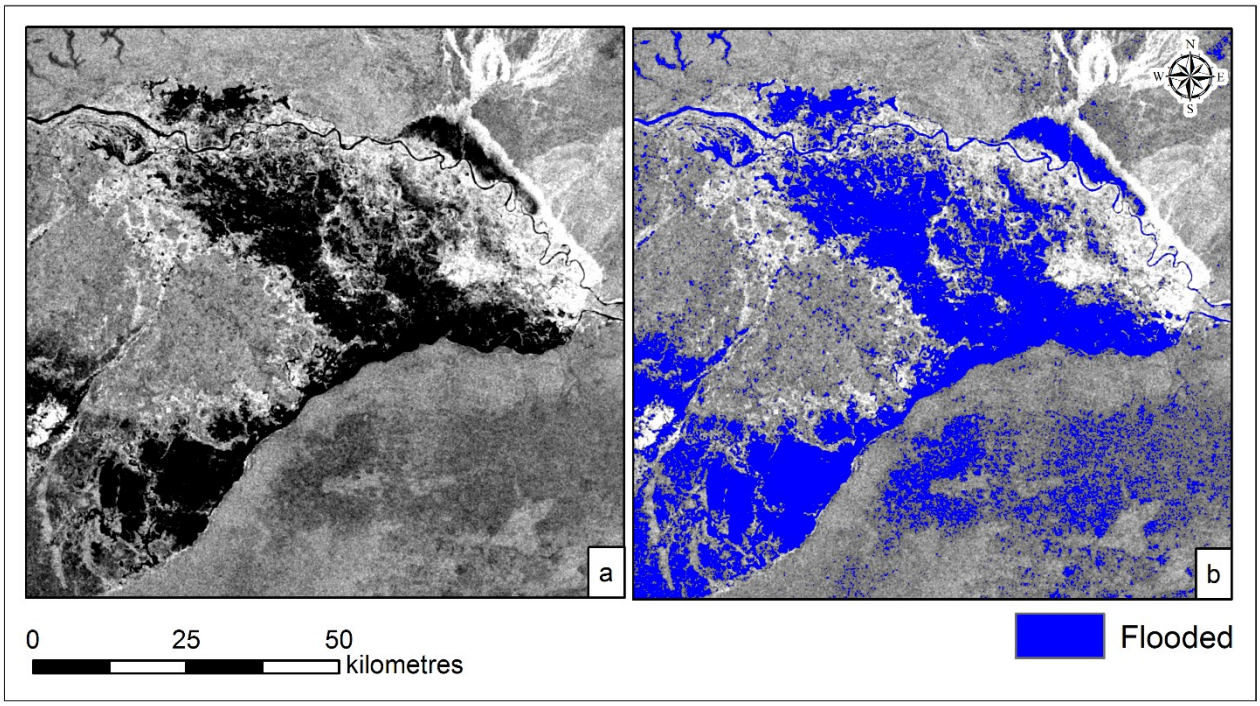

Figure E.5: Unclassified ASAR WSM 25 April 2009 (a). Classified image, threshold – -12 dB (b)

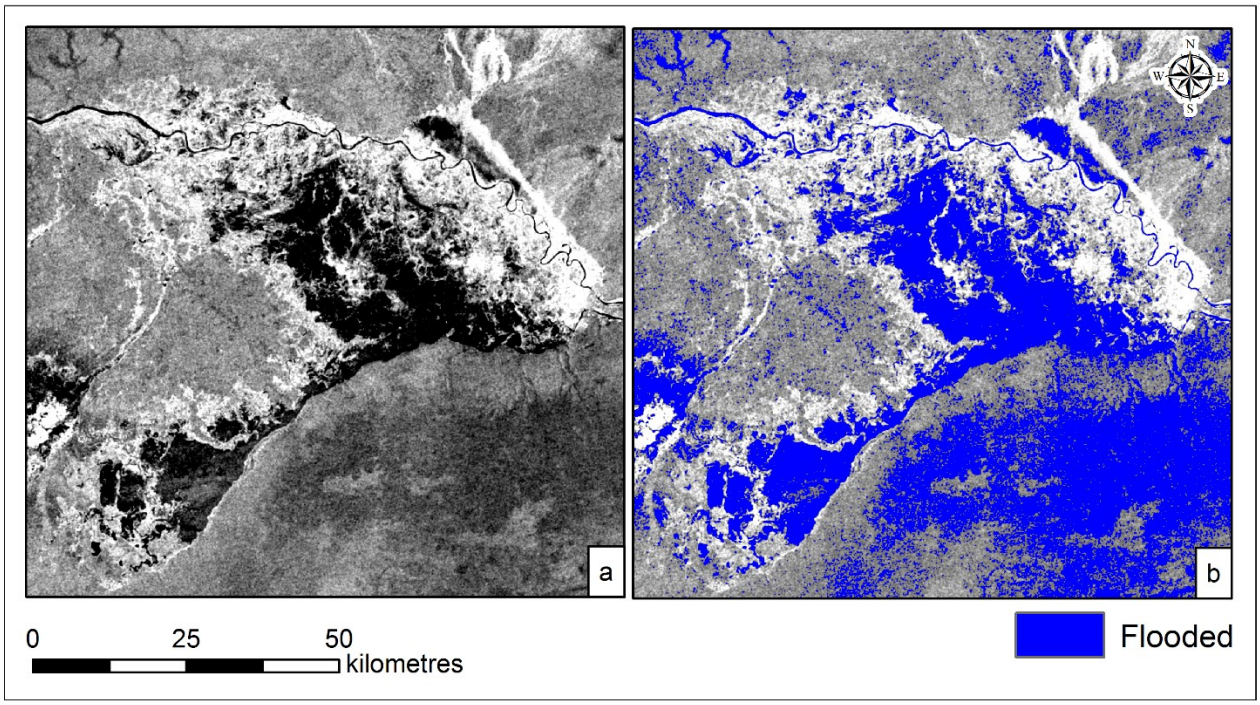

Figure E.6: Unclassified ASAR WSM 10 May 2009 (a). Classified image, threshold – -10.5 dB (b)

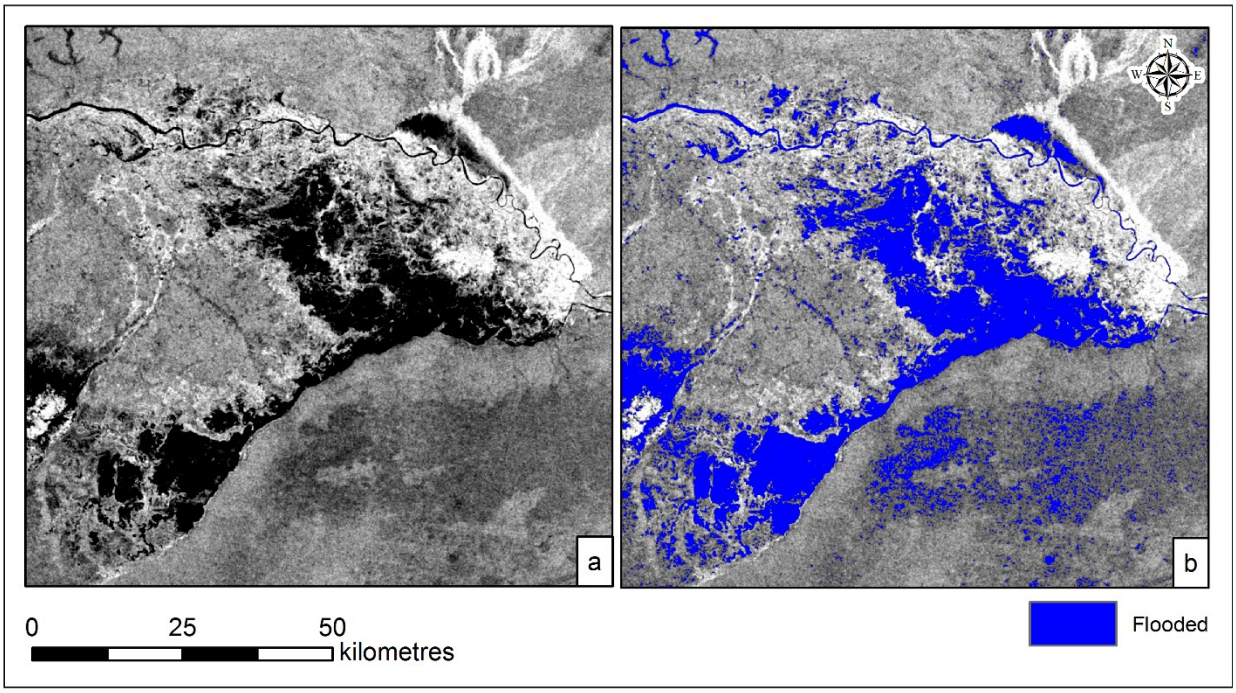

Figure E.7: Unclassified ASAR WSM 11 May 2009 (a). Classified image, threshold – -13 dB (b)

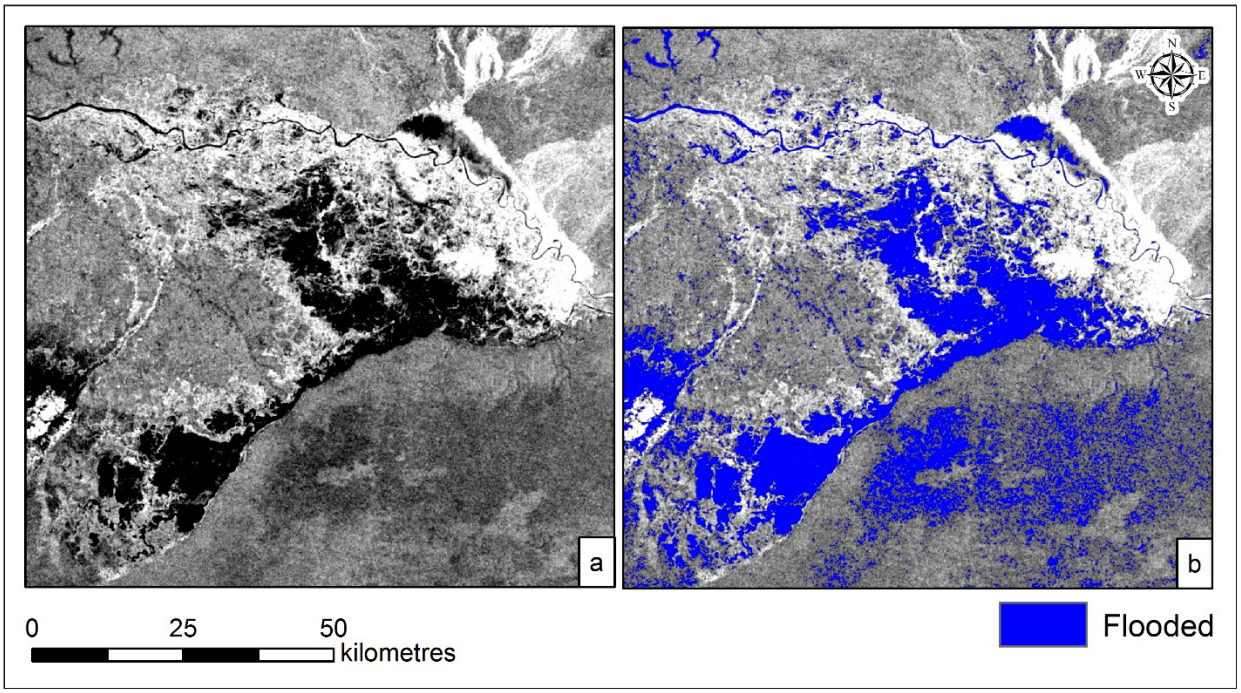

Figure E.8: Unclassified ASAR WSM 14 May 2009 (a). Classified image, threshold – -12 dB (b)

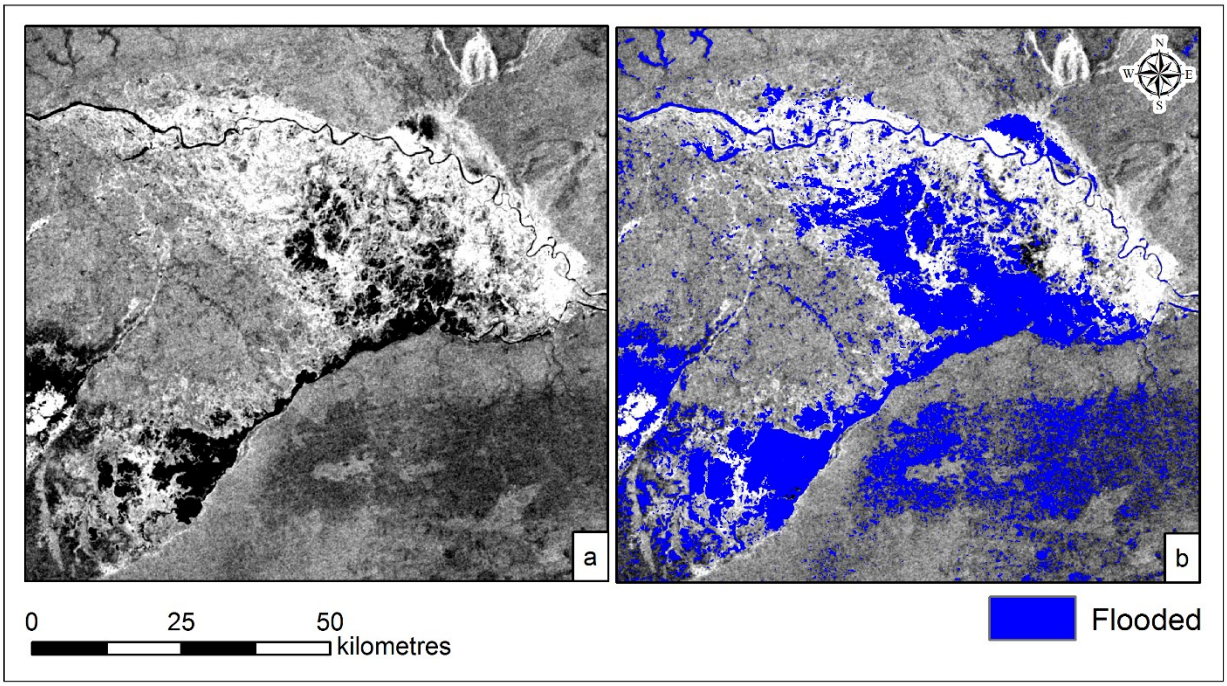

Figure E.9: Unclassified ASAR WSM 29 May 2009 (a). Classified image, threshold – -12.5 dB (b)

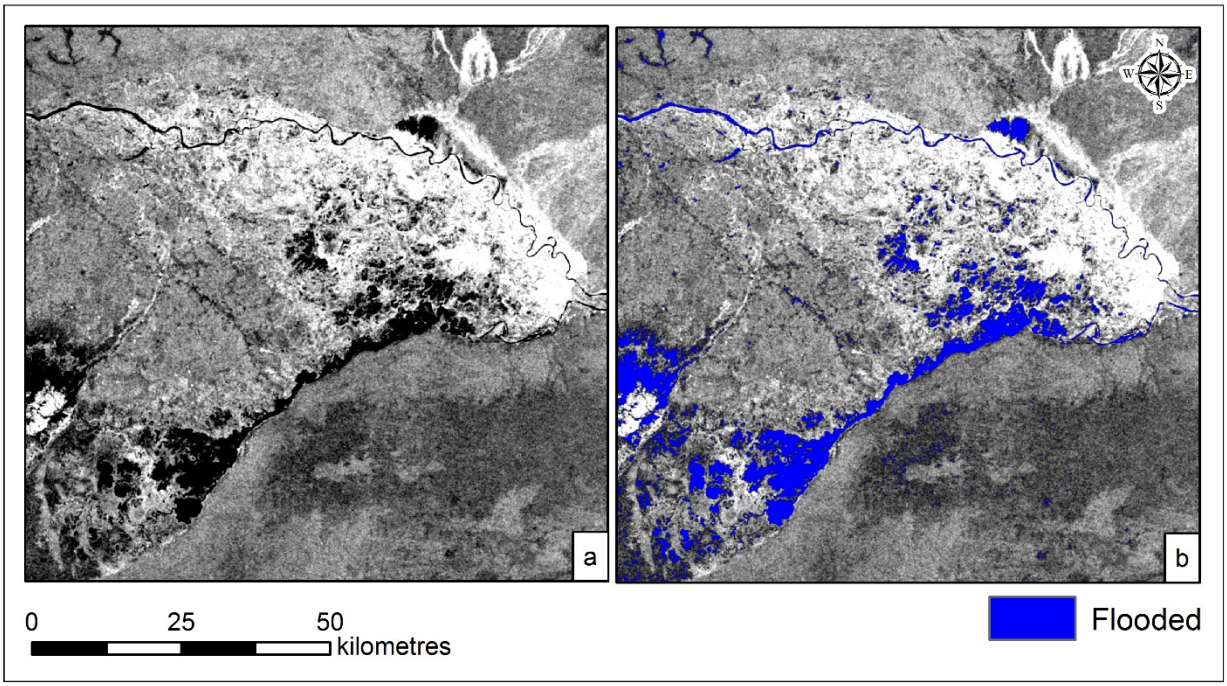

Figure E.10: Unclassified ASAR WSM 30 May 2009 (a). Classified image, threshold – -14 dB (b)

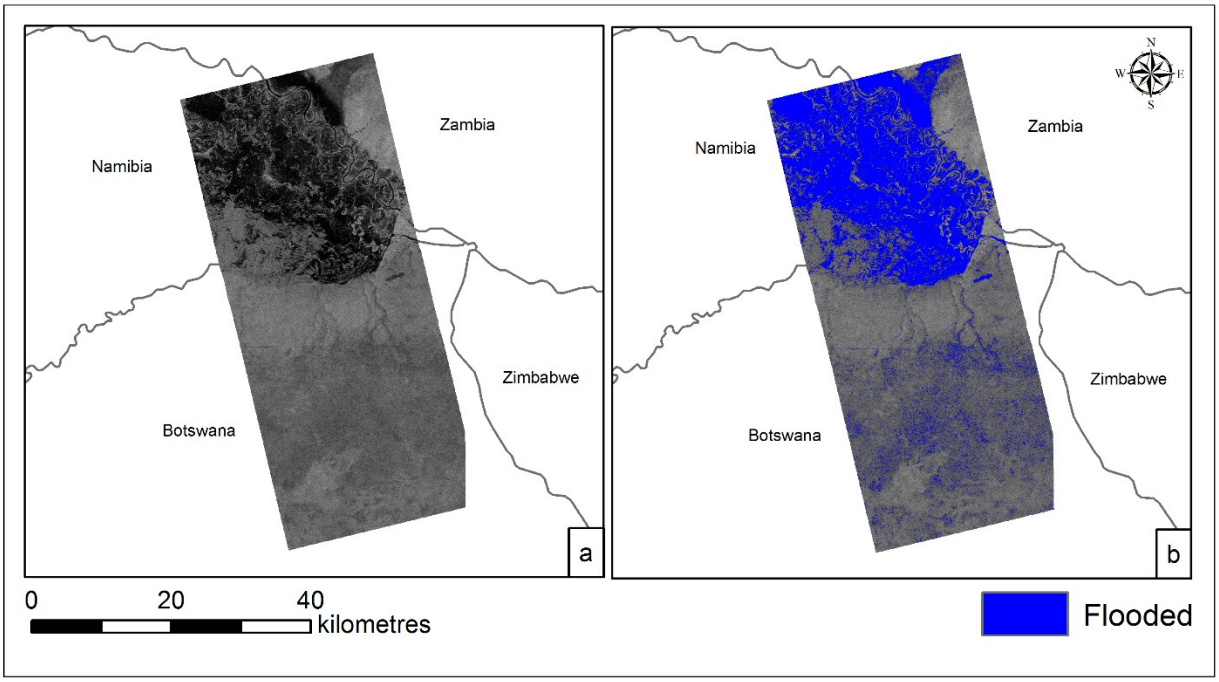

Figure E.11: Unclassified PALSAR PLR 19 March 2009 (1) – HH-polarisation (a). Classified image, threshold _– -17.5 dB (b). © ESA

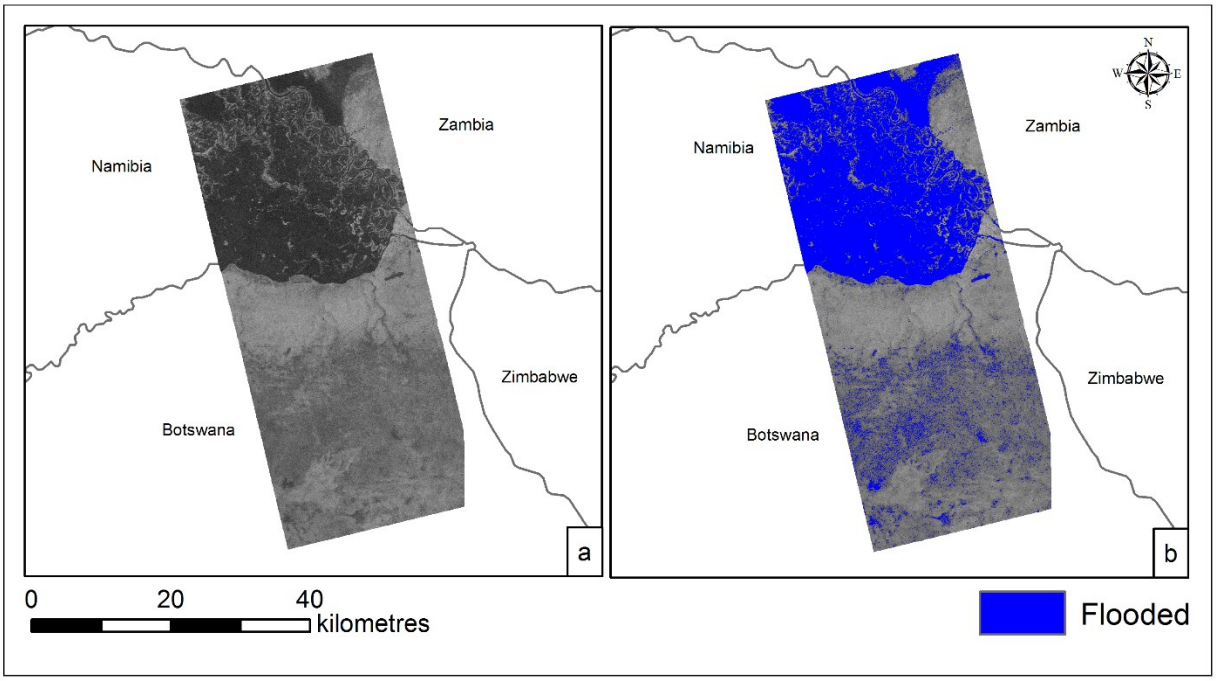

Figure E.12: Unclassified PALSAR PLR 19 March 2009 (1) – HV-polarisation (a). Classified image, threshold – -27 dB (b). © ESA

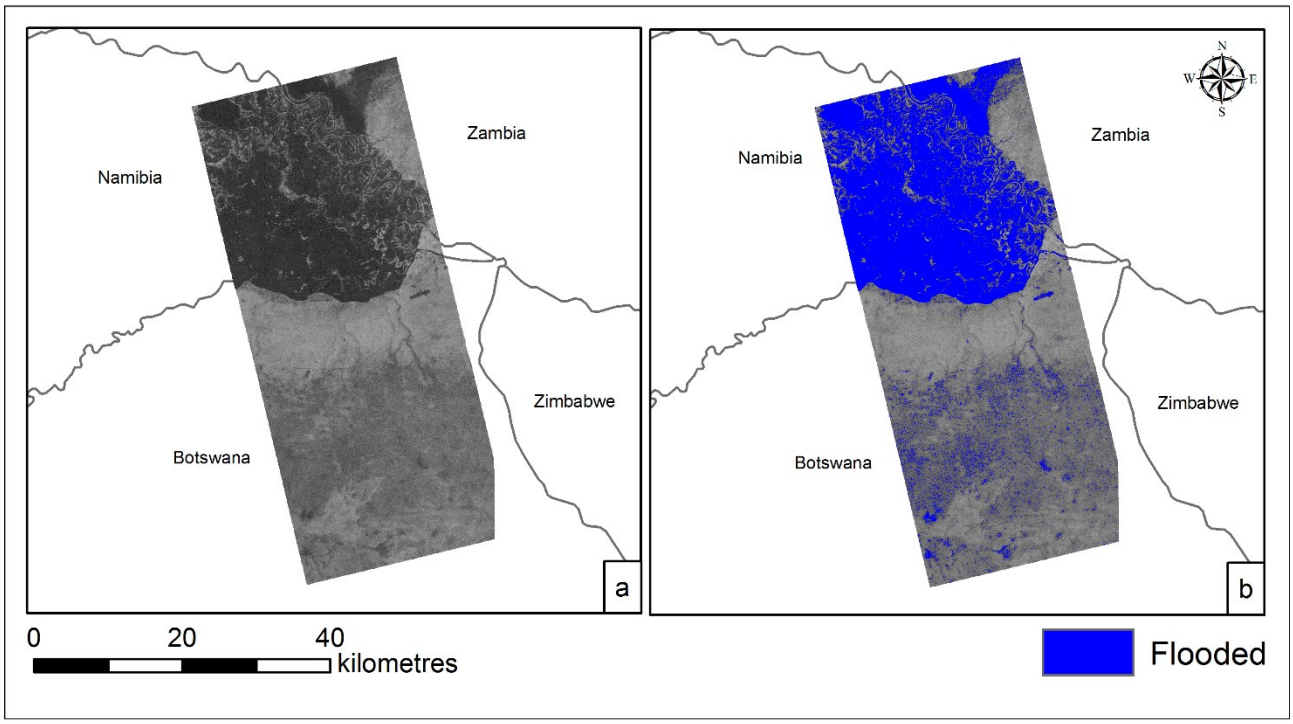

Figure E.13: Unclassified PALSAR PLR 19 March 2009 (1) – VH-polarisation (a). Classified image, threshold _– -27.5 dB (b). © ESA

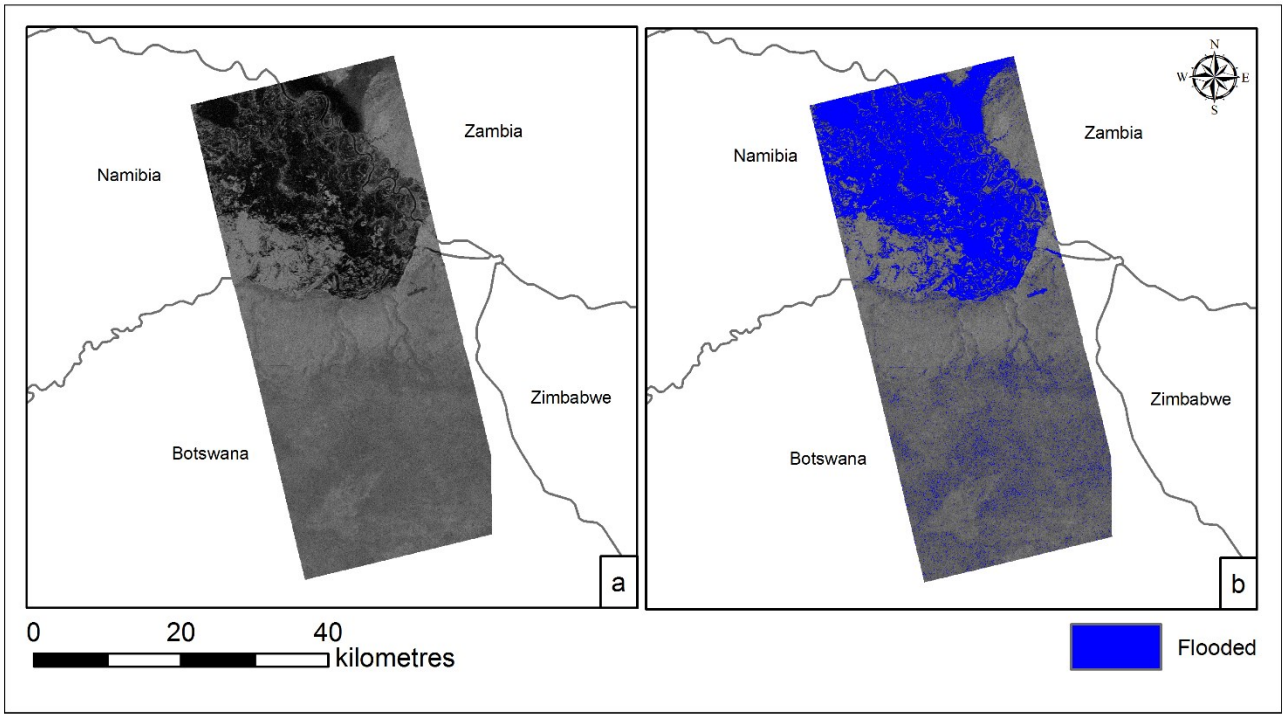

Figure E.14: Unclassified PALSAR PLR 19 March 2009 (1) – VV-polarisation (a). Classified image, threshold -19 dB (b). © ESA

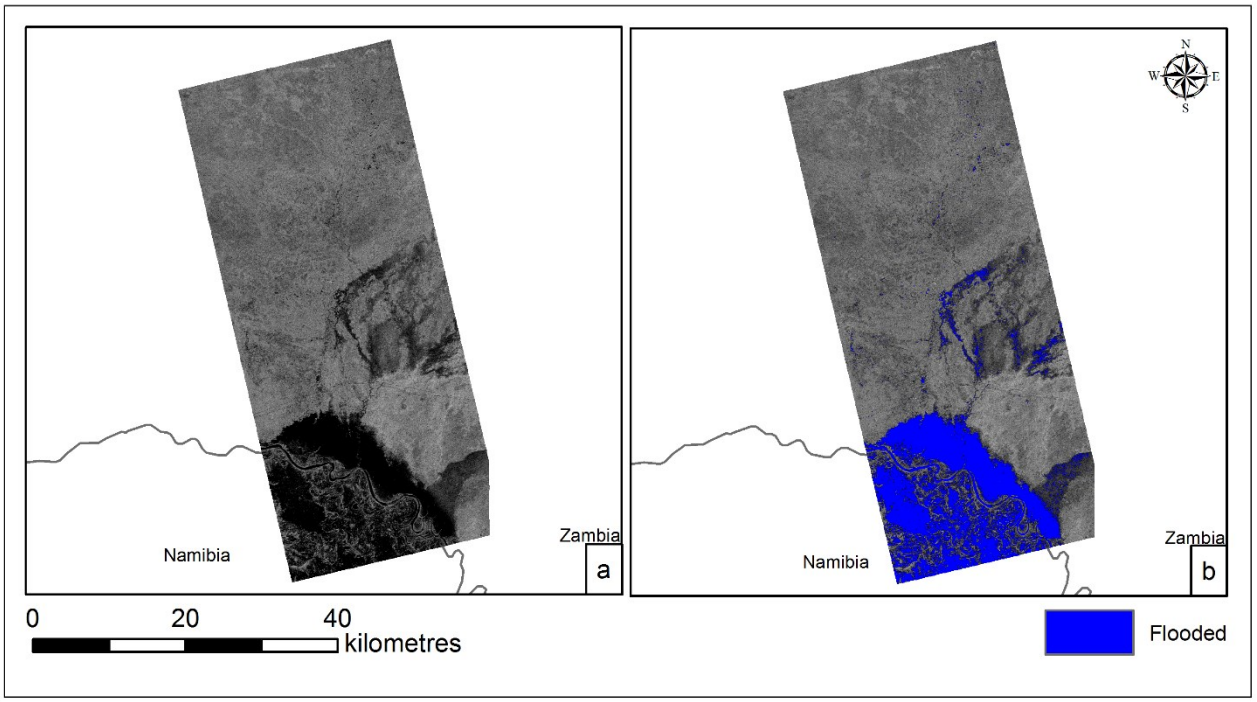

Figure E.15: Unclassified PALSAR PLR 19 March 2009 (2) – HH-polarisation (a). Classified image, threshold -21 dB (b). © ESA

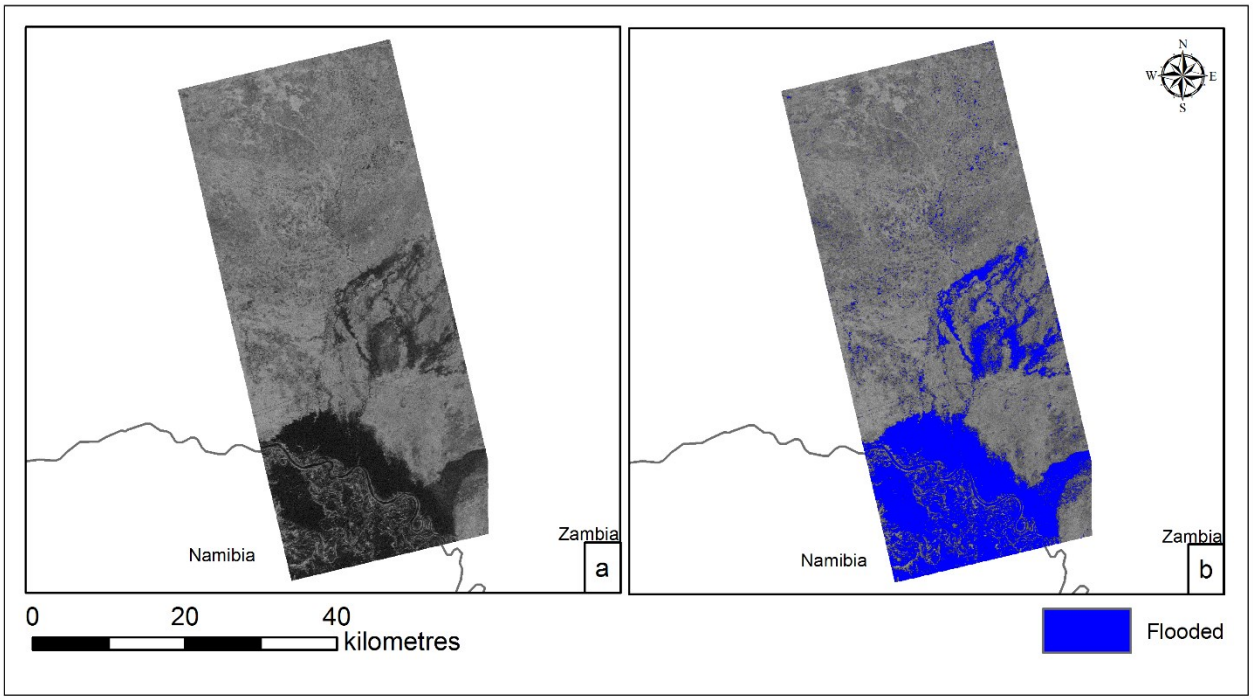

Figure E.16: Unclassified PALSAR PLR 19 March 2009 (2) – HV-polarisation (a). Classified image, threshold– -27 dB (b). © ESA

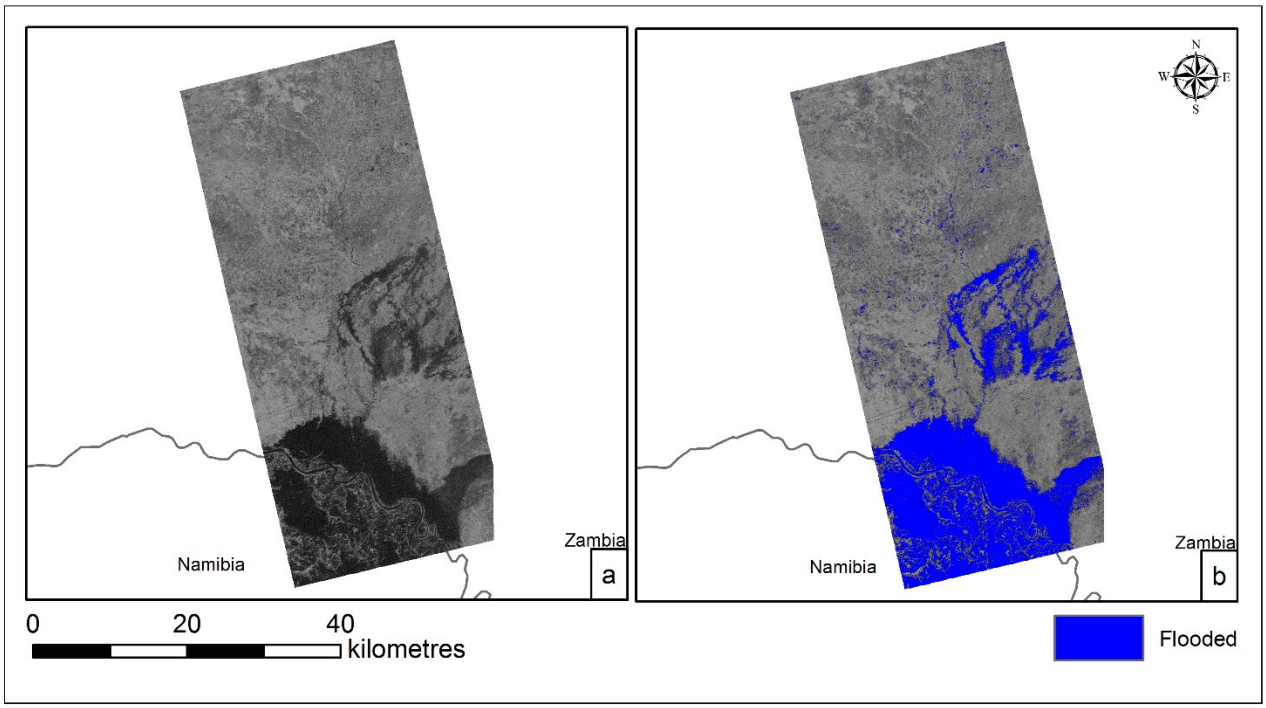

Figure E.17: Unclassified PALSAR PLR 19 March 2009 (2) – VH-polarisation (a). Classified image, threshold _– -27 dB (b). © ESA

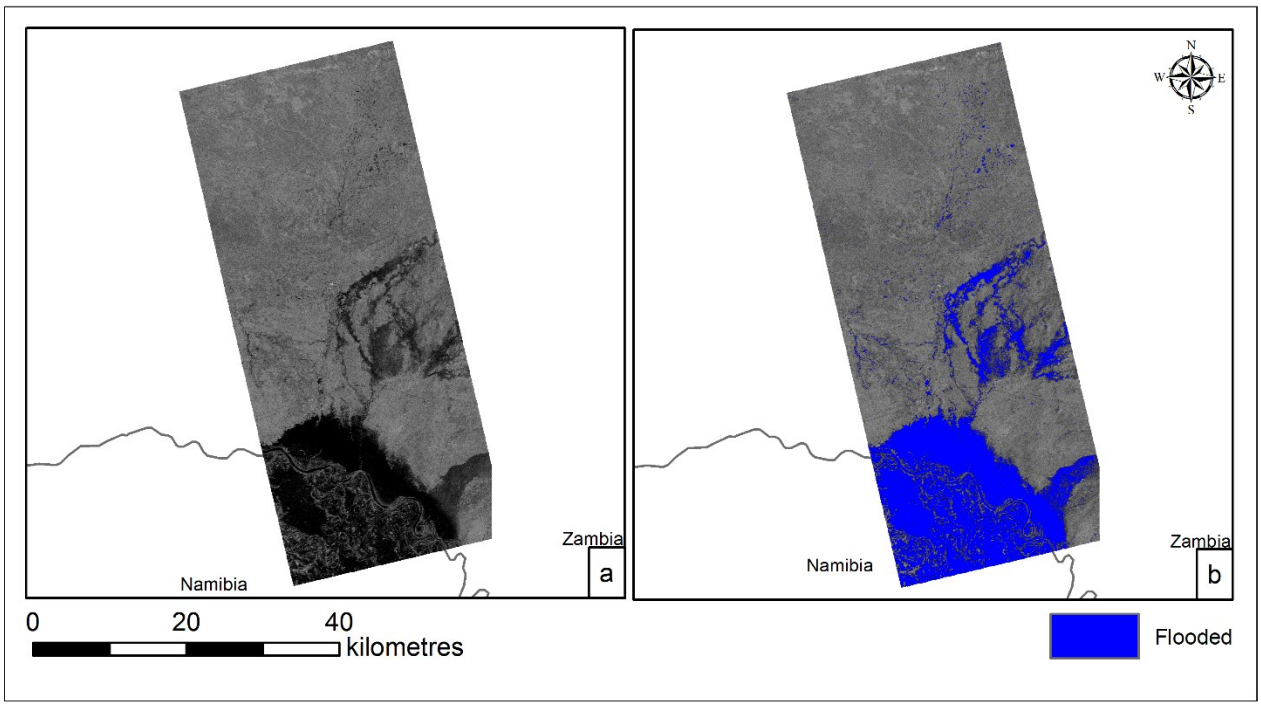

Figure E.18: Unclassified PALSAR PLR 19 March 2009 (2) – VV-polarisation (a). Classified image, threshold – -21 dB (b). © ESA

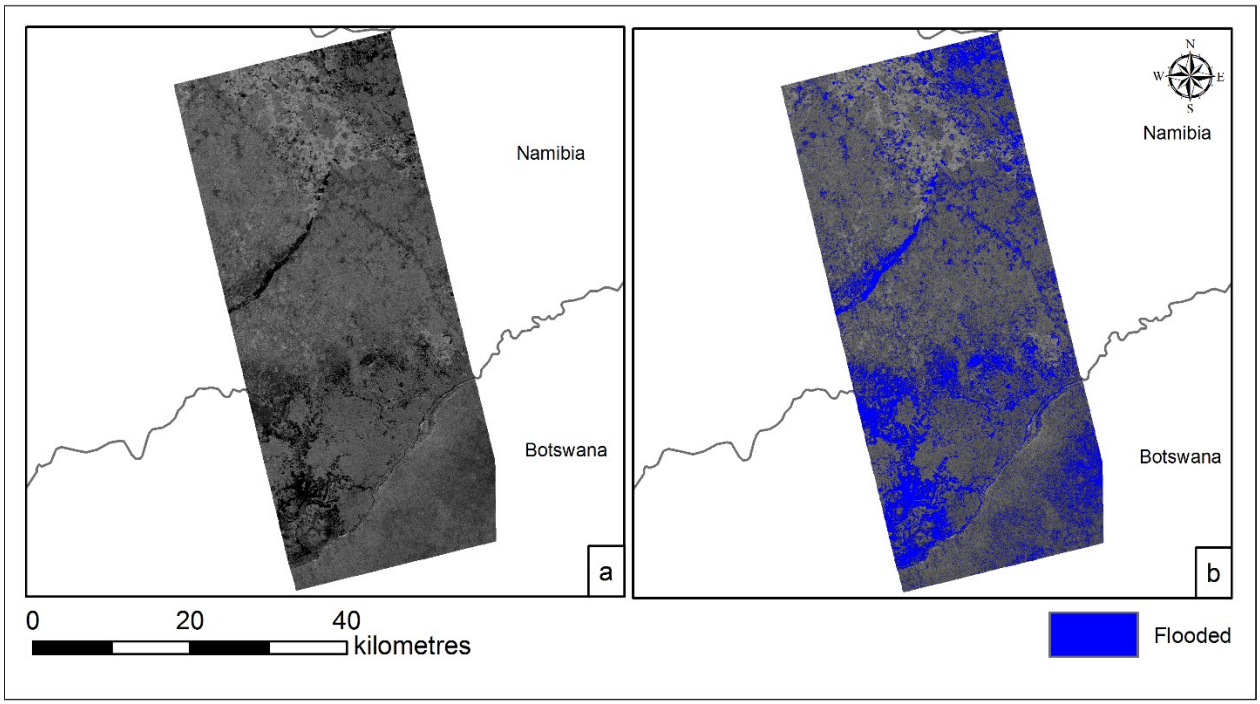

Figure E.19: Unclassified PALSAR PLR 5 April 2009 – HH-polarisation (a). Classified image, threshold – -17 dB (b). © ESA

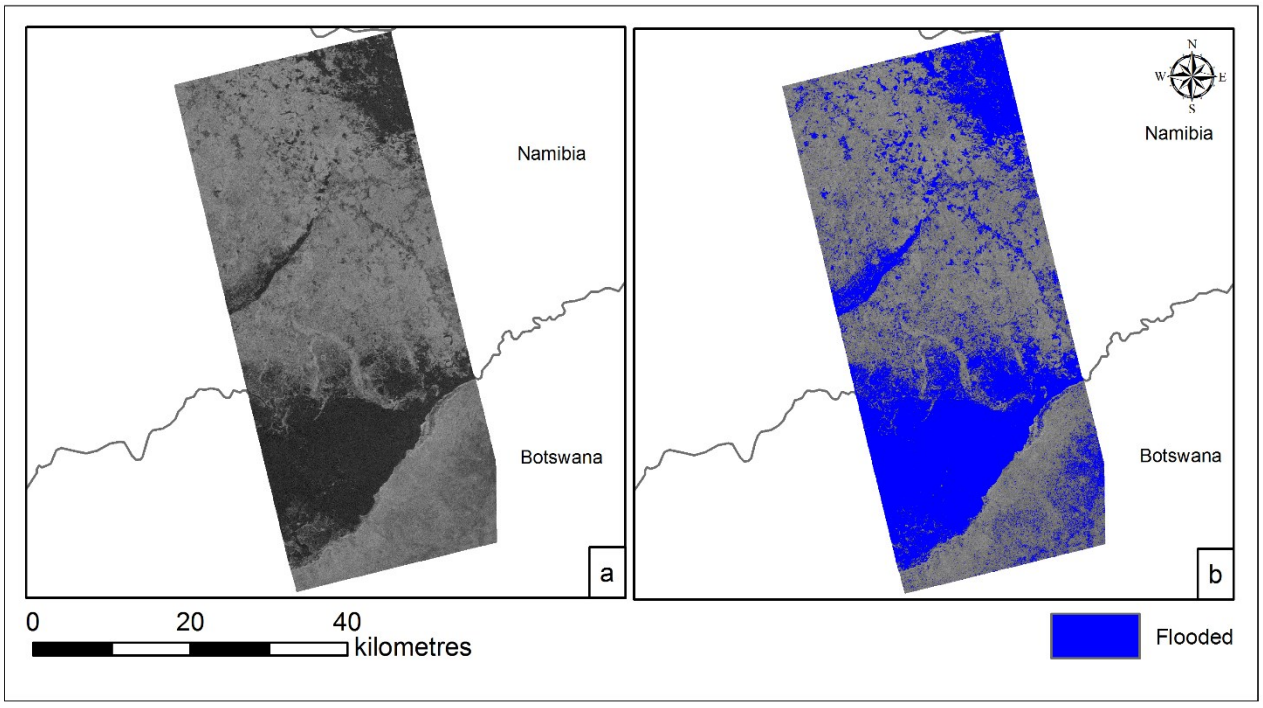

Figure E.20: Unclassified PALSAR PLR 5 April 2009 – HV-polarisation (a). Classified image, threshold – -24.5 dB (b). © ESA

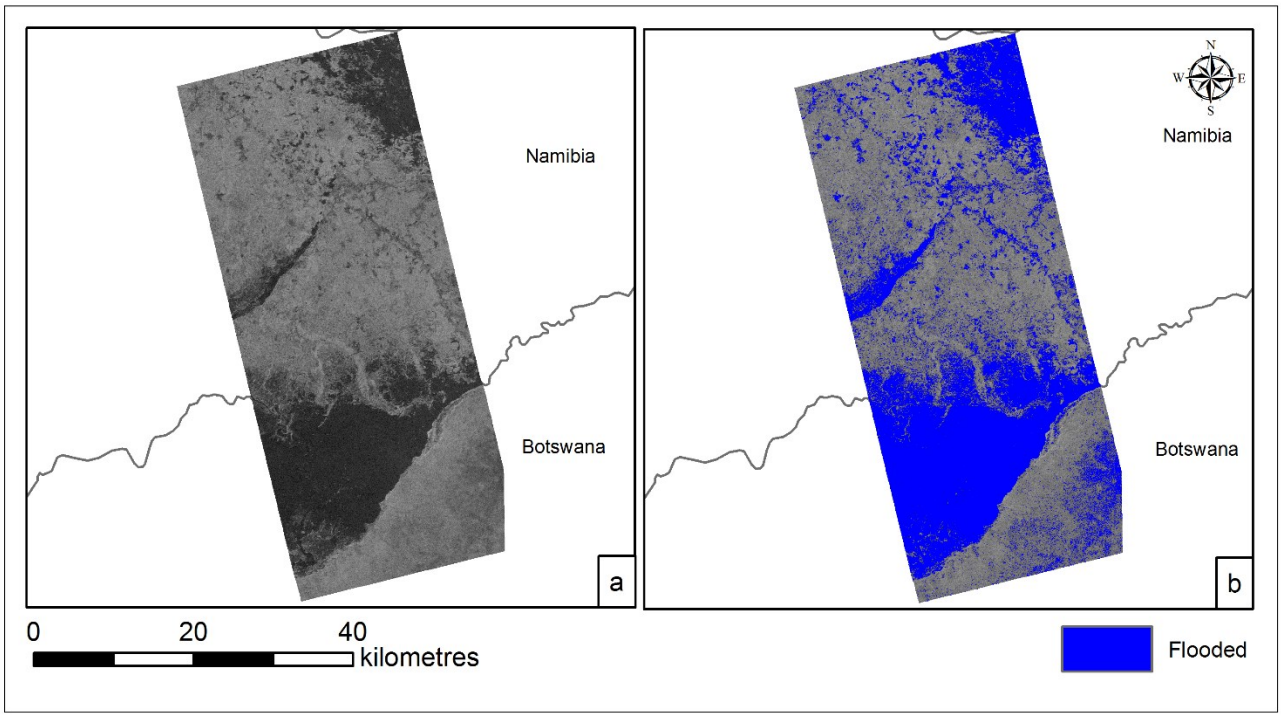

Figure E.21: Unclassified PALSAR PLR 5 April 2009 – VH-polarisation (a). Classified image, threshold – -4.5 dB (b). © ESA

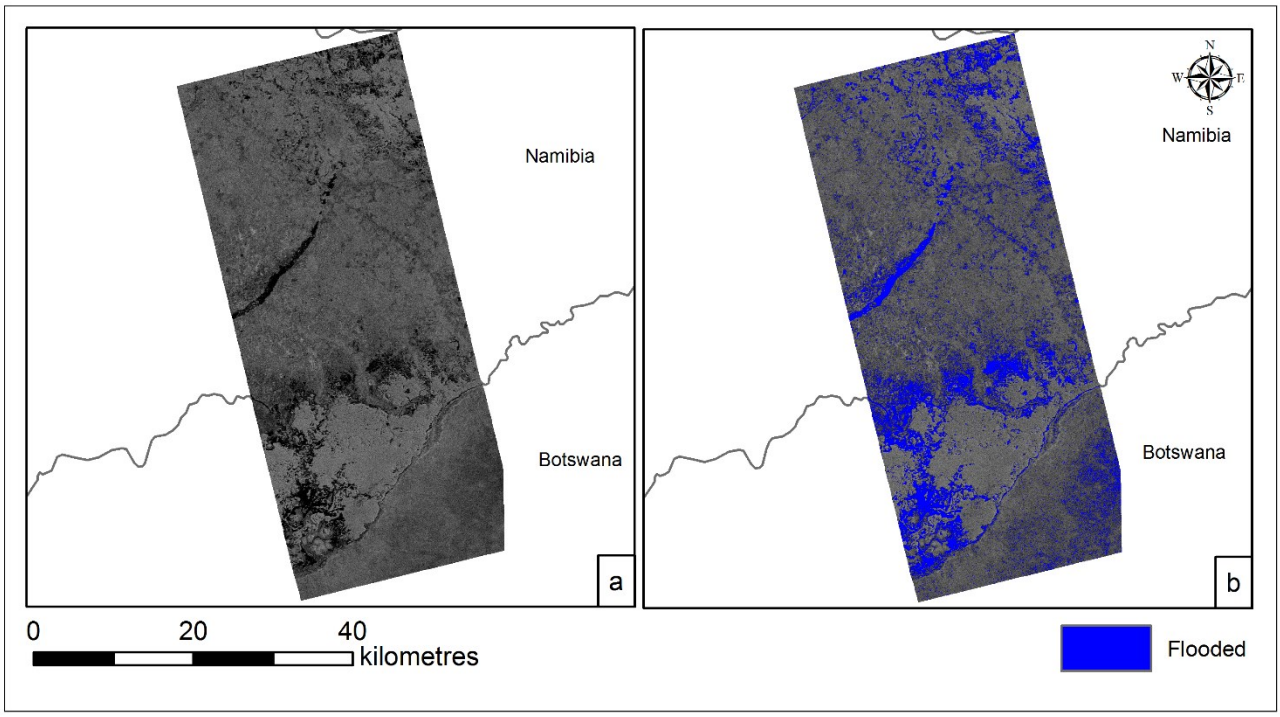

Figure E.22: Unclassified PALSAR PLR 5 April 2009 – VV-polarisation (a). Classified image, threshold – -19 dB (b). © ESA

D.2: ACTIVE CONTOUR MODELS

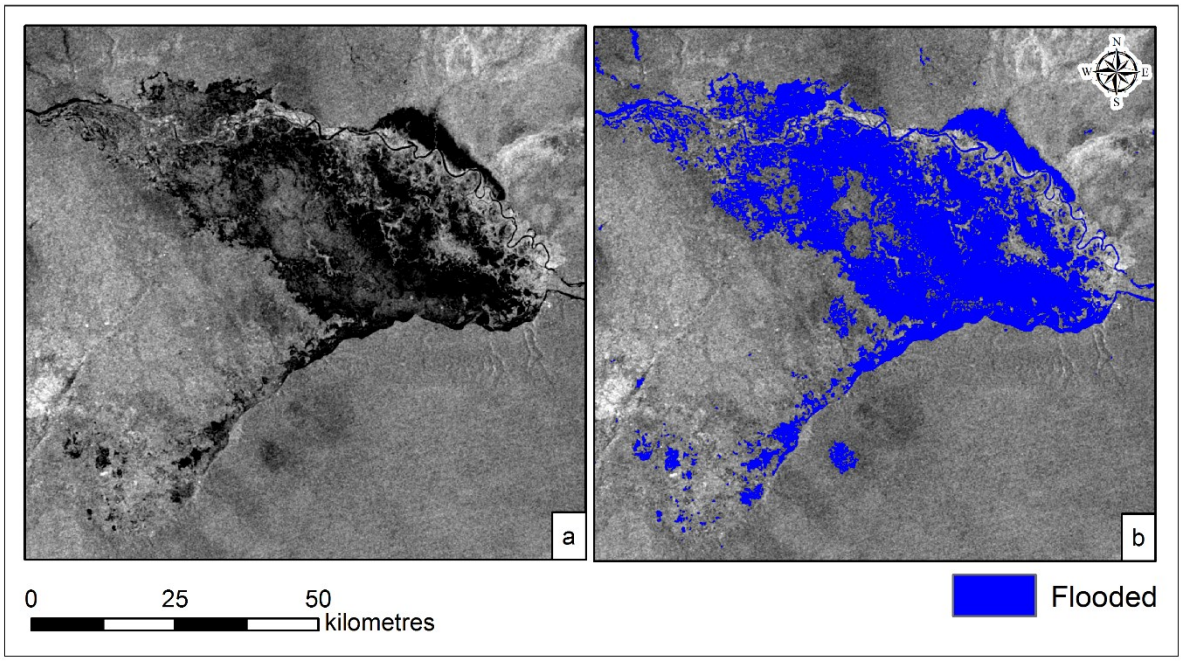

Figure E.23: Unclassified ASAR WSM 17 March 2009 (a). Classified image, Iterations – 1000. Canny scalar – 0.2 (b)

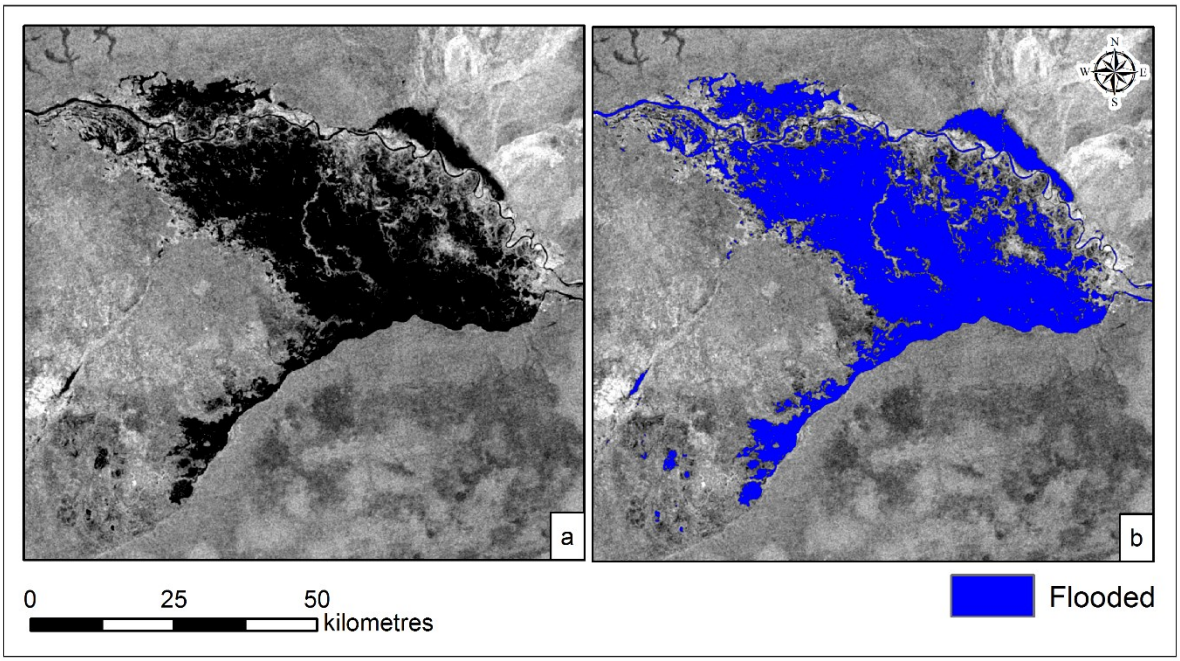

Figure E.24: Unclassified ASAR WSM 20 March 2009 (a). Classified image, Iterations – 1000. Canny scalar – 0.3 (b)

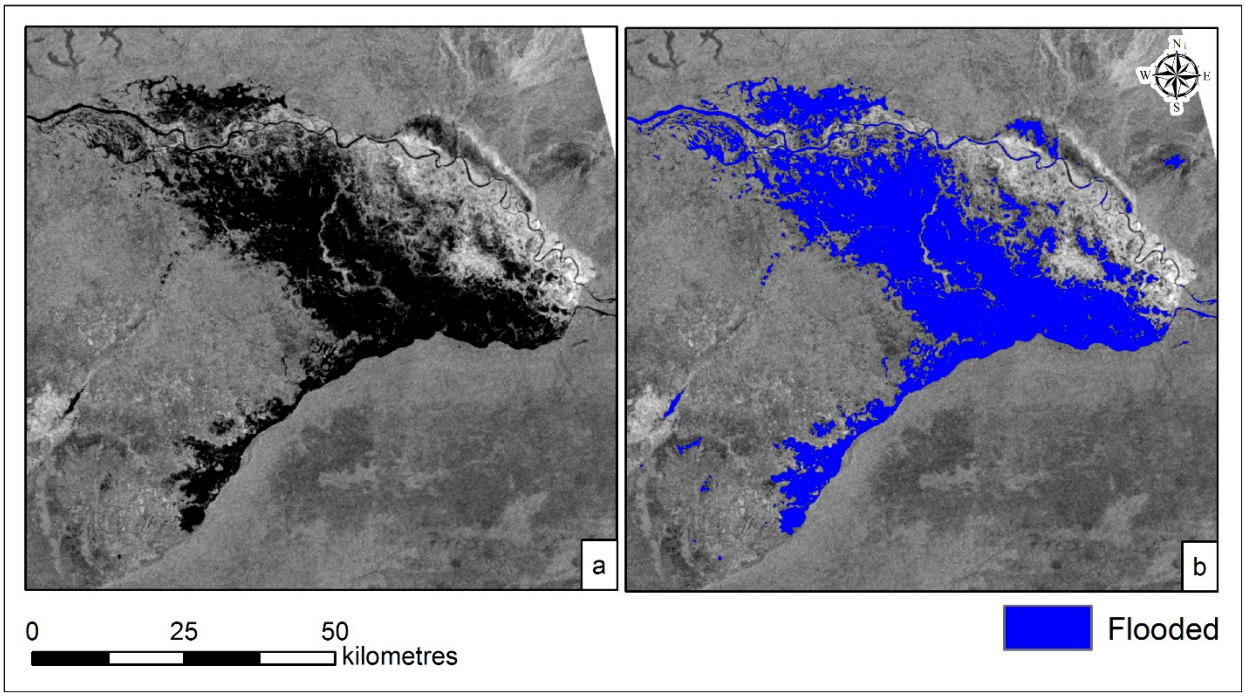

Figure E.25: Unclassified ASAR WSM 23 March 2009 (a). Classified image, Iterations – 1000. Canny scalar – 0.3 (b)

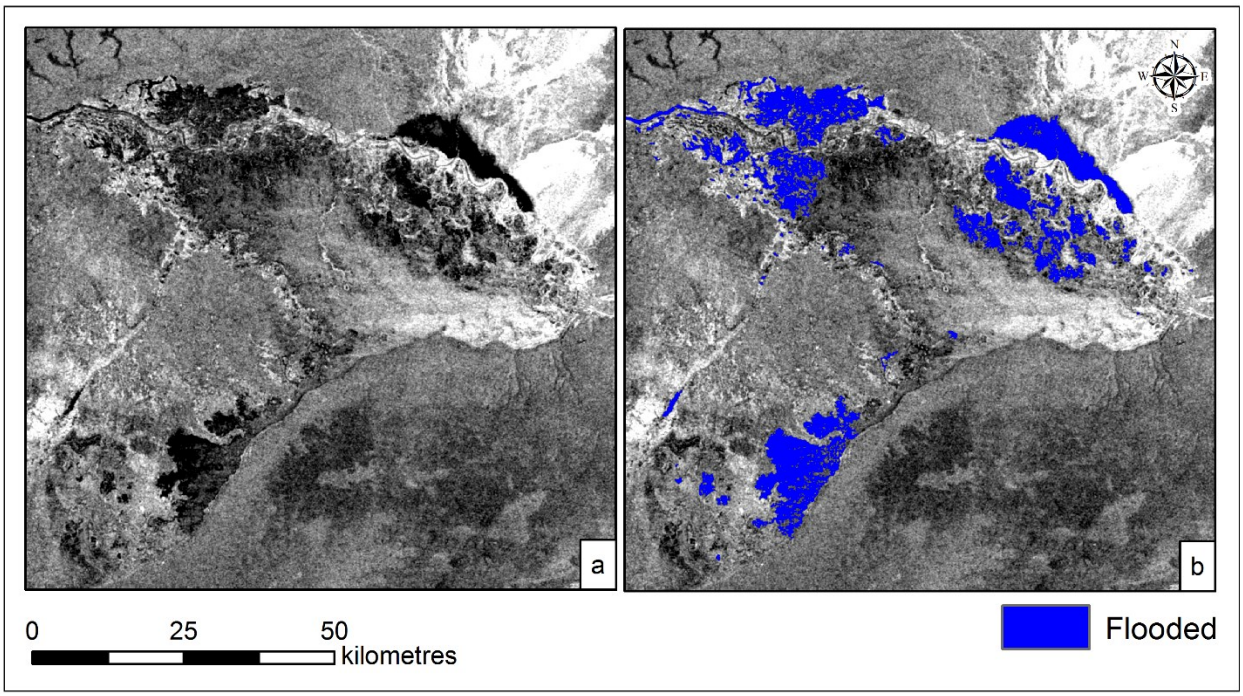

Figure E.26: Unclassified ASAR WSM 24 March 2009 (a). Classified image, Iterations – 1000. Canny scalar – 0.4 (b)

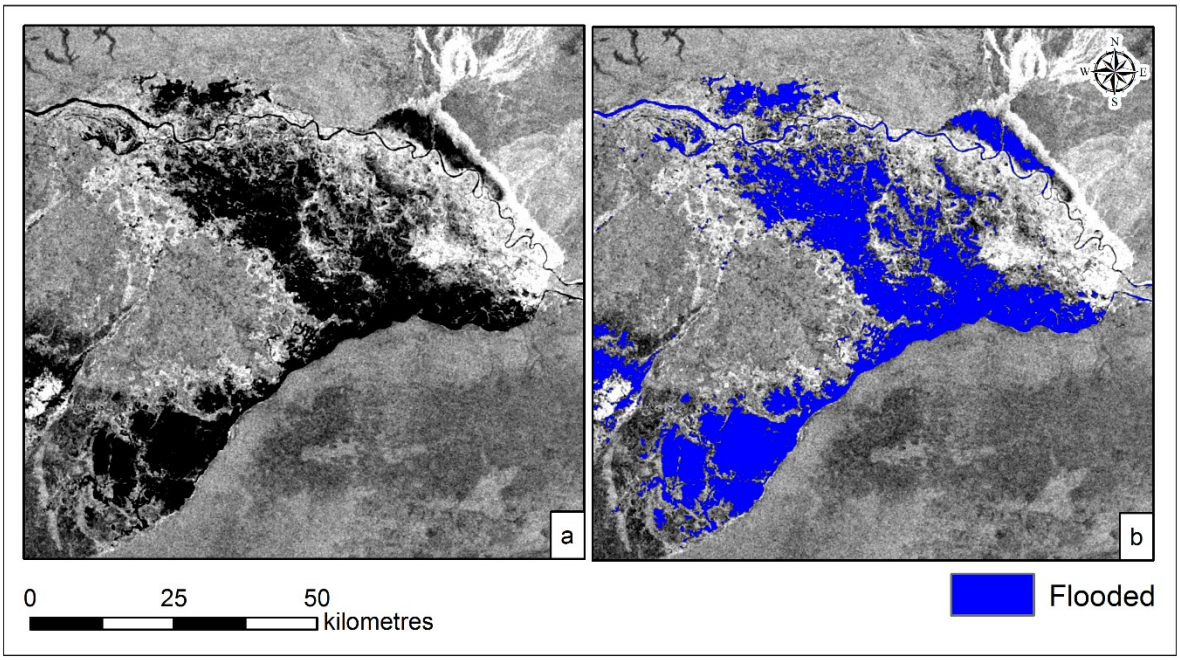

Figure E.27: Unclassified ASAR WSM 25 April 2009 (a). Classified image, Iterations – 1000. Canny scalar – 0.3 (b)

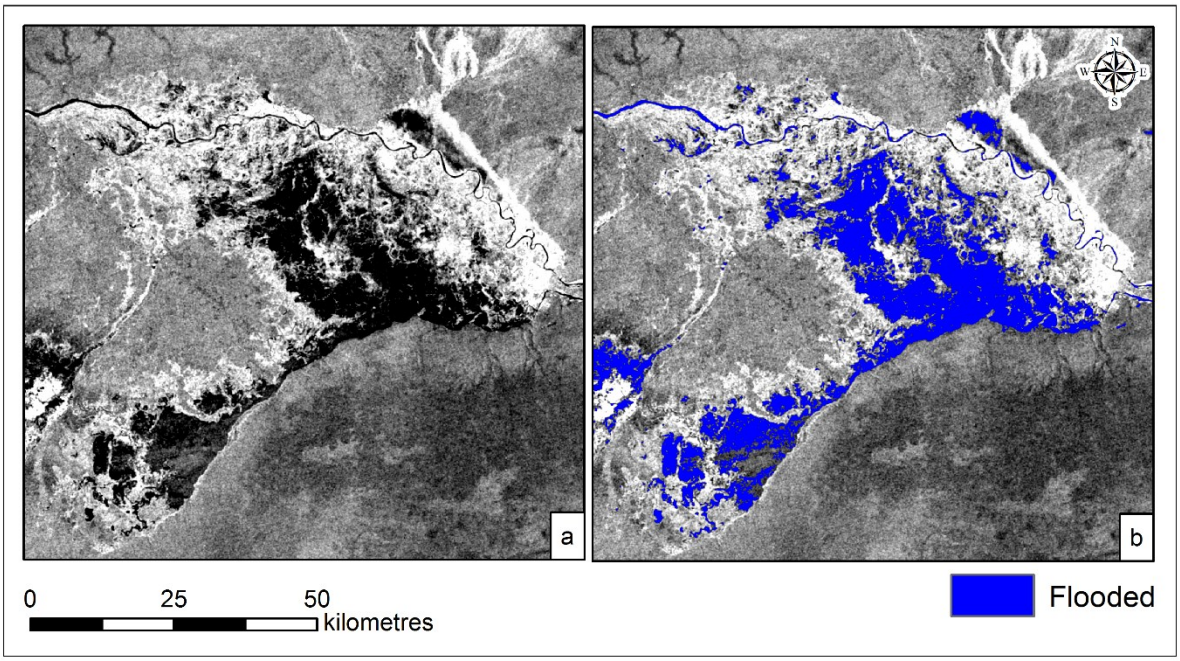

Figure E.28: Unclassified ASAR WSM 10 May 2009 (a). Classified image, Iterations – 1000. Canny scalar – 0.3 (b)

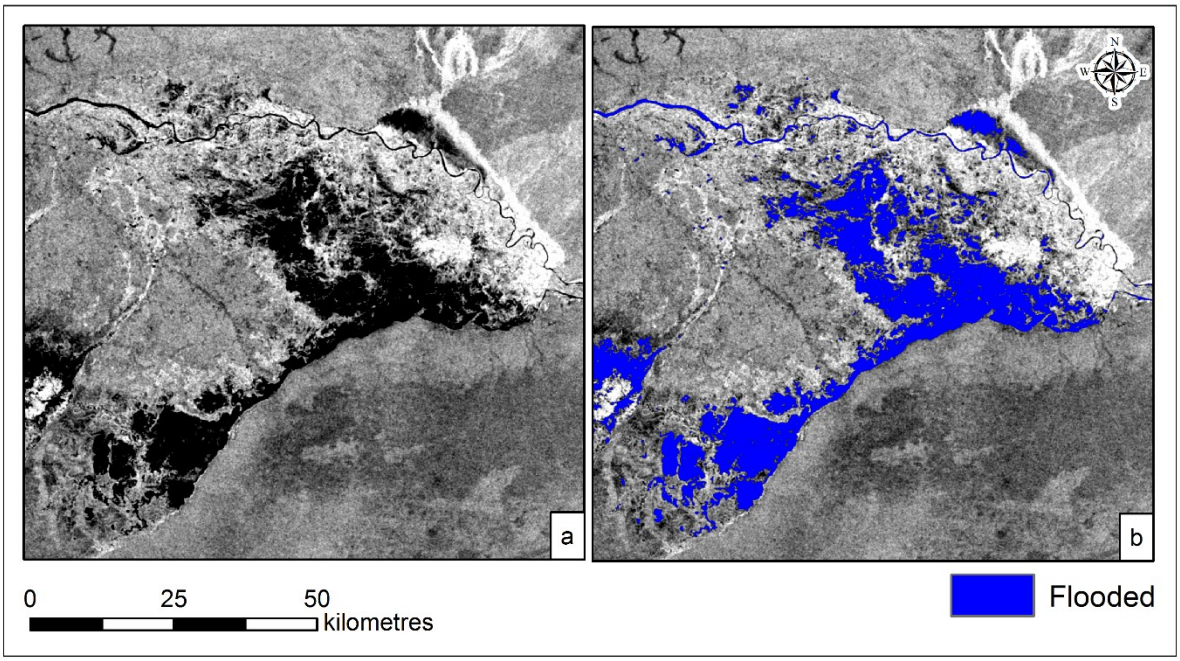

Figure E.29: Unclassified ASAR WSM 11 May 2009 (a). Classified image, Iterations – 1000. Canny scalar – 0.3 (b)

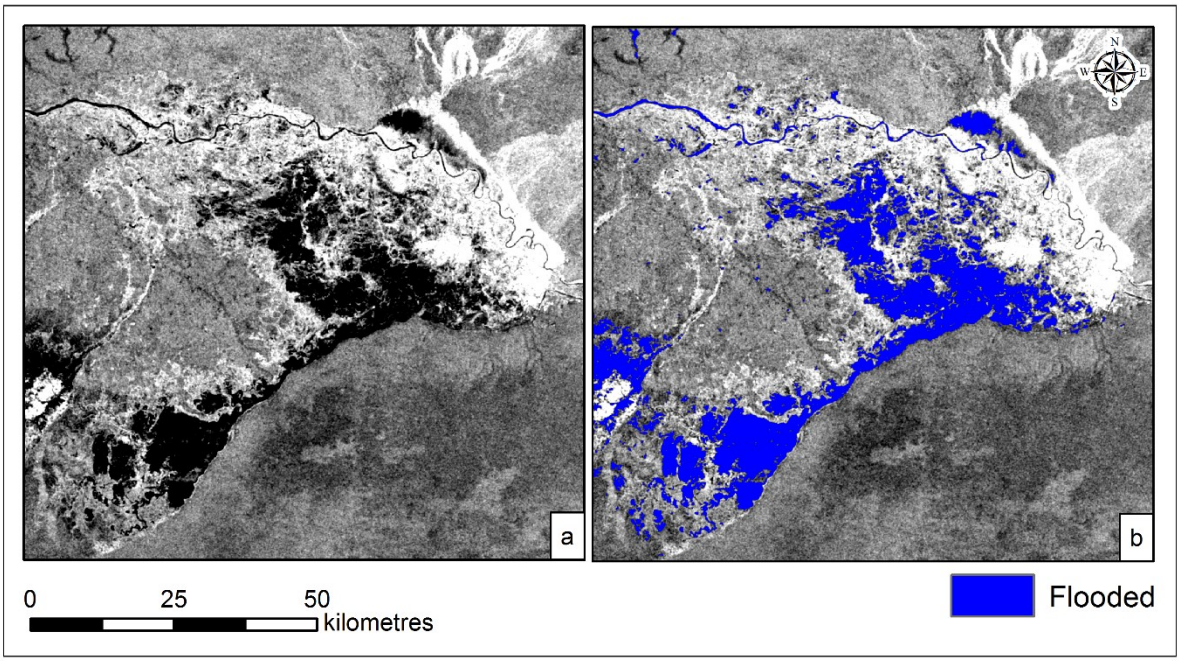

Figure E.30: Unclassified ASAR WSM 14 May 2009 (a). Classified image, Iterations – 1000. Canny scalar – 0.3 (b)

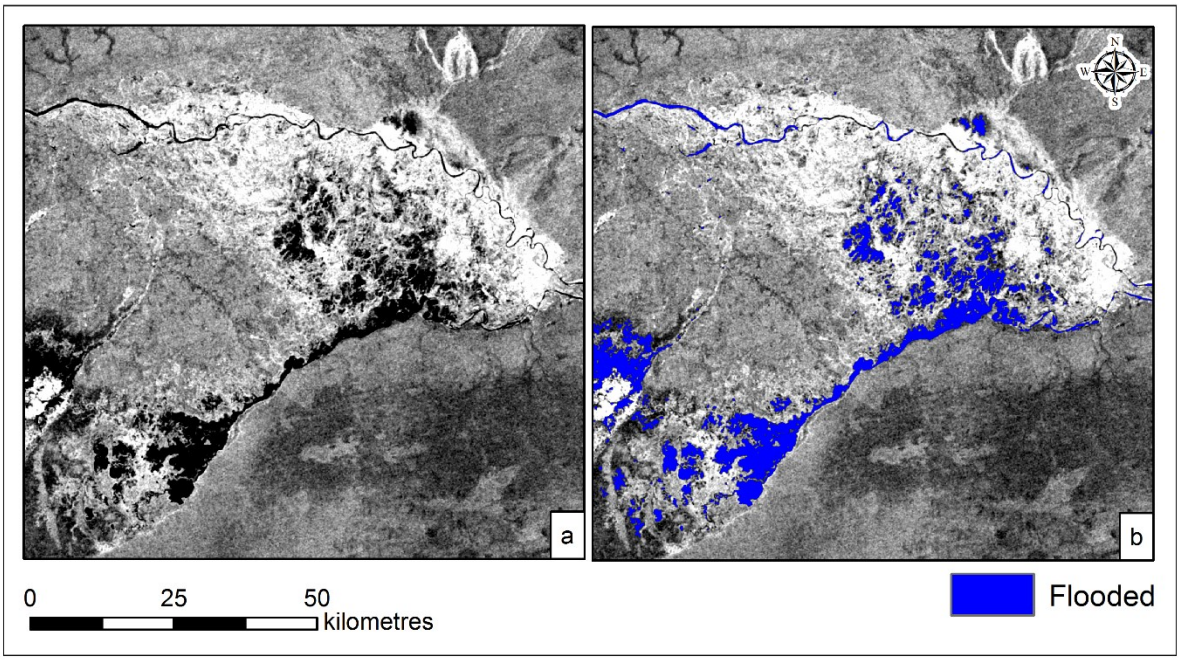

Figure E.31: Unclassified ASAR WSM 29 May 2009 (a). Classified image, Iterations – 1000. Canny scalar – 0.3 (b)

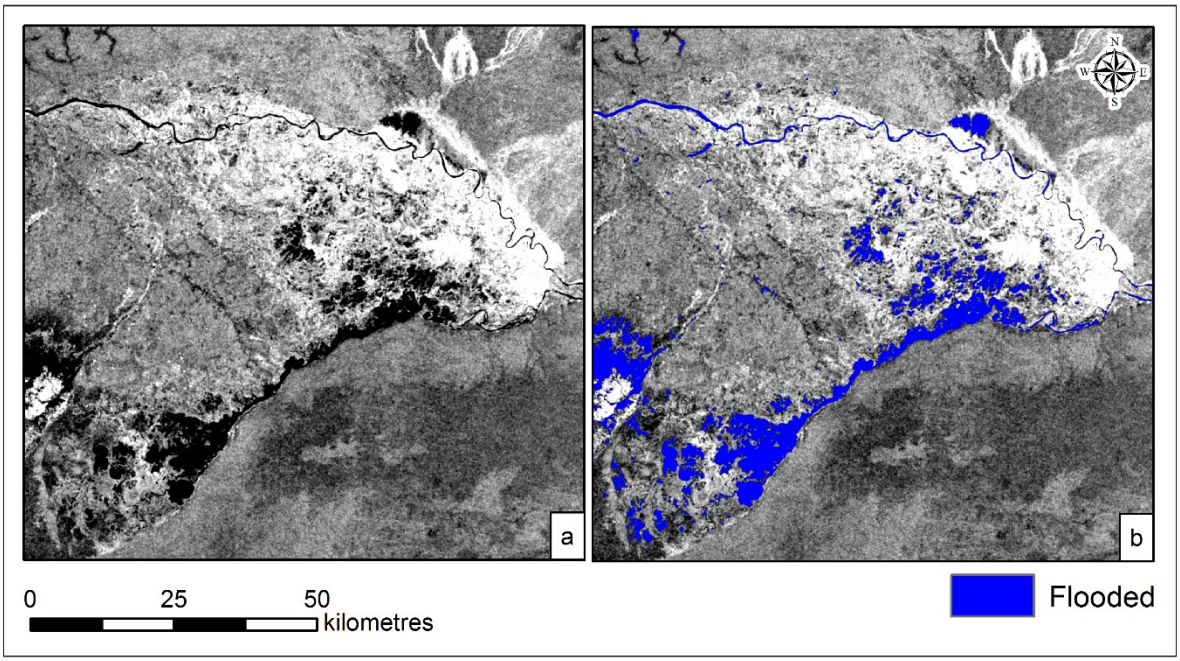

Figure E.32 Unclassified ASAR WSM 30 May 2009 (a). Classified image, Iterations – 1000. Canny scalar – 0.3 (b)

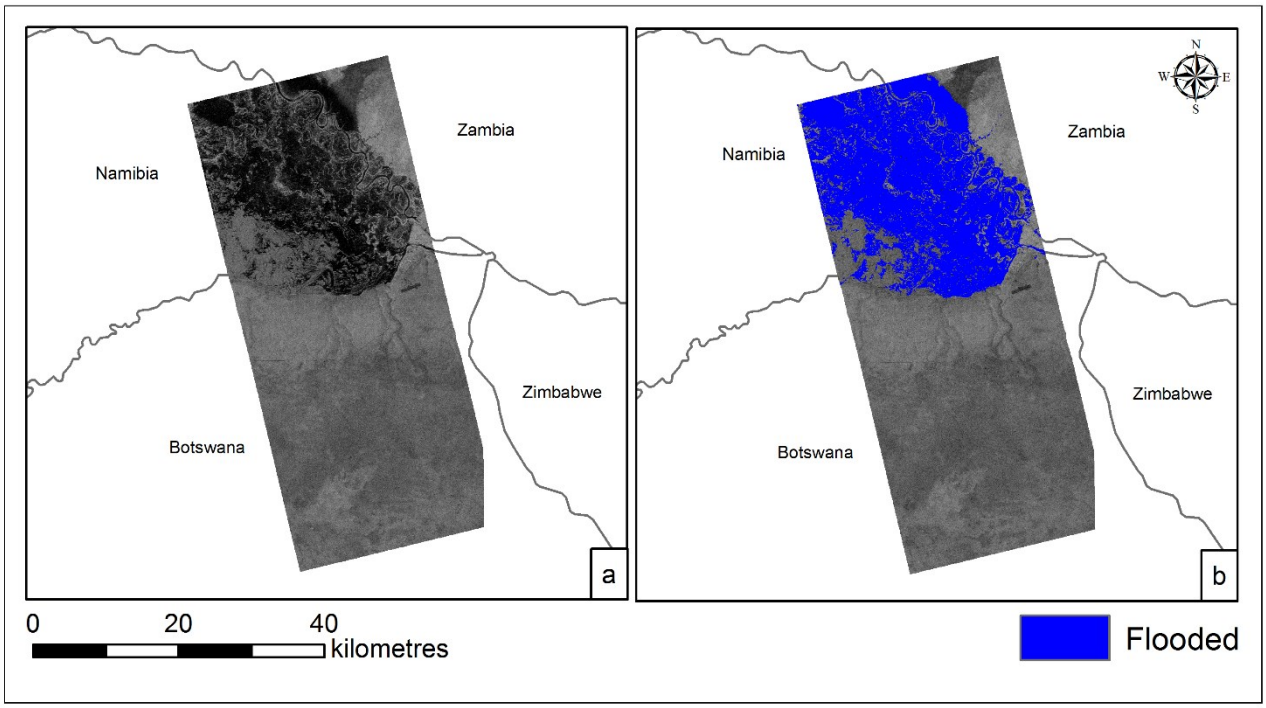

Figure E.33: Unclassified PALSAR PLR 19 March 2009 (1) – HH-polarisation (a). Classified image, Iterations – 200. Canny scalar – 0.3 (b). © ESA

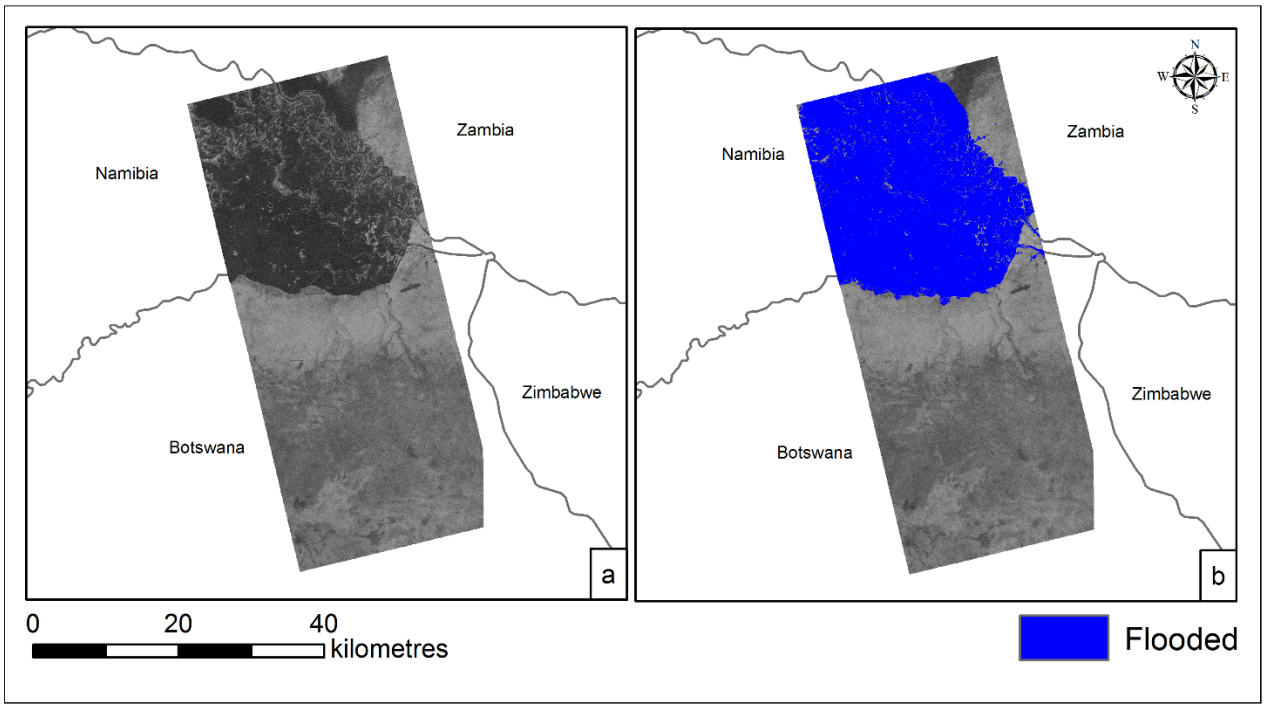

Figure E.34: Unclassified PALSAR PLR 19 March 2009 (1) – HV-polarisation (a). Classified image, Iterations – 300. Canny scalar – 0.3 (b)

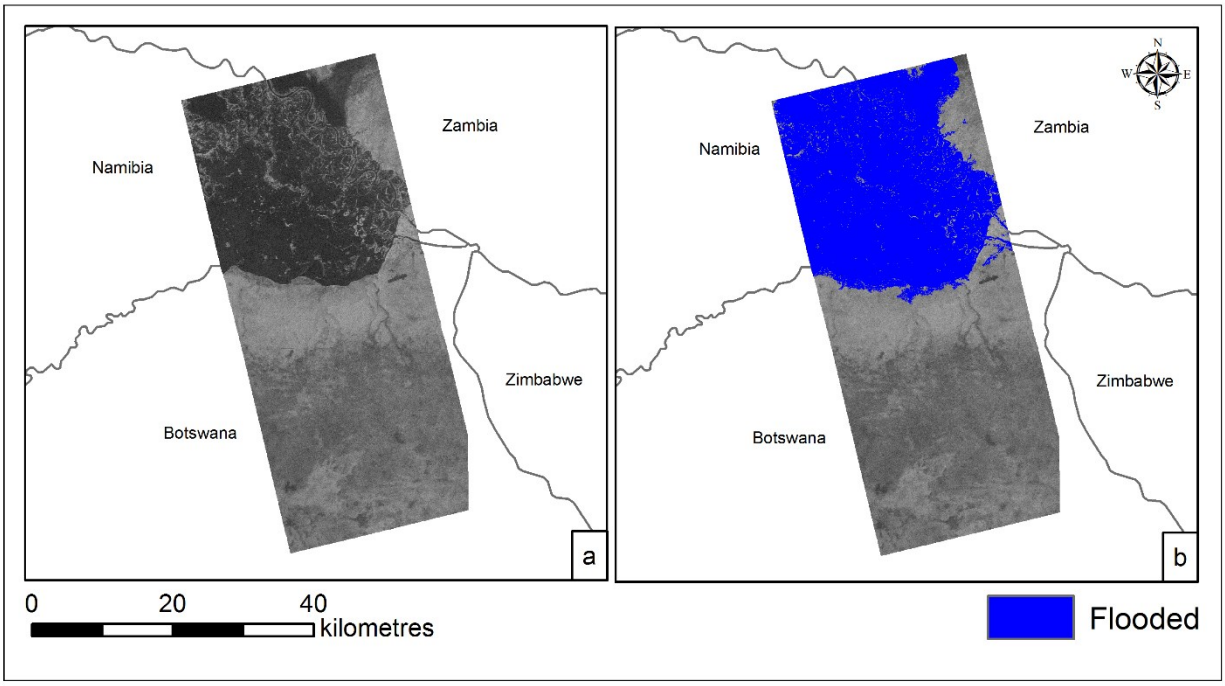

Figure E.35: Unclassified PALSAR PLR 19 March 2009 (1) – VH-polarisation (a). Classified image, Iterations – 1000. Canny scalar – 0.3 (b). © ESA

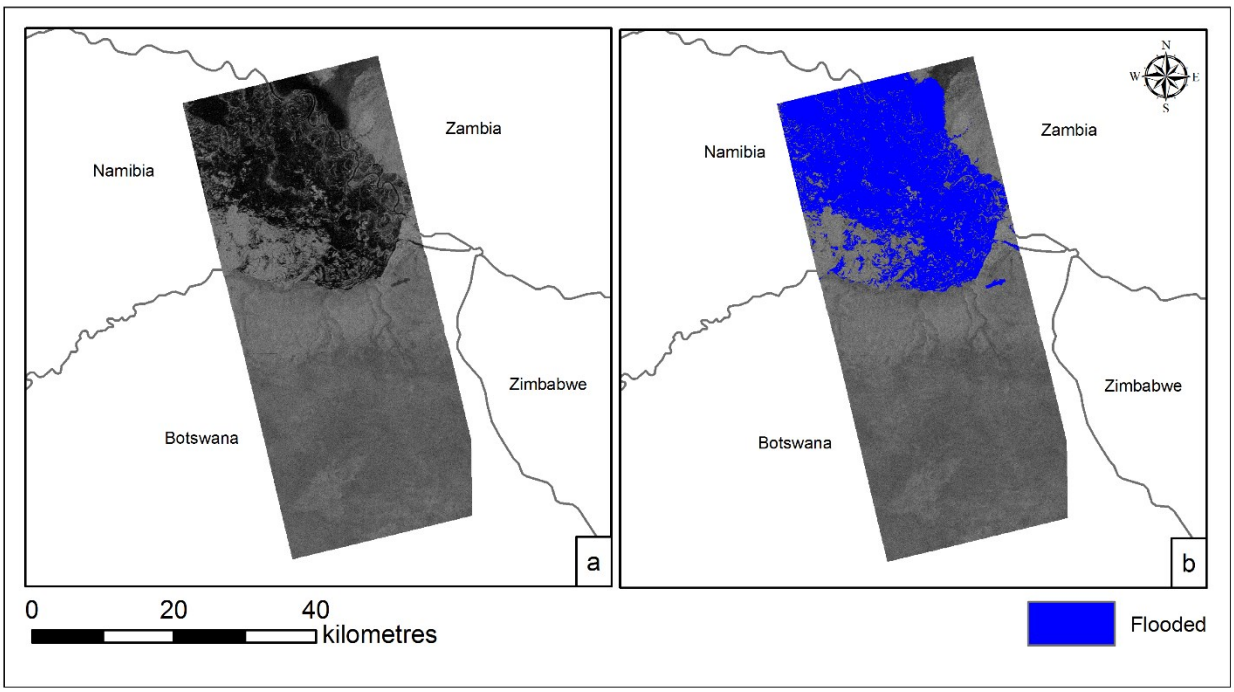

Figure E.36: Unclassified PALSAR PLR 19 March 2009 (1) – VV-polarisation (a). Classified image, Iterations – 500. Canny scalar – 0.3 (b). © ESA

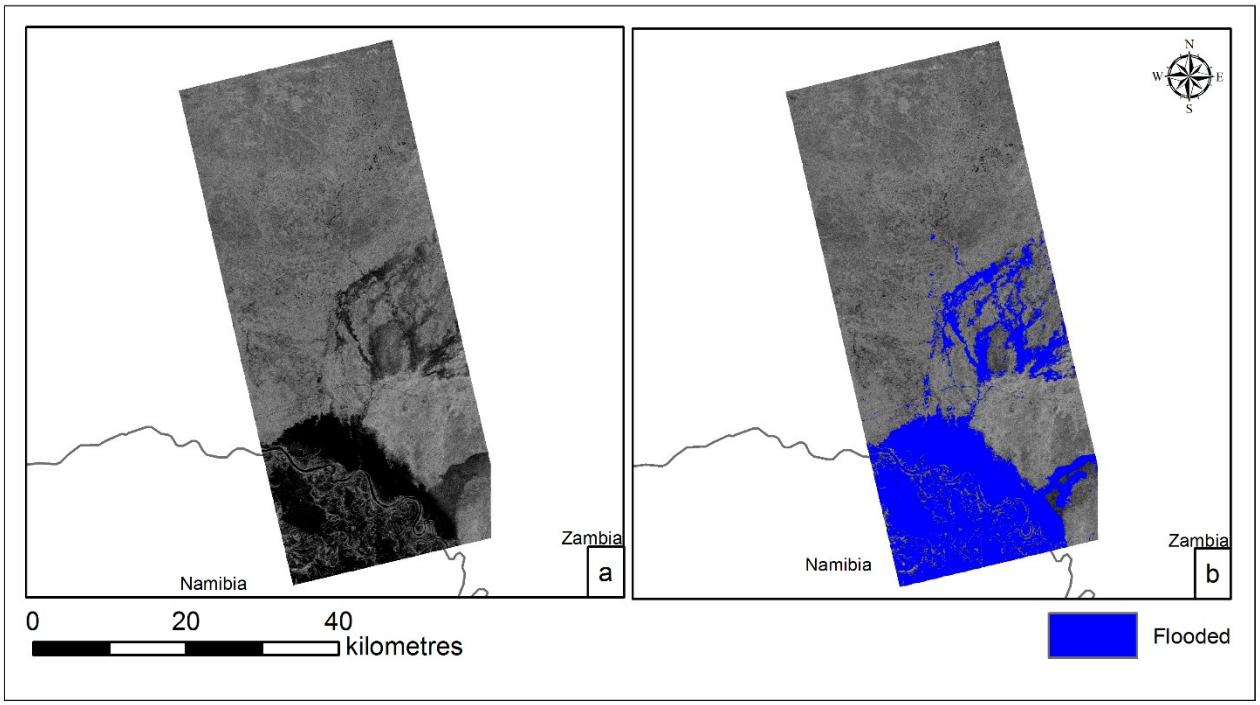

Figure E.37: Unclassified PALSAR PLR 19 March 2009 (2) – HH-polarisation (a). Classified image, Iterations _– 200. Canny scalar – 0.3 (b). © ESA

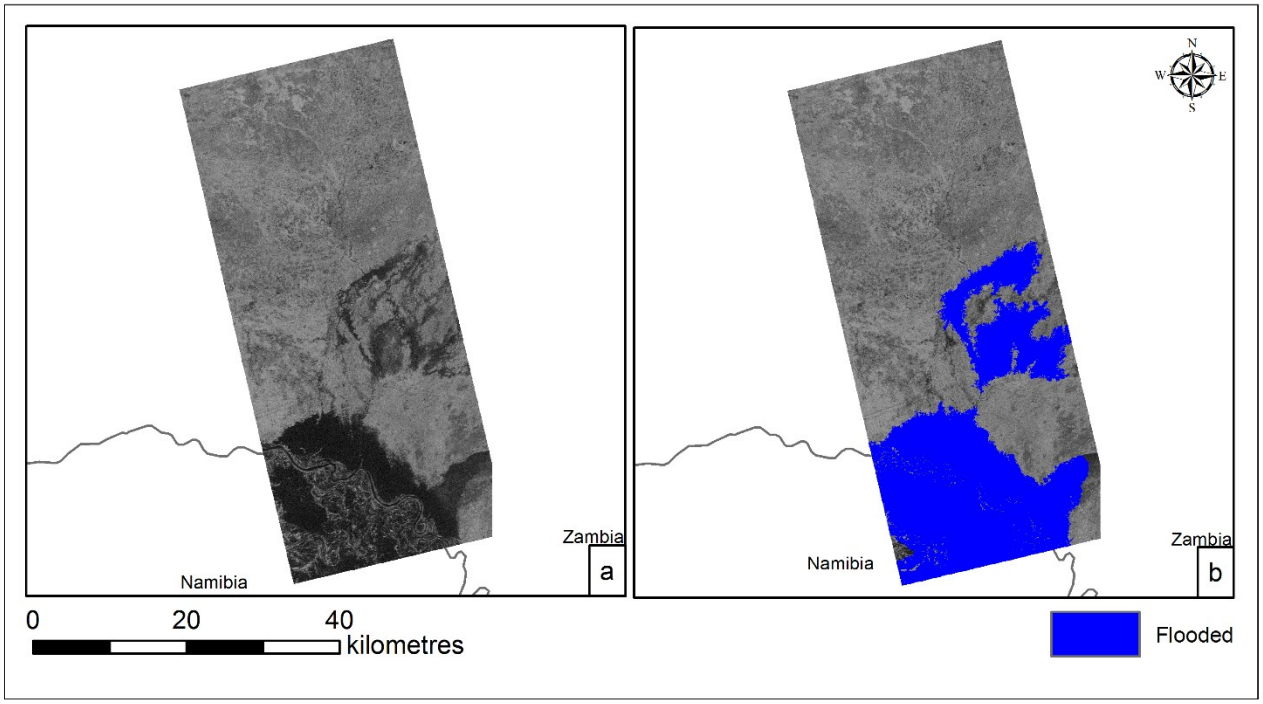

Figure E.38: Unclassified PALSAR PLR 19 March 2009 (2) – HV-polarisation (a). Classified image, Iterations – 200. Canny scalar – 0.3 (b). © ESA

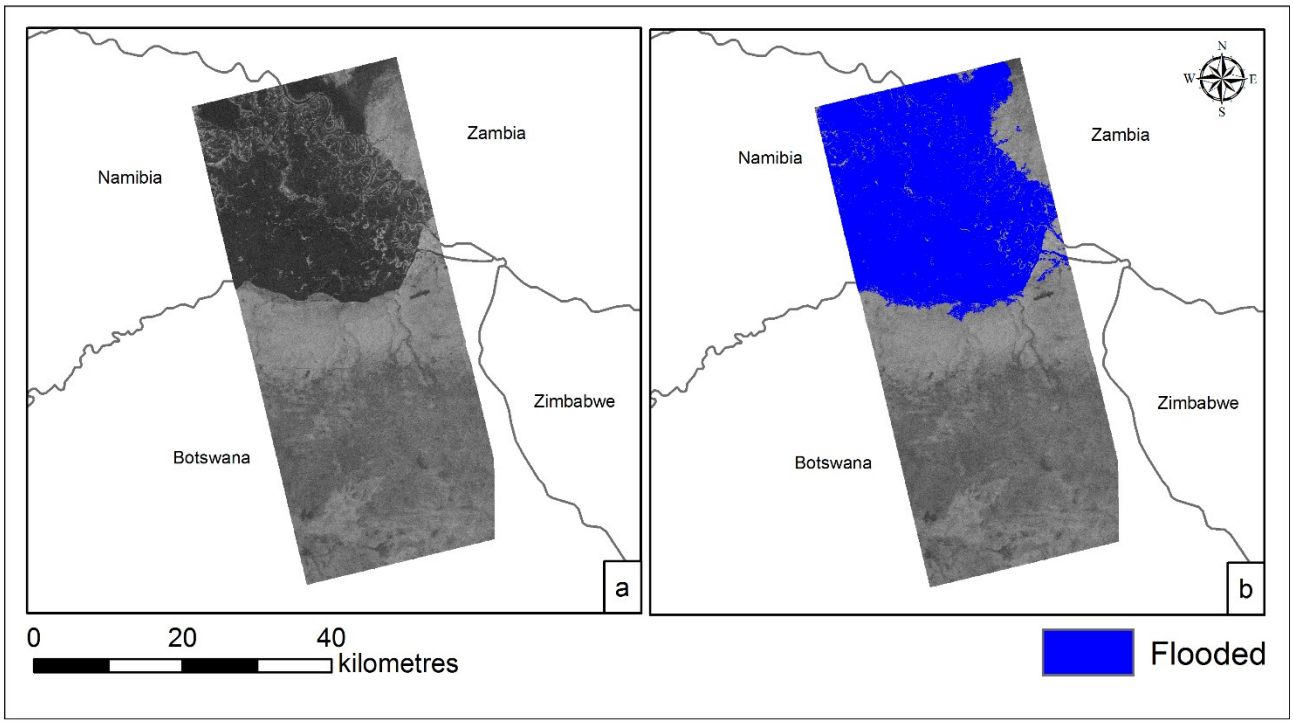

Figure E.39: Unclassified PALSAR PLR 19 March 2009 (2) – VH-polarisation (a). Classified image, Iterations – 200. Canny scalar – 0.3 (b). © ESA

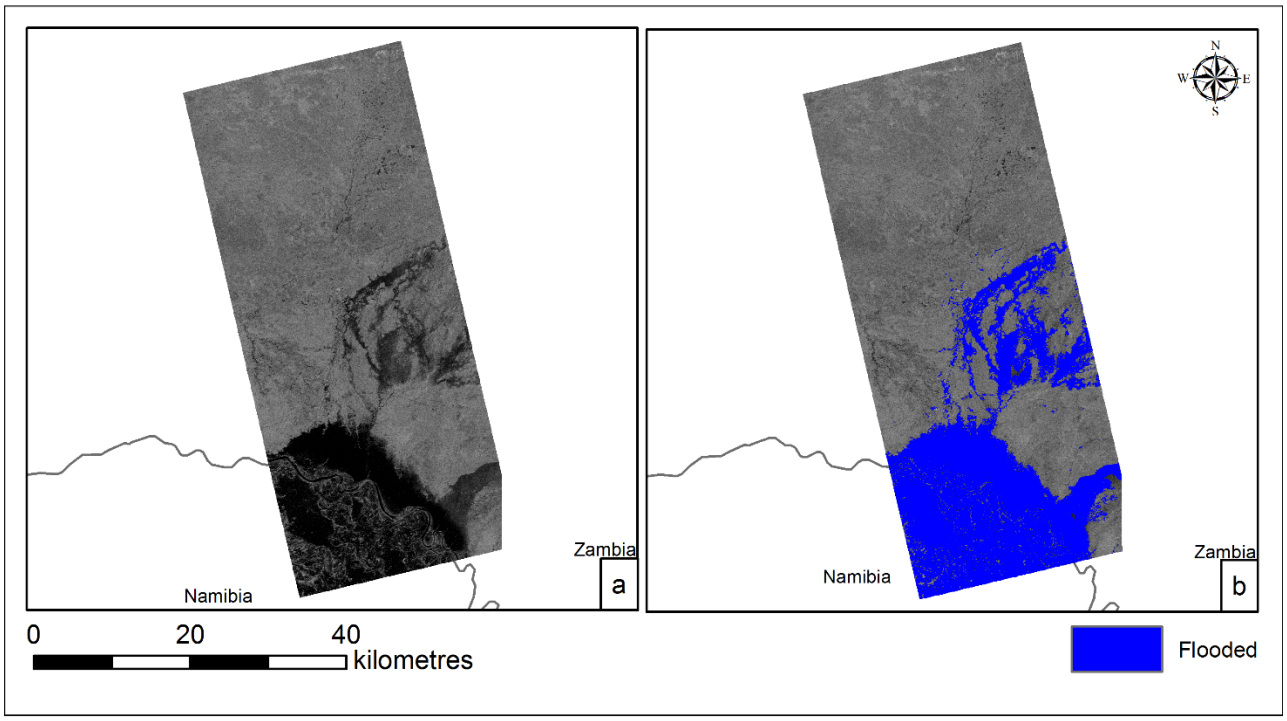

Figure E.40: Unclassified PALSAR PLR 19 March 2009 (2) – VV-polarisation (a). Classified image, Iterations – 200. Canny scalar – 0.3 (b). © ESA

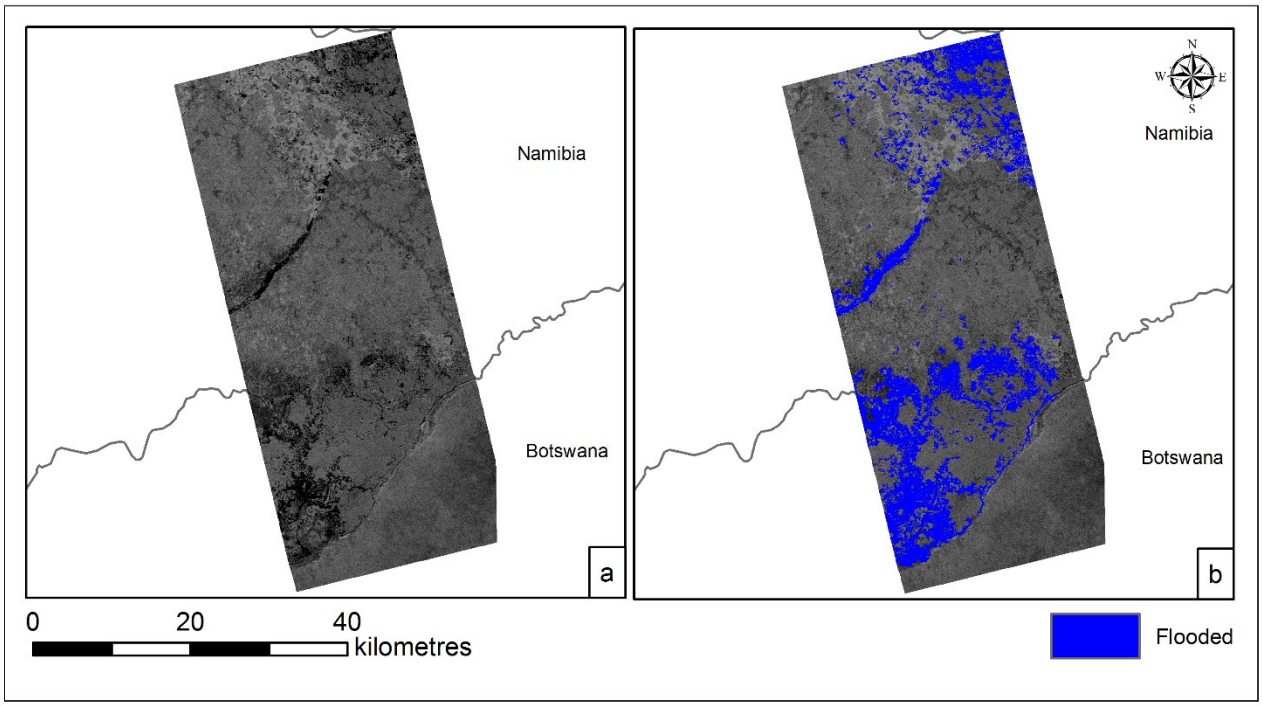

Figure E.41: Unclassified PALSAR PLR 5 April 2009 – HH-polarisation (a). Classified image, Iterations –100. Canny scalar – 0.3 (b). © ESA

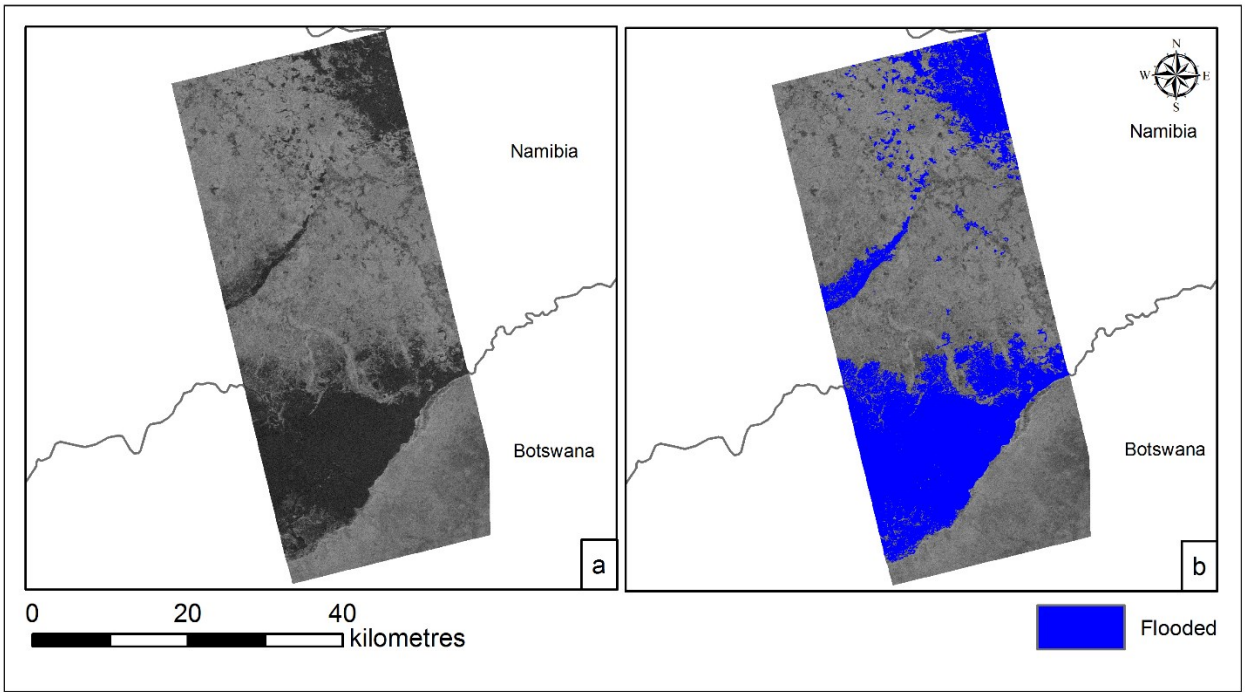

Figure E.42: Unclassified PALSAR PLR 5 April 2009 – HV-polarisation (a). Classified image, Iterations – 700. Canny scalar – 0.3 (b). © ESA

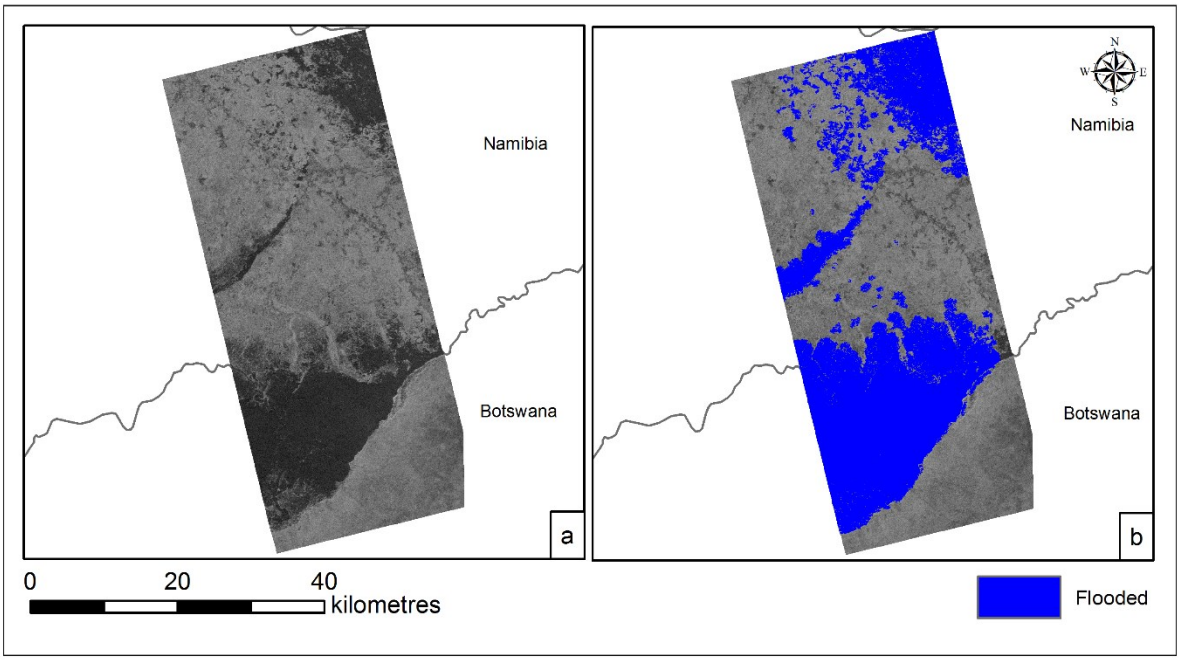

Figure E.43: Unclassified PALSAR PLR 5 April 2009 – VH-polarisation (a). Classified image, Iterations – 200. Canny scalar – 0.3 (b). © ESA

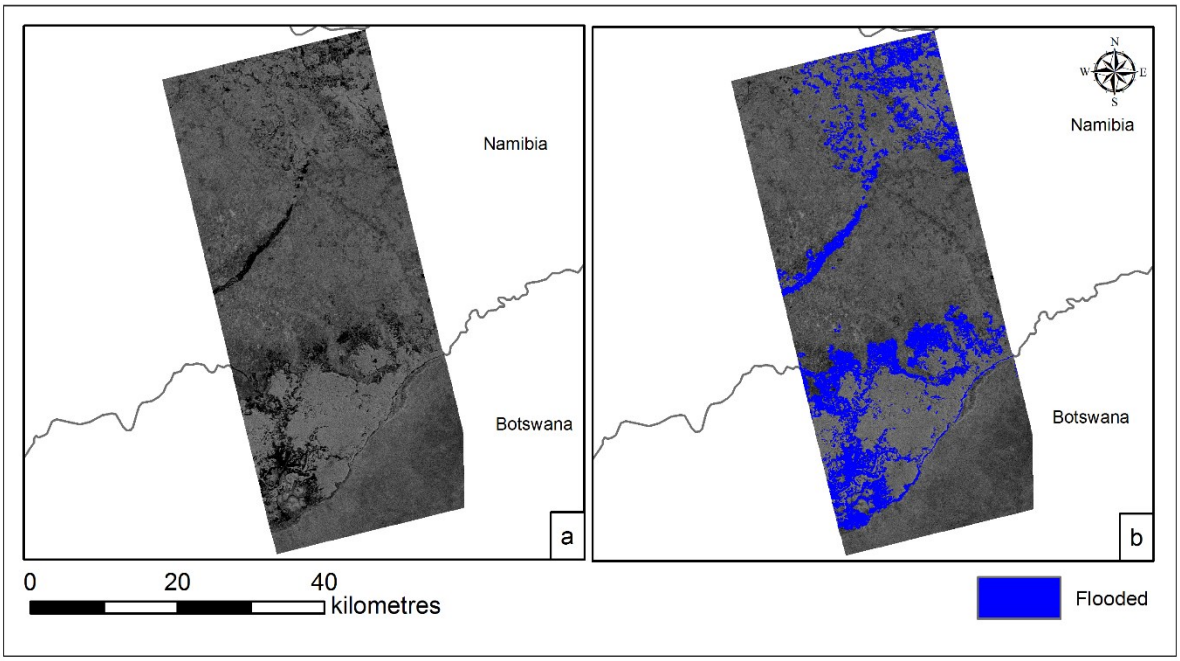

Figure E.44: Unclassified PALSAR PLR 5 April 2009 – VV-polarisation (a). Classified image, Iterations – 100. - Canny scalar – 0.3 (b). © ESA